

**Mechanization and Assessment of Regenerative Therapies for Peripheral Nerve Injury and  
the Associated Muscle Atrophy**

by

**Benjamin K. Schilling**

Bachelor of Science, Rensselaer Polytechnic Institute, 2012

Master of Science, University of Pittsburgh, 2017

Submitted to the Graduate Faculty of the  
Swanson School of Engineering in partial fulfillment  
of the requirements for the degree of  
Doctor of Philosophy

University of Pittsburgh

2021

UNIVERSITY OF PITTSBURGH

SWANSON SCHOOL OF ENGINEERING

This dissertation was presented

by

**Benjamin K. Schilling**

It was defended on

March 8, 2021

and approved by

Brian E. Moyer, PhD, Department of Bioengineering

Julie A. Phillippi, PhD, Department of Cardiothoracic Surgery

J. Peter Rubin, MD, Department of Plastic Surgery

William R. Wagner, PhD, Departments of Surgery, Chemical Engineering, & Bioengineering

Dissertation Director: Kacey G. Marra, PhD, Department of Plastic Surgery

Copyright © by Benjamin K. Schilling

2021

# **Mechanization and Assessment of Regenerative Therapies for Peripheral Nerve Injury and the Associated Muscle Atrophy**

Benjamin K. Schilling, PhD

University of Pittsburgh, 2021

Peripheral nerve injury (PNI) not only results in nerve dysfunction but also induces adverse changes in the muscular microenvironment, resulting in muscle atrophy (MA). The time needed for nerve regeneration results in downstream, distal musculature denervation. Muscle denervation prompts significant stiffening, fiber shrinkage, and decrease or loss in force generation. Additionally, the probability of restoring muscle to the preinjury state is proportional to the time of nerve healing, where longer healing time lessens the likelihood that the muscle will regain function, even if the nerve itself is regenerated. While surgical treatment of PNI includes an assortment of interventions, no specific interventions are indicated for MA at the time of PNI. Rather, physical rehabilitation after nerve repair is prescribed, but is presupposed by partial muscle reinnervation. The lack of specific interventions led to the central hypothesis that MA occurring after PNI can be minimized by administering an intramuscular therapy directly into a denervated muscle, altering fibrogenesis, lipogenesis, and inflammation.

In the sciatic nerve injury model, atrophy of distal muscle, including the gastrocnemius, occurred. Both cellular and acellular therapies were administered directly into gastrocnemii, being adipose-derived stem cells (ASCs), a preparation of emulsified adipose tissue (“Nanofat”), and a skeletal muscle-derived extracellular matrix (skECM). Additionally, in select conditions a polycaprolactone nerve wrap was applied at the nerve injury site to assess cotreatment of muscle and nerve. Two automated devices were created to produce neuromuscular therapies: An

automated dip coating device was used to fabricate nerve wraps and an automated perfusion machine was used to produce skECM. Studies were conducted with postoperative analyses performed at 6, 9, 12, and 20 weeks, which included gait assessment, force production, cytokine quantification, and histological analysis. Intramuscular therapies, particularly skECM, were shown to be beneficial against non-injected muscle controls across all time points and showed no significant difference to uninjured muscle at 20 weeks. Cytokines interleukin (IL)-1 $\beta$ , IL-18, and vascular endothelial growth factor (VEGF) appeared to mediate regeneration throughout. Statistical regression implicated IL-1 $\beta$ , IL-18, and their interacting effects as strong predictors of muscle contraction. These investigations implicate intramuscular treatment as a worthwhile co-therapy for the PNI patient population.

**Table of Contents**

**Acknowledgements ..... xxi**

**Abbreviations ..... xxiv**

**List of Equations ..... xxvii**

**1.0 Introduction: Muscle Atrophy after Nerve Injury and its Physiological and Socioeconomical Impacts.....1**

**1.1 Trauma-Induced Peripheral Nerve Injury and Mechanisms to Muscle Reinnervation..... 5**

**1.2 Types of Injuries and Assessments for *In Vivo* Models of PNI/MA..... 9**

**1.3 Prospective Impacts of Automation in Neuromuscular Tissue Engineering ..... 11**

**1.4 Translational Considerations for Muscle and Nerve Therapies ..... 12**

**2.0 Development of a Denervation Atrophy Model and Automating Methods for Nerve Wrap Fabrication .....14**

**2.1 Construction of an In Vivo Model for Gastrocnemius Muscle Atrophy after Injury to the Sciatic Nerve ..... 14**

**2.2 Intramuscular Injection of Adipose-Derived Stem Cells Mitigates Muscle Atrophy after Critical Size Denervation Injury ..... 16**

**2.2.1 Methods .....18**

**2.2.1.1 Harvesting, Expansion, and Labeling of ASCs ..... 18**

**2.2.1.2 Sciatic Nerve Injury and ASC Injection into Gastrocnemius ..... 19**

**2.2.1.3 Histological, Immunohistochemical (IHC), and Immunofluorescent (IF) Staining of Muscle Sections ..... 21**

2.2.1.4	Muscle Fiber Diameter Quantification .....	22
2.2.1.5	Statistical Analyses .....	22
2.2.2	Results from Intramuscular Injection of ASCs into the Gastrocnemius .....	23
2.2.2.1	Muscle Mass Quantification and Gross Imaging.....	23
2.2.2.2	Visualization of Microenvironment and Fiber Diameter using Masson’s Trichrome, Oil Red O and Dystrophin IHC .....	26
2.2.2.3	Muscle Fiber Area Quantification via Dystrophin IHC in ASC- Treated Muscle.....	28
2.2.2.4	Immunomodulatory Markers toward Muscle Regeneration, iNOS and IL-10.....	31
2.2.2.5	Reconstructive Markers toward Muscle Regeneration, Ki67 and MMP-2 .....	33
2.2.3	Discussion on Intramuscular ASCs Study with 1.5cm PNI .....	34
2.2.3.1	Limitations of the Intramuscular ASCs Study .....	39
2.3	Development of a Method for Rodent Gait Analysis .....	40
2.3.1	Details for 3D Printing Walking Track for Gait Analysis .....	41
2.3.2	Calculation and Derivation of the SFI Equation.....	42
2.4	Development of an Electrophysiology System Capable of Measuring Contraction Force .....	45
2.4.1	Reprogramming a Data Acquisition System for Electrophysiology .....	47
2.4.2	Fabrication of Stimulation Cuffs .....	52
2.4.3	Rodent Knee Securement Gantry and Gastrocnemius Contraction Force Measurement .....	54

<b>2.5 Validation of the Denervation Atrophy Model with a Transection Injury .....</b>	<b>55</b>
<b>2.5.1 Methods.....</b>	<b>56</b>
<b>2.5.1.1 Construction of an Automated tool for Nerve Wrap Fabrication ....</b>	<b>56</b>
<b>2.5.1.2 Creation of Injectable Intramuscular Therapies.....</b>	<b>60</b>
<b>2.5.1.3 Method of Nanofat Processing.....</b>	<b>60</b>
<b>2.5.1.4 Method of skECM Processing .....</b>	<b>62</b>
<b>2.5.2 Transection Injury to the Sciatic Nerve and Application of Therapies .....</b>	<b>64</b>
<b>2.5.2.1 Measurement of Contraction Force.....</b>	<b>67</b>
<b>2.5.2.2 Statistical Analyses .....</b>	<b>67</b>
<b>2.5.3 Results .....</b>	<b>68</b>
<b>2.5.3.1 Walking Track Analysis and SFI.....</b>	<b>68</b>
<b>2.5.3.2 Gastrocnemius Muscle Mass Measurements .....</b>	<b>69</b>
<b>2.5.3.3 Contraction Force Analysis .....</b>	<b>70</b>
<b>2.5.4 Discussion of the Muscle and Nerve Interventions Study .....</b>	<b>75</b>
<b>2.5.4.1 Limitations of the Pilot Co-Therapeutics Study .....</b>	<b>78</b>
<b>2.6 Chapter Concluding Remarks.....</b>	<b>79</b>
<b>3.0 Clinically Translatable Cellular Therapy for Mitigating Gastrocnemius</b>	
<b>Denervation Atrophy after Sciatic Nerve Transection.....</b>	<b>81</b>
<b>3.1 Rationale for Use of Nanofat, an Emulsified Adipose Preparation .....</b>	<b>81</b>
<b>3.2 Methods .....</b>	<b>82</b>
<b>3.2.1 Adipose Harvest and Nanofat Preparation.....</b>	<b>82</b>
<b>3.2.2 Induction of Sciatic Nerve Injury via Transection, Repair, and Application</b>	
<b>of Nanofat.....</b>	<b>83</b>

3.2.3 Measurement of Tetanic Contraction Force and Euthanasia.....	85
3.2.4 Muscle Assessment and Histology .....	85
3.2.5 Gene Expression .....	86
3.2.6 Multiplexing.....	87
3.2.7 Statistical Analyses.....	88
3.3 Results from Intramuscular Nanofat in Denervated Gastrocnemii .....	88
3.3.1 Changes in Architecture and Cytokines from Whole Fat to Nanofat .....	88
3.3.2 Walking Track and Sciatic Function Analyses .....	90
3.3.3 Muscle Mass, Architecture, and Contraction Force .....	90
3.3.4 Gene Expression in Nanofat-Injected Gastrocnemii .....	96
3.3.5 Cytokine Quantification in Nanofat-Injected Gastrocnemii and TAs .....	98
3.4 Discussion for Intramuscular Nanofat for Treating Denervated Muscle .....	100
3.4.1 Limitation of the Intramuscular Nanofat Study .....	103
3.5 Chapter Conclusions .....	104
<b>4.0 Acellular, Extracellular Matrix-Based Therapies for Mitigating Gastrocnemius</b>	
<b>Denervation Atrophy after Sciatic Nerve Transection.....</b>	<b>105</b>
<b>4.1 Design of an Automation-Capable Perfusion Platform for Skeletal Muscle Tissue</b>	
<b>Decellularization .....</b>	<b>106</b>
4.1.1 3D Printing Parameters for the TIPD.....	107
4.1.2 Machine Design and Assembly .....	107
4.1.3 TIPD Proof of Concept through Skeletal Muscle Infusion Decellularization	
.....	121
4.1.3.1 H&E Staining of Skeletal Muscle.....	122

4.1.3.2	DNA Quantification of Skeletal Muscle.....	122
4.1.3.3	TIPD Study Statistical Analysis .....	122
4.1.4	Results of TIPD Fabrication and Skeletal Muscle Decellularization .....	122
4.1.4.1	LabVIEW VI, Automation, and Fluid Flow Capabilities .....	122
4.1.4.2	TIPD Decellularization of Skeletal Muscle.....	126
4.1.5	Discussion on Automated Systems for producing ECMs .....	128
4.1.6	Limitations of the TIPD Design .....	131
4.2	Application of Intramuscular Skeletal Muscle Derived ECM for Mitigating Denervation Atrophy.....	132
4.2.1	Methods .....	133
4.2.1.1	Decellularization of Porcine Skeletal Muscle .....	133
4.2.1.2	Scanning Electron Microscopy .....	135
4.2.1.3	Transection Injury to the Sciatic Nerve and Intramuscular skECM Injection .....	135
4.2.1.4	Walking Track Analysis.....	136
4.2.1.5	Contraction Force Measurement .....	137
4.2.1.6	Histology .....	137
4.2.1.7	Protein Quantification.....	138
4.2.1.8	Statistical Analysis .....	138
4.2.2	Results from skECM.....	139
4.2.2.1	Ultrastructure of Porcine Muscle and skECM .....	139
4.2.2.2	Walking Track Analysis.....	140
4.2.2.3	Gastrocnemii and TA Muscle Mass Analysis.....	141

4.2.2.4 Muscle Contraction Force.....	143
4.2.2.5 skECM Histology .....	145
4.2.2.6 Quantified Proteins in Gastrocnemii .....	148
4.2.3 Discussion.....	150
4.2.3.1 Regulatory Considerations of skECM.....	157
4.2.4 Limitations of the skECM in the Gastrocnemii Study .....	158
4.3 Chapter Conclusion.....	158
<b>5.0 Statistical Correlations of Muscle Mass, Contraction Force, and Measured Proteins .....</b>	<b>160</b>
5.1 Statistical Methods for Correlation Analyses .....	160
5.2 Predicting Force Generation by Intramuscular Cytokine Concentration .....	161
5.2.1 Cytokine Analysis of Nanofat-Injected Rodent Gastrocnemii and their Correlation to Contraction Force.....	161
5.2.2 Cytokine Analysis of skECM-Injected Rodent Gastrocnemii and their Correlation to Contraction Force .....	168
5.2.2.1 Relation of Force, IFN $\gamma$ , IL-1 $\beta$ , and IL-18 .....	170
5.2.2.2 Relation of IL-4, IL-6, and MuSK.....	172
5.3 Discussion on Correlations Data .....	175
5.3.1 Correlations Studies Limitations.....	179
5.4 Chapter Conclusions .....	180
<b>6.0 Dissertation Conclusions and Contemplations.....</b>	<b>181</b>
6.1 Future Work .....	182
6.1.1 Regulatory Considerations for Nanofat, ECMs, and ASCs .....	184

6.1.2 Scaling for Manufacturing in ASCs and ECMs .....	187
Appendix A ASCs in Nerve Injury Models .....	191
Appendix B TIPD Construction Parts Details .....	200
Appendix C Perfusion Decellularization Using TIPD .....	202
Appendix C.1 Kidney Perfusion Decellularization .....	202
Appendix C.2 Perfusion Decellularization of the Rodent Free Flap.....	204
Appendix C.2.1 Methods for Harvesting Rodent Epigastric Free Flaps .....	208
Appendix C.2.2 Methods for Decellularizing Epigastric Free Flaps.....	210
Appendix C.2.3 DNA Quantification and Analyses After Free Flap Decellularization .....	211
Appendix D Individual Biocontainment Unit for Preventing Spread of Infectious Respiratory Air during the COVID-19 Pandemic .....	217
Appendix D.1 Abridged Content from Submission for EUA .....	219
Appendix D.2 Detailed Product and Component Description.....	220
Appendix D.3 FDA’s Approval Status and Adequacy of Current Technologies.....	225
Appendix D.4 Risks & Usability Hazards, and Controls & Mitigations .....	229
Appendix D.4.1 Benefits of IBU Usage .....	233
Appendix D.4.2 Summary of Risk-Benefit Analysis Limitations, Uncertainty, and Data Gaps .....	234
Appendix D.5 Manufacturing and Controls.....	235
Appendix D.5.1 Assembly of Final Product.....	236
Appendix D.6 Quality Control, Shipping and Adverse Event Tracking & Reporting.....	236
Appendix D.7 Quantity and Scale-up Considerations.....	237
Appendix D.8 Instructions for Healthcare Facilities and Cleaning Instructions.....	238

<b>Appendix D.9 Packaging and Labeling.....</b>	<b>243</b>
<b>Appendix D.10 Current EUA Status of the IBU .....</b>	<b>244</b>
<b>Bibliography .....</b>	<b>245</b>

## List of Tables

<b>Table 1: Nerve Injury Grading System.</b> .....	<b>6</b>
<b>Table 2: Surface Markers of ASCs.</b> .....	<b>17</b>
<b>Table 3: Summary of Study involving Intramuscular ASCs Injection(s).</b> .....	<b>28</b>
<b>Table 4: Pilot Study Conditions Breakdown.</b> .....	<b>56</b>
<b>Table 5: Normalized Contraction Force (N/kg) at 80Hz Stimulation.</b> .....	<b>72</b>
<b>Table 6: RT-PCR Primers, Mechanisms, and their Reference.</b> .....	<b>87</b>
<b>Table 7: TIPD Quarter Scaffold Part Family.</b> .....	<b>110</b>
<b>Table 8: TIPD Peristaltic Pump Part Family.</b> .....	<b>112</b>
<b>Table 9: TIPD Valve Operation Part Family.</b> .....	<b>115</b>
<b>Table 10: TIPD Chamber Support Part Family</b> .....	<b>117</b>
<b>Table 11: Color Coding of PCB Objects and Layers from Figure 50.</b> .....	<b>119</b>
<b>Appendix Table 1 Studies of Cavernous Nerve Injury.</b> .....	<b>191</b>
<b>Appendix Table 2: Studies of Facial Nerve Injury.</b> .....	<b>193</b>
<b>Appendix Table 3: Studies of Laryngeal Nerve Injury.</b> .....	<b>194</b>
<b>Appendix Table 4: Studies of Peroneal Nerve Injury.</b> .....	<b>194</b>
<b>Appendix Table 5: Studies of Sciatic Nerve Injury.</b> .....	<b>195</b>
<b>Appendix Table 6: Free Flap Donor Site Morbidities.</b> .....	<b>205</b>
<b>Appendix Table 7: Anticipated Uses and Use Cases of the IBU.</b> .....	<b>220</b>
<b>Appendix Table 8: IBU Traceability Matrix.</b> .....	<b>223</b>
<b>Appendix Table 9: Comparison of Approved Technologies.</b> .....	<b>225</b>
<b>Appendix Table 10: Tabularized PAO Capture Results and Face Velocities.</b> .....	<b>227</b>

<b>Appendix Table 11: Components, Materials, and Biocompatibility.....</b>	<b>228</b>
<b>Appendix Table 12: IBU Risks and Risk Controls .....</b>	<b>230</b>
<b>Appendix Table 13: IBU Usability Hazards.....</b>	<b>231</b>
<b>Appendix Table 14: Severity Rating and Description. ....</b>	<b>232</b>
<b>Appendix Table 15: Probability Rating and Frequency. ....</b>	<b>232</b>
<b>Appendix Table 16: Semi-Quantitative Risk Assessment. ....</b>	<b>233</b>
<b>Appendix Table 17: IBU Industry Guidance-Based Benefit Analysis. ....</b>	<b>234</b>
<b>Appendix Table 18: Manufacturer and Sourcing Information.....</b>	<b>235</b>
<b>Appendix Table 19: IBU Full Components List.....</b>	<b>242</b>
<b>Appendix Table 20: Symbols to be Printed on IBU Label. ....</b>	<b>243</b>

## List of Figures

<b>Figure 1: Overview of Muscle Atrophy after Nerve Injury .....</b>	<b>3</b>
<b>Figure 2: Anatomical Illustration of a Peripheral Nerve .....</b>	<b>5</b>
<b>Figure 3: Breakdown of PNI Models by Species and Nerve. ....</b>	<b>15</b>
<b>Figure 4: Illustration of PNI and Images of Nerve Surgery. ....</b>	<b>20</b>
<b>Figure 5: Representative images of the gastrocnemii from the intramuscular ASC study. ....</b>	<b>24</b>
<b>Figure 6: Comparison of Resulting Gastrocnemii Masses after ASC Treatment. ....</b>	<b>25</b>
<b>Figure 7: Representative Histological Staining of Gastrocnemii after ASC Treatment. ....</b>	<b>27</b>
<b>Figure 8: Muscle Fiber Area Residuals Histograms Pre- and Post-Transformation. ....</b>	<b>29</b>
<b>Figure 9: Muscle Fiber Area after Normalizing Transformation. ....</b>	<b>30</b>
<b>Figure 10: Muscle Fiber Area Quantification after Reverse Transformation .....</b>	<b>31</b>
<b>Figure 11: DiR-Labeled ASCs in the Gastrocnemius. ....</b>	<b>32</b>
<b>Figure 12: IF Markers in Gastrocnemii after ASC Treatment. ....</b>	<b>34</b>
<b>Figure 13. CAD Rendering and Construction of Collapsible Rodent Walking Track.....</b>	<b>41</b>
<b>Figure 14: Still of Rodent Walking with Resulting Pawprints. ....</b>	<b>43</b>
<b>Figure 15: Electrophysiology Equipment including Stimulator and Amplifier.....</b>	<b>46</b>
<b>Figure 16: Data and Algorithm Flow of Original Electrophysiology Equipment. ....</b>	<b>47</b>
<b>Figure 17: Data and Algorithm Flow of Reprogrammed Electrophysiology Equipment....</b>	<b>48</b>
<b>Figure 18: Entire LabVIEW Block Diagram for Governing Electrophysiology Equipment. .....</b>	<b>50</b>
<b>Figure 19: LabVIEW Case for Reading Force Data in Real-Time. ....</b>	<b>51</b>
<b>Figure 20: LabVIEW Case for Collecting Force Data from the DAQ.....</b>	<b>52</b>

<b>Figure 21: Image Flow of Nerve Stimulation Cuff Fabrication. ....</b>	<b>54</b>
<b>Figure 22: Nerve Cuff Placement and Knee-Securing Gantry with Load Cell.....</b>	<b>55</b>
<b>Figure 23: Glass Mandrels Before and After PCL Dip Coating. ....</b>	<b>57</b>
<b>Figure 24: Automated Dip Coating Mechanism for Wrap Fabrication. ....</b>	<b>59</b>
<b>Figure 25: Harvest and Preparation of Emulsified Adipose, Nanofat.....</b>	<b>62</b>
<b>Figure 26: Process Flow for making d-skECM.....</b>	<b>64</b>
<b>Figure 27: Illustration of Anatomy and Wrap/Injection Therapies Rendered.....</b>	<b>65</b>
<b>Figure 28: Sciatic Nerve Transection with Wrap and Injection Therapies. ....</b>	<b>66</b>
<b>Figure 29: SFI Results and Analysis. ....</b>	<b>69</b>
<b>Figure 30: Gastrocnemii Masses Normalized to Contralateral and Body Mass.....</b>	<b>70</b>
<b>Figure 31: Force Data Across All Stimulation Frequencies.....</b>	<b>71</b>
<b>Figure 32: Normalized Contraction Force (N/kg) at 80Hz Stimulation, All Conditions.....</b>	<b>74</b>
<b>Figure 33: Normalized Contraction Force (N/kg) at 80Hz Stimulation, Co-Therapies Omitted. ....</b>	<b>75</b>
<b>Figure 34: Rodent Nanofat Preparation. ....</b>	<b>83</b>
<b>Figure 35: Exposure of Sciatic Nerve and Intramuscular Injection of Nanofat. ....</b>	<b>84</b>
<b>Figure 36: Architecture and Cytokines in Whole Fat and Nanofat.....</b>	<b>89</b>
<b>Figure 37: Linear Regression and Log-Worth Chart for Sciatic Function Index. ....</b>	<b>90</b>
<b>Figure 38: Gross Appearance of Muscle and Sciatic Nerve.....</b>	<b>91</b>
<b>Figure 39: Gastrocnemius and TA Muscle Comparisons. ....</b>	<b>92</b>
<b>Figure 40: Trichrome staining of Control and Nanofat-Treated Gastrocnemii. ....</b>	<b>92</b>
<b>Figure 41: Contraction Forces Generated Normalized by Rodent Body Mass [N/kg].....</b>	<b>94</b>
<b>Figure 42: Contraction Forces Generated Normalized by Gastrocnemius Mass [N/g]. ....</b>	<b>96</b>

<b>Figure 43: Gene Transcription in Nanofat-Injected and Non-Treated Gastrocnemii. ....</b>	<b>97</b>
<b>Figure 44: Significantly-Expressed Cytokines in Gastrocnemii. ....</b>	<b>99</b>
<b>Figure 45: CAD/CAM Renderings of the TIPD Assemblies. ....</b>	<b>108</b>
<b>Figure 46: TIPD after 3D Printing and Assembly. ....</b>	<b>109</b>
<b>Figure 47: Exploded Views of the TIPD Quarter Scaffold Family Assembly. ....</b>	<b>111</b>
<b>Figure 48: TIPD Subassemblies of the Peristaltic Pump and Valve Rotator. ....</b>	<b>114</b>
<b>Figure 49: TIPD Exploded Chamber Assembly. ....</b>	<b>118</b>
<b>Figure 50: TIPD Printed Circuit Board Design and Population. ....</b>	<b>120</b>
<b>Figure 51: TIPD GUI of the Control Page VI. ....</b>	<b>124</b>
<b>Figure 52: TIPD GUI in the Automation panel ....</b>	<b>125</b>
<b>Figure 53: TIPD Pump/Fluid Velocity Relationship. ....</b>	<b>126</b>
<b>Figure 54: Decellularization of Skeletal Muscle using the TIPD. ....</b>	<b>127</b>
<b>Figure 55: Flow Diagram to for Production of skECM. ....</b>	<b>134</b>
<b>Figure 56: Illustration of Anatomy and skECM Injection Therapies Rendered. ....</b>	<b>136</b>
<b>Figure 57: SEM of Native Muscle, p-skECM, and d-skECM. ....</b>	<b>140</b>
<b>Figure 58: Representative Pawprints and Resulting SFI Analysis. ....</b>	<b>141</b>
<b>Figure 59: Gastrocnemii and TA Mass Normalizations. ....</b>	<b>143</b>
<b>Figure 60: Gastrocnemii Contraction Force Normalized to Rodent Body Mass. ....</b>	<b>144</b>
<b>Figure 61: Gastrocnemii Contraction Force Normalized to the Gastrocnemius Muscle... ..</b>	<b>145</b>
<b>Figure 62: Masson’s Trichrome Staining of Gastrocnemii. ....</b>	<b>146</b>
<b>Figure 63: Oil Red O Staining of Gastrocnemii. ....</b>	<b>147</b>
<b>Figure 64: Cytokines in skECM-Injected Gastrocnemii (Set 1 of 2). ....</b>	<b>149</b>
<b>Figure 65: Cytokines in skECM-Injected Gastrocnemii (Set 2 of 2). ....</b>	<b>150</b>

<b>Figure 66: Mutlivaraite Analysis Correlating Cytokines and Contraction Force [N/kg].</b>	<b>162</b>
<b>Figure 67: Contribution of Cytokine Concentration to Tetanic Force.</b>	<b>163</b>
<b>Figure 68: Contribution of IL-1<math>\beta</math> and IL-18 to Predict Force in Correlative Modeling.</b>	<b>164</b>
<b>Figure 69: Force Predicted from IL-1<math>\beta</math> and IL-18 against Measured Force.</b>	<b>165</b>
<b>Figure 70: Mutlivariate Analysis Correlating Cytokines and Contraction Force [N/g].</b>	<b>166</b>
<b>Figure 71: Regression of Contraction Force [N/g] at 50Hz predicted by Cytokines.</b>	<b>167</b>
<b>Figure 72: Mutlivaraite Analysis Correlating Cytokines and Contraction Force.</b>	<b>169</b>
<b>Figure 73: Color Map of p-values for Correlations based on skECM Multivariate Assessment (Figure 72).</b>	<b>170</b>
<b>Figure 74: Contraction Force as Predicted by IFN<math>\gamma</math>, IL-1<math>\beta</math>, and IL-18.</b>	<b>172</b>
<b>Figure 75: IL-4 Concentration Predicted by Concentration of Intramuscular Cytokines.</b>	<b>175</b>
<b>Appendix Figure 1: Rodent Kidney Perfusion Decellularization using the TIPD.</b>	<b>203</b>
<b>Appendix Figure 2: Schematic and CAD/CAM Rendering of TIPD (Modified from Figure 45).</b>	<b>207</b>
<b>Appendix Figure 3: Rodent Free Flap in TIPD Chamber Prior to Decellularization.</b>	<b>208</b>
<b>Appendix Figure 4: Harvest of the Rodent Epigastric Free Flap.</b>	<b>209</b>
<b>Appendix Figure 5: Flow Diagram of Free Flap Perfusion Scheme.</b>	<b>210</b>
<b>Appendix Figure 6: Skin and Subcutaneous View of Decellularized Free Flaps.</b>	<b>211</b>
<b>Appendix Figure 7: Decellulairzation Efficiency based on Process and Compartment.</b>	<b>213</b>
<b>Appendix Figure 8: Decellulairzation Efficiency based on Process, Compartment, and Region.</b>	<b>215</b>
<b>Appendix Figure 9: Conceptual Flow of Free Flap Engineering in TIPD.</b>	<b>216</b>
<b>Appendix Figure 10: IBU Confiburations with Multiple Vacuum Sources.</b>	<b>219</b>

<b>Appendix Figure 11: Demonstrations of IBU Modes of Use.....</b>	<b>222</b>
<b>Appendix Figure 12: PAO Monitoring Positions and Capture Results.....</b>	<b>226</b>
<b>Appendix Figure 13: Stills from Videography of Smoke Testing.....</b>	<b>228</b>
<b>Appendix Figure 14: IBU General Assembly Drawing. ....</b>	<b>238</b>
<b>Appendix Figure 15: Breakdown of IBU Components. ....</b>	<b>239</b>

## Acknowledgements

As the proverbial curtains close on this endeavor, there are of course many, many people to whom I owe my profound gratitude. To all who have helped me along the way, we share this work.

To Drs. Marra and Rubin: thank you for believing in me in my days before graduate school, and particularly in the days when admission into the program was certainly not a given. To my dissertation advisor, Dr. Marra: Thank you for allowing me the independence to explore, fail, and grow. Thank you for challenging me, thank you for letting me be challenging. Thank you for being a mentor, and for letting me be a mentor in your example. Thank you for the emphasis on family and for building a lab that feels like one. Of all things, I am most grateful for your trusting me. Thank you. Thank you.

To Drs. Hirschman and Gurleyik: Thank you for bringing me into the MS-MPE program. If not for your belief in me, none of this would have been possible. I can only hope I gave back in some small measure.

To Drs. A. Ejaz, L. Kokai, R. Orizondo: For the time spent debating projects, mechanisms, aims, experiments and philosophizing (or, pontificating) funding and regulatory policy, I will be eternally fond. Your insights, perspectives, and depths of knowledge are inspirational. To Dr. B. Moyer: You have made me a better engineer. Thank you. To Drs. M. Solari and C. Komatsu: Thank you for bringing me into the VCAM lab and making it a second home.

To the late-night development team of the Individual Biocontainment Unit, Drs. D. Turer, C. Good, J. Chang, H. Ban, and S. Zappia: I had hoped by the time I was writing this our EUA would have been authorized, but alas, we wait! What a ride it has been.

To Drs. W. Chen and D. Bourne: My deepest gratitude for inviting me into your projects and trusting me with the analyses, but most importantly, for exposing me to the work that still needs to be done by all of us toward parity in our field and in our leadership. To Dr. Beschoner: TA'ing Applied Biostatistics made me fall in love with statistics again; I am forever grateful for that. To B. Frankowski: Your teaching me to machine was a bit of Zen in the chaos.

To Bryan Choi: Without your persistent, incessant encouragement, I would never have thought to make this leap; thank you. To the crew at MTF Biologics: Simply put, without your guidance during my time in industry, I would not be the engineer I am today.

To my lab mates past and present, A. Cottrill, G. DiBernardo, C. Fedor, M. Johngrass V. Nerone, A. Repko, R. Schroth, and Drs. B. Bengur, A. Kelmendi-Doko, Drs. C. Mahoney, D. Minter, S. Wang: While there are so many specifics for which to appreciate, in brief, thank you for always being there for me. One single specific, to G. DiBernardo: Thanks for deleting the entire contents of my phone and making me realize that sometimes you just have to laugh.

To my mentees past and present, J. Baker, K. Byrd, K. Klett, K. Lamberti, G. Panagis, M. Snowden: your respective desires to learn and understand have been nothing short of inspirational. I can only hope to have taught you as much as you have taught me.

To my dissertation committee: Thank you for your insight, criticisms, and challenges, but most importantly, your understanding in what has been a strange and difficult pandemic.

To my parents, family, and friends: I love you all dearly. Your support has meant the world and back.

To my wife, Andrea: I couldn't have done this without you; I wouldn't have wanted to do this without you.

—

*The end of a melody is not its goal: but nonetheless, had the melody not reached its end it would not have reached its goal either. A parable. Friedrich Nietzsche (Human, All Too Human)*

## Abbreviations

ABS.....	Acrylonitrile Butadiene Styrene (chemical, filament)
ANOVA .....	Analysis of Variation (statistics)
ASC.....	Adipose-Derived Stem Cell
BLA.....	Biologics License Application (FDA Pathway)
CAD/CAM.....	Computer Aided Design/Computer Aided Manufacturing
CBER .....	Center for Biologics Evaluation and Research (FDA)
CFR.....	Code of Federal Regulation (U.S.)
CMAP .....	Compound Muscle Action Potential
CO <sub>2</sub> .....	Carbon Dioxide
CSV.....	Comma-Separated Values (file format)
DAQ.....	Data Acquisition System
DNA.....	Deoxyribonucleic Acid (protein)
ECM.....	Extracellular Matrix
ELISA .....	Enzyme-Linked Immunosorbent Assay
EUA .....	Emergency Use Authorization (FDA Pathway)
FDA.....	Food & Drug Administration (U.S.)
FFF.....	Fused Filament Fabrication (3D printing)
GUI .....	Graphical User Interface
GM-CSF.....	Granulocyte Macrophage-Colony Stimulating Factor (protein)
GMP .....	Good Manufacturing Practices (manufacturing/fabrication)
GRAS.....	Generally Regarded as Safe (Risk Assessment)

H&E .....	Hematoxylin & Eosin (histological stain)
HEPA .....	High Efficiency Particulate Air (filter)
HSD.....	Honesty Significant Difference ( <i>statistical post hoc</i> )
Hz.....	Hertz [1/s] (unit of measure)
IBU.....	Individual Biocontainment Unit
IDE.....	Integrated Development Environment (programming)
IFN $\gamma$ .....	Interferon- $\gamma$ (protein)
IGF .....	Insulin-Like Growth Factor (protein)
IF.....	Immunofluorescence (histology)
IHC.....	Immunohistochemistry (histology)
IL.....	Interleukin (protein)
iNOS .....	Inducible Nitrox Oxide Synthase (protein)
MA .....	Muscle Atrophy
MMP.....	Matrix Metalloproteinase (Protein)
MuSK.....	Muscle Skeletal Receptor Tyrosine-Protein Kinase (protein)
OSH.....	Open-Source Hardware
PCB.....	Printed Circuit Board
PCL .....	Polycaprolactone (chemical)
PLA.....	Polylactic Acid (chemical, filament)
PNI .....	Peripheral Nerve Injury
PPE.....	Personal Protective Equipment
PTFE .....	Polytetrafluoroethylene (chemical)
PVA.....	Polyvinyl Acetate (chemical)

RNA .....Ribonucleic Acid (protein)  
RT-PCR.....Reverse Transcription Polymerase Chain Reaction  
SDS .....Sodium Dodecyl Sulfate (chemical)  
SEM .....Scanning Electron Microscopy (*disambiguated throughout*)  
SEM .....Standard Error of the Mean (*disambiguated throughout*)  
skECM .....Skeletal Muscle-Derived ECM  
STL .....Stereolithography (file format)  
TIMP.....Tissue Inhibitor of Metalloproteinases (protein)  
TIPD.....Tissue Infusion/Perfusion Device  
TNF.....Tumor Necrosis Factor (protein)  
ULPA .....Ultra-Low Particulate Air (filter)  
VEGF .....Vascular Endothelial Growth Factor (protein)  
VI .....Virtual Instrument (LabVIEW file format)  
VIPM.....Virtual Instrument Package Manager (LabVIEW)  
WAT .....White Adipose Tissue

## List of Equations

<b>Equation 2-1: Johnson’s Bounded Transformation of Muscle Fibers Analysis Data Set....</b>	<b>29</b>
<b>Equation 2-2: Reverse Transformation of Muscle Fibers Analysis Data Set.....</b>	<b>30</b>
<b>Equation 2-3: Fraction of Intermediary Toe Spread in Calculating SFI.....</b>	<b>44</b>
<b>Equation 2-4: Fraction of Toe Spread in Calculating SFI. ....</b>	<b>44</b>
<b>Equation 2-5: Fraction of Paw Length in Calculating SFI. ....</b>	<b>44</b>
<b>Equation 2-6: Function for Calculating SFI.....</b>	<b>44</b>
<b>Equation 3-1: Johnson’s Bounded Transformation of Sciatic Function Index.....</b>	<b>88</b>
<b>Equation 5-1: Linear Correlation of Force [N/kg] at 50 Hz to IL-1<math>\beta</math> and IL-18 .....</b>	<b>164</b>
<b>Equation 5-2: Linear Correlation of Force [N/kg] at 75 Hz to IL-1<math>\beta</math> and IL-18 .....</b>	<b>165</b>
<b>Equation 5-3: Linear Correlation of Force [N/kg] at 100 Hz to IL-1<math>\beta</math> and IL-18 .....</b>	<b>165</b>
<b>Equation 5-4: Linear Correlation of Force [N/g] at 50 Hz by Significantly-Expressed Cytokines. ....</b>	<b>167</b>
<b>Equation 5-5: Linear Correlation of Force by IFN<math>\gamma</math>.....</b>	<b>170</b>
<b>Equation 5-6: Linear Correlation of Force based on Full Factorial Model with IFN<math>\gamma</math>, IL-1<math>\beta</math>, and IL-18.....</b>	<b>171</b>
<b>Equation 5-7: Interacting Effects of IFN<math>\gamma</math>, IL-1<math>\beta</math>, and IL-18.....</b>	<b>171</b>
<b>Equation 5-8: Linear Correlation of IL-4 to Significant and Near-Significant Proteins..</b>	<b>173</b>
<b>Equation 5-9: Linear Correlation of IL-4 to VEGF, MuSK, and IL-6.....</b>	<b>174</b>

**Equation 5-10: Linear Correlation of IL-4 to IL-4 to VEGF, MuSK, and IL-6 and their Interactions..... 174**

**Equation 5-11: Interacting Effects of IL-6, MuSK, and IL-6..... 174**

## **1.0 Introduction: Muscle Atrophy after Nerve Injury and its Physiological and Socioeconomical Impacts**

The burden of peripheral nerve injury (PNI) and the associated muscle atrophy (MA) are twofold: not only does it present in the United States healthcare system as a \$150 billion annual expenditure, it also weighs on the economic infrastructure as 40% of individuals experiencing PNI/MA are unable to return to work one year post-injury due to residual complications (Jaquet, Luijsterburg et al. 2001, Bruyns, Jaquet et al. 2003). Contributing to these burdens, PNI/MA disproportionality affects young populations of individuals. Significant advancements in nerve regeneration therapies have been made in recent years, though innovative treatments for denervated muscle have lagged. Nerve reconstruction coupled with sensory re-education and physical/electrostimulation therapies remain at the clinical forefront aiding in functional recovery of the injured nerve, but have yielded inconsistent successes, varying site-to-site and patient-to-patient, with respect to the muscle function (Novak, Anastakis et al. 2010). Since muscle function is contingent on its innervation, physical rehabilitation is limited by its need for at least partial reinnervation post-PNI. In an effort to mitigate the physical and financial burden from PNI/MA, a need exists for therapies that may be administered in a single procedure addressing not only the nerve, but also the anticipatory denervation effects that will occur within the musculature during the regeneration and reinnervation phases of the healing nerve.

PNI not only results in the dysfunction of the affected nerve, but also induces adverse changes in the muscular microenvironment, resulting in MA. Despite intervention to the nerve itself, the time needed for nerve restoration leaves the downstream musculature in the atrophic state. This state induces significant stiffening due to collagenous deposition, shrinkage, and

decrease or loss in the muscle force generation (Burnett and Zager 2004, Corona, Wu et al. 2013). Additionally, the probability of restoring atrophic muscle to the preinjury state is proportional to the time of nerve healing, where a longer healing time of the nerve lessens the likelihood that the muscle will regain function, even if the nerve itself is regenerated (Jonsson, Wiberg et al. 2013). Surgical treatment of PNI includes several interventions (suturing, autografting, allografting, synthetic devices), though no specific interventions are indicated for MA other than physical and sensory rehabilitation during the months after nerve repair and at least partial muscle reinnervation (Robinson 2000, Grinsell and Keating 2014) as Illustrated in **Figure 1**. The lack of specific interventions that address muscle atrophy led to the central hypothesis that MA occurring after PNI can be minimized by administering therapies to the downstream musculature and may even be enhanced when cotreatment is rendered, that is, treatment to *both* the denervated muscle as well as the injured nerve.

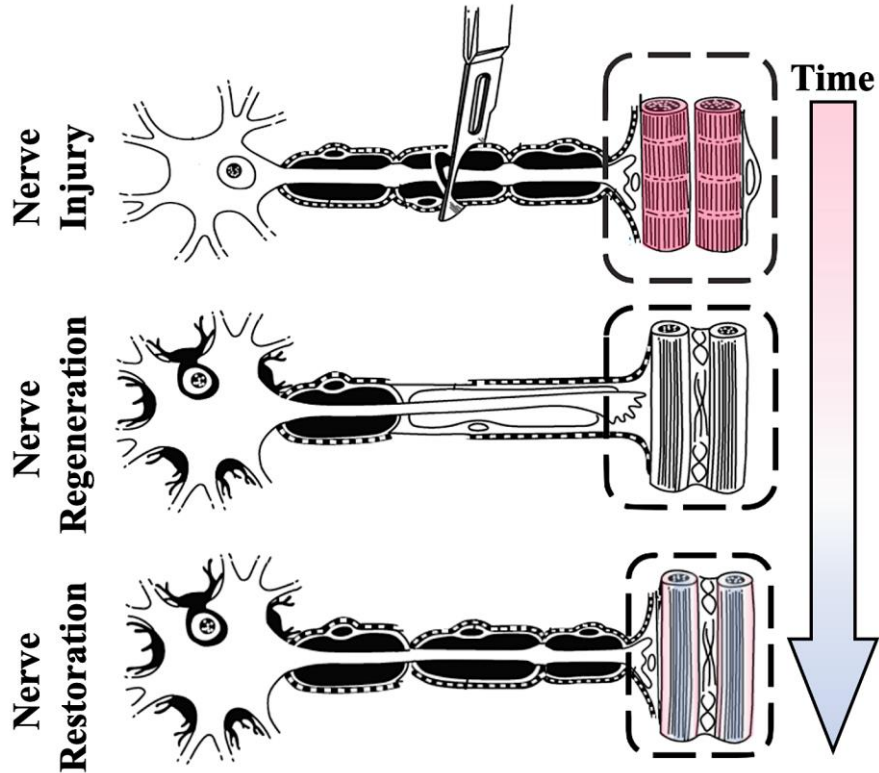


**Figure 1: Overview of Muscle Atrophy after Nerve Injury**

Specifically, the objective of the following studies is to design and construct automated systems for fabricating neuromuscular therapies, and then to validate those therapies in a rodent model. An automated device to fabricate polycaprolactone (PCL) nerve wraps will be leveraged to repeatably produce a therapeutic capable of mending a lacerated nerve. With respect to the denervated muscle, both cellular and acellular therapies will be administered intramuscularly, namely adipose-derived stem cells (ASCs), a preparation of emulsified adipose tissue (“Nanofat”), and a skeletal muscle-derived extracellular matrix (skECM), will be injected directly into the denervated musculature. The basis for these treatments is that similar interventions have been engineered to mimic the cell and protein constituency of healthy musculature, promoting upregulation or continued satellite cell differentiation (Philippou, Maridaki et al. 2007, DeQuach,

Lin et al. 2012, Ungerleider, Johnson et al. 2016). The hypothesis is that preinjury neuromuscular function can be better restored by administering therapies into musculature at the time of surgical intervention due to attenuation of the inflammatory response, and specifically, the modulation of pro-inflammatory cytokines in the interleukin family.

With approximately 20 million Americans currently experiencing PNI/MA (Grinsell and Keating 2014), technologies being developed to address this notable shortcoming in clinical care should be designed with specific focus on clinical translation. To meet this end, independent systems for automated fabrication of nerve conduits/wraps and skECM were developed, increasing their likelihood for clinical translation based on repeatability of methods. Integrating both laboratory and manufacturing design considerations will enable both translation of previously-established protocols for nerve conduits/wraps and ECM fabrication into a Good Manufacturing Practices (GMP) facility, while also serving the research community seeking to address the limitations of current PNI/MA therapies. These systems yield the distinct interventions for both the nerve and muscle, which together are anticipated to better mitigate denervation atrophy. Importantly, to the best of our knowledge, intramuscular therapy has not been investigated for treatment of post-PNI. Hence, this work will further the understanding of neuromuscular therapy and the ability to treat MA at the site, within the musculature downstream/distal of the nerve injury.

## 1.1 Trauma-Induced Peripheral Nerve Injury and Mechanisms to Muscle Reinnervation

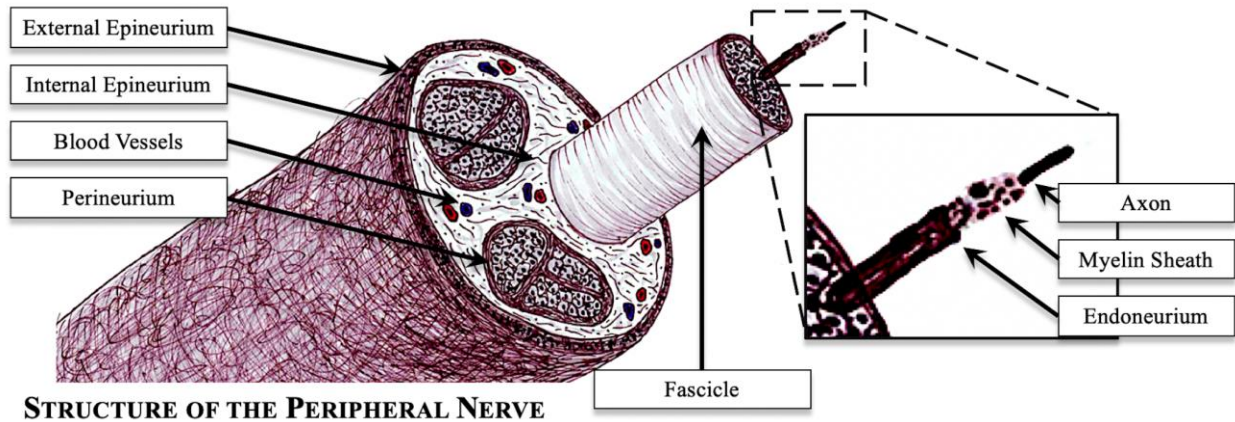


Figure 2: Anatomical Illustration of a Peripheral Nerve

Nerve injuries can be characterized broadly into three categories: (1) mechanical or traumatic, (2) vascular or ischemic, and (3) chemical or neurotoxic (Jortner 2000, Brull, Hadzic et al. 2015). The focus herein will primarily consider mechanical and/or traumatic PNI (Lim, Shi et al. 2015). Such injuries affect the various structures of the nerve and are assessed over five levels of severity in the Seddon and Sunderland grading system (Sunderland 1951). This system of grading was expanded to include a sixth (VI) classification by MacKinnon & Dellon, which includes combinations of Grade III-V injuries along a damaged peripheral nerve segment (Mackinnon and Dellon 1988). These classifications are presented in **Table 1**. The severity and type of the peripheral nerve injury determines the potential and quality of native recovery or the need for surgical intervention. Injuries increasing in severity, i.e., past Grade III, can result in serious complications and have been historically difficult to treat without long-term or permanent discomfort as well as diminished mobility and sensation. While the body has native repair mechanisms in place, this process is timely and in the case of motor nerves, results in substantial

muscle atrophy (Menorca, Fussell et al. 2013, Chhabra, Ahlawat et al. 2014). In the post-PNI healing process, reinnervation can occur in two ways, by collateral branching and axonal regeneration. This dichotomy is based on severity of trauma, where collateral branching is induced in more minor instances versus axonal regeneration, which is activated in the event of moderate to severe PNI. In collateral branching intact axons sprout toward a target organ or tissue. This is the primary form of recovery for minor injuries when approximately 20-30% of the axon has been damaged (Grades I & II). This process begins four days after injury and the healing process continues for several months where an excessive amount of axonal branching results in some terminal ends not innervating the end terminus. These non-terminating, non-innervating ends will eventually be phagocytized by resident and infiltrating inflammatory cells as a part of the naturally-occurring healing cascade (Gibson and Ma 2011). Notably, this process of collateral branching also occurs in nerve turnover, being an innate mechanism of the PNS health (Gallo 2011).

**Table 1: Nerve Injury Grading System.**

<b>Injury</b>		<b>Myelin</b>	<b>Axon</b>	<b>Endoneurium</b>	<b>Perineurium</b>	<b>Epineurium</b>
Neurapraxia	I	De-myelinated	Intact			
Axonotmesis	II		Damaged	Intact		
Axonotmesis/ Neurotmesis	III			Damaged	Intact	
Axonotmesis/ Neurotmesis	IV				Damaged	Intact
Axonotmesis/ Neurotmesis	V					Transected
Mixed Injury	VI			Varying injury levels	Varying injury levels	Varying injury levels

More severe injuries are quantified by significant damage to the axonal segment when damage to the endoneurium and beyond are imminent. In these instances, it is estimated that

approximately 90% of axon damage has occurred, classified as Grade III or beyond (Lunn, Brown et al. 1990). The process of regeneration occurs over two locations, being the proximal and distal nerve segments, and in three phases beginning with Wallerian degradation (primarily distal), followed by axonal regeneration (proximal), and result in the third phase, being target reinnervation (Huebner and Strittmatter 2009). Following a crush or transection injury, Wallerian degeneration takes place at the distal stump and without it, the recovery potential of the nerve is limited. This process involves clearing of axons and inhibitory cellular debris including myelin that is distal to the injury lesion. In turn, this degradation creates a favorable environment for regenerating axons to extend towards their target reinnervation site. Triggering this regenerative degeneration is a rapid innate-immune response, involving Schwann cells, fibroblasts, macrophages, endothelial cells, and their corresponding secretome (George and Griffin 1994, Gaudet, Popovich et al. 2011, Rotshenker 2011, Llobet Rosell and Neukomm 2019). Macrophages are recruited by several proinflammatory cytokines such as monocyte chemoattractant protein-1 (MCP-1, alternatively CCL2), macrophage inflammatory protein (MIP)- $\alpha$ , tissue necrosis factor (TNF)- $\alpha$  and interleukin (IL)-1 $\beta$  to phagocytose debris and to activate Schwann cells, which have two roles: assisting phagocytosis and, later on, guiding regenerating axons (Jessen and Mirsky 2016, Stratton and Shah 2016). In distal degradation, macrophages and other phagocytes clear axonal debris, removing molecules that could inhibit future nerve regeneration. In the neural cell body region, macrophages trigger the conditioning lesion response, a process in which neurons increase their regeneration after a prior lesion (Zigmond and Echevarria 2019). In distal regeneration, Schwann cells proliferate to form the bands of Büngner and secrete neurotrophic factors that travel retrogradely (distal to proximal) to guide regenerating axons (Frostick, Yin et al. 1998). Additionally, exosomal and extracellular vesicular content such as miR-132, expressed

by mature nerve tissue, and miR-3099, overexpressed during injury and at the proximal stump, has been implicated as an activator of Schwann cells in PNI for inducing the recovery response (Yao, Shi et al. 2016, Liu, Miao et al. 2019).

After PNI, axonal regeneration occurs at the proximal stump near the musculature, where some Wallerian degeneration does occur, though in a retrograde fashion up to the first node of Ranvier (Burnett and Zager 2004). Within a few hours neuronal sprouts are formed with terminal growth cones searching for neurotrophic factors secreted from the distal stump (Liu, Shi et al. 2005, Kalil, Li et al. 2011). A neuronal cell body post-PNI will undergo chromatolysis, a process where the cell body swells, its nucleus migrates peripherally with respect to the cell body, and the neuronal protein synthesis sites, termed Nissl bodies, will deconstruct and disperse (Evans 2001). When the regenerating axons successfully reach the matrix of the distal stump, they will grow within the bands of Büngner formed by Schwann cells (Bunge, Bunge et al. 1989). Schwann cells continue congregating to form Büngner Bands, aligning along the basal lamina, basement membrane, or connective tissue left behind after axonal and myelin degradation created distal to the injury site. This helps guide axons towards their target for reinnervation and eventually return to function. Throughout the time course of nerve regeneration post-PNI approximately 40% of the dorsal root ganglions will undergo apoptosis (Schmidt and Leach 2003). Though some of this cell death is prospective and advantageous for reinnervation, deficient target-derived neurotrophic support may exacerbate apoptosis, and lead to a dampening of distal signaling and lead to scar formation (Lisa, Murolo et al. 2016).

Wallerian degeneration, axonal regeneration, and terminal reinnervation are all affected by the type of injury (i.e., crush, partial laceration, full transection), the physical length and duration of injury, and the quality of the Wallerian degeneration. Crush injuries do not sever connective

tissue while transection injuries do; severed axons regenerate after a crush injury but typically do not after a transection, as the transection requires complete turnover at the injury site involving axonal degeneration along with myelin sheath detachment and degradation (Alvites, Rita Caseiro et al. 2018). The capacity for the Schwann cell to regenerate the injury site is limited (Hoke 2006, Gordon, Tyreman et al. 2011), where their decreased regenerative capacity parallels a decrease in neurotrophic factors as well as the reconstructive turnover of the basal lamina (Terenghi 1999, Walsh, Gordon et al. 2010). Understanding these distinct sites of regeneration and the limitations of the sequential phenomena toward muscle reinnervation may better assist the rationale of an intramuscular therapy in terms of both application site as well as the time of administration within the nerve healing cascade.

## **1.2 Types of Injuries and Assessments for *In Vivo* Models of PNI/MA**

The type of injury to a nerve impacts its regeneration as well as the functional return in the distal musculature. A minimally-detrimental traumatic injury model results from the crushing or compression to a peripheral nerve. Crush or compression injuries can be achieved through bluntly crushing and/or compressing the nerve segment, or via ligation (Dowdall, Robinson et al. 2005). A crush or compression PNI involves applying force to the nerve to interrupt the continuity of the axonal structure while leaving the connective scaffold intact, thereby maintaining the continuity of the nerve trunk. This continuity is particularly advantageous for providing an optimal pathway for axonal regrowth throughout the regeneration process resulting in eventual reinnervation at the original target site (Menorca, Fussell et al. 2013). Several surgical tools and devices have been developed to aid in rendering a crush and/or compression injury, therefore decreasing variability

in animal injury models. Crush/compression surgical procedures only involve exposing the target nerve, which is a relatively simplistic surgical procedure when compared to surgical anastomosis of two nerve segments as must be done in transection or gap-and-repair models (Liu, Chen et al. 2018). Once the nerve is exposed, however, the compression can be delivered by many methods, either via ligation or the preferred crush method (e.g., forceps, vasculature clamps, pressure-inducing conduits). Given the relative ease with which the crush injury can be induced and the common tools necessary for its creation, it has become a common model for the assessment of regrowth and recovery (Ronchi, Nicolino et al. 2009, Ronchi, Raimondo et al. 2010). Despite its attractiveness, the main disadvantage of the crush/compression model is its limited clinical translation particularly due to the relative size between the rodent versus the human nerve in the context of a crush. While crushes are certainly a relevant phenomenon clinically, they typically are presented with polytrauma involving transection or laceration of the nerve as well (Ronchi, Morano et al. 2019).

PNI models can also be induced through the total or partial transection/laceration of a nerve, or through the creation of a gap in the length of the nerve, yielding a proximal and distal stump. Such models are used to better mimic injury mechanics, surgical anatomies, and the longer-term healing and compensatory mechanisms that ensue post-injury. In animal models, gap lengths typically do not exceed 20mm, where the most common range for inducing a gap-based PNI is 6-10mm (Angius, Wang et al. 2012). Notably, clinical standards of practice can be modeled in the laceration or gap creation models, suturing the nerve together after injury and/or suturing a cuff or conduit onto the site of injury. The clinical standard for repairing gapped segments is autografting, where the removed segment is addressed most commonly with the sural nerve, medial cutaneous antebrachial nerve, or saphenous nerve, and can be mismatched diametrically and/or in sensory

versus motor function (Cinteza, Persinaru et al. 2015). Due to regulations and ethical considerations for animal usage, autografts typically do not mimic the clinical scenarios due to the inherent trauma of the donor site; it is typical of autografts in animal-based PNI models that the length of the nerve be rotated 180° creating a “reverse polarity” autograft, or “isograft” for addressing the gap. Whether a more clinically relevant donor site will yield increasingly translatable information is at this point, speculative (Roberts, Thibaudeau et al. 2017).

### **1.3 Prospective Impacts of Automation in Neuromuscular Tissue Engineering**

Described here are the construction and validation of independent systems capable of producing PCL nerve conduits and wraps, as well as a modular perfusion bioreactor platform for generation of ECMs. While the context of this work will use the perfusion bioreactor system to produce a specific ECM type from skeletal muscle, the generation of decellularized ECMs in general has become a staple of tissue engineering in the recent decades, which has extended from the research setting to clinical usage. Though methods and protocols for tissue decellularization are abundant throughout the literature, these procedures can be time-intensive and typically necessitate specific overhead in terms of equipment.

To better standardize methods for nerve wraps and ECMs fabrication, novel, functional and reproducible prototypes of an Automated Dip Coating Mechanism and a Tissue Infusion/Perfusion Device (TIPD) have been designed and fabricated using 3D printed parts in conjunction with commercially available components. These platforms can be fabricated in the laboratory setting and modified for many conduit fabrication protocols or ECM types beyond the methods that are used here. These design considerations have been undertaken in an effort to

increase the reproducibility of experiments, as well as to promote an open-source hardware (OSH) initiative in the field of tissue engineering. Both platforms were conceptualized and prototyped with modifiable and printable part files, but also lend themselves to construction from prototyping materials more robust than 3D printed parts (e.g., extruded rod) if and/or when 3D printing becomes impractical. However, a major advantage of 3D printing is that the source files for creating parts and structure can be made available for fabrication of the respective systems as a whole, where minimal design or fabrication expertise is necessary to construct such systems. Alternatively, such platforms could also allow development of new methods to address similar indications, or applications entirely outside the scope of this work.

#### **1.4 Translational Considerations for Muscle and Nerve Therapies**

In conjunction with the development of these two fabrication platforms, the target indication of PNI/MA remains a significant clinical need as there are *currently no approved clinical therapies* indicated to anticipate denervation atrophy after PNI. Rather, after experiencing intervention to address a PNI, the patient must undergo cumbersome physical rehabilitation and/or electrostimulation, the benefits of which are only seen with daily patient compliance, ideally committing 1-2 hours per day (Gordon and English 2016). The combination of therapies proposed here seeks to address muscle atrophy with a therapy that can be injected intramuscularly at the same time as the nerve is repaired, and in turn, mitigates the patient compliance to a physical therapy regimen. It is anticipated that this approach will aid in the return of muscle function better than an independent therapy alone. While this co-therapeutic approach is innovative, it is being designed to be readily translational. Both polymeric nerve conduits and ECM protein-derived

therapies have historically fallen into FDA Device pathways (510(k), *de novo*, or PMA), which traditionally have been faster to the clinic than the Drug (IND, e.g., small molecule) or Biologics License Application (BLA, e.g., metabolic therapy) pathway counterparts. Though initial investigations of these technologies will be studied in denervation atrophy models, the prospective impacts span considerably broader than the PNI-induced atrophy indication alone. Like PNI, considerable volumetric muscle loss can be associated with traumatic incidents, which also require intervention to repair and regenerate the damaged muscle. In the event of hard tissue fracture, even with no specific damage to musculature, the fixation required to induce bone healing will contribute to immobilization-induced MA. It is anticipated that the therapies studied here could extend to serve each of these additional niches.

## **2.0 Development of a Denervation Atrophy Model and Automating Methods for Nerve Wrap Fabrication**

### **2.1 Construction of an In Vivo Model for Gastrocnemius Muscle Atrophy after Injury to the Sciatic Nerve**

Crush, transection, and gap PNI models result not only in damage to the affected nerve but lead to denervation and the eventual atrophy of the distal musculature. This process will begin immediately after nerve injury occurs, where the electrochemical signaling pathway to the target muscle ceases, and deterioration of function, upregulation of inflammation, and potential fibrosis ensues. Loss of function and sensation in the hindlimb is a consequence of the rapid and aggressive muscle atrophy which is associated with gap and transection nerve injuries (Afshari, Nguyen et al. 2018, Schilling, Schusterman et al. 2019). This effect of PNI on the musculature is often telling as the dysfunction can be measured using various functional tests which are well documented in the literature. Such tests typically include walking track analysis (Varejao, Meek et al. 2001, Sarikcioglu, Demirel et al. 2009), gait kinematics (Kappos, Sieber et al. 2017), sensory/stimuli response (Kim, Yun et al. 2015), nerve conduction velocity (Walsh, Sloane et al. 2015), and electrophysiological outputs such as the generation of isometric contraction force (Merritt, Hammers et al. 2010) or compound muscle action potential (CMAP) (Mallik and Weir 2005, Arnold, Sheth et al. 2015). There is speculation about the reliability of many commonly-used tests which rely on monitoring and quantifying animal behavior, such as sciatic nerve indexing (SFI) and stimuli-dependent sensory tests. Despite this, the literature contains many animal models that

leverage injury to a variety of nerves for studying PNI and MA as shown in **Figure 3**, modified from (Angius, Wang et al. 2012).

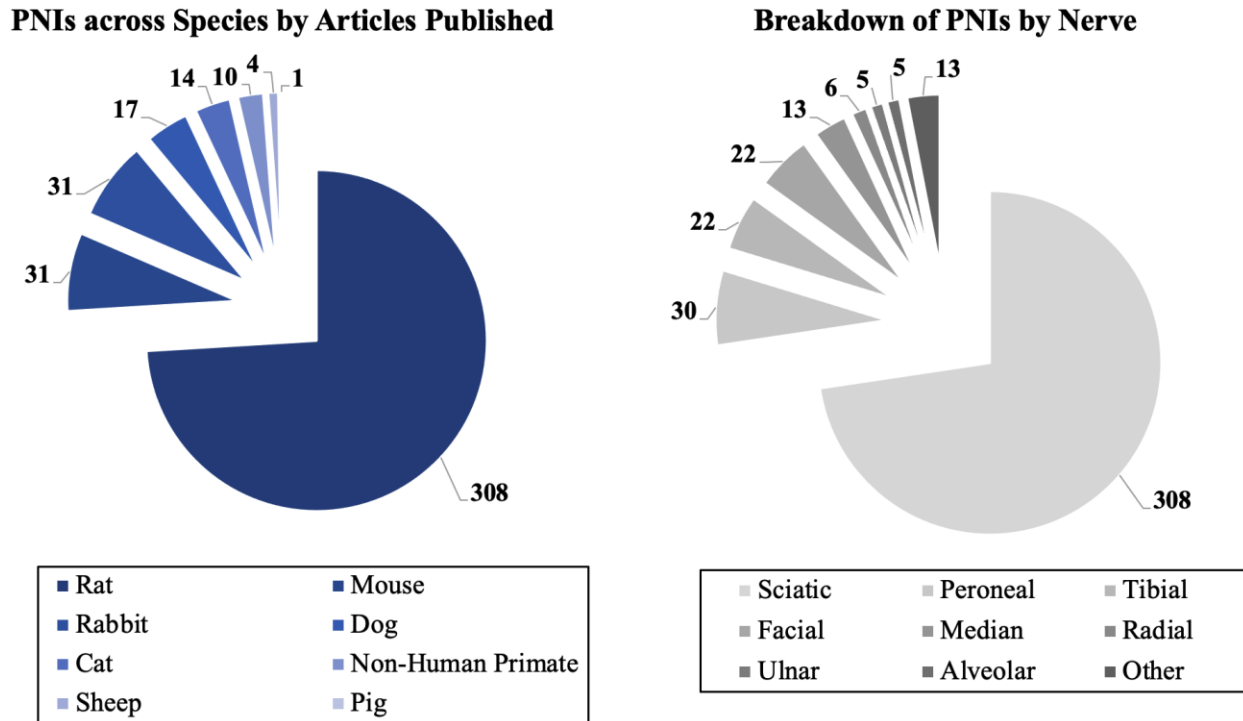


**Figure 3: Breakdown of PNI Models by Species and Nerve.**

Electrophysiological testing tends to produce a more robust assessment of functionality and muscular health in PNI models relative to histology alone, though the tradeoff is the highly invasive nature of such examinations (Geuna 2015). Induction of median, ulnar, or radial nerve injury in bipedal models (i.e., non-human primates) specifically, can yield assessments that better mimic functional return in humans. Such analyses include grasping strength as well as the fidelity and accuracy of digit motion. These tests are more translationally akin to human upper extremity function relative to the quadrupedal counterparts, but such modeling does not come absent of cost

or controversy (Cabaud, Rodkey et al. 1980, 2011, Wang, Huang et al. 2014). Use of the sciatic nerve in the rat has been most the most widely utilized model, due to its cost effectiveness, ease of access to the nerve, and abundance of tests able to be performed with respect to function and histological outcomes.

## **2.2 Intramuscular Injection of Adipose-Derived Stem Cells Mitigates Muscle Atrophy after Critical Size Denervation Injury**

Autologous adipose-derived stem cell (ASC) therapy represents a potentially promising strategy to address the detrimental changes in muscular denervation. ASCs can be obtained in a non-invasive manner, can be characterized by a broad range of surface markers (**Table 2**), can undergo significant expansion within weeks (Kolle, Fischer-Nielsen et al. 2013), and, processes are currently being developed to make ASCs increasingly accessible at the point-of-care (Gimble, Katz et al. 2007). Though stem cells exist in brown and beige fat, the adipose-derived stem cell population of interest here is resident of white adipose tissue (WAT). There typically is not a distinction made between the stem cell population retrieved, being either from visceral WAT, subcutaneous WAT, or a mixture. Further, that visceral and subcutaneous WAT share a common precursor stem cell is yet to be fully elucidated. Direct observation of the ASC *in situ* has yet to be determined, due to a lack of single distinguishing surface marker.

Dissent around the exact niche of the ASC exists, but this cell population is thought to reside either within the adipose tissue (Zimmerlin, Donnenberg et al. 2010), or immediately adjacent to the vasculature (Zannettino, Paton et al. 2008). Either of these locales can be rationalized because they both would support crosstalk between the ASCs and the local adipocytes

though cell-cell interactions. These locales would also provide a means to detect systemic circulatory signals from bloodborne adipokines regulating adipose turnover, which is approximately 10% per year (Spalding, Arner et al. 2008). Since discovery, the stem cell population residing within WAT has been given several acronyms: PLA for “processed lipoaspirate cell”, ADSC for “adipose-derived stem cell”, AT-MSC or WAT-MSC for “adipose tissue mesenchymal stem cell” or “white adipose tissue mesenchymal stem cell”, respectively. Herein, ASC will be used to define the stem cell type. ASC is shorthand for “adipose-derived stem cell”, but here, the word “derived” is ignored in the acronym (Schilling and Marra 2019).

**Table 2: Surface Markers of ASCs.**

<b>Surface Marker</b>	<b>Expression</b>	<b>Synonyms</b>	<b>Functions</b>
CD36	+	Platelet Glycoprotein 4 (GPIV), SCARB3	Cell adhesion, cholesterol transport
CD44	+	H-CAM, Extracellular Matrix Receptor III	Cell adhesion, cell migration
CD73	+	NT5E, NTE, eNT	Hydrolysis of extracellular nucleotides
CD90	+	Thy-1	Cell adhesion
CD105	+	Endoglin, HHT1	Angiogenesis via TGF $\beta$ interactions
CD166	+	AL-CAM, SC-1, BEN	Cell adhesion
CD11	-	Dependent on marker subtype	Inflammation, adaptive immune response
CD14	-	Integrin $\alpha$ D (ITGAD)	Regulator of innate immune response
CD34	-	Hematopoietic progenitor cell antigen 1	Cell adhesion
CD45	-	Leukocyte common antigen	Mediator of antigen receptor signaling
CD106	-	VCAM-1, INCAM-100	Cell adhesion to vasculature endothelium

While there is an abundance of literature describing the application of ASCs to nerve tissue after PNI (**Appendix A**), few studies have sought to understand the impact of ASCs introduced directly into muscle after PNI. Two rodent studies have shown that ASCs promote muscle mass retention after PNI when administered into the denervated muscle and show cellular regeneration in both muscle ischemia (Di Rocco, Iachininoto et al. 2006) and muscle atrophy-inducing burn models (Wu, Huang et al. 2015). Additionally, the inflammatory response in muscle repair is essential to its healing process (Tidball 2017). ASCs have been implicated as having an innate mechanism to mediate local inflammatory responses (Leto Barone, Khalifian et al. 2013, Jin, Shen et al. 2017). Ideally, these ASC characteristics result in a therapy that protects against loss of muscle mass while shifting the inflammatory response toward a pro-regenerative, rather than pro-fibrotic microenvironment when administered into denervated muscle.

## **2.2.1 Methods**

### **2.2.1.1 Harvesting, Expansion, and Labeling of ASCs**

Inguinal, perirenal, and epididymal adipose was harvested aseptically from twelve male Lewis rats (LEW/Crl) yielding 6-8 grams adipose per rat, 200,000-300,000 ASCs per gram. Immediately after harvest, adipose was minced, digested in collagenase II (60 minutes, 37°C), and then centrifuged at 1000 RPM (10 minutes, 4°C). After separation the lipid supernatant was removed and the digested adipose was re-suspended in lysis buffer at 1ml per gram adipose; lysis buffer was comprised of 154 mM ammonium chloride, 10mM potassium bicarbonate, and 1mM EDTA in deionized (DI) water. Centrifugation was repeated and the supernatant removed. Resulting cells were re-suspended in plating media comprised of 10% fetal bovine serum in DMEM (Fisher Scientific, Waltham, MA), and then plated onto culture flasks coated with rat tail

collagen at  $5\mu\text{g}/\text{cm}^2$  (Millipore Sigma, St. Louis, MO). ASCs were plated at 5,000 cells per  $\text{cm}^2$  and expanded ( $37^\circ\text{C}$ , 5%  $\text{CO}_2$ ). Passage-three ASCs were labeled with DiR (Invitrogen, San Diego, CA), solubilized in absolute ethanol at 2.5mg/ml, and then added to culture in serum-free media (20 minutes,  $37^\circ\text{C}$ ). Labeled cells were centrifuged at 1500 RPM (5 minutes, ambient temperature) and washed in serum-containing medium four times to ensure unbound dye was completely removed.

#### **2.2.1.2 Sciatic Nerve Injury and ASC Injection into Gastrocnemius**

Briefly, all animals underwent sedation by inhalation of 2% isoflurane in oxygen. The surgical site was prepared by trimming fur and applying betadine to skin. The sciatic nerve was accessed through a 2cm transverse incision at the inguinal region of the right hindlimb. The gluteus muscle was dissected to expose the sciatic nerve, and a 1.5cm nerve segment was resected in all animals. The defect was either left empty or the nerve was re-sutured with 8-0 nylon as a reverse polarity autograft in distal-to-proximal orientation. **Figure 4** presents an illustration of the 1.5cm nerve surgery with images of the nerve access site and the sciatic nerve after its placement and suturing as a reverse-polarity autograft. The wound opening was repaired with absorbable suture.

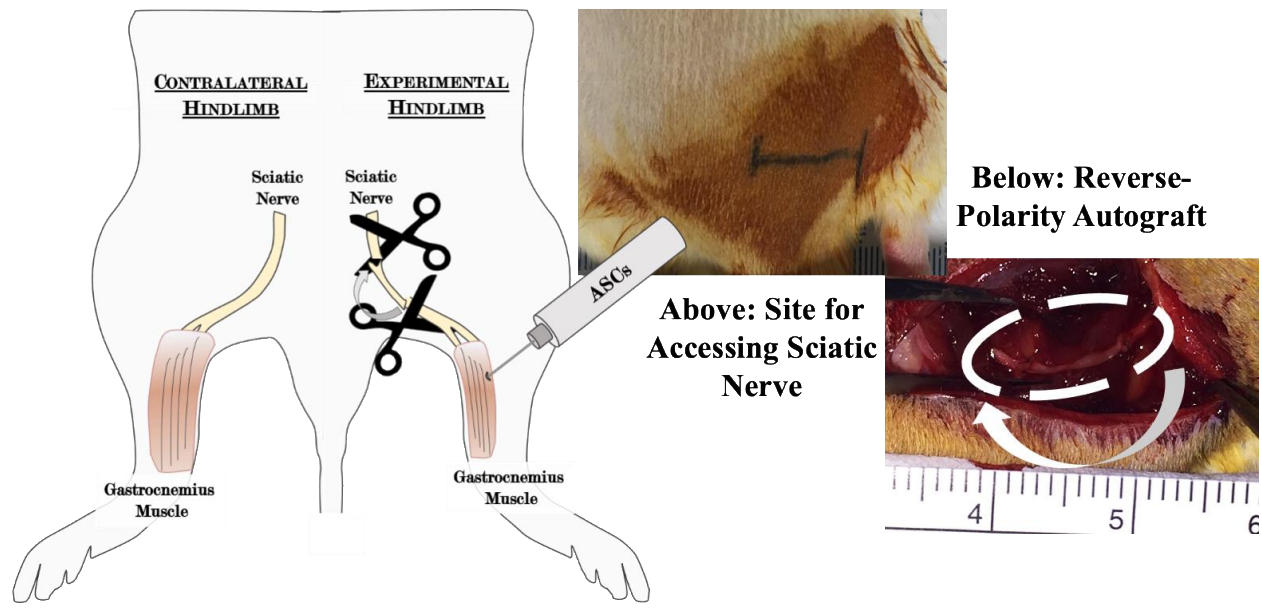


**Figure 4: Illustration of PNI and Images of Nerve Surgery.**

Syngeneic ASCs suspended in phosphate buffered saline (PBS) at a dose of 1 million cells per 0.5ml were injected into the gastrocnemius after nerve injury immediately after wound closure in two of the four cohorts using a 27Gx1.5” needle affixed to a 1ml syringe. The needle was inserted through skin at the base of the Achilles tendon, extending proximally on the hindlimb. Prior to this experimentation, injections were practiced on deceased rats, where methylene blue was injected in this manner, and complete muscular dissection revealed diffuse injection throughout the gastrocnemius muscle. One cohort having received an ASC injection immediately post-operatively also received an ASC injection of the same volume and concentration three weeks post-operatively, chosen as the midpoint of the in-life study. Two control groups did not receive ASCs injection: one control represented a worst-case scenario, being a nerve resection (Empty Defect), and second control represented the standard-of-care, being an autograft (Autograft Only); both received PBS injection of the same volume. A single operator performed all procedures to minimize surgical and injection rate variability. All animals were euthanized via CO<sub>2</sub> asphyxiation

followed by cervical dislocation six week postoperatively, a timepoint used in several studies to evaluate nerve regeneration both functionally and histologically (Dinh, Hazel et al. 2009, Mendez, Seikaly et al. 2016, Jeong, Kung et al. 2017). Gastrocnemius muscles harvested from both the operated (right) and non-operated (left) hindlimbs of all rats after euthanasia were imaged (Nikon D3400 digital camera) and weighed. Denervated muscles were normalized against their non-operated contralateral counterparts. All muscles were bisected, and one half was flash-frozen in liquid nitrogen and the other half was fixed in 10% neutral-buffered formalin. All statistical and histological analyses were based on the 6-week sacrifice. IACUC approval for animal research was obtained prior to all animal experimentation.

### **2.2.1.3 Histological, Immunohistochemical (IHC), and Immunofluorescent (IF) Staining of Muscle Sections**

For staining of paraffin-embedded slides, deparaffinization was performed at 60°C for 60 minutes. Slides were hydrated in two exchanges of xylenes, absolute ethanol, 95% ethanol and 70% ethanol, respectively. **Masson's Trichrome:** was stained per manufacturers' instruction (American MasterTech, Lodi, CA). **Dystrophin IHC:** antigen retrieval was performed in EDTA (1x, pH 8.0) for 25 minutes at 95°C and then allowed to cool at room temperature for 35 minutes; rabbit anti-dystrophin (Abcam AB15277, Cambridge, MA) primary antibody was diluted 1:150 in PBS and 1:100 bovine serum albumin (BSA) and was incubated at 4°C overnight; goat anti-rabbit secondary (Novus Biologicals NB7156, Littleton, CO) was diluted 1:200 in 1xPBS and 1:100 BSA, and sections were serially exposed to ABC and AEC kits (both Vector Laboratories, Burlingame, CA), respectively, for chromogen development; Mayer's hematoxylin was used as a nuclear counterstain (Millipore Sigma). **Oil Red O:** Frozen sections (7µm) were dehydrated in 60% 2-propanol; lipid was stained with 0.05% Oil Red O (Millipore Sigma) and Wiegert's

hematoxylin (Millipore Sigma) counterstain was applied. **iNOS/IL-10 IF**: antigen retrieval was performed in 10mM citric acid in 0.05% Tween-20 at pH 6.0 for 25 minutes at 95°C and then allowed to cool at room temperature for 35 minutes; mouse anti-IL-10 (PeproTech 500-P60, Rocky Hill, NJ) primary antibody was diluted 1:100 in 1xPBS and 1:100 BSA, and then incubated at 4°C overnight; exposure to rabbit anti-iNOS (Abcam AB15323, Cambridge, MA) primary antibody followed, which was diluted 1:100 in 1xPBS and 1:100 BSA and then incubated at 4°C overnight; VectaFluor Duet (Vector Laboratories, DK-8828) was applied to sections for 30 minutes for fluorescent binding. **Ki67/Matrix Metalloproteinase-2 (MMP-2) IF**: was performed using methods similar to iNOS/IL-10 staining, using mouse anti-MMP-2 (Novus Bio NB200-113, Littleton, CO) primary antibody diluted 1:100 in 1xPBS and 1:100 BSA, and then rabbit anti-Ki67 (Abcam AB15580, Cambridge, MA) primary antibody, diluted 1:100 in 1xPBS and 1:100 BSA. Imaging was performed using a Nikon 90i (Melville, NY).

#### **2.2.1.4 Muscle Fiber Diameter Quantification**

IHC sections stained against anti-dystrophin were imaged at 20x magnification and eighty-four images were obtained from randomly imaging segments of muscle from all conditions. Each image file was randomized, and fiber quantification was performed by three blinded reviewers using ImageJ (National Institutes of Health, Bethesda, MD). Data were de-randomized for statistical analyses.

#### **2.2.1.5 Statistical Analyses**

On completion of the 6-week *in vivo* study, an observational (*post hoc*) calculation of statistical power was performed using  $\alpha=0.05$ , the total sample size of 17 animals distributed over the four experimental conditions, and a Cohen's f-value (Effect Size) of 1.99 as determined from

the ANOVA results. Normalized muscle mass and fiber area quantification data sets were subjected to Levene's Test for equal variance followed by one-way ANOVA, with either a parametric (Tukey Honestly Significant Difference [HSD]) or non-parametric (Games-Howell Pairwise Comparison) *post hoc* based on the results of Levene's Test. Normality of residuals was then tested using a Shapiro-Wilk W Test. In the muscle fiber diameter dataset Johnson's Sb Transformation was used to normalize residuals after non-normality was established, violating assumptions of the ANOVA analyses; Levene's Test was again applied to the transformed data for selection of appropriate one-way ANOVA. Statistical analyses were performed using Minitab 17 statistical software (State College, PA) for all analyses except observational calculation of statistical power, where G\*Power 3 (Düsseldorf, Germany) was used.

## **2.2.2 Results from Intramuscular Injection of ASCs into the Gastrocnemius**

### **2.2.2.1 Muscle Mass Quantification and Gross Imaging**

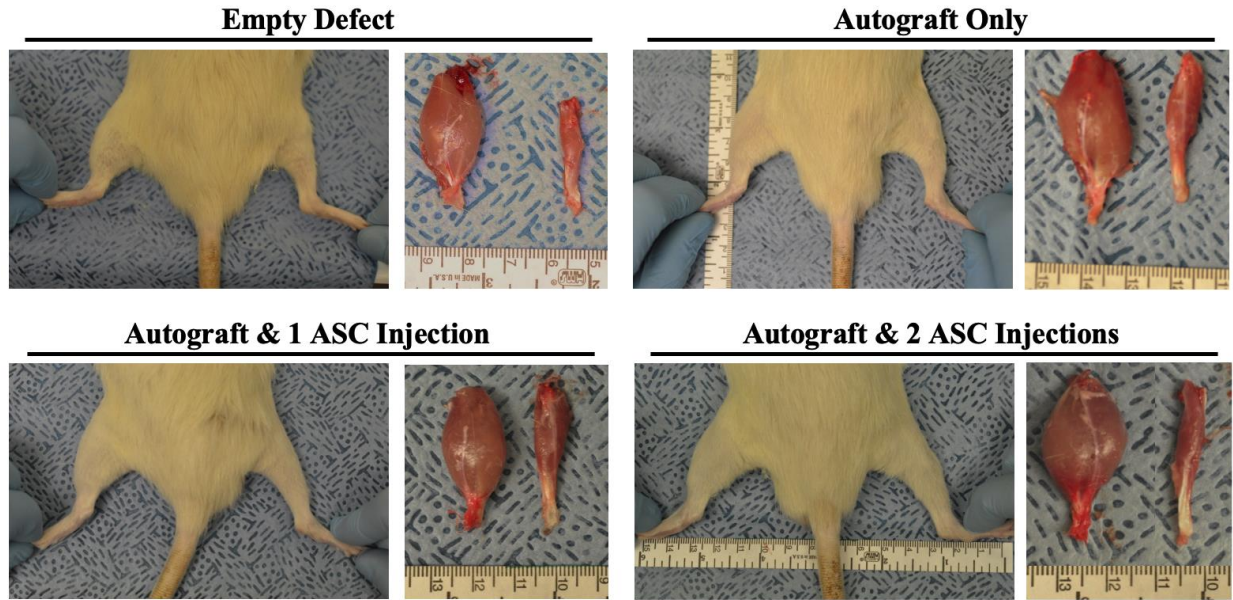


**Figure 5: Representative images of the gastrocnemii from the intramuscular ASC study.**

**Non-operated (left) hind-limbs with the contralateral operated (right) hind-limbs. Images comparing the excised gastrocnemius muscles at Day 42 displays reductions in size in all cases but was least appreciable in the cohort receiving an autograft followed immediately by an injection of ASCs.**

**Figure 6** quantifies the resulting gastrocnemii masses as a normalization of the operated (denervated) gastrocnemius to the contralateral non-operated gastrocnemius. Results from Levene's Test suggested equal variance within groups after normalization of gastrocnemius masses ( $p=0.573$ ) and normality of residuals was confirmed via Shapiro-Wilk W Test ( $p=0.783$ ), therefore a one-way ANOVA with a Tukey HSD *post hoc* analysis for multiple comparisons was performed.

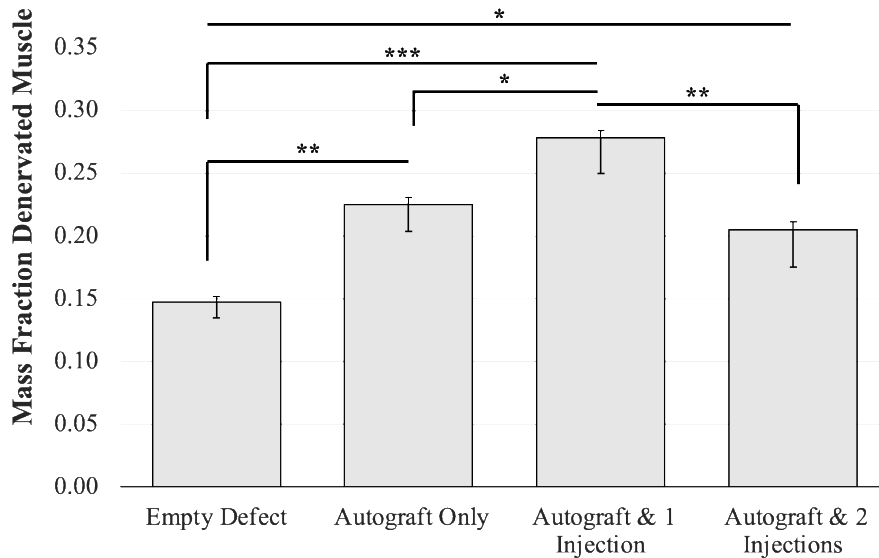


**Figure 6: Comparison of Resulting Gastrocnemii Masses after ASC Treatment.**

**Gastrocnemius muscles from both operated and non-operated hind-limbs were extracted and weighed. Muscles were normalized based on the muscle mass from the contralateral, non-operated hindlimb. Means are shown with error bars presenting standard error of the mean above and standard deviation below.**

**Statistics from ANOVA with a Tukey HSD *post-hoc* (\* $p < 0.05$ , \*\*  $p < 0.01$ , \*\*\*  $p < 0.001$ ).**

Initially, each of the four groups contained five animals. Three rodents did not survive surgeries however, and groups were redistributed as outlined in **Table 3**. An observational power analysis was performed yielding a statistical power of 0.999, suggesting sufficient sample sizes given the results. Post hoc analysis from the ANOVA yielded the average normalized gastrocnemius mass from the Autograft & 1 Injection cohort was statistically distinct from all other conditions ( $p < 0.001$ , model), each having lesser normalized mass. Normalization showed the Autograft Only cohort as averaging slightly higher than the Autograft & 2 Injections cohort, but this difference was not significant ( $p = 0.652$ , adjusted); the Empty Defect cohort was significantly less than all normalizations regardless of cohort.

### **2.2.2.2 Visualization of Microenvironment and Fiber Diameter using Masson's Trichrome, Oil Red O and Dystrophin IHC**

Masson's Trichrome was used to visualize the cellular infiltration, relative amounts of fibrosis, and overall structure of the fibers amongst cohorts, shown in **Figure 7**. Fibers from the non-operated control stained red, indicating the presence of keratin, as is typical of healthy muscle; contrastingly, all operated cohorts stained blue denoting dense deposits of collagen-based fibrosis. Subjectively, lipid presence as confirmed by Oil Red O staining showed an increased presence in the control cohorts relative to the native muscle and the cohorts injected with ASCs. IHC staining against dystrophin, a cytoplasmic protein surrounding the perimeter of the cell, was performed to quantify the area of the muscle fibers. The panel of dystrophin staining in the rightmost column of **Figure 7** displays selected images representing approximate average fiber sizes from each cohort. In total, 84 images were obtained and used for fiber area quantification. **Table 3** displays the breakdown of images and fibers quantified.

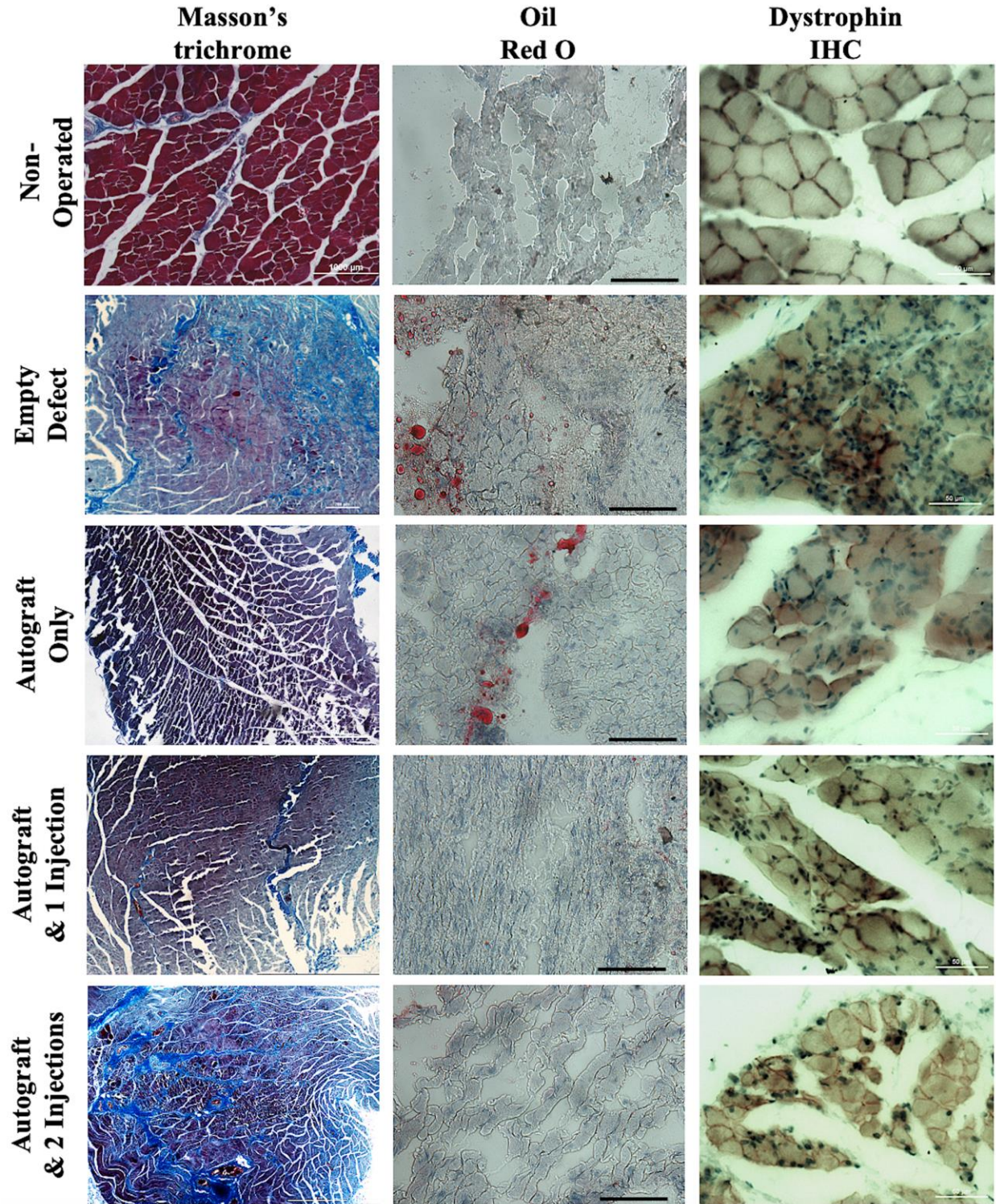


**Figure 7: Representative Histological Staining of Gastrocnemii after ASC Treatment.**

Masson's trichrome (left, scale bar: 1000µm), Oil Red O (center, scale bar: 100µm),

and dystrophin IHC images (left, scale bar: 50µm).

**Table 3: Summary of Study involving Intramuscular ASCs Injection(s).**

Presents the four cohorts present in the study: (1) injury only, (2) autograft only, (3) autograft and a single ASC injection post-operatively, and (4) autograft and an ASC injection post-operatively and then a second injection at three weeks post-operatively, at the midpoint of the study (abbreviation: Contralateral, CL)

Cohort	Autograft	Animal Count	ASC Injection	Dystrophin Images Count	Fibers Quantified
1, Empty Defect	No	3	No	Injured: 10 CL: 10	Injured: 1,052 CL: 766
2, Autograft Only	Yes	4	No	Injured: 5 CL: 5	Injured: 479 CL: 499
3, Autograft & 1 Injection	Yes	5	Yes, after injury	Injured: 15 CL: 15	Injured: 2,138 CL: 1,295
4, Autograft & 2 Injections	Yes	5	Yes, after injury and at 3 weeks	Injured: 10 CL: 14	Injured: 1,046 CL: 654

### 2.2.2.3 Muscle Fiber Area Quantification via Dystrophin IHC in ASC-Treated Muscle

Sections IHC-stained against dystrophin were imaged at 20x magnification over random locations, which were obtained by subdividing muscle sections into quadrants to minimize the risk of overlap and sampling bias, and then imaging. This yielded 84 images, or approximately 5 images per rat, used for muscle fiber area quantification. Each image file was randomized and analyzed by three blinded reviewers, where approximately 7,900 fibers were quantified via ImageJ from all images. Due to non-normality of residuals ( $p < 0.01$ , Shapiro Wilk W Test), data was transformed ( $T_{Area}$ ) via Johnson's Bounded (Sb), yielding **Equation 2-1**.

**Equation 2-1: Johnson’s Bounded Transformation of Muscle Fibers Analysis Data Set**

$$T_{Area} = \log\left(\frac{Area - 5.707}{48255 - Area}\right) \cdot 0.6812 + 0.9564 \quad (\text{Equation 2-1})$$

Residuals before and after transformation are presented in **Figure 8**, graphing residuals of the muscle area pre- and post-transformation, establishing normality.

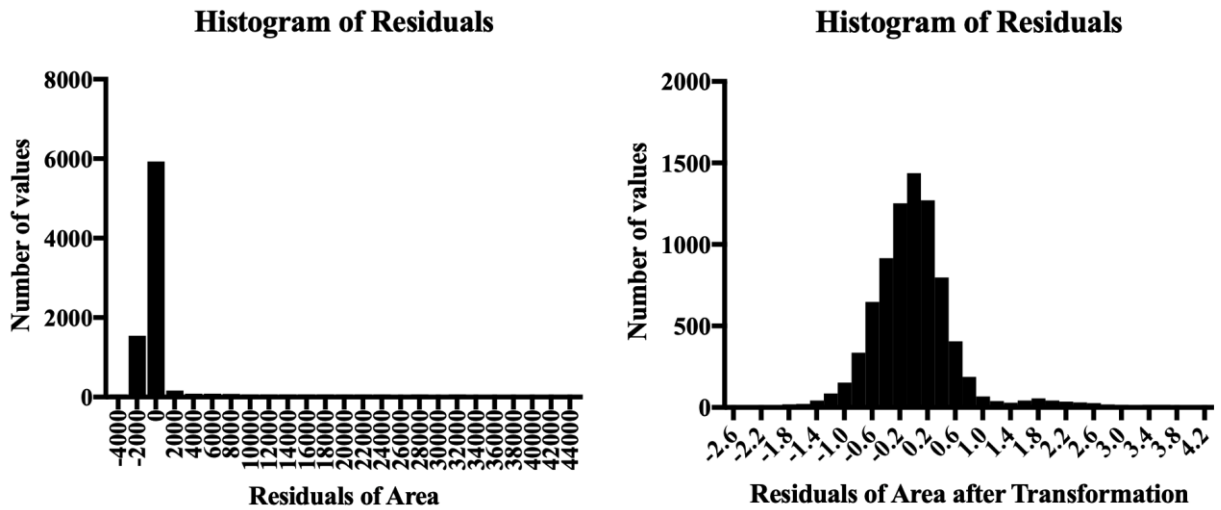


**Figure 8: Muscle Fiber Area Residuals Histograms Pre- and Post-Transformation.**

These Histograms display the residuals of the Muscle Fiber Area before and after Johnson Sb Transformation of the Fiber Area values, where transformation resulted in a more normal distribution relative to the retransformed values.

Levene’s Test was again performed on the transformed data, determining unequal variances between groups ( $p < 0.001$ ) and therefore conditions were analyzed for significance using Games-Howell Pairwise ANOVA. Data was reverse transformed ( $RT_{Area}$ ), yielding **Equation 2-2**.

**Equation 2-2: Reverse Transformation of Muscle Fibers Analysis Data Set**

$$RT_{Area} = \frac{-48255e^{1.468T_{Area}} - 23.2356}{-e^{1.468T_{Area}} - 4.07142} \quad \text{(Equation 2-2)}$$

**Figure 9** presents the muscle fiber quantification data if left in as transformed values per **Equation 2-1**. Data was assessed with ANOVA and Tukey HSD *post hoc*, the groupings of which are shown below the error bars. Prior to the reverse transformation, it can be seen that the results values are negative, which misrepresents the data set as the source data represent area measurements of muscle fibers and therefore cannot be of negative area. Due to this, the reverse transformation is necessary.

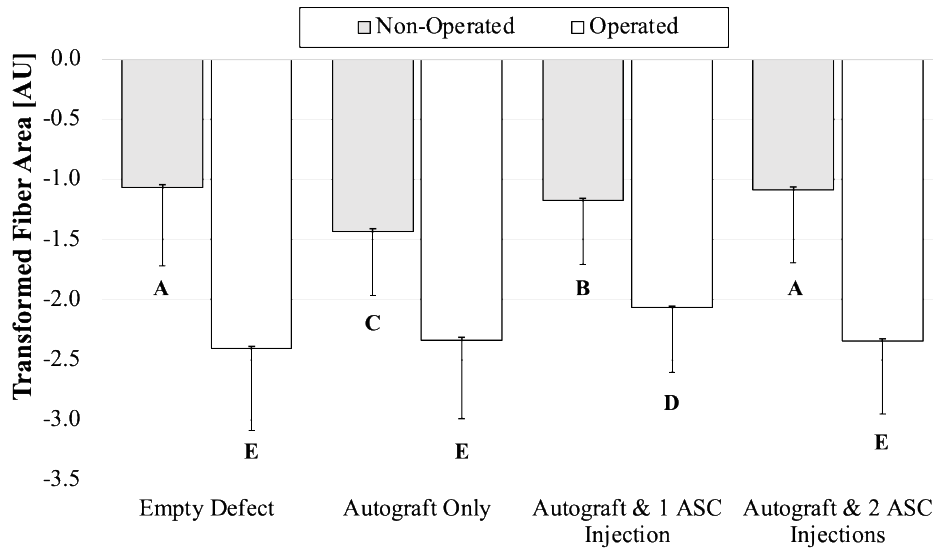


**Figure 9: Muscle Fiber Area after Normalizing Transformation.**

Muscle fiber area quantification from blinded dystrophin IHC fiber analysis graphing data after Johnson’s Sb Transformation. Means are shown with error bars presenting standard error of the mean above and standard deviation below. Statistical analysis was performed using Games-Howell Pairwise ANOVA, where groups that do not share a letter are different with statistical significance ( $p < 0.001$  for all comparisons).

**Figure 10** displays results from fiber area quantification after reverse transformation per **Equation 2-2**. In all cases, the fiber areas of the non-operated, contralateral muscle were significantly larger than their denervated counterparts. Corroborating the mass normalization data, the Games-Howell test resulted in the Autograft & 1 Injection cohort having significantly larger fiber area relative to the other operated.

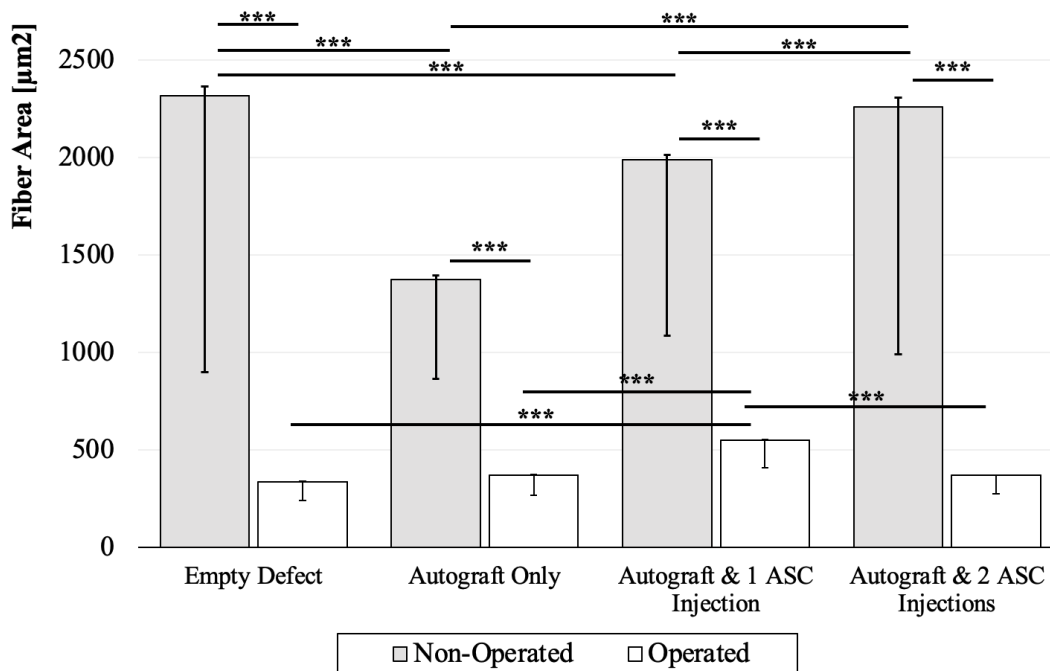


**Figure 10: Muscle Fiber Area Quantification after Reverse Transformation**

Means are shown with error bars presenting standard error of the mean above and standard deviation below.

Statistical analysis was performed using Games-Howell Pairwise ANOVA (\*\*p < 0.01, \*\*\*p < 0.001).

#### 2.2.2.4 Immunomodulatory Markers toward Muscle Regeneration, iNOS and IL-10

DiR-labeled ASCs were confirmed at Day 1 post-injection as shown in Figure 11. DiR-labeled ASCs are shown to remain in the muscle as shown throughout **Figure 12**. **Figure 12A** displays sections that were dual-labeled against inducible nitric oxide synthase (iNOS, red) and

interleukin-10 (IL-10, green) and counterstained with DAPI (blue). A fourth channel (cyan) for DiR can be seen below the composite-channel IF images.

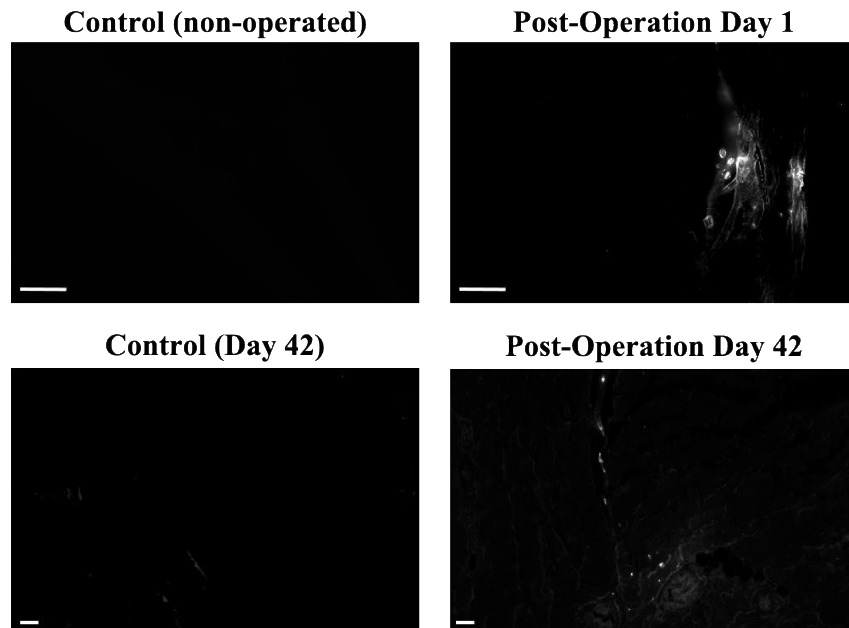


**Figure 11: DiR-Labeled ASCs in the Gastrocnemius.**

**Images of DiR marker at Day 1 and Day 42 post-operatively, confirming the presence of labeled ASCs in the gastrocnemius muscle throughout the *in vivo* investigation. Scale bars: 100 $\mu$ m.**

**Figure 12** also displays presence of both IL-10 and iNOS in non-operated muscle, where IL-10 appeared consistently stronger than iNOS. Similar IL-10 and iNOS presence was seen consistently throughout the Autograft & 1 Injection cohort, however far more nuclei were present in each image relative to the non-operated control images. DiR-labeled ASCs were found throughout and appeared to be localized to some areas of IL-10 and iNOS presence. Nuclear infiltration of similar magnitude to the Autograft & 1 Injection cohort is shown in the other three cohorts. IL-10 presence and intensity appear similar in Autograft Only and Autograft & 2

Injections cohorts. The Empty Defect cohort appeared to have the highest presence of iNOS throughout and limited presence of IL-10.

#### **2.2.2.5 Reconstructive Markers toward Muscle Regeneration, Ki67 and MMP-2**

**Figure 12B** displays sections that were dual-labeled against Ki67 (red) and MMP-2 (green) and then counterstained with DAPI (blue). Again, a fourth channel (cyan) for DiR is shown. Both the Non-Operated and Empty Defect cohorts were vacant of Ki67 and MMP-2 presence throughout. Ki67 was present in the Autograft Only cohort and appeared more prevalent in the Autograft & 1 Injection cohort. Both cohorts receiving ASC injections showed presence of MMP-2, albeit sparse. The DiR-labeled ASCs did not appear to be localized to the presence of either Ki67 or MMP-2 in the Autograft & 1 Injection cohort; in contrast, the DiR-labeled ASCs of the Autograft & 2 Injections cohort seemed to be localized about the presence of MMP-2, although this was not necessarily true for each DiR-labeled punctum, as can be seen in the image in the figure.

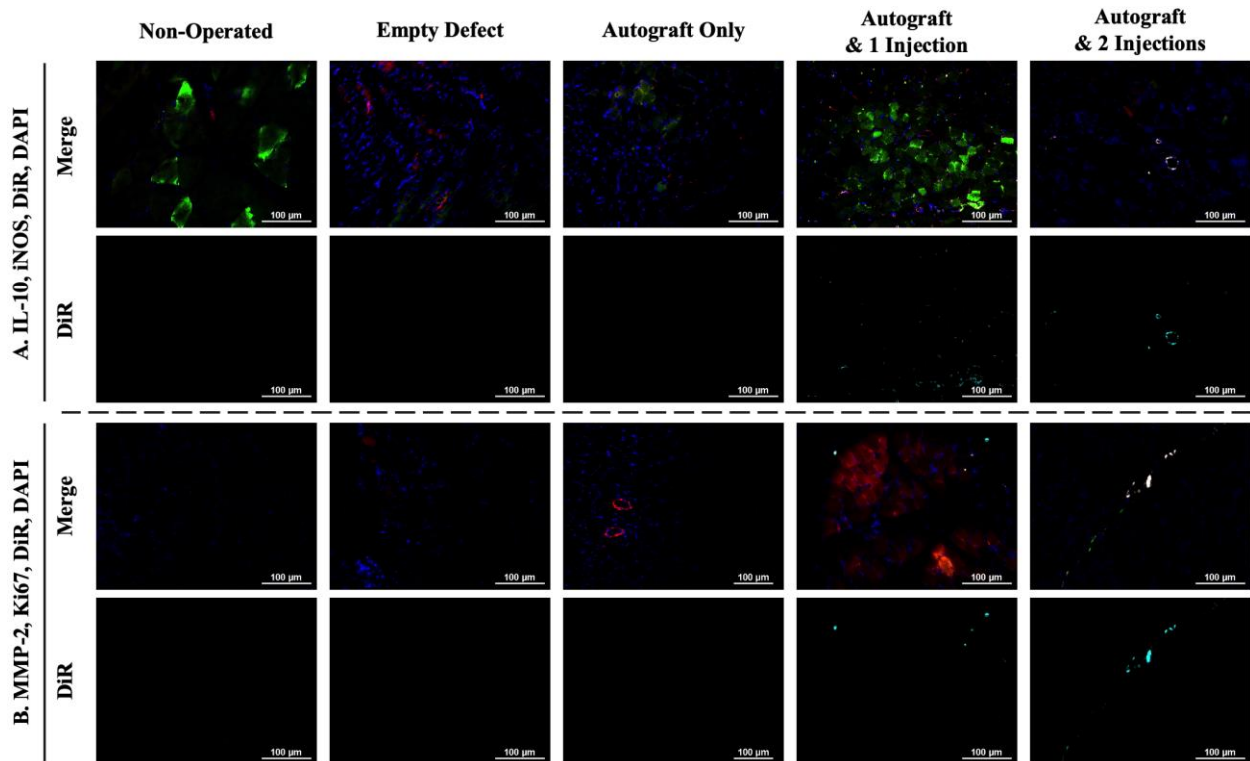


Figure 12: IF Markers in Gastrocnemii after ASC Treatment.

Panel A (*top two rows*): IL-10 (green), iNOS (red), ASCs (DiR, cyan – channel shown as bottom row), and nuclei (DAPI, blue). IL-10 is prevalent in native muscle and injured muscle having received a single injection of ASCs. iNOS prevalence was increased in all conditions relative to the non-operated muscle.

Panel B (*bottom two rows*): MMP-2 (green), Ki67 (red), ASCs (DiR, cyan – channel shown as bottom row), and nuclei (DAPI, blue). MMP-2 prevalence was negligible amongst conditions, although was shown to be present surrounding sites of Ki67-positive cells in muscle having received ASC injections. All scale bars 100µm.

### 2.2.3 Discussion on Intramuscular ASCs Study with 1.5cm PNI

Clinical challenges remain for restoring muscle after PNI-induced-denervation. Exercise therapies, electrostimulation, and muscular re-education each have drawbacks for restoring function (Geere, Chester et al. 2007, Oud, Beelen et al. 2007, Novak and von der Heyde 2013), and can fail to mitigate denervation. Within the microenvironment of human muscle, denervation-

induced atrophy shows a reduction of approximately 70% of the overall fiber cross-sectional area at two months after trauma (Burnett and Zager 2004). Similarly, appreciable discrepancies in muscle size can be visualized in **Figure 5**, the four cohorts show non-operated (left) hind-limbs with the contralateral operated (right) hind-limbs. Images comparing the excised gastrocnemius muscles at Day 42 displays reductions in size in all cases but was least appreciable in the cohort receiving an autograft followed immediately by an injection of ASCs. Normalized muscle masses showed that the Autograft & 1 Injection into the gastrocnemius immediately after autograft therapy was superior to other therapies and were consistent with those presented in a recent study that also injected ASCs into the gastrocnemius after sciatic nerve injury (Schaakxs, Kalbermatten et al. 2013). This model utilized a smaller, 1.0cm nerve defect, and their functional results showed some ASC-mediated repair based on walking track accuracy but were not compared to animals not having denervated muscle.

Interestingly, the cohort that received two injections of ASCs did not provide superior mass results relative to a single injection of ASCs. Rather this cohort performed similarly to the Autograft Only cohort. Although all animals regardless of cohort received an injection immediately post-operatively, either of ASCs or of PBS, the Autograft & 2 Injections cohort was the only cohort to receive an injection at the 3-week midpoint. The repeat injection may have contributed to a secondary traumatic response, altering the healing cascade. This assertion is speculative as the second injection was not controlled for in the other cohorts. Repeat injections, however, have been presented in the literature as trauma-inducing (Burnham, McNeil et al. 2006). The normalized mass results seen here may suggest a latency of the ASCs regenerative effects. The initial trauma may not be immediately overcome by presence of ASCs alone, but rather requires some duration before the regenerative effects can be appreciated. Such a time period is

apparently greater than the three weeks allocated after the second ASCs injection but may be less than the six weeks duration of the study.

Corroborating the results from the muscle mass normalization was the quantification of muscle fiber area. Dystrophin has been used for IHC or IF labeling followed by quantification of muscle properties (Brown, Marathi et al. 2012, Beekman, Sipkens et al. 2014). **Figure 10** highlights the expectedly large variations in individual fiber area variability (Ceglia, Niramitmahapanya et al. 2013), but consistent variability about the means given the large data set. This provides a level of assurance that the means can be compared with statistical confidence despite the high variability in individual fibers. Results from the Games-Howell Pairwise ANOVA corroborated the normalized muscle mass data, where the average transformed muscle fiber area from the Autograft & 1 Injection cohort was statistically greater than all other conditions; all other operated hindlimbs were not statistically different. In all cases, the average muscle fiber area from the non-operated gastrocnemius quantification was significantly greater than that of their operated counterparts.

Atrophying muscle begins to show fibrosis (Cholok, Lee et al. 2017) and lipid accumulation (Hamrick, McGee-Lawrence et al. 2016) within the inactive muscle. Masson's trichrome staining was performed to assess fibrosis of the gastrocnemius muscle as well as Oil Red O staining to appreciate lipid accumulation (Uezumi, Ito et al. 2011). Though not explicitly quantified here, **Figure 7** suggests that ASCs do not appear to reduce fibrosis, an inconsistent finding amongst recent publications. A 2-week investigation of three ASC injections into the denervated rat gastrocnemius reported a reduction in fibrosis relative to non-injected groups (Park and Kwon 2017), though this result was not reproduced perhaps due to fewer injections, the longer in-life duration, or some combination. Oil Red O staining appeared to present less lipid

accumulation in the cohorts having received ASC injections as shown in **Figure 7**. This is consistent with previous investigations suggesting that ASC secretome is capable of reducing lipid content in rotator cuff injuries (Sevivas, Teixeira et al. 2016). This finding, however, is not consistent amongst the literature where injections of human vascular and adipose-derived stem cells isolated from human stromal vascular fraction did not display significant changes in lipid reduction (Gumucio, Flood et al. 2016).

Upon denervation, the local cellular environment of skeletal muscle becomes altered, where presence of inflammatory cells amongst the muscle fibers increases (Dumont and Frenette 2010). Dual-IF staining was performed to assess macrophage presence as macrophages are essential to muscle turnover in normal and degenerative states (Bosurgi, Manfredi et al. 2011). For investigation into their subtypes, secretory factors iNOS and IL-10 were used as markers for M1 and M2 macrophages, respectively, consistent with previous reports (Qin, Holdbrooks et al. 2012, Novak, Weinheimer-Haus et al. 2014, Sciorati, Rigamonti et al. 2016). Further, the muscle healing cascade upregulates iNOS first, and IL-10 is upregulated after iNOS is downregulated, signaling the end of the healing phase (Tidball 2017), where absence of IL-10 has been shown to significantly impair the muscle healing cascade (Deng, Wehling-Henricks et al. 2012). The Empty Defect appeared to have the most prevalence of iNOS amongst any of the conditions (**Figure 12**), potentially suggestive of a degenerative environment (Buck and Chojkier 1996). ASCs may be involved in upregulation of these macrophage-secreted signals as localization of the DiR-labeled ASCs appear to be near signals of IL-10 presence, suggesting proximity to M2 macrophages and consistent with other reports of ASC-induced M2 macrophage recruitment (Young, Flynn et al. 2018, Zhao, Shang et al. 2018). These anti-inflammatory macrophages have been implicated in preventing the loss of overall muscular protein in atrophy models, and also protect from decreases

in loss of heavy-chain myosin (Dumont and Frenette 2010), a potential mechanism of action resulting in increased muscle mass and fiber diameter as a result of the pro-regenerative crosstalk from the injected ASCs after intramuscular residence.

The Ki67 staining for proliferative cells serves as an indicator of the changing microenvironment. **Figure 12B** presents muscles absent of injected ASCs showed little presence of Ki67, potentially representative of stasis in the non-operated muscle, and perhaps of the slow regeneration and scar formation consistent with injury to the gastrocnemius in laceration models (Pereira, Tan et al. 2012). Presence of Ki67 was observed has having increased prevalence in the Autograft & 1 Injection cohort relative to the others, which may be a corollary to an increased inflammatory response as suggested by the iNOS/IL-10 staining, and consistent with an advanced stage of healing per the normalized muscle mass results. Ki67 was attempted to be localized about MMP-2 as an additional indicator of the microenvironment. The matrix metalloproteinases have vast implications in muscle repair both in the normal as well as the dysfunctional or degenerative states (Carmeli, Moas et al. 2004, Kandarian and Jackman 2006). Ki67 has been used as a marker for proliferating satellite cells, which are approximately 1% of satellite cell population in normal muscle and its turnover (Mackey, Kjaer et al. 2009), consistent with the observation from the non-operated cohort. Exceedingly small signals of MMP-2 presence were found throughout the cohorts, with some presence being observed in the cohorts having received ASC injections. Particularly in the case of the Autograft & 2 Injections cohort, localization of the DiR-labeled ASCs and MMP-2 prevalence can be seen. MMP-2 has been implicated in the regenerative phase of muscle healing, whereas MMP-9 predominantly upregulates high-inflammatory pathologies (Fukushima, Nakamura et al. 2007), suggesting that perhaps MMP-9 may serve as a stronger indicator and comparator in future investigations.

### **2.2.3.1 Limitations of the Intramuscular ASCs Study**

Several limitations exist in the (Schilling, Schusterman et al. 2019) study. Foremost, functional characterization is essential to understanding reparations of denervation atrophy within the context of this injectable therapy and its capacity to heal beyond increasing muscle mass. Such functional outcome measures may include a method to analyze gait as a return to neuromuscular function or electrophysiological considerations like the quantification of muscle force by contraction or the assessment of the CMAP by electromyography (EMG). The 6-week in-life duration of this study was likely not of sufficient length to appreciate relevant changes in the functional outcomes due to the size of the defect created. Therefore, a future investigation should either seek to lengthen the investigation perhaps to 10 weeks or longer (Kokai, Bourbeau et al. 2011) or to reduce the gap-and-repair length, perhaps to a transection and repair. Finally, despite the histological characterizations administered, quantitative analyses into each of the characteristics investigated would provide a more thorough understanding of their respective contributions to the healing process.

Despite these limitations, this study was able to show that a single injection of ASCs immediately post-operatively were capable of surviving in atrophying muscle and were able to delay muscle atrophy as quantified by the increased resultant mass of the gastrocnemius, supported by the quantification of muscle fiber area across conditions. It appeared from this investigation, that an intermittent injection of ASCs at the midpoint of the study did not provide any benefit to the healing process, and that the number of injections may be relevant toward minimizing healing time. Additionally, ASC injection appeared to increase expression for IL-10 and Ki67 relative to all other conditions, while also reducing the overall presence of intramuscular lipid. Given the ease of acquisition and prospective relevancy to clinical translation possessed by intramuscular ASC

therapies, future investigations should seek to address longer-term studies (e.g., 16 weeks or longer) with characterization of functional recovery relative to physical activity as the current standard of care.

### **2.3 Development of a Method for Rodent Gait Analysis**

To offer further quantitative insight into neuromuscular regeneration after denervation atrophy, a method of gait analysis was adapted where sciatic function index (SFI) was performed consistent with previously-established methods of toe spread measurement (Varejao, Meek et al. 2001, Clavijo-Alvarez, Nguyen et al. 2007). An expandable walking track (**Figure 13**) was designed (Solid Works CAD/CAM). Three parts were designed to assembled into the walking track: the Door, the Main Segment, and the End Segment. Main Segments had the dimensions of 10cm length by 8cm width, where six bores (6mm diametrical by 3mm deep) were designed into both faces of the part such that magnets could be press-fitted into the faces. Eight Main Segments were printed, each having magnets press-fitted into their faces, making assembly, disassembly, and cleaning simple after each use. The Door was designed to overhang the walls of each Main Segment such that a rodent could be gently pushed with the door if a prompt was needed for it to begin walking. The End Segment covered both the top and the rear exit, creating a darkened space into which the rodent was enticed to walk, and therefore traverse the walking track, imprinting its pawprints. Each rodent's hind-feet were coated with water-soluble paint, and imprinted their pawprints onto the paper as they walked from the door-side of the walking track and into to the End Segment. For capturing the pawprints, standard receipt paper was laid into the track so that pawprints were embossed upon walking. The paper removed and then a clean sheet was applied

for capturing the prints of the next rodent. On completion, the walking track was disassembled, washed, and then disinfected with spray Cavicide disinfectant as ABS is not autoclavable.

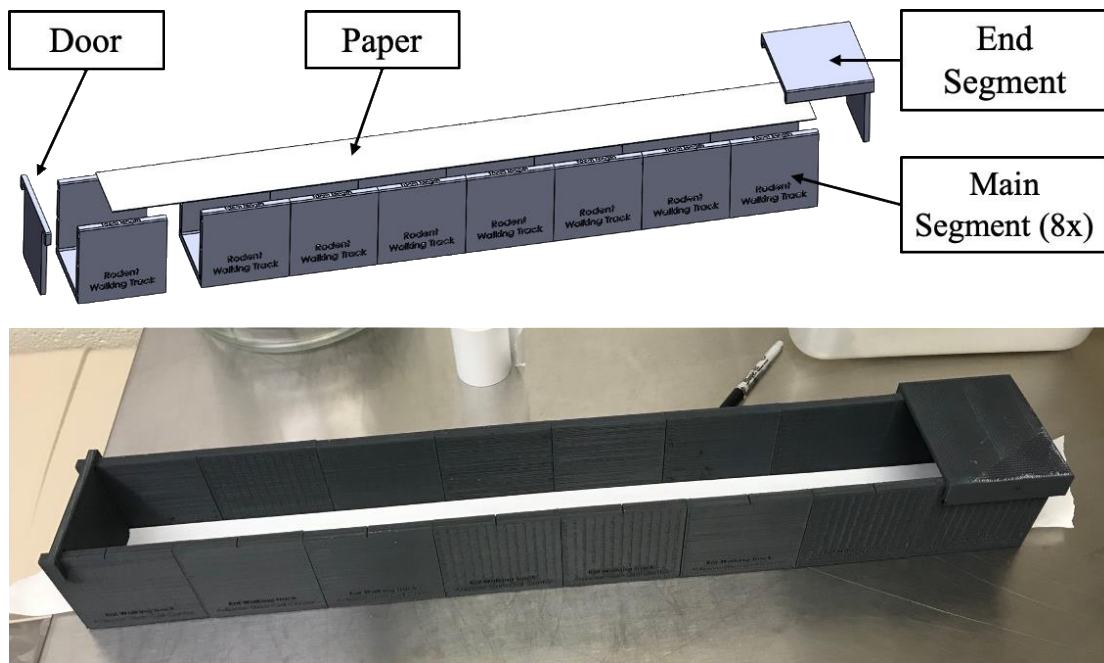


**Figure 13. CAD Rendering and Construction of Collapsible Rodent Walking Track.**

### **2.3.1 Details for 3D Printing Walking Track for Gait Analysis**

All parts were 3D printed from acrylonitrile butadiene styrene (ABS, 1.75mm diameter, MatterHackers, Lake Forest, CA) using a Raise3D N2+ printer (Irvine, CA). ABS filament was extruded through a 0.4mm nozzle at 265°C onto a heated bed with a thick coat of Disappearing Purple Elmer's Glue (Westerville, OH) to facilitate first-layer adhesion, atop a BuildTak surface (Maplewood, NJ) with the heated bed set to 110°C. Parts were printed using a skirt (single layer

of filament printed 5mm away from the boundary of the model on the initial layer only) to facilitate direct adhesion onto the glue-laden heated print bed. Parts were printed at a speed of 50mm/s with three shells, infills at 15% or greater, and with support structures at 10% infill where any overhang angle greater than 40° received support. The Raise3D N2+ was furnished with a printing hood, which encloses the printing area, and therefore better retains the heat of the part during printing to prevent the ABS from warping due to thermal mismatch between layers.

### **2.3.2 Calculation and Derivation of the SFI Equation**

SFI was calculated using measurements across the pawprint of the rodent, as presented in **Figure 14**. Three lines, being the intermediary toe spread (ITS), toe spread, (TS) and print length (PL) were used in the calculation of SFI throughout recovery. **Figure 14** displays the pawprint line nomenclature as described from (Varejao, Meek et al. 2001) with a representative normal limb pawprint (left) and representative injured limb pawprint obtained using the designed walking track. Note that the TS was not capable of being measured in the injured limb pawprint and therefore is not denoted with a line in the Injured Limb Pawprint.

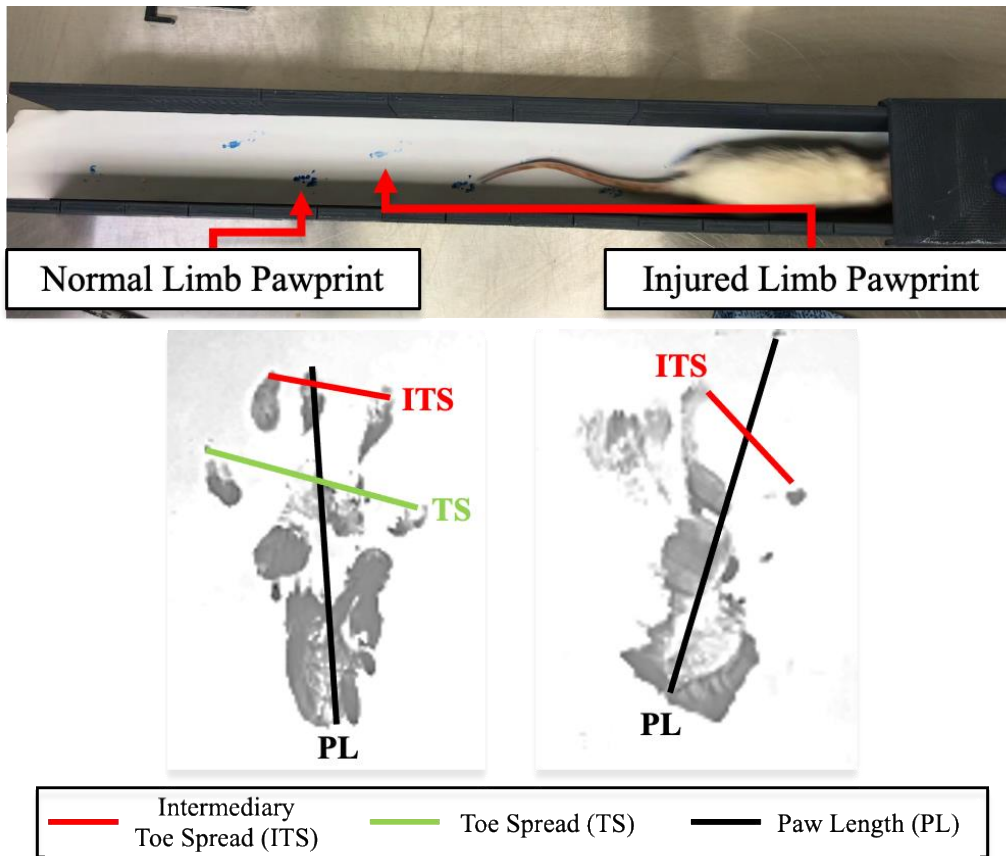


**Figure 14: Still of Rodent Walking with Resulting Pawprints.**

SFI is a measurement that originated in the rodent PNI literature to reduce the associations of electrophysiology data, like force generation, to more complex physiological phenomena like gait kinematics. The SFI is meant to deter the potentially inappropriate interpretation of return of function in the absence of gait-based analysis (Kanaya, Firrell et al. 1996). The SFI Equation was based upon the use of paired pawprint analysis, where the injured paw is compared to the non-injured, contralateral paw over each of the three measurements. This is shown in **Figure 14**, giving what is a fraction equation for each of the three line measurements, PL, ITS, and TS. Fractional relationships,  $F$ , are presented in **Equation 2-3** for ITS, **Equation 2-4** for TS, and **Equation 2-5**

for PL, where the subscript “c” denotes the print measurement from the contralateral limb and the subscript “i” denotes the print measurement from the injured limb.

**Equation 2-3: Fraction of Intermediary Toe Spread in Calculating SFI.**

$$F_{ITS} = \frac{ITS_i - ITS_c}{ITS_c} \quad \text{Equation 2-3)}$$

**Equation 2-4: Fraction of Toe Spread in Calculating SFI.**

$$F_{TS} = \frac{TS_i - TS_c}{TS_c} \quad \text{Equation 2-4)}$$

**Equation 2-5: Fraction of Paw Length in Calculating SFI.**

$$F_{PL} = \frac{PL_i - PL_c}{PL_c} \quad \text{Equation 2-5)}$$

Per (Varejao, Meek et al. 2001), the method was then optimized into the final SFI Equation by use of multiple linear regression analysis, determining the significance and worth contribution to the final equation, which is presented in **Equation 2-6**.

**Equation 2-6: Function for Calculating SFI.**

$$SFI = -38.2F_{PL} + 109.5F_{TS} + 13.2F_{ITS} - 8.8 \quad \text{Equation 2-6)}$$

In deriving this equation, the authors stated that regression analysis was performed such that values produced from the SFI Equation (**Equation 2-6**) that are approximately -100 denote total impairment and values that are approximately 0 denote normal function. There is, however, no

limits within the mathematics of **Equation 2-6** that inherently bound the linear equation within 0 and -100, therefore the SFI values produced may fall beyond the range.

## **2.4 Development of an Electrophysiology System Capable of Measuring Contraction Force**

Equipment for electrophysiology was reworked for additional function from what had previously been performed in the laboratory (Kokai, Bourbeau et al. 2011). **Figure 15** displays the hardware being a custom enclosure housing an NI MyDAQ (National Instruments, Austin, TX), which receives an analog input signal from the loadcell that is affixed immediately above the platform. Stimulation of the nerve was achieved using a World Precision Instruments IsoStim Stimulation Generator (Sarasota, FL A320R with A362 Battery Charger) with “Output” channels stimulating the sciatic nerve via nerve cuff (see **Section 2.4.2** for Nerve Cuff Details).

The custom enclosure with the imbedded DAQ was signaled to and by the Stimulation Generated through BNC (abbreviation: Bayonet Neill-Concelman) connector cables (BNC-59-106 BNC to BNC 75-Ohm Coax Cable, 6 feet, Hosa, Buena Park, CA). Two digital channels of the NI MyDAQ were utilized for signal generation, where the first channel was used to send a digital square wave to the Stimulation Generator, which would in turn, produce a stimulation (**Figure 15**, white labels); the second digital channel was split using a BNC T-Connector (BNC Male Connector to BNC Double Female Adaptor), which was used as a monitoring channel so that once a pulse was recorded, the DAQ could be notified to begin recording the analog data produced from the load cell. The hardware also included a BMA-200 Bio-Amplifier & ISO-Z Isolation Head Stage for measurement of electromyography (EMG), connected to the DAQ also via BNC

connection cables (**Figure 15**, green labels) though signals from these equipment pieces were not utilized (both CWE, Ardmore, PA).

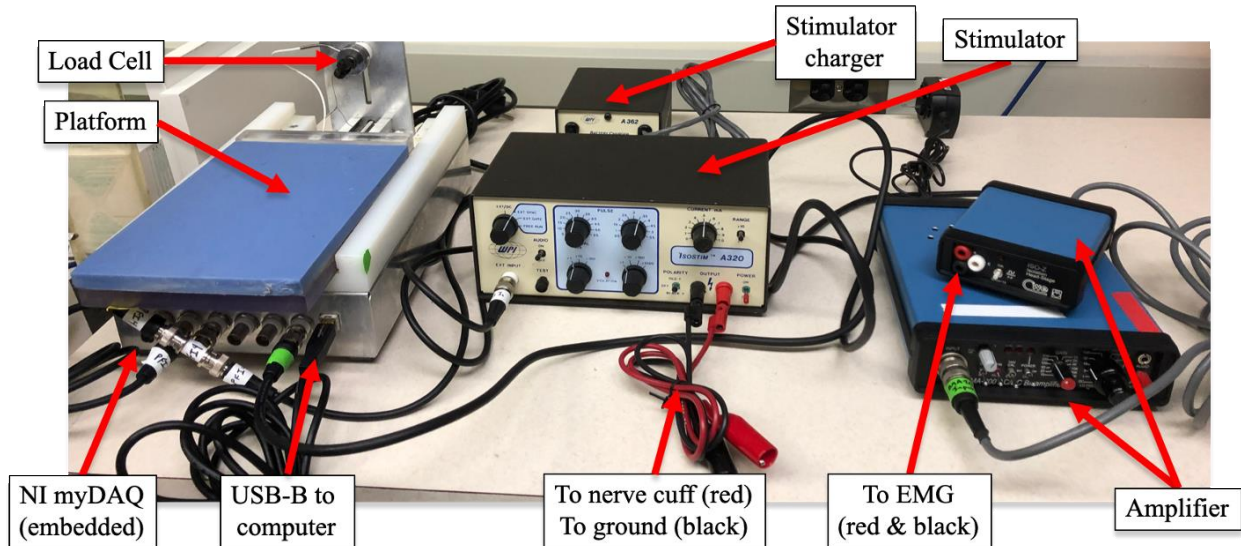


**Figure 15: Electrophysiology Equipment including Stimulator and Amplifier.**

Historically, the equipment was only sufficient to generate single stimulations, inducing a twitch contraction in the innervated based on the virtual interface that was present (Kokai, Bourbeau et al. 2011), where **Figure 16** displays a flow of the data and control of the equipment as written in the LabVIEW Virtual Instrument (VI). A single stimulation inducing a twitch is insufficient to measure the maximum contraction force due to the relaxation of the muscle after a single action potential (Posterino, Lamb et al. 2000, Moss, Lynch et al. 2017), and therefore the equipment required reprogramming to address the shortcoming if tetanic contraction force of the gastrocnemius was to be studied.

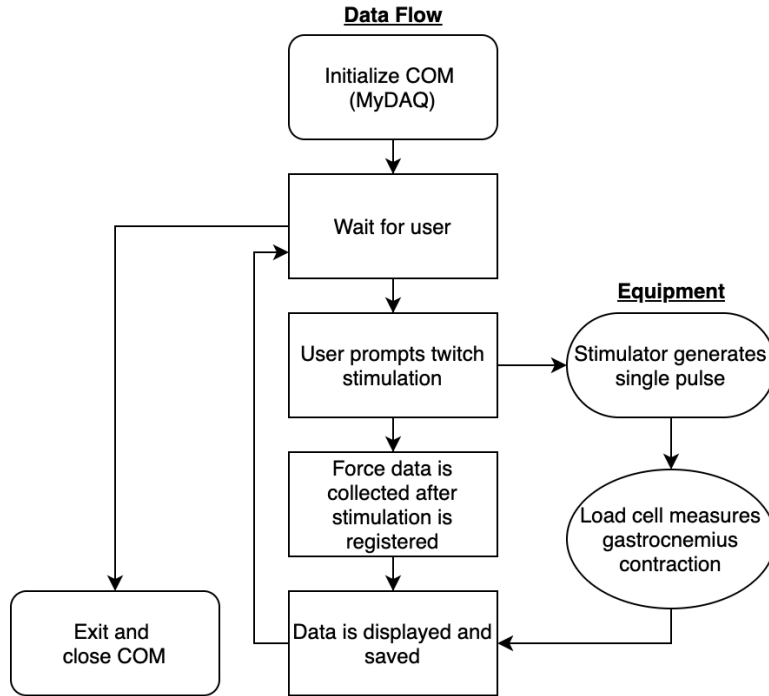


**Figure 16: Data and Algorithm Flow of Original Electrophysiology Equipment.**

### 2.4.1 Reprogramming a Data Acquisition System for Electrophysiology

The NI MyDAQ is able to interface with either LabVIEW or the NI MAX (Measurement and Automation Explorer) via USB-B cable and *requires* the NI-DAQmx driver package to be installed prior to its use; the driver package will not deploy from the hardware itself and requires an internet download for the appropriate version of LabVIEW being used, which typically corresponds to the year-version being used. The “COM” or “Dev” is then recognized based on the presence of the appropriate driver after its installation. The data flow in **Figure 17** displays the actions after initializing the COM and VI.

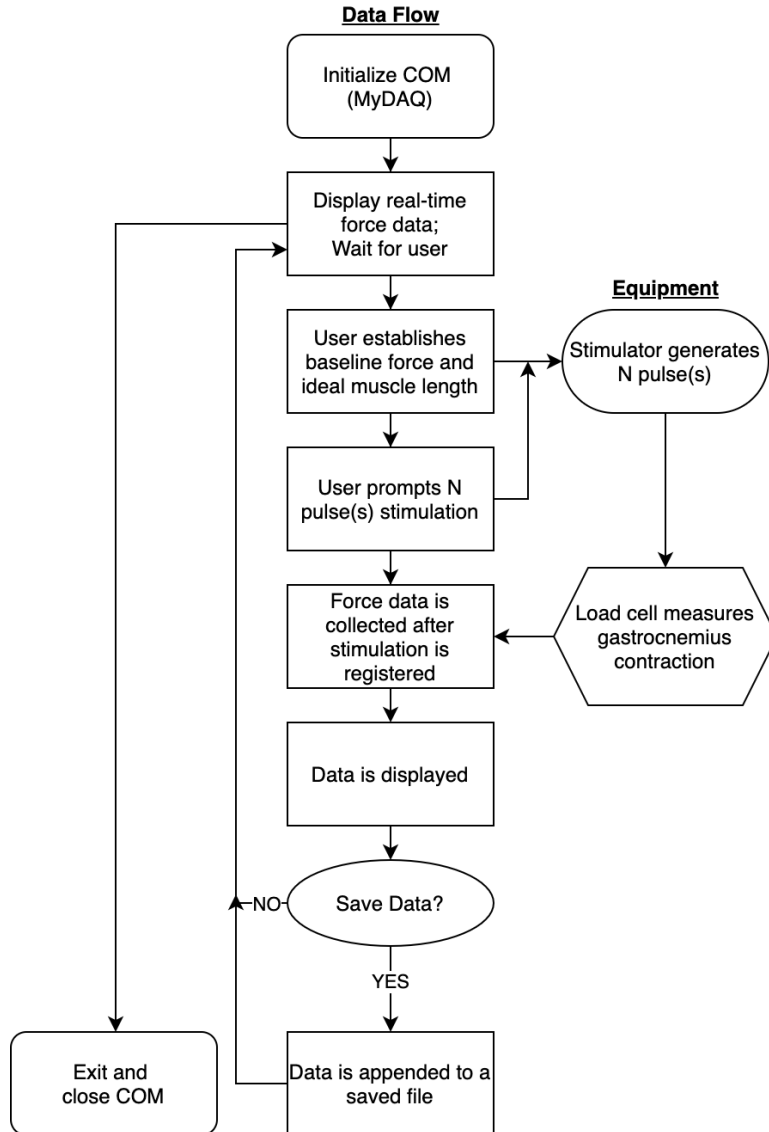


**Figure 17: Data and Algorithm Flow of Reprogrammed Electrophysiology Equipment.**

The extension of, and therefore tension on, a muscle will affect its ability to generate force, and therefore requires the optimal length to be found prior to testing the tetanic contraction force. Do to so, a real-time data read was implemented into the code such that simulation could be delivered and observed while extending or contracting the muscle tethered to the load cell using the Platform, where the Platform is affixed to a linear actuator that is able to move closer to or further from the load cell by a lead screw. Once the ideal muscle length was found, a stimulation

sweep was induced to establish the maximal contraction force between 1Hz and 150Hz, with all stimulatory square waves occurring over 1 second. All active pulses (square wave, value high) occur over a 0.01 second duration, and therefore the duration in between pulses (square wave, value low) are adjusted such that the peaks are equally spaced within the 1 second duration.

The VI in its entirety is presented in **Figure 18** presenting three parallel loops, being the Recording Event Structure, the Stimulation Event Structure, and an Independent While Loop that records the active time and performs some minimal manipulation on the analog data coming from the load cell. The VI was reprogrammed to utilize two distinct, non-parallel structures of data collection (being real-time, and continuous with N data points) within a single independent event structure, the “Recording Event Structure” as shown in **Figure 18**. The advantage to this architecture was to move the recording of the measured load cell data off of the VI-executing processor and onto the processor existing in the MyDAQ. This was done as the MyDAQ has a greater resolution for collecting data relative to the computer on which the VI was being executed and is able to measure with higher precisions (e.g., rates greater than 1 kHz). The LabVIEW VI was reprogrammed with “Tasks”, which were defined in the MAX IDE and then implemented within broader architecture in the main VI such that specific parameters like the file path, data sampling/recording, and baseline force (a function of the ideal isometric length) could each be customized and saved for each hindlimb being tested. A Digital Pulse Task was created to generate square waves, which were then sent to the Simulation Generator to induce N-pulses as defined by the user. The “Event Cases” structure that is called out in **Figure 18** displays the “waiting case”. The two additional cases essential to function are shown in **Figure 19** and **Figure 20**.

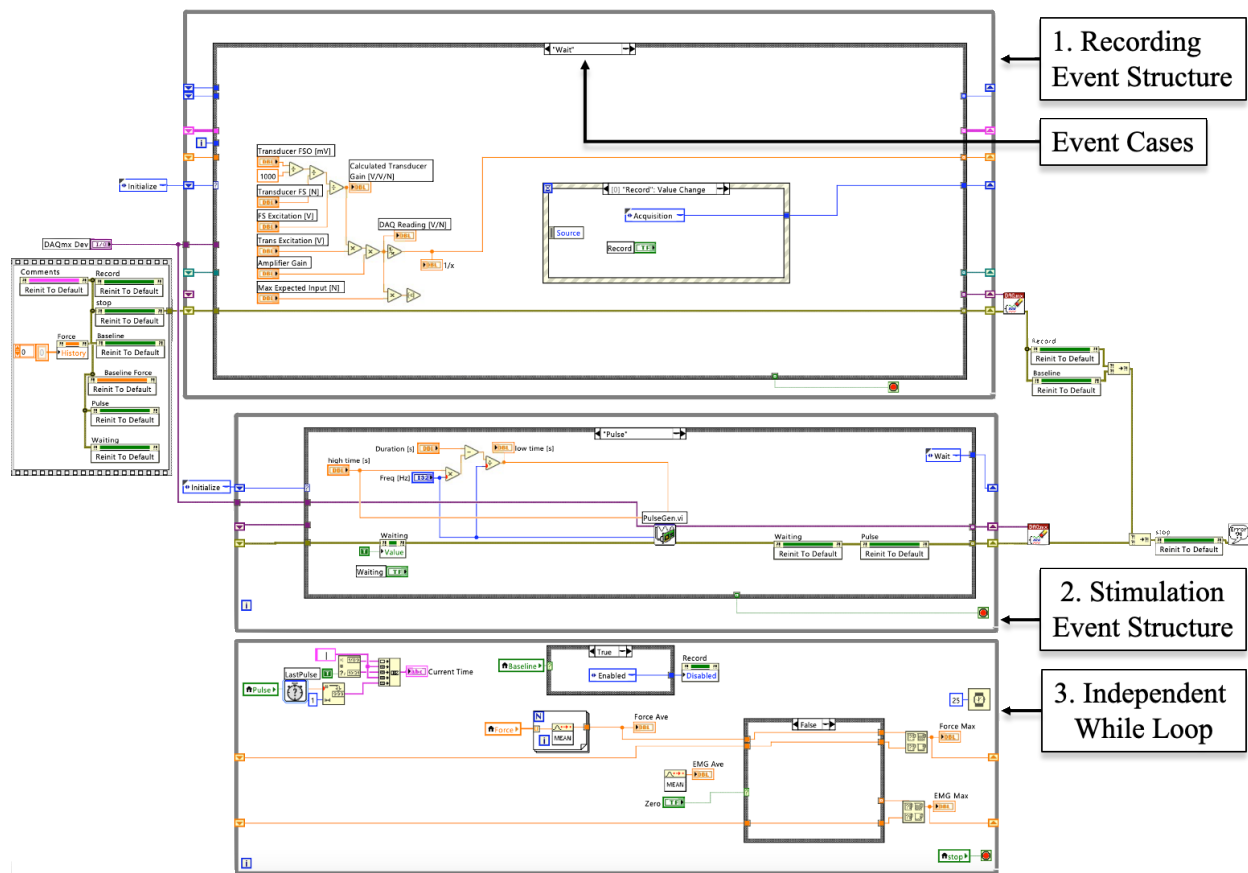
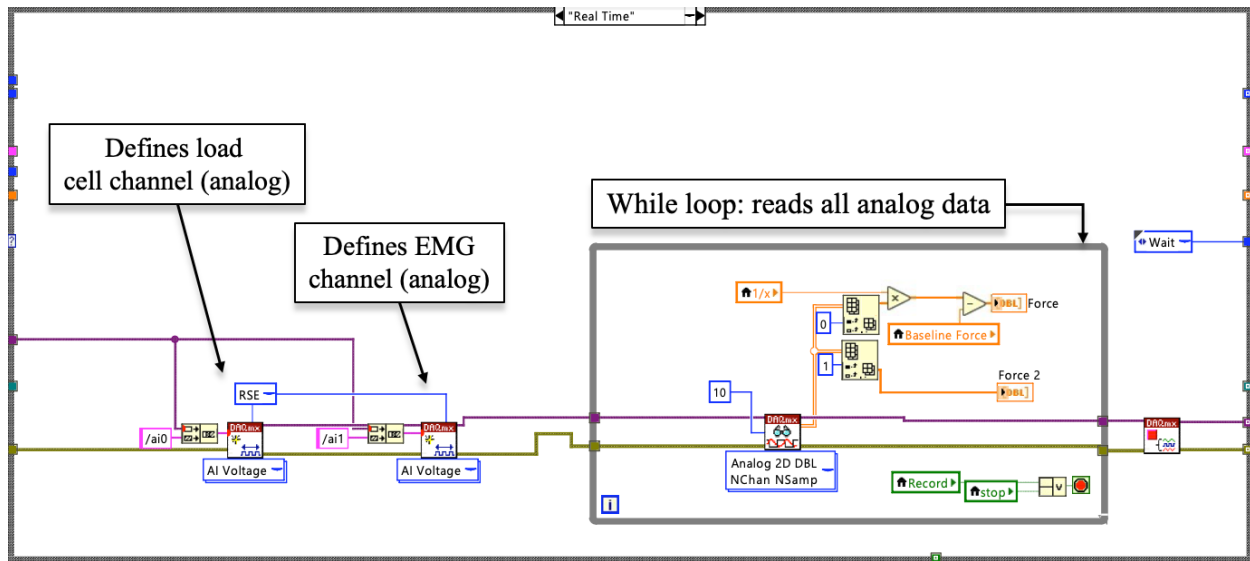


Figure 18: Entire LabVIEW Block Diagram for Governing Electrophysiology Equipment.

Figure 19 displays the VI block diagram with functions broken out from a MAX Task. This case prompts two analog channels of the DAQ to open, one for the load cell and the other for EMG reading, though the latter is not used. The following While Loop iterates at approximately 100Hz, continuously collecting data form the load cell and displaying it for the user at the graphical user interface (GUI). When the user initiates a pulse on the GUI, the “Stimulation Event Structure” (Figure 18) becomes active, acting irrespective of the tasks occurring in the “Recording Event Structure”.



**Figure 19: LabVIEW Case for Reading Force Data in Real-Time.**

**Figure 20** displays the case that is capable of collecting and saving data from the DAQ at sampling rates greater than what the PC processor itself is capable of. This structure is utilized after the user defines the baseline force, and then the user may then prompt a recording at some specified sample recording rate (typically set to 500Hz but can achieve a recording rate of 50kHz if necessary). Similar to the case presented in **Figure 19**, the analog channels responsible for reading the load cell and the EMG amplifier data (the latter of which is unused here) are defined; additionally, the digital channel for monitoring the pulse signal is defined. The program then waits until a pulse signal is received from the Stimulation Generator, at which point, the data collection for the user-specified duration and at the user-specified sampling rate (finite sampling as opposed to continuous) ensues; the pulse is generated from user interaction at the GUI (see **Figure 18**, “Stimulation Event Structure”). Finally, the data being received from the DAQ is parsed in the For Loop, where it is timestamped and then passed into the next case (not shown) to be saved into an appended text file.

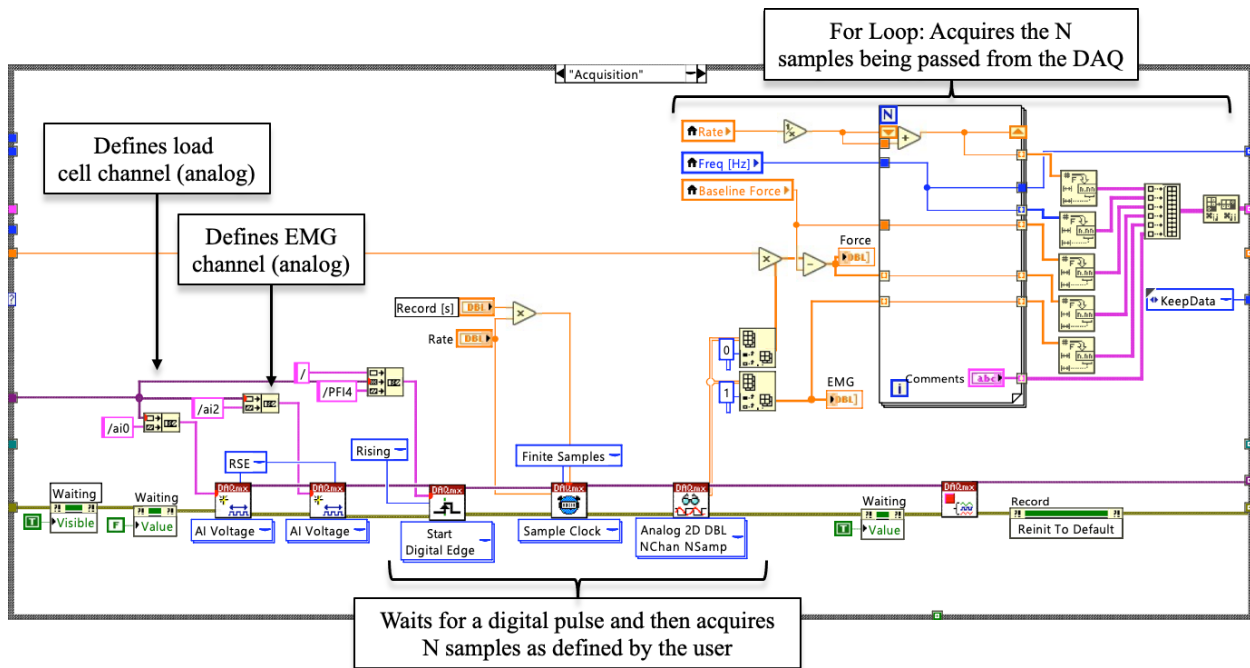


Figure 20: LabVIEW Case for Collecting Force Data from the DAQ.

## 2.4.2 Fabrication of Stimulation Cuffs

For stimulating the sciatic nerve and generating a contraction force at the gastrocnemius, stimulation cuffs were fabricated from tubing and specialty wire, which could then generate a stimulation of a known frequency using the electrophysiology equipment operated by the rewritten VI. The following paragraph describes the flow of images displayed in **Figure 21**.

For making a nerve cuff, a segment of tubing (5155T12, 1/16" ID Tygon tubing, McMaster-Carr, Robbinsville, NJ) approximately 1cm in length was cut. A length-wise segment was then removed using a scalpel such that approximately two-thirds of the tube circumference remained (**Figure 21A**). A 20G needle was then fed through the cross-section of the tubing (**Figure 21B**), creating a channel for the wire (Cooner Wire AS-631, Chatsworth, CA) to be fed through.

The wire was guided through the needle from the luer junction through the sharp-tip until it protrudes (**Figure 21C**). Then needle was then removed, leaving only the wire. The wire was then cut to approximately 10cm (length). Both side of the wire were de-insulated, where the “tubing side” was de-insulated approximately 5mm, and the “stimulator side” about 1cm (**Figure 21D**). These steps were repeated on the opposing side of the nerve cuff at a distance of 5mm from the previous wire insertion point, which was measured with precision calipers (**Figure 21E**). Both of the shorter de-insulated segments were glued to the outside of the nerve cuff (**Figure 21F**). The longer de-insulated segments of the wire were soldered onto a segment of de-insulated wire from subdermal needle electrodes (RLSND107-1.5, Rhythm Link, Columbia, SC); the soldering wire junction was then protected by electrical tape (**Figure 21G,H**). Finally, the opposing ends, of the subdermal needle electrodes were also de-insulated and were connected to the stimulator via alligator-to-banana cables (6927K42, Sleeved Alligator Clip x Stackable Banana Plug, McMaster-Carr). The alligator clips were fastened to the de-insulated ends of the subdermal needle electrodes and the banana plugs insert directly into the Stimulation Generator.

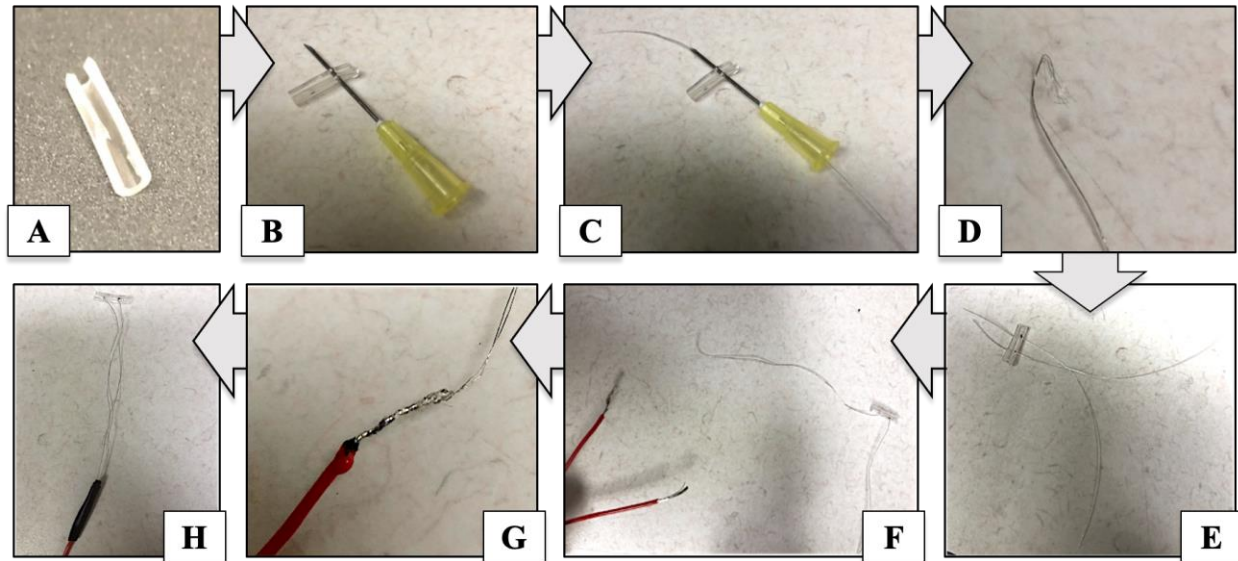


**Figure 21: Image Flow of Nerve Stimulation Cuff Fabrication.**

### **2.4.3 Rodent Knee Securement Gantry and Gastrocnemius Contraction Force**

#### **Measurement**

As shown in **Figure 22**, the nerve cuff is placed under the sciatic nerve, which is carefully dissected away from the surrounding soft tissue such that the nerve cuff can be manipulated under the nerve. This resulted in the nerve resting within the trough of the cuff, contacting the two electrodes. For securing the rodent in place during contraction force testing, a gantry was constructed from T-slotted framing rails (47065T101, McMaster-Carr) onto which flanged bearings were mounted. The flanged bearings were affixed with a screw-clamp mechanism (47065T959, McMaster-Carr) that allowed the gantry to move about the length, width, and height of the rodent on the Platform so that the knee could be secured in a manner that did not impede on the collinearity of the gastrocnemius to the load cell. As shown in **Figure 22**, the gantry is used to

fix the knee into place using the Knee Tie, which prevents the gastrocnemius from pulling the rodent in the direction of the load cell.

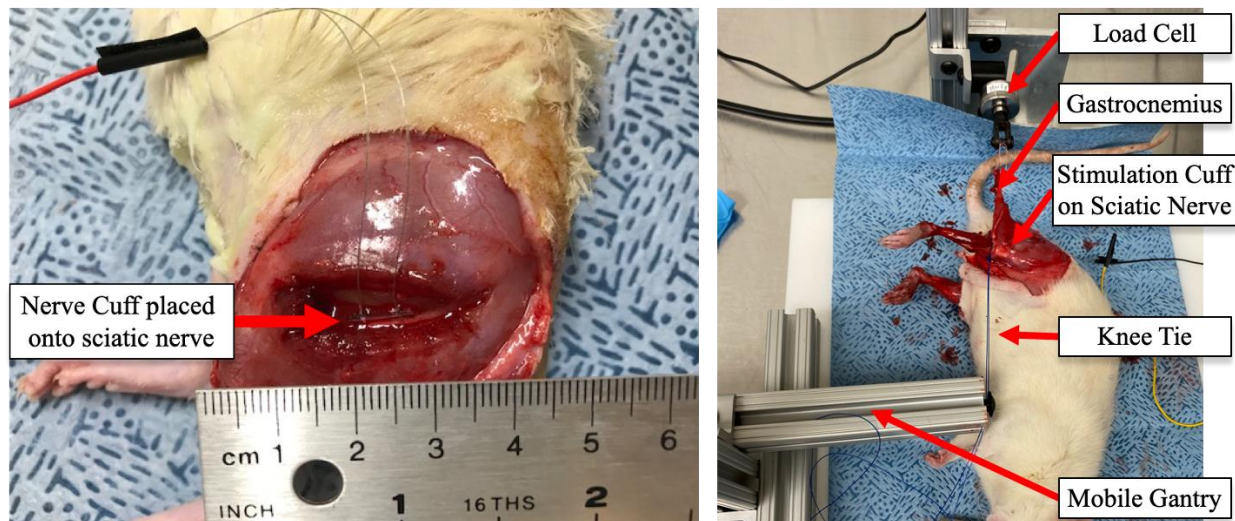


**Figure 22: Nerve Cuff Placement and Knee-Securing Gantry with Load Cell.**

## **2.5 Validation of the Denervation Atrophy Model with a Transection Injury**

To validate the methods described above, being gait analysis, and contraction force measurement, a 6-week pilot study to investigate the effects of multiple therapies was performed, a duration mimicking the length of the ASCs Intramuscular Injection Study (see **Section 2.2**). To hasten nerve healing, the 1.5cm reverse-polarity autograft model was substituted for a transection and suture-based repair; this was done anticipating a quicker reinnervation of the distal muscle after the sciatic nerve injury so that any given muscle therapy could be better appreciated (Vela, Martinez-Chacon et al. 2020), when measuring the return of contraction force or improvement of gait kinematics.

To in a pilot study to assess co-therapeutic treatment to the injured nerve as well as muscle, nerve wraps in conjunction with intramuscular injectables were studied. A PCL nerve wrap, fabricated from an Automated Dip Coating System described below, and a commercial collagen nerve wrap (Integra NeuraWrap) were compared in conjunction with emulsified adipose (Nanofat) and a pepsin-digested skeletal-muscle derived extracellular matrix (skECM) over 6 weeks. The breakdown of animals and conditions is presented in **Table 4**.

**Table 4: Pilot Study Conditions Breakdown.**

<b>Nerve Treatment</b>	<b>Muscle Treatment</b>	<b>N (6 weeks)</b>
Suture (control)	Saline (control)	4
PCL Nerve Wrap	Saline (control)	4
Suture (Control)	Nanofat	4
PCL Nerve Wrap	Nanofat	4
Collagen Nerve Wrap	Saline (control)	3
Suture (Control)	d-skECM	4
PCL Nerve Wrap	d-skECM	4

## **2.5.1 Methods**

### **2.5.1.1 Construction of an Automated tool for Nerve Wrap Fabrication**

Historically, many dip-coated polymeric nerves guides have been fabricated entirely by hand, without use of repeatable tools (Sivak, Bliley et al. 2014). Such processes leave room for error, limit reproducibility between both guides and operators, and would typically allow for only a single guide to be fabricated at a time. Anticipating a clinically-translatable fabrication process for a polymeric nerve wrap, a Dip Coating Mechanism was developed. The Dip Coating

Mechanism features a 3D printable scaffold, which was assembled with standard hardware (various M3-sized hardware, McMaster-Carr). This system is driven by two stepper motors, which receive feedback from integrated limit switches/end stops and a rotary encoder that track distance and rotation, respectively. Components are automated through LabVIEW and the LINX package such that an Arduino can be governed by a VI. **Figure 23** displays the assembly onto which nerve conduits are fabricated, the conduits after dip-coating, and then the nerve wraps after being cut from conduits after being removed from the glass mandrels. Glass mandrels (10cm length) are press fitted into a 3D printed Mandrel Base (2.5cm by 2.5cm square). The mandrel base was 3D printed with ABS, though does not have explicit material limitations (for details on 3D printing with ABS, see **Section 2.3.1**). The base was wraps printed such that up to four mandrels could be press-fitted, hastening the fabrication of nerve wraps. The glass mandrels also determine the inner lumen diameter of the nerve wraps, here being 0.8mm diametrically, being fabricated for use on sciatic nerve injury.

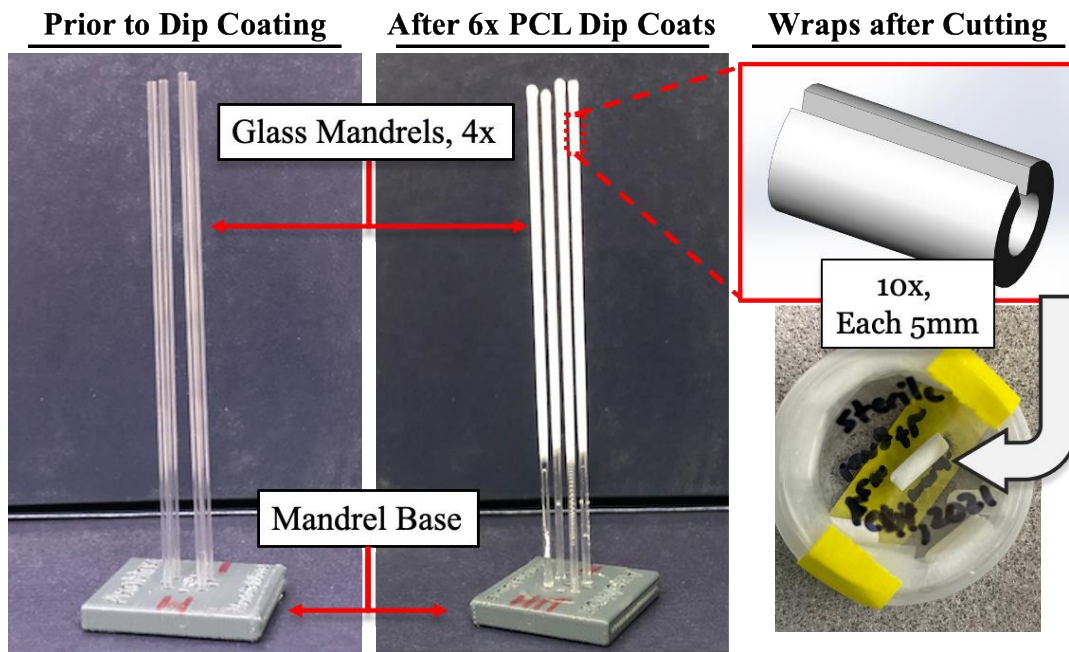


**Figure 23: Glass Mandrels Before and After PCL Dip Coating.**

Mandrels, once press-fitted into the Mandrel Base, are coated with polyvinyl acetate (PVA), which is solubilized in water after the dipping process is complete for removing the PCL nerve guides. **Figure 24A** presents a CAD rendering with callouts of the components comprising the Dip Coating Mechanism. The nerve wraps process requires six dips in a salt (NaCl)/PCL solution, which is contained in the Solution Jar. Each dip requires two minutes of drying time, while also being placed under constant inversion. There are two main actions needed to dip coat the mandrels toward fabricating nerve wraps, being (1) dip-coating and (2) drying. For dip-coating, a stepper motor drives a lead screw such that the Jar Holder moves upward and downward about the z-axis; to ensure that the stepper drives the appropriate distance, a feedback loop using an End-Stop is integrated. Once the mandrel is dipped and the Jar Holder is lowered to a sufficient distance such that it will not impede rotation, the Theta-Axis Stepper Motor rotates the Mandrel Holder circularly for 2 minutes, drying the PCL onto the Glass Mandrel(s). After this time has elapsed, the Rotary Encoder provides the location between  $0^\circ$  and  $360^\circ$  of the Mandrel Base, forming a feedback loop to position the Theta-Axis Stepper Motor such that the Glass Mandrel(s) is again oriented downward. This process is repeated over six dip-coats, providing the layer-by-layer thickness to the nerve wraps, targeting a wall thickness of  $750\mu\text{m} \pm 50\mu\text{m}$ . The assembled Dip Coating Mechanism with Glass Mandrels is shown in **Figure 24B**, where the mandrels are oriented downward and into the Solution Jars. Once the process is completed, the Theta-Axis Stepper Motor again orients the Mandrel Holder to  $0^\circ$  such that the user may remove the PCL conduits into water, where they stay until all of the NaCl is eluted from the PCL (creating pores in the conduit walls) while also solubilizing the PVA, allowing the conduit to slide off of the mandrel with minimal physical disruption. Once removed the conduits were cut into 5mm segments, and then cut again

perpendicular to the radial axis, creating an opening such that the polymer construct could be “wrapped” around a nerve (refer to **Figure 23** for a depiction of the conduit cutting). *In situ* placement of a nerve wrap is presented in **Figure 28E,F**.

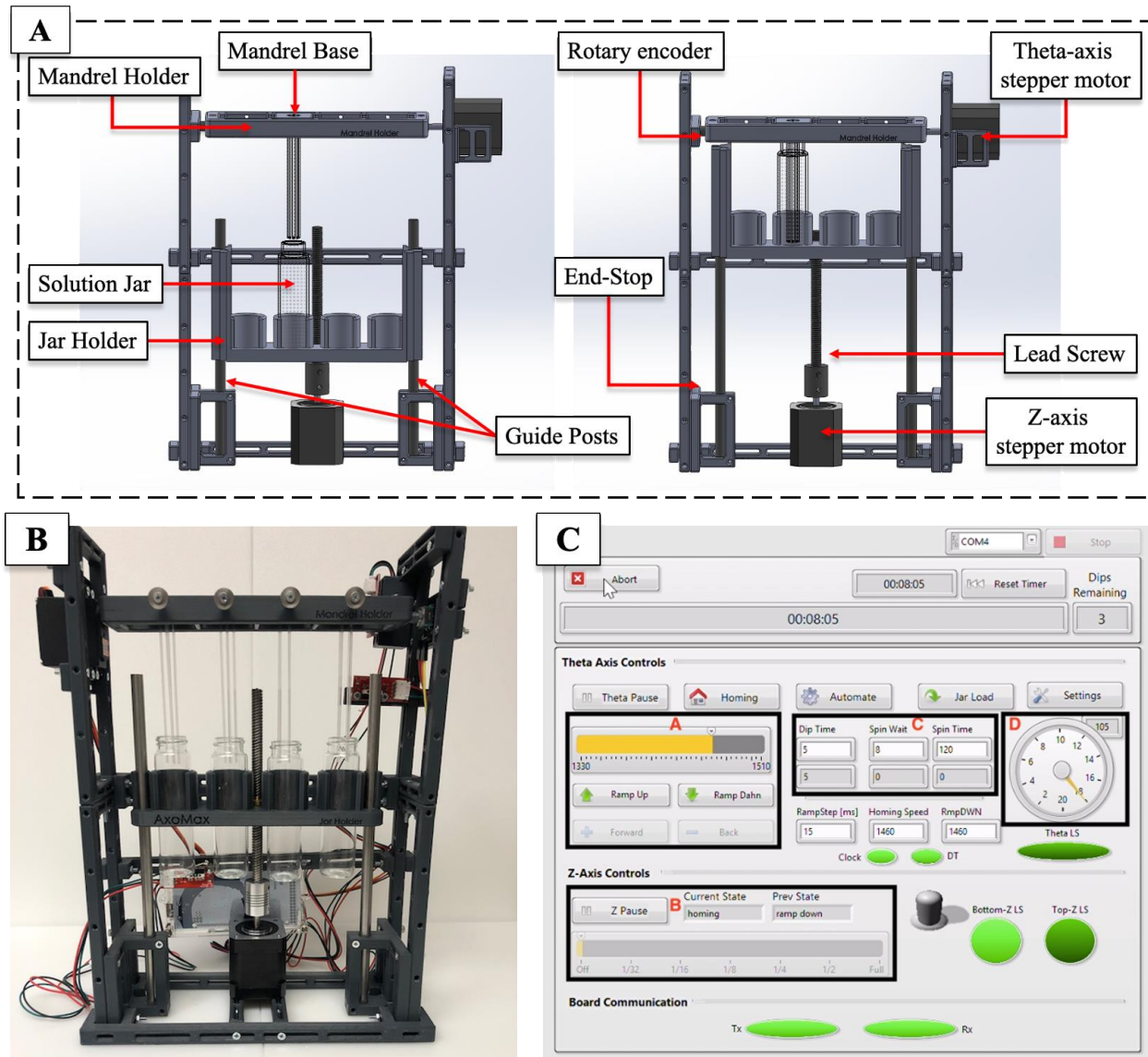


**Figure 24: Automated Dip Coating Mechanism for Wrap Fabrication.**

**Figure 24C** shows the LabVIEW GUI, which allows the user control over all of the components and variables within the dipping process. Four Segments, A-D, determine the function

of the system and the parameters of dip coating. Segment A controls the rotational speed of the Theta-Axis Stepper Motor, which is responsible for spinning the Mandrel Holder into which the Mandrel Bases are affixed. Segment B controls the direction and speed with which the jar holder is raised. Segment C communicates with the stepper motors controlling the time the glass rods are immersed in the PCL solution, the amount of time before the mandrel holder begins to spin, and the duration of the spin time. Segment D tracks the rotation of the mandrel holder and communicates with the corresponding stepper motor to stop rotating at a specified point.

### **2.5.1.2 Creation of Injectable Intramuscular Therapies**

Two injectable therapies for intramuscular injection were created being emulsified rodent adipose tissue decanted of its oil fraction, Nanofat, and an ECM derived from porcine skeletal muscle. The methods of fabrication are presented in the following subsections below, **2.5.1.3** and **2.5.1.4**, for Nanofat and d-skECM, respectively.

### **2.5.1.3 Method of Nanofat Processing**

Adipose tissue has long been used clinically in cosmetic and reconstructive application, with its first published use of the “fat graft” in 1893 for scar revision (Bellini, Grieco et al. 2017). Adipose tissue, and therefore the fat graft, contains many cell-adhesive matrix proteins such as collagens, fibronectin and laminin promote regenerative effects at the site of injection, as well as a rich stromal vascular fraction inclusive of ASCs and other tissue-resident cells (Schilling and Marra 2019). Nanofat is an emulsified preparation of adipose tissue, that has been used clinically in facial rejuvenation through subcutaneous injections (Daumas, Magalon et al. 2020, Menkes, Luca et al. 2020), but has seen exceedingly limited study outside of cosmetics either pre- or clinically. Perhaps interestingly, the name Nanofat for the adipose preparation is a misnomer,

being neither “nano” nor “fat”; in the process the primary constituent of adipose tissue, the lipid-laden adipocyte, are removed, leaving a protein and stromal cell-rich injectable which is indeed larger than the nano-scale as injection volumes typically range in the 1-to-10 of milliliter range.

The process of rendering Nanofat from adipose tissue, and here, from rodent adipose tissue, is presented in **Figure 25**, where adipose tissue is taken from the rodent fat pad (**Figure 25A-C**), minced with fine surgical scissors, loaded into a syringe and then sequentially passed through a series of single-bored luer-lock female-to-female adapters, progressively emulsifying the adipose tissue; as shown in **Figure 25D**, these adapters consisted of pore-size openings of 2.0mm, 1.6mm, and 1.0mm, each further breaking down the ultrastructure of the tissue. The lipid-laden fraction, whose constituent cell is the adipocyte, is then extracted or decanted away, essentially removing the “fat” component from the preparation. Finally, **Figure 25E** presents the preparation with the lipid decanted and prepared for injection.

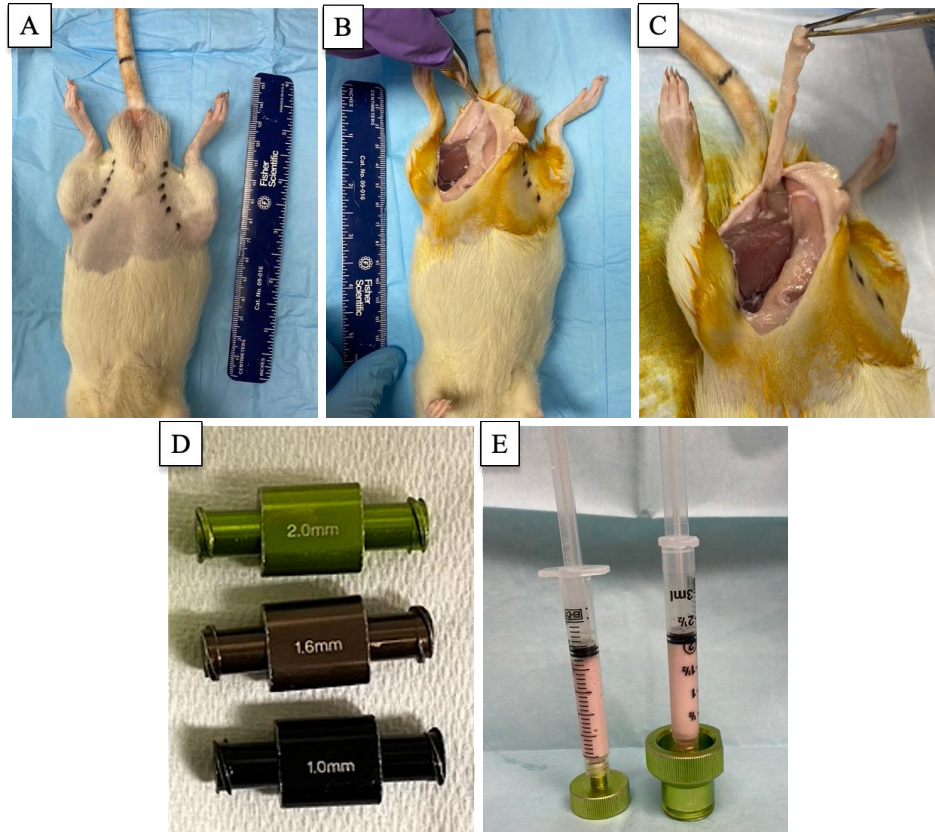


**Figure 25: Harvest and Preparation of Emulsified Adipose, Nanofat.**

Note: additional details on Nanofat and its use as an intramuscular therapy for prevention of muscle atrophy after PNI are presented in **Section 3.0 Clinically Translatable Cellular Therapy for Mitigating Gastrocnemius Denervation Atrophy after Sciatic Nerve Transection.**

#### **2.5.1.4 Method of skECM Processing**

Studies utilizing muscle cell-specific therapies introduced into damaged muscle have resulted in limited myogenesis, and proportionally, insignificant increases in functional output (Montarras, Morgan et al. 2005, Hall, Banks et al. 2010, Tedesco, Dellavalle et al. 2010). This is perhaps due to the profound impact the damaged niche plays on the implanted cells, where the

adverse cues from the damaged extracellular environment dampen the therapeutic benefits able to be offered by the cell therapies. A review on repair of skeletal muscle tissue addressed the various pathologies of muscle damage, where ECM-based therapies were used in circumstances of volumetric loss typically due to trauma, but not in cases of either PNI-induced atrophy or disuse atrophy (Liu, Saul et al. 2018).

**Figure 26** displays the process flow chart for producing d-skECM. Porcine skeletal muscle was harvested from the hindlimbs of recently-deceased Yorkshire pigs. All collected skeletal muscle was aliquoted into 20-gram batches and then frozen at  $-80^{\circ}\text{C}$  until decellularization. Prior to chemical exposure, all muscle was cut into segment approximately of  $1\text{cm}^3$  and then placed into an Erlenmeyer flask at a mass to solution ratio of 1g tissue to 10ml solution; this mass-to-solution ratio was maintained throughout the decellularization process. All processes through disinfection were performed under constant rotation of a spinner flask. Sodium dodecyl sulfate (SDS) Triton X-100, and peracetic acid (PAA) were all performed at 1% concentration [w/v], and pepsin digestion was performed at 10mg pepsin per 1mg tissue dry weight. PAA-based disinfection and all subsequent processes were performed aseptically to maintain sterility. After the final freeze-drying process (e.g., after pepsin digestion), the d-skECM was sealed and stored at ambient temperature until rehydration and injection. Rehydration was performed at 8% [w/v], that is 8mg d-skECM to 92mg USP injectable saline. Note: additional details on skECM as an intramuscular therapy for the prevention of muscle atrophy after PNI are presented in **Section 4.0 Acellular, Extracellular Matrix-Based Therapies for Mitigating Gastrocnemius Denervation Atrophy after Sciatic Nerve Transection.**

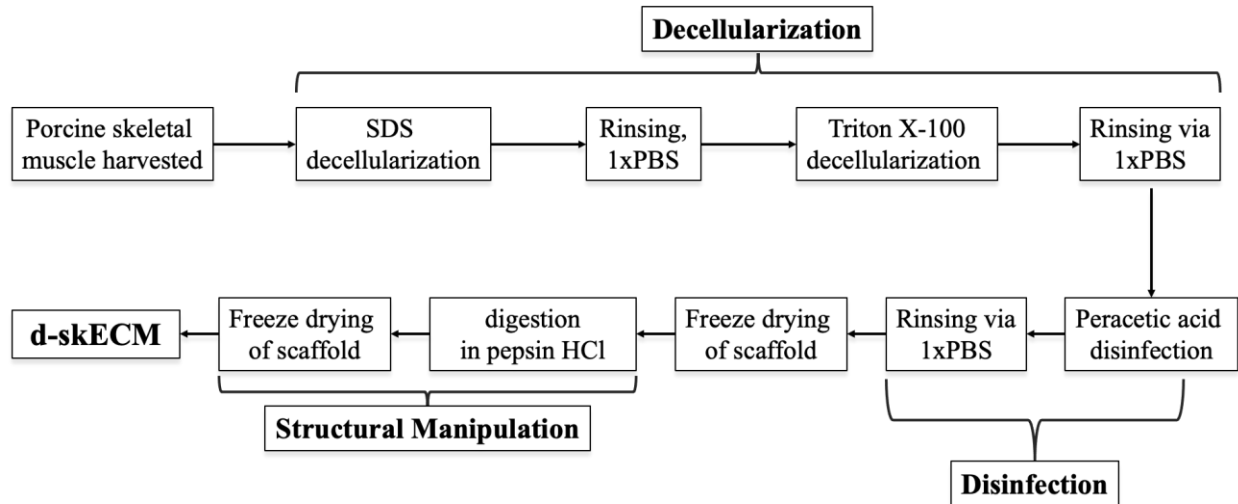
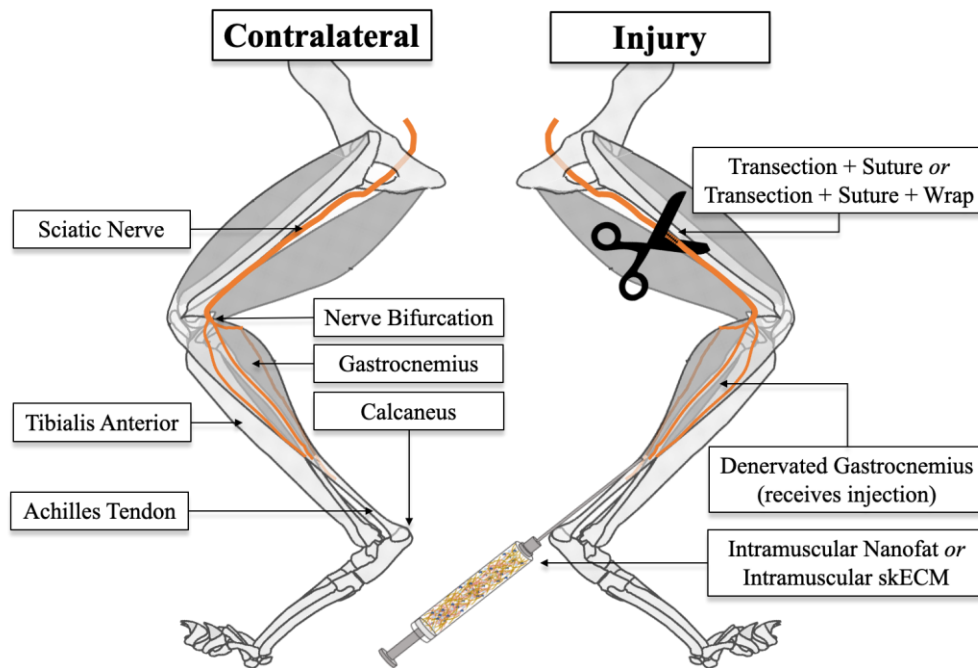


Figure 26: Process Flow for making d-skECM.

## 2.5.2 Transection Injury to the Sciatic Nerve and Application of Therapies

Figure 27 displays an illustration of the hindlimb anatomy and conditions, with the contralateral being an unoperated conditions in all animals; adapted from (Harris and Steudel 2002). Figure 28 displays images presenting the sciatic nerve transection injury, wrap placement, and intramuscular injection. Figure 28A-C displays the creation of the nerve injury, where the surgical site was prepared by removing the fur with an electric razor and then the sciatic nerve was accessed via 2 cm transverse incision at the inguinal region of the right hindlimb (all injuries were performed on the right hindlimb and the left hindlimb was left as a the uninjured contralateral). The gluteus muscle was dissected to expose the sciatic nerve, and injury was induced by transecting the nerve approximately 0.5cm from the bifurcation (Figure 28B). Shown in Figure 28C, the transection was repaired with 9-0 nylon microsuture (Microsurgery Instruments, Inc., Bellaire, TX).



**Figure 27: Illustration of Anatomy and Wrap/Injection Therapies Rendered.**

For rodents receiving nerve therapy beyond the suture-based repair, either a PCL nerve wrap, or a collagen nerve wrap, was placed under the sciatic nerve and then oriented such that the nerve inserted into the trough of the wrap, similar to the placement and orientation of the simulation cuff. Wrap were fixed using a single microsuture at the approximate center of the wrap, which coaptated both sides of the transected nerve while closing and securing the wrap around the nerve (**Figure 28D,E**).

The wound opening for accessing the sciatic nerve was repaired with 5-0 absorbable suture (Ethicon, Somerville, NJ), shown in **Figure 28F**. For rodents receiving intramuscular therapy, approximately 0.35cc of either d-skECM or Nanofat from donor rats was injected into the gastrocnemius immediately after closure of the wound (**Figure 28G-I**, d-skECM presented). The

needle was inserted through skin at the base of the Achilles tendon, extending proximally on the hindlimb and therapy was injected over approximately five passes.

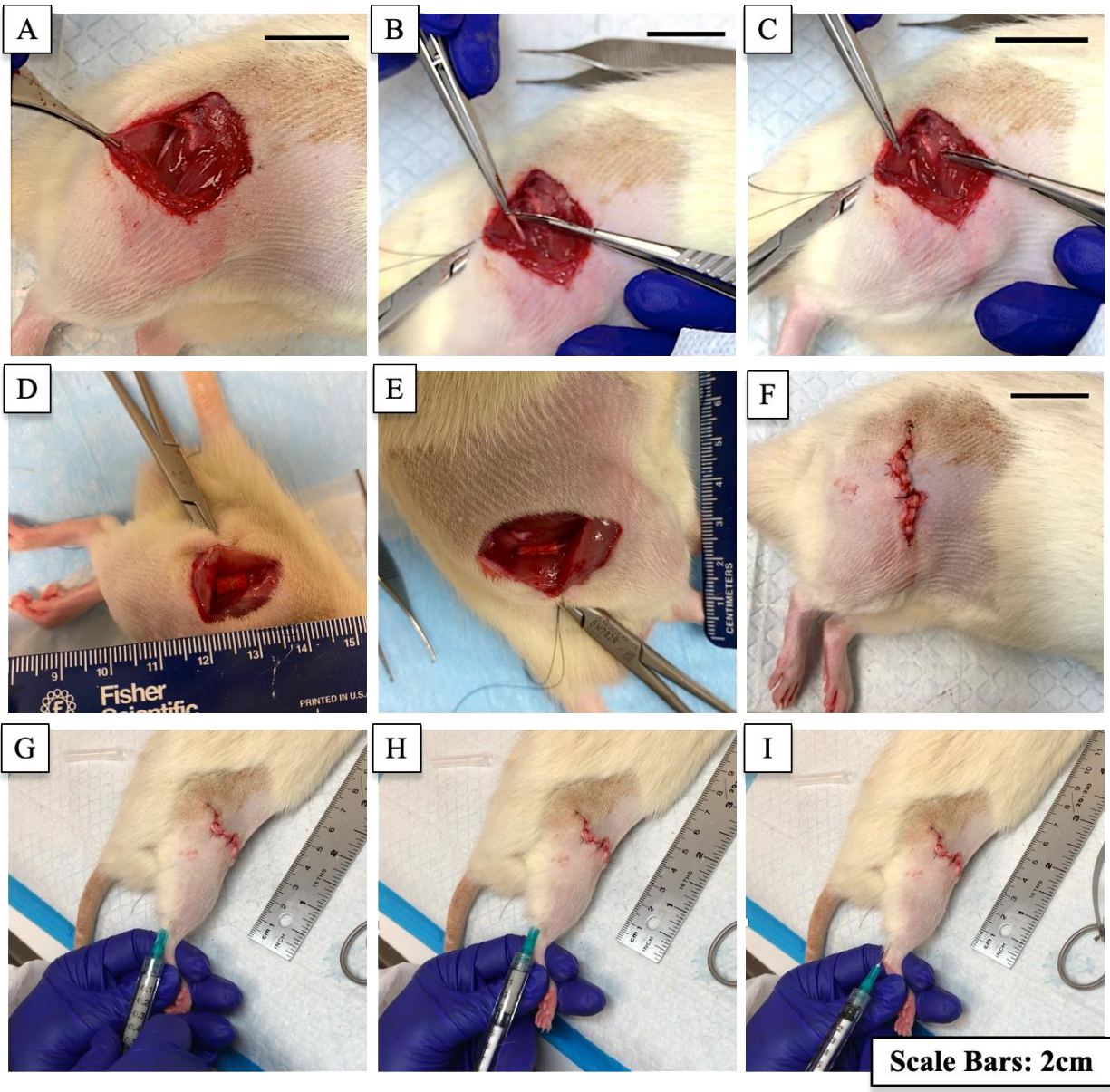


**Figure 28: Sciatic Nerve Transection with Wrap and Injection Therapies.**

### **2.5.2.1 Measurement of Contraction Force**

Prior to contraction force assessment, each rodent was anaesthetized, the gastrocnemius dissected by cutting the calcaneus, and then securing the bone with braided suture to the load cell. The nerve cuffs and knee securement gantry were fabricated and used as described in **Section 2.4.2** and **Section 2.4.3**, respectively. Stimulation of the nerve cuff was induced by the Stimulation Generator (refer to **Figure 15**) set to 0.5mA (A320, World Precision Instruments, Sarasota, FL), and the contraction force of the load cell was read via MyDAQ data acquisition device using a custom program written in LabVIEW (both National Instruments, Austin, TX). Peak isometric force generation was performed by establishing the optimum fiber length, which consisted of increasing the tension on the tethered gastrocnemius until the highest twitch force was established. Tetanic force generation was induced via stimulation frequency sweep of 1Hz, 10Hz, 20Hz, 30Hz, 40Hz, 50Hz, 60Hz, 70Hz, 80Hz, 100Hz, and 150Hz over a 1 second duration. After each stimulation of 70Hz or below, 40 seconds of rest was allocated, and at 80Hz and above, 60 seconds were allocated. After completing contraction assessment on both hindlimbs, animals were euthanized via CO<sub>2</sub> asphyxiation followed by cervical dislocation, their gastrocnemii removed and weighed.

### **2.5.2.2 Statistical Analyses**

All statistical analyses were performed in JMP Pro (Cary, NC). One-way ANOVA with Tukey HSD *post hoc* was used for comparing the resulting gastrocnemii masses after confirming normality of residuals were normal by Shapiro-Wilk W test and equal variance between groups with Welch's F Test. Mixed Modeling using standard least squares was used to determine the significance of two factors and their interacting effect for predicting SFI, being Week (continuous variable) and Treatment (categorical variable). The resulting model gave linearized results based

on the SFI dataset. Repeated Measures ANOVA was performed on the force data after confirming normality of residuals were normal by Shapiro-Wilk W test. Tukey HSD *post hoc* was used to assess significance between groups.

### **2.5.3 Results**

#### **2.5.3.1 Walking Track Analysis and SFI**

**Figure 29** displays results from the walking track analysis, showing the SFI calculation over 5 weeks of the 6-week study as well as the results from the standard least squares mixed modeling of continuous (Week) and categorical (Treatment) variables. Based on the log worth plot, being a metric of variables' contribution to statistical significance of a linear model, it is shown that both the Treatment and the Treatment over Time (Treatment\*Time) are significantly predictive of the SFI; Week as a standalone variable, however, is not. SFI is typically interpreted on a scale of 0 to -100, though the mathematics of its calculation (see **Equation 2-6**) do not preclude values beyond that range, above or below. Additionally, the interacting effect of Treatment\*Time is an interpretation of the line slope, where, a positive slope indicates return of gait function, and a negative slope indicates continued impairment.

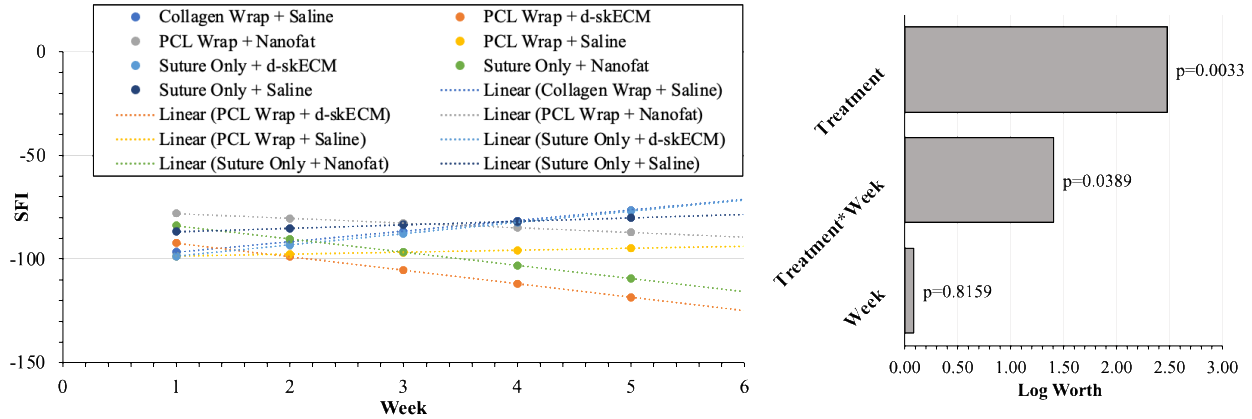


**Figure 29: SFI Results and Analysis.**

From **Figure 29**, the Saline Only + d-skECM and Collagen Wrap + Saline treatments trend most positively with respect to the line derivative, SFI over time; the treatments of the PCL Wrap + Saline and the Control (Suture Only + Saline) follow, trending positively. All other conditions are negatively trending, suggesting continued impairment over the duration of the 6-week experiment with SFI measurement.

### 2.5.3.2 Gastrocnemius Muscle Mass Measurements

Immediately after sacrifice, the gastrocnemii of both hindlimbs were removed and weighed. **Figure 30A** presents the injury side gastrocnemii normalized to its contralateral gastrocnemii, giving a mass fraction in units of *g/g*, and **Figure 30B** presents the injury side gastrocnemii normalized to the rodent body weight, giving mass in units of *g/kg*. Comparisons between all groups revealed no significant difference in any Treatment when normalizing by the contralateral hindlimb (adjusted  $p > 0.62$  for any comparison). Similarly, comparisons between all groups revealed no significant difference in any Treatment when normalizing by the rodent body weight (adjusted  $p > 0.16$  for any comparisons).

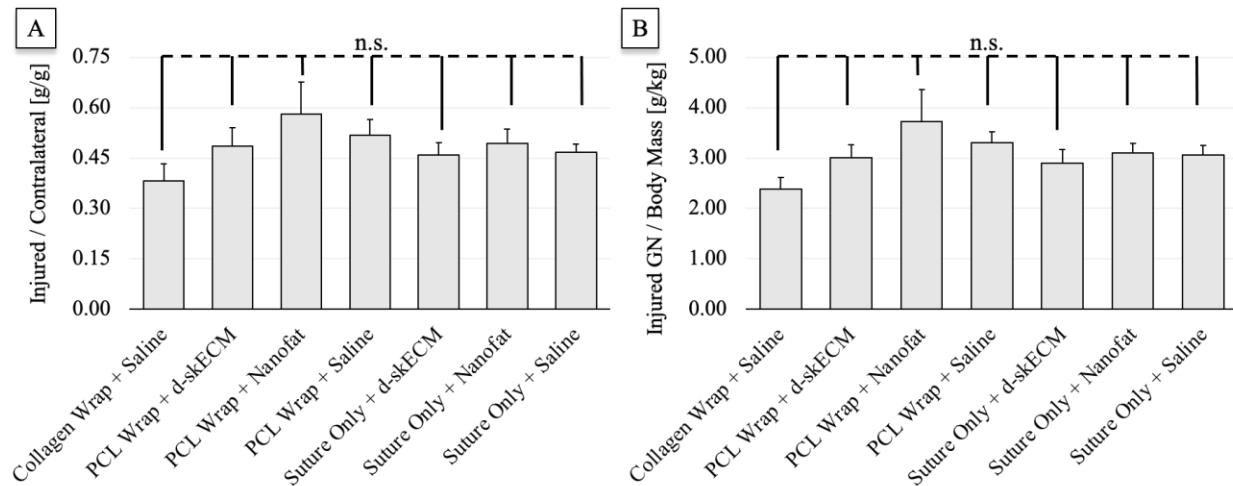


**Figure 30: Gastrocnemii Masses Normalized to Contralateral and Body Mass.**

**Mean  $\pm$  SEM, n.s. denotes  $p > 0.05$ .**

### 2.5.3.3 Contraction Force Analysis

All raw contraction force values (Newton, [N]) were normalized to the mass of the rodent, giving units of N/kg. Forces were measured over ten frequencies ranging from 1Hz to 150Hz, the data from which is shown in **Figure 31**. In the topmost scatter plot, all contralateral values are averaged, and in the bottom-most scatter plot, the contralateral values are removed so that the discrepancies between injury groups can be better appreciated.

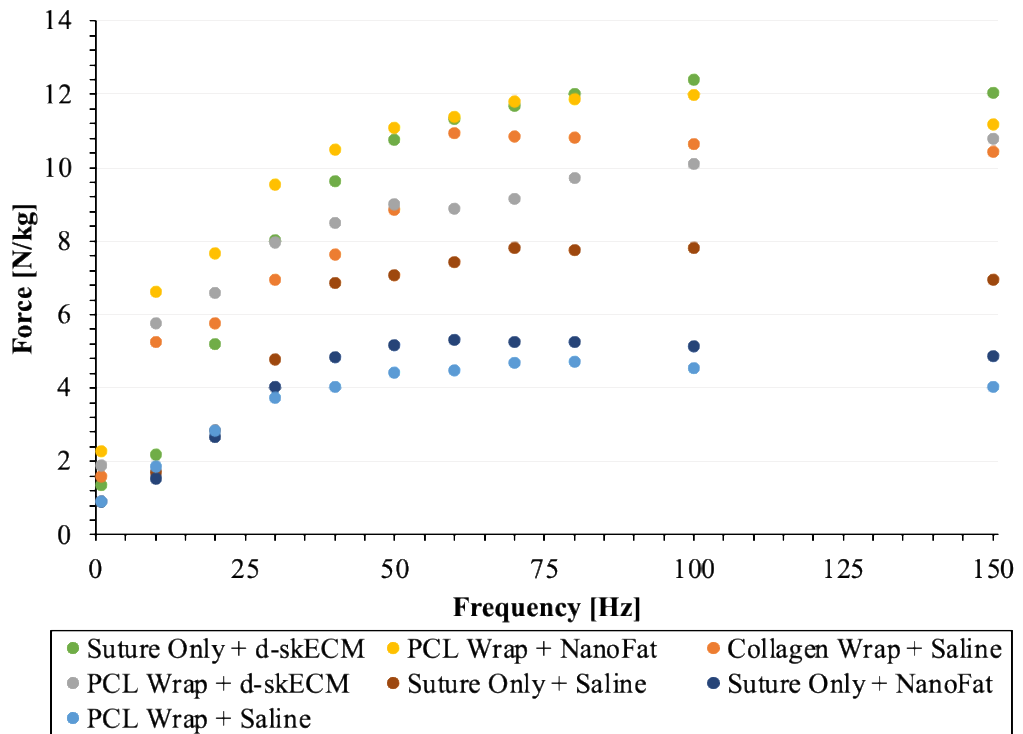
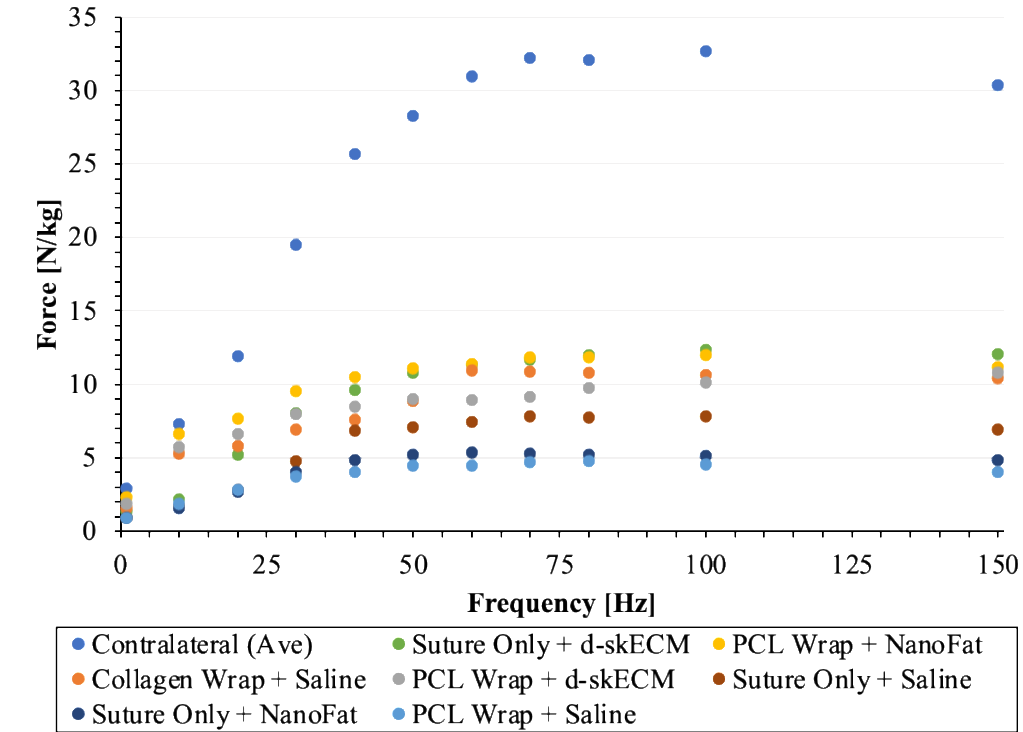


**Figure 31: Force Data Across All Stimulation Frequencies.**

It was shown that 80Hz was able to generate the maximum tetanic contraction force and forces above 80Hz overstimulated the muscle; therefore, the maximum force generated at those frequencies declined relative to those at 80Hz. The normalized force data from all conditions is presented in **Table 5** with the results from a Tukey HSD *post hoc* analysis after a repeated measures ANOVA was performed. The vertical black line in the Tukey HSD Groupings section of the table separates the contralateral, non-injured hindlimbs from their injured counterparts showing that no injured gastrocnemius returned to a force similar to a contralateral hindlimb of any condition.

**Table 5: Normalized Contraction Force (N/kg) at 80Hz Stimulation.**

Nerve Treatment	Muscle Treatment	Limb	Mean (Force [N/kg])	Std Dev (Force [N/kg])	Tukey HSD Groupings	
Suture Only	Saline	Contra	39.500	1.287	A	
Suture Only	Saline	Injury	7.756	0.957		G
Suture Only	Nanofat	Contra	36.161	3.505	B	
Suture Only	Nanofat	Injury	5.247	0.818		H
PCL Wrap	Nanofat	Contra	30.814	1.819	C	
PCL Wrap	Nanofat	Injury	11.849	2.303		E
Suture Only	d-skECM	Contra	25.734	8.651	D	
Suture Only	d-skECM	Injury	12.020	3.529		E
PCL Wrap	d-skECM	Contra	31.476	2.544	C	
PCL Wrap	d-skECM	Injury	9.715	1.198		F
PCL Wrap	Saline	Contra	31.180	4.726	C	
PCL Wrap	Saline	Injury	4.727	2.663		H
Collagen Wrap	Saline	Contra	30.445	1.742	C	
Collagen Wrap	Saline	Injury	10.822	0.413		E

**Figure 32** displays the data from the Injured hindlimb forces of **Table 5** though the forces of all contralateral hindlimbs have been pooled to limit the conditions and statistical comparisons

presented. Mixed effects in combining nerve and muscle therapies are shown. Conditions with nomenclature of “Suture Only” and “Saline” denote controls, where the d-skECM with no nerve treatment beyond a standard repair performed most favorably, though was not significantly different than a combined therapy of a PCL Nerve Wrap and an intramuscular injection of Nanofat; as a standalone therapy, the commercially-available collagen nerve wrap also performed without statistical difference to the two aforementioned conditions. Based on the data, the addition of a PCL wrap to the intramuscular injection of d-skECM appeared to be deleterious to the resulting contraction force ( $p < 0.0001$ ). Further, intramuscular injection of Nanofat without additional intervention to the nerve (Suture Only + Nanofat) as well as the cohort receiving PCL Wrap without further intervention to the muscle were outperformed by the control condition which received a suture-based repair and saline injection into the muscle ( $p < 0.0001$ ). Despite the relatively low numbers of animals per group ( $n=4$ , except for the collagen wrap cohort, being  $n=3$ ), an observational post-hoc for statistical power yielded  $>0.95$ , suggesting sufficient data for the determination that these trends have not occurred by chance.

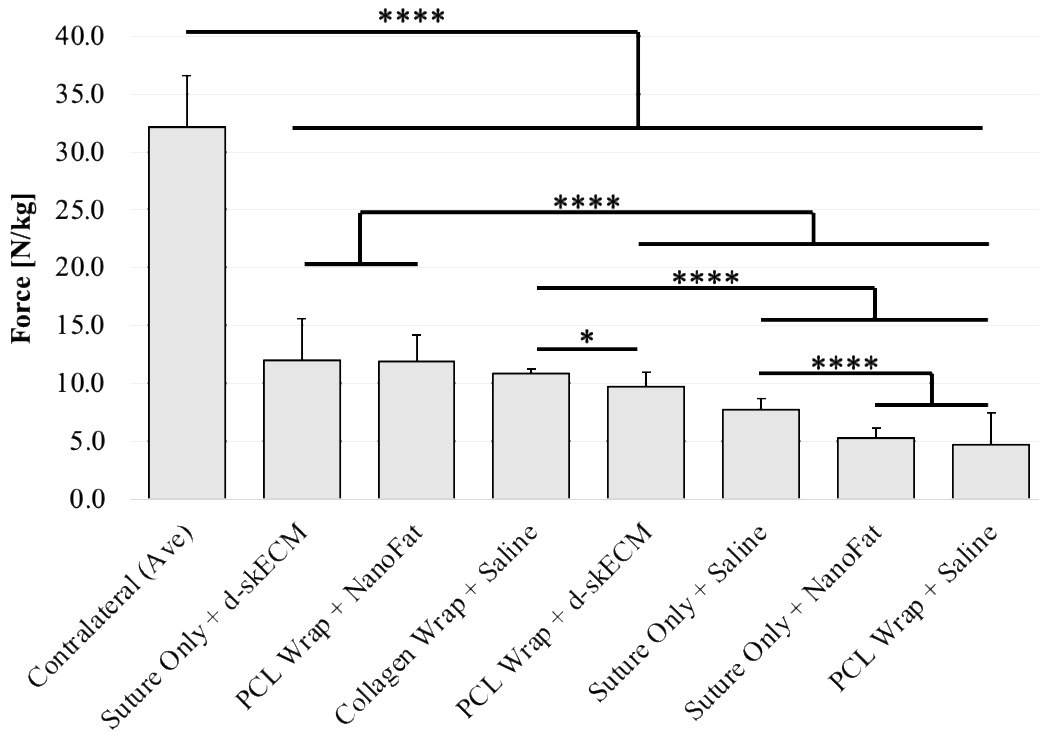


**Figure 32: Normalized Contraction Force (N/kg) at 80Hz Stimulation, All Conditions.**

Mean ± SEM, \*p<0.05, \*\*p<0.01, \*\*\*p<0.001, \*\*\*\*p<0.0001.

Given the relatively high number of comparisons in the analysis, the statistical error rate and the variance are adjusted when omitting the co-therapies conditions, that is PCL Wrap + Nanofat, PCL Wrap + d-skECM, and the Collagen Wrap + Saline. In doing so, the significance levels are altered somewhat. **Figure 33** presents five of the eight comparisons, with the result of d-skECM yielding higher force relative to all other injury conditions (p<0.0001); however, it is shown relative **Figure 32**, that no significant difference exists between the study control (Suture Only + Saline), the PCL Wrap + Saline cohort, and Suture Only + Nanofat (p>0.97 for all comparisons).

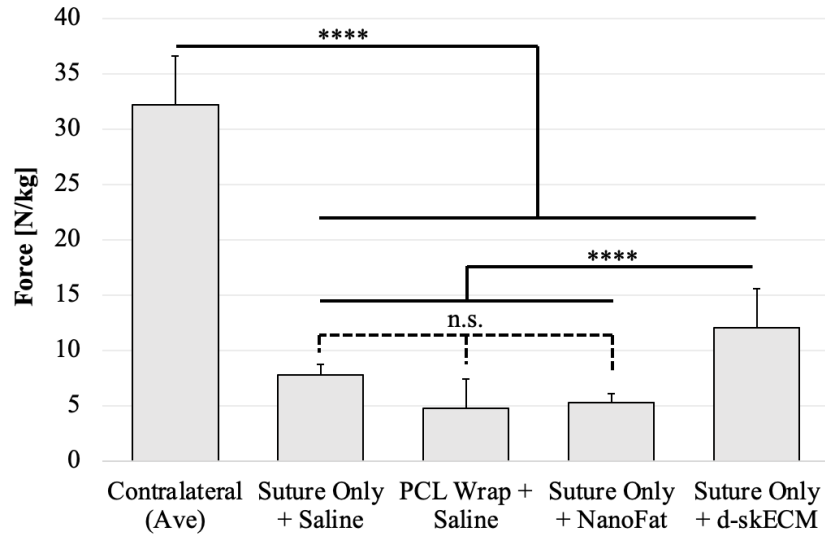


**Figure 33: Normalized Contraction Force (N/kg) at 80Hz Stimulation, Co-Therapies Ommitted.**

**Mean ± SEM, \*p<0.05, \*\*p<0.01, \*\*\*p<0.001, \*\*\*\*p<0.0001.**

#### **2.5.4 Discussion of the Muscle and Nerve Interventions Study**

Seven treatments were rendered in a 6-week pilot investigation, being serving three purposes: First, the sciatic injury model was to be validated, moving from a critical-sized defect of 1.5cm to a transection; second, this study served as a means to ensure the functional outcome measures could quantitatively assess the changes in gait and contraction force functions; third, this study sought to understand changes in healing when investigating therapies rendered to the injured nerve, denervated musculature, or both. It was shown that transection and suture-based repair, a clinical standard for epineural repair (Saied, Shekaari et al. 2015), did indeed denervate the nerve sufficiently to change the gait kinematics in the rodents, induce a reduction in muscle mass as well as a reduction in the muscle force at the 6-week timepoint.

Both the gait analyses and contraction force quantification were able to show discrete differences between the conditions, the former being perhaps more nuanced to interpret. The analysis utilized was a mixed statistical model using both continuous (Time) and categorical variables (Treatment). This resulted in a linear regression, where the *predicted* values of each time point (as opposed to the data measured) are plotted in **Figure 29** to emphasize the trendline. This give an appreciation for the regression and shows that the combinatorial effect of the Treatment over Time (Treatment \* Time) is of significant contribution to SFI. It would perhaps be best however, to analyze the continuous Time variable as an Ordinal variable, which, in statistical modeling, would treat the analysis like a multiway ANOVA rather than a multiple regression. Though this would dampen the ability to compare the trend lines directly, it would provide the ability to *post hoc* each condition throughout the time-course of the study, ease interpretation at each of the individual weeks.

Muscle mass measurements have been used as a means of quantifying denervation atrophy (Mohammadi, Yadegarazadi et al. 2014), though these studies typically do not have a substantial bulk being injected into the muscle, where d-skECM and the Nanofat injections were 15-20% of the initial mass of the gastrocnemius into which they were injected. The mass of the contralateral gastrocnemii on harvest was  $2.36\text{g} \pm 0.20\text{g}$ . Assuming this mass was the approximate initial gastrocnemius mass into which each intramuscular therapy was injected (0.35cc per injection or approximately 15% of the overall mass), it stands to reason that the cohorts receiving an injection would have a higher muscle mass at the end of the 6-week study. Based on the results presented in **Figure 30**, however, this expectation was not presented. Rather, normalizations both to the contralateral gastrocnemius mass, as well as to the overall body mass of the rodent, resulted in no significant differences of normalized gastrocnemii mass between cohorts.

PCL is a synthetic semi-crystalline, hydrophobic, biodegradable polyester that is increasingly common in the fabrication of nerve guides. PCL can be processed into scaffolds that are contiguous/non-porous, aligned, fibrous, or a combination thereof. This is due to the easily tailored mechanical properties of PCL, along with its ease of processability. Eventually PLLA is eliminated as water and carbon dioxide from the lungs (Sheikh, Najeeb et al. 2015). Nerve wraps fabricated from synthetic polymers, and particularly, PCL have seen substantial use in preclinical modeling (Wang and Cai 2010) as well as in clinical application (Arslantunali, Dursun et al. 2014). NeuroCap and NeuraLac (Polyganics, Groningen, The Netherlands) are FDA-cleared medical devices of co-polymeric lactide and caprolactone indicated for the capping of a peripheral nerve stump (K172866) and reconstruction of a peripheral nerve up to 20 mm (K050573), respectively. Here, a PCL nerve wrap was fabricated using an Automated Dip Coating Mechanism for use as a covering that protects the coaptation site during the regeneration process. Despite the history of pre- and clinical use, the PCL wrap here did not outperform the control, being a suture-based repair to the transected sciatic nerve with respect to force generation. This finding is not incompatible however, with the published literature, where nerve wraps have been shown to aid in axonal development as assessed histologically (Lopez, Xin et al. 2018), which was not performed here.

The analyses and interpretation of the force measurements was performed using a repeated measures ANOVA. Since the data analyzed was a compilation of the fifty highest data point per frequency stimulation, the repeated measures assessment controlled the contribution of each individual hindlimb to the overall assessment. In all cases, the contralateral, uninjured gastrocnemius was capable of generating significantly more force than its injured counterpart ( $p < 0.0001$  for all comparisons) and were averaged into a single group for ease of comparison in **Figure 32** and **Figure 33**.

Interestingly, the intramuscular injections when not coupled with a wrap performed at least as well as the PCL Only nerve treatment with respect to contraction force generated. The intramuscular Nanofat cohort (Suture Only + Nanofat) performed on par with the PCL Wrap + Saline, and the Suture Only + d-skECM outperformed all conditions when omitting co-therapeutic treatments, as shown in **Figure 33**. Alternatively, when comparing all conditions (**Figure 32**), the Suture Only + d-skECM cohort, Collagen Wrap + Saline cohort, and the PCL Wrap + Nanofat cohort all performed without significant difference ( $p > 0.10$  for all three comparisons). While it was hypothesized that the co-treatment of muscle and nerve would result in a more rapid recovery, this phenomenon was not explicitly clear based on the return to function as quantified by SFI and contract force. It may be the case that the PCL nerve wrap did not offer any advantage relative to the suture alone, being a protective mechanism rather than a regenerative one. Conversely, the collagen nerve wrap appears to offer regenerative signals to the healing nerve. Based on the similarity in resulting contraction force and SFI measurement, it appears that the intramuscular injection of d-skECM and collagen applied to the nerve offer greatest benefits to the denervation injury. These distinct cohorts, being d-skECM injected into the muscle and the collagen wrap applied to the nerve, seemingly function through distinctly separate pathways given the physical distance and anatomical disparities between the two application sites.

#### **2.5.4.1 Limitations of the Pilot Co-Therapeutics Study**

Though functional characterization is essential to understanding regeneration in denervation, the ability to characterize and correlate functional healing to histological outcomes and intramuscular proteomics would be beneficial to better understanding the mechanism at play. Similar to the study using intramuscular injection of ASCs, the 6-week duration was not sufficiently long to see a return to baseline of neither force nor gait; fidelity between therapy

cohorts was however, able to be shown at the 6-week timepoint. Indeed, a histological assessment of the muscle and/or nerve would be ideal to better elucidate mechanisms of cell infiltration and spatially orient the presence of distinct proteins via IHC or IF.

## 2.6 Chapter Concluding Remarks

Two 6-week *in vivo* pilot studies were performed in the rodent model. The first studied the capacity for intramuscular ASCs to mitigate muscle atrophy in a 1.5cm sciatic nerve reverse-polarity autograft defect model; the second compared the regenerative effects of both nerve wraps and intramuscular injections of emulsified adipose (Nanofat) and d-skECM. In both studies it was shown that an intramuscular injection into denervated muscle significantly alters the atrophic cascade. A single injection of ASCs immediately post-operatively were capable of surviving in atrophying muscle and were able to delay muscle atrophy as quantified by the increased resultant mass of the gastrocnemius, supported by the quantification of muscle fiber area across conditions. It appeared from this investigation, that an intermittent injection of ASCs at the midpoint of the study did not provide any benefit to the healing process, and that the number of injections may be relevant toward minimizing healing time. Additionally, ASC injection appeared to increase markers for IL-10 and Ki67 relative to all other conditions, while also reducing the overall presence of intramuscular lipid.

Successful development and implementation of gait analysis by sciatic function index was shown along with the measurement of tetanic contraction force of injured and uninjured gastrocnemii. For calculation of SFI, a walking track was designed and fabricated, and for contraction force measurement, a VI algorithm was written to manipulate a DAQ and a Simulation

Generator based on user input. Using these functional measures, comparison of nerve wrap and intramuscular therapies resulting in a tissue engineered skeletal muscle ECM performing with statistical distinction. Given the high clinical translatability of Nanofat relative to a cellular therapy (e.g., ASCs), however, its use as an intramuscular therapy post-PNI also merits further investigation.

### **3.0 Clinically Translatable Cellular Therapy for Mitigating Gastrocnemius Denervation Atrophy after Sciatic Nerve Transection**

#### **3.1 Rationale for Use of Nanofat, an Emulsified Adipose Preparation**

It is well-reported that adipose and its injectable preparations possess a capacity for regenerating a diverse array of injury states including scars (Klinger, Caviggioli et al. 2013, Jan, Bashir et al. 2019, Brown, Shang et al. 2020, Klinger, Klinger et al. 2020, Krastev, Schop et al. 2020), burns or thermal injuries (Ranganathan, Wong et al. 2013, Borrelli, Patel et al. 2019, Piccolo, Piccolo et al. 2020), ulcers (Strong, Rubin et al. 2019, Fukuba, Uozaki et al. 2020, Smith, Leigh et al. 2020), and have been used in pain management (Caviggioli, Maione et al. 2011, Fredman, Edkins et al. 2016, Deng, Yao et al. 2019). While grafting autologous adipose tissue directly into or near muscle has been performed clinically for aesthetic reconstruction (Roberts, Toledo et al. 2001, Godoy and Munhoz 2018), the therapeutic capacity of fat injection within the intramuscular space has remained largely overlooked. Additionally, controversy has surrounded intramuscular injection of adipose tissue, especially in cases of gluteal augmentation (Del Vecchio, Villanueva et al. 2018, Turin, Fracol et al. 2020).

An immunocompetent rat model was leveraged to study the effects of syngeneic adipose, prepared in a manner clinically-analogous to Nanofat (Tonnard, Verpaele et al. 2013), for mitigation of MA after a sciatic nerve injury. Even with nerve regeneration after injury, regaining muscle power and function to its pre-atrophied condition is not a forgone conclusion. As previously stated, current techniques to mitigate nerve injury-induced MA fail to adequately restore muscle function in about half of all patients (Geere, Chester et al. 2007, Oud, Beelen et al.

2007, Novak and von der Heyde 2013). As there are no treatments outside of physical exercise or electrical stimulation specific to reinnervating muscle after nerve injury (Herbison, Jaweed et al. 1980, Gramsbergen, J et al. 2000, Vivo, Puigdemasa et al. 2008, Asensio-Pinilla, Udina et al. 2009), it is hypothesized that an intramuscular injection of a mesenchymal tissue source into the muscle, also being a mesenchymal tissue, may be beneficial in restoring atrophy after denervation injury.

## **3.2 Methods**

### **3.2.1 Adipose Harvest and Nanofat Preparation**

All protocols were approved by the University of Pittsburgh IACUC prior to initiating animal research. Inguinal and anterior subcutaneous adipose tissue was harvested from six donor rodents (LEW/crl, male) immediately after sacrifice (**Figure 34A**). Fur was removed and skin disinfected with iodine and ethanol wipes. Adipose was minced with surgical scissors. Based on Nanofat preparation techniques (Tonnard, Verpaele et al. 2013), minced adipose was loaded into 3cc syringes and then sequentially passed approximately 25 times each through Luer-lock adapters of pore sizes 2.0mm, 1.6mm, and then 1.0mm (Spiral Surgical, Pakistan) for rendering the Nanofat preparation (**Figure 34B**). The lipid fraction was decanted from the protein fraction and then was discarded (**Figure 34C**).

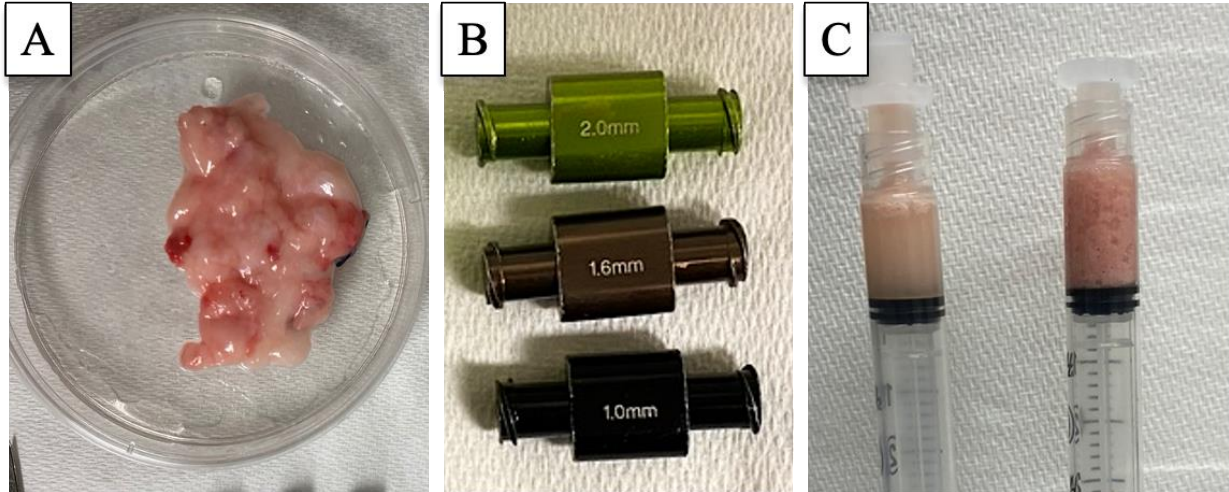


**Figure 34: Rodent Nanofat Preparation.**

**A. Gross appearance of whole inguinal fat collected from six syngeneic donor rats. B. Luer-lok components of Nanofat kit used to mechanically disrupt whole fat, utilized from largest to smallest inner-bore size. C. Resulting gravimetric separation of adipose after mechanical disruption (*left*: lipid fraction, discarded; *right*: protein fraction used for injection).**

### **3.2.2 Induction of Sciatic Nerve Injury via Transection, Repair, and Application of Nanofat**

Rodents were sedated by 2% isoflurane in oxygen. The sciatic nerve was accessed via 2cm transverse incision at the inguinal region of the right hindlimb. The gluteus was dissected exposing the sciatic nerve; injury was induced by transection approximately 0.5cm away from the bifurcation (**Figure 35A**). The transection was repaired with 9-0 nylon suture (Microsurgery Instruments, Inc., Bellaire, TX) and the wound was closed with 5-0 absorbable suture (Ethicon, Somerville, NJ). Approximately 0.5cc of Nanofat was injected into gastrocnemii after nerve injury after wound closure rats using a 21Gx0.5" needle and 1ml syringe (**Figure 35B**). The needle was inserted through skin at the base of the Achilles tendon and Nanofat injected over five passes. Gastrocnemii of control rats were not manipulated.

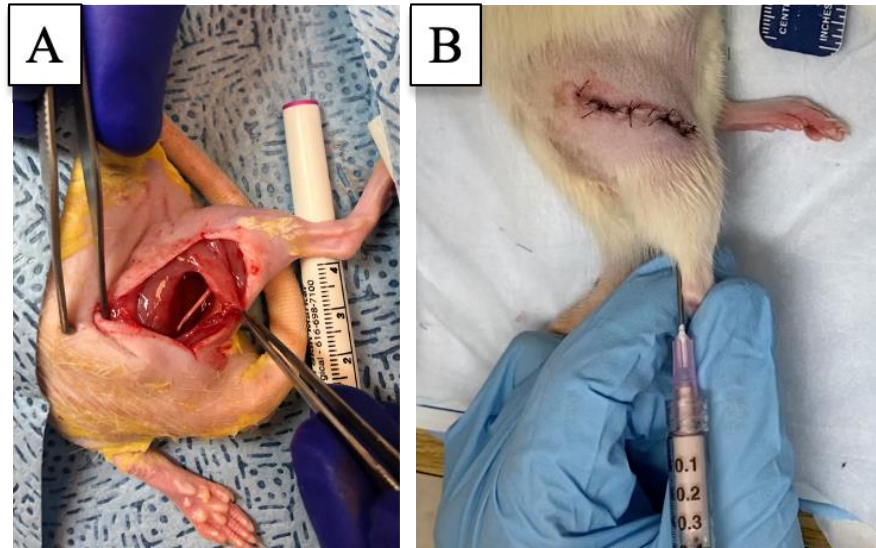


**Figure 35: Exposure of Sciatic Nerve and Intramuscular Injection of Nanofat.**

**A. Exposure of the sciatic nerve, where a transection injury was rendered approximately 5mm proximal to the bifurcation followed by surgical repair with microsuture. B. Intramuscular (gastrocnemius) injection of 0.5mL Nanofat preparation.**

*Functional Measurements:* Sciatic function index (SFI) was performed consistent with previously-established methods of toe spread measurement (Varejao, Meek et al. 2001, Clavijo-Alvarez, Nguyen et al. 2007). A walking track was fabricated (80cm length x 8cm width) such that paper could be laid into the track (see 2.2.3 for additional details). Each rodent's hind-feet were coated with water-soluble paint, imprinting footprints onto the paper. Six footprints per walk were used to calculate SFI. Evaluators were blinded to groups prior to walking.

### **3.2.3 Measurement of Tetanic Contraction Force and Euthanasia**

Each rodent was sedated, the gastrocnemius was dissected by cutting the calcaneus, and then securing the bone to a loadcell. A custom gantry was used to secure the knee. Briefly, nerve cuffs (1cm length) were fabricated from 1/16" ID Tygon tubing (McMaster-Carr 5155T12); two de-insulated wires (Cooner Wire AS-631) were inserted through tubing and glued into place 5mm apart (see **2.4.2 Fabrication of Stimulation Cuffs** for additional details). Stimulation was induced by stimulus isolator at 0.50mA (A320, World Precision Instruments, Sarasota, FL), and the contraction force of the load cell was read via MyDAQ coded in LabVIEW (NI, Austin, TX). Optimum fiber length was established by tensioning gastrocnemii until the highest twitch force was established. Tetanic force generation was induced via stimulations of 1Hz, 10Hz, 25Hz, 50Hz, 75Hz, 100Hz, and 150Hz over a 1 second duration. After stimulations of  $\leq 75\text{Hz}$ , 40 seconds of rest was allocated, and at 100Hz and 150Hz, 60 seconds were allocated. Animals were euthanized via CO<sub>2</sub> asphyxiation on completion of electrophysiology (see **2.4 Development of an Electrophysiology System Capable of Measuring Contraction Force** for additional details).

### **3.2.4 Muscle Assessment and Histology**

After sacrifice (9-weeks postoperatively), the gastrocnemii and tibialis anterior (TA) muscles were isolated and removed from both hindlimbs, weighed, flash-frozen in liquid nitrogen, and then stored at -80°C. For histology, 8 $\mu\text{m}$  cryo-sections were stained with Masson's trichrome (HT15-1KT, Millipore Sigma, St. Louis, MO) per manufacturer's instructions. H&E on rat fat was stained per manufacturer's instructions (Millipore Sigma).

### 3.2.5 Gene Expression

Muscle (200-300mg) was homogenized on ice (Bio-Gen PRO200) in RLT buffer. Afterward, proteinase K (Thermo Scientific AM2548) was added to each tube for 15mins at 55°C, samples centrifuged (6 minutes, 10,000xg), the supernatant extracted, and 70% ethanol added at 1:1 [v/v]. RNA was isolated using RNeasy Plus Micro kit (Qiagen, Germantown, MD) according to instructions. RNA quantity and purity were assessed via plate-reader (Tecan Infinite M200, Morrisville, NC) at 260nm/280nm ratio. cDNA was reverse-transcribed using a total of 1µg RNA with Superscript IV VILO Master Mix (11756500, Thermo Scientific). Comparative RT-PCR was the performed using the Taqman primers listed in **Table 6**.

**Table 6: RT-PCR Primers, Mechanisms, and their Reference.**

<b>Category/ Mechanism</b>	<b>Gene</b>	<b>Full Name</b>	<b>TaqMan Reference</b>
Adipogenic	AdipoQ	Adiponectin	Rn00595250_m1
Adipogenic	PLIN1	Perilipin-1	Rn00558672_m1
Adipogenic	FABP4	Fatty Acid Binding Protein 4	Rn00670361_m1
Hypoxia	HIF1 $\alpha$	Hypoxia Inducible Factor 1 Subunit $\alpha$	Rn01472831_m1
Hypoxia	FGF2	Fibroblast Growth Factor 2 (Basic)	Rn00570809_m1
Hypoxia	EDN1	Endothelin 1	Rn00561129_m1
Inflammation	CD68	Macrophage Antigen CD68	Rn01495634_g1
Inflammation	iNOS	Inducible Nitric Oxide Synthase	Rn00561646_m1
Myogenic	MYOD	Myoblast Determination Protein 1	Rn00598571_m1
Myogenic	MYH2	Myosin Heavy Chain 2	Rn01470656_m1
Myogenic	MYH1	Myosin Heavy Chain 1	Rn01751056_m1
Myogenic	SLC16A1	Solute Carrier Family 16 Member 1	Rn00562332_m1
ECM Synthesis	TGFB1	Transforming Growth Factor Beta 1	Rn00572010_m1
ECM Synthesis	Col1a1	Collagen Type I Alpha 1 Chain	Rn01463848_m1
ECM Synthesis	Col3a1	Collagen Type III Alpha 1 Chain	Rn01437681_m1

### 3.2.6 Multiplexing

Samples were extracted in 4M guanidine HCl in 0.05M Trizma Base (both Millipore Sigma, St. Louis, MO). Extracts were purified using 15k MWCO filtration columns and then reconstituted in 1xPBS. Cytokine quantification was performed using a Luminex assay (LXSARM-12, R&D Systems, Minneapolis, MN), which included granulocyte-macrophage colony-stimulating factor (GM-CSF), interferon (IFN)- $\gamma$ , IL-1 $\beta$ , IL-4, IL-6, IL-10, IL-13, IL-18, Tissue inhibitor of metalloproteinase (TIMP)-1, tissue necrosis factor (TNF)- $\alpha$ , and vascular endothelial growth factor (VEGF). Quantification was performed using Bio-Plex 200 (Bio-Rad, Hercules, CA).

### 3.2.7 Statistical Analyses

All statistical analyses were performed in JMP Pro (Cary, NC). A repeated measures ANOVA was used to assess SFI, which was transformed to meet assumption of residuals normality by **Equation 3-1**.

**Equation 3-1: Johnson's Bounded Transformation of Sciatic Function Index**

$$SFI_{Tx} = -1.197 + 0.859 \cdot \operatorname{arcsinh}\left(\frac{SFI + 133.743}{4.020}\right) \quad \text{Equation 3-1}$$

For comparing muscle masses and force data, ANOVAs were used with a Tukey HSD *post hoc* and a Steel-Dwass Pairwise Comparisons nonparametric *post hoc*, respectively, after assessing homoscedasticity with Welch's F Test. Gene expressions were compared with Robust ANOVA due to the high coefficients of variation in data sets. Kolomogrov's D test was used for testing goodness of fit of the cytokine distribution, governing the appropriate selection of generalized regression, either exponential or lognormal. Significance was accepted at  $p < 0.05$  throughout.

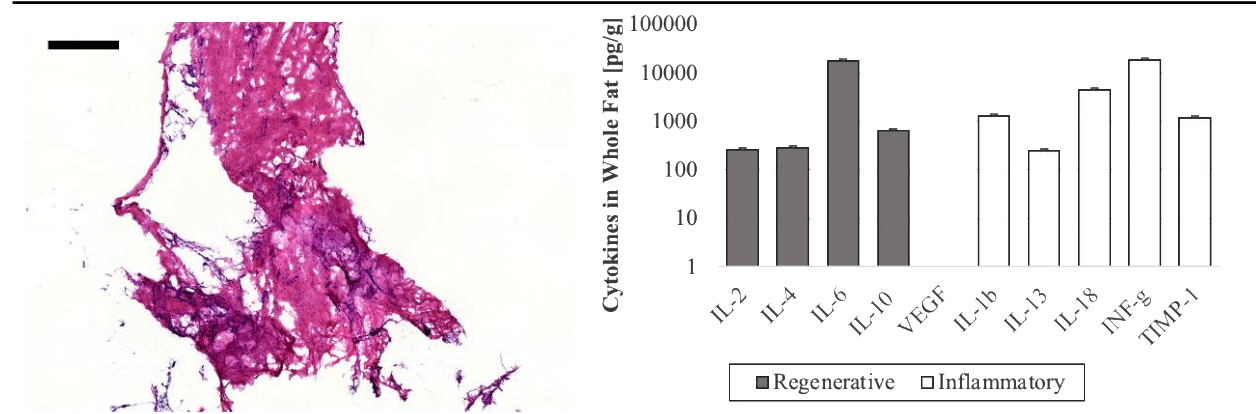
## 3.3 Results from Intramuscular Nanofat in Denervated Gastrocnemii

### 3.3.1 Changes in Architecture and Cytokines from Whole Fat to Nanofat

Excised inguinal adipose and Nanofat H&E, along with quantification of their cytokine content are shown in **Figure 36**. From whole fat to Nanofat, it can be seen that the structure of eosin-stained cytoplasm becomes increasingly stranded. Similarly, adipocyte-laden areas of whole

fat no longer appear present in the Nanofat. The cytokine panel also shows the changes in the cytokine content when manipulating adipose tissue into its emulsified, Nanofat preparation. Since lipid is removed, concentration of the proteins is expected, though the data does not show that particular phenomenon exclusively. Rather, IL-2, IL-4, and VEGF are shown to be most concentrated, while the remaining cytokines remain approximately constant or decrease.

### Whole Fat: H&E and Cytokine Quantification



### Nanofat H&E and Cytokine Quantification

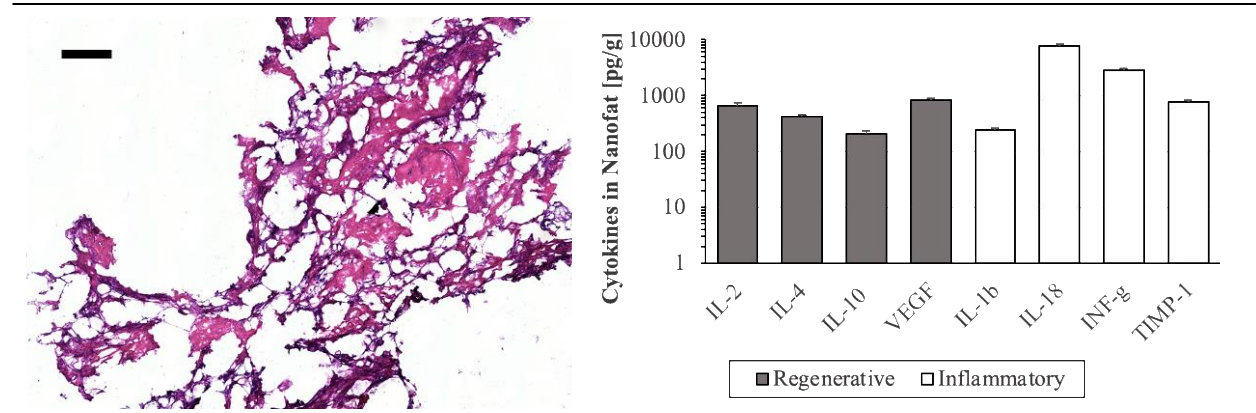
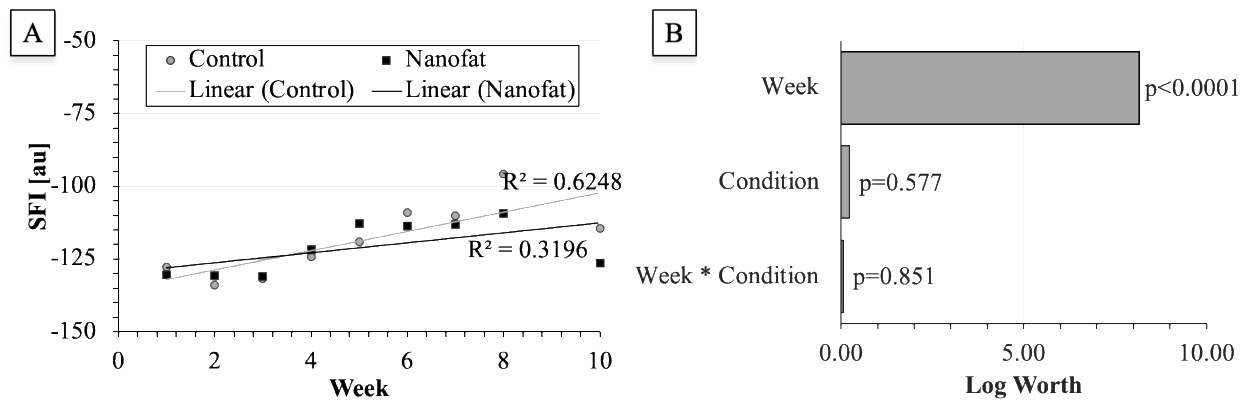


Figure 36: Architecture and Cytokines in Whole Fat and Nanofat.

H&E staining and cytokine quantification of whole rat adipose tissue taken from the inguinal fat pad (top). H&E staining and cytokine quantification of Nanofat after mechanical disruption and removal of lipid fraction (bottom). Mean  $\pm$  SEM. Scale bar: 500 $\mu$ m.

### 3.3.2 Walking Track and Sciatic Function Analyses

Both the Nanofat and control conditions showed significant improvement in SFI over the duration of the 12-week study ( $p < 0.001$ ), with moderately correlated regressions (**Figure 37A**). The Nanofat versus control conditions, however, were not significantly different ( $p = 0.239$ ), nor were their interacting effects ( $p = 0.851$ ) with respect to SFI over time (**Figure 37B**).



**Figure 37: Linear Regression and Log-Worth Chart for Sciatic Function Index.**

**A.** Linear regression of SFI over 10 weeks of the 12-week study, where  $R^2$  values from both conditions denote moderate correlation. **B.** Log-worth worth contribution to the SFI regressions where SFI significantly improves over time ( $p < 0.0001$ ) but is not affected by the Conditions ( $p = 0.577$ ) nor the interacting effect of the Time and the Conditions ( $p = 0.851$ ).

### 3.3.3 Muscle Mass, Architecture, and Contraction Force

Gastrocnemii and TA masses were normalized to the rodent mass [g/kg]. Neither the gastrocnemius comparisons or the TA comparisons resulted in any significant differences in mass between Nanofat-injected and control conditions (adjusted  $p > 0.05$  for all conditions, ANOVA, Tukey *post hoc*). Gross images of the muscles are shown in **Figure 38** and normalized data are in

**Figure 39.** All gastrocnemii were trichrome-stained and no major architectural differences between control conditions or Nanofat Conditions were observed between 9-weeks and 12-weeks. Representative histological images are shown in **Figure 40**. Visually, increased collagen deposition in the control gastrocnemii can be seen in sections relative to their Nanofat-injected counterparts.

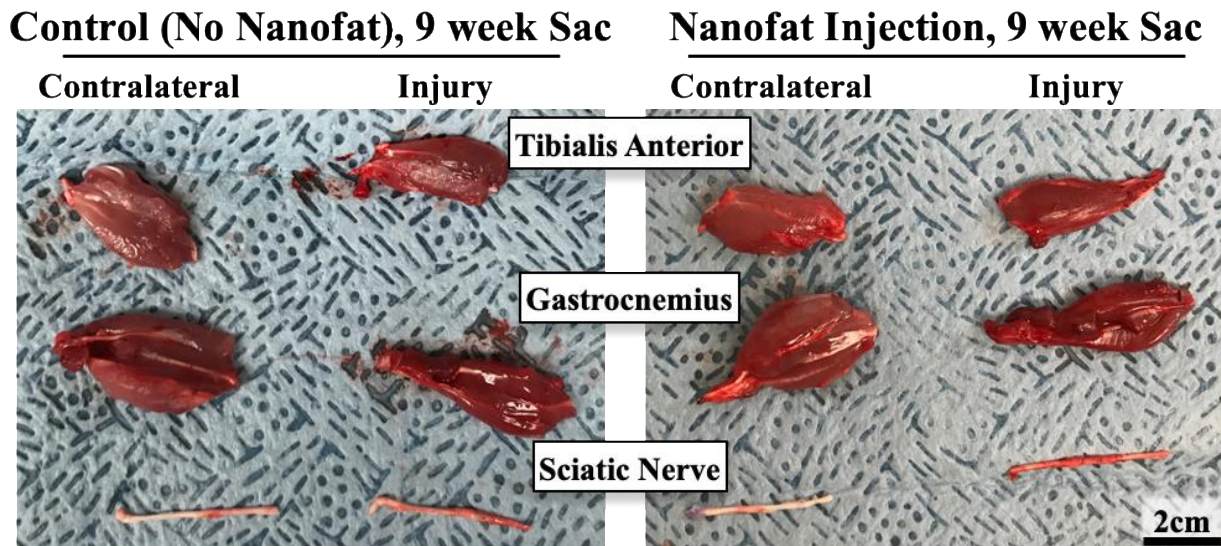


**Figure 38: Gross Appearance of Muscle and Scaitic Nerve.**

**Representative gross images of the gastrocnemius, tibialis anterior, and sciatic nerve of control and Nanofat-injection conditions.**

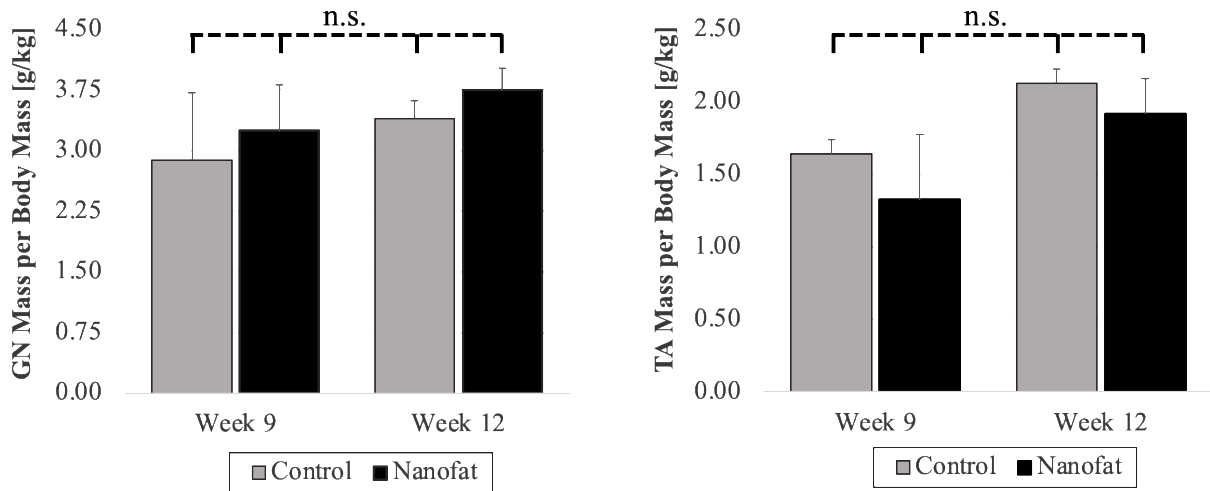


**Figure 39: Gastrocnemius and TA Muscle Comparisons.**

Gastrocnemius mass normalized to rodent body mass at 9 and 12 weeks (left). Tibialis anterior mass normalized to rodent body mass at 9 and 12 weeks (right).

Mean  $\pm$  SEM,  $p > 0.05$  for all comparisons.

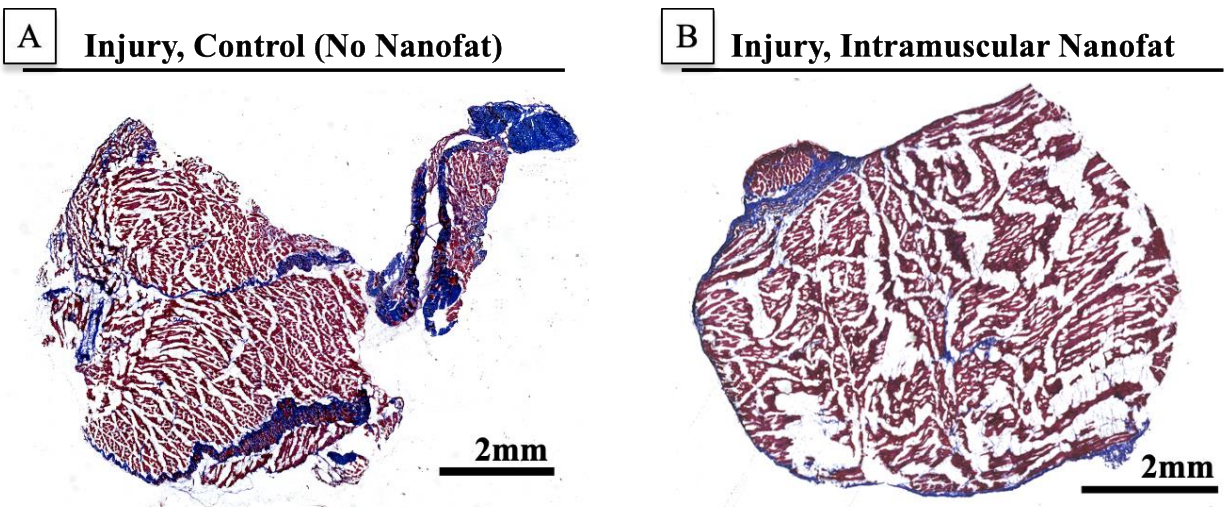


**Figure 40: Trichrome staining of Control and Nanofat-Treated Gastrocnemii.**

A. Representative Masson's trichrome staining of a Control (not Nanofat-injected) gastrocnemius, and;  
 B. representative Masson's trichrome staining of a Nanofat-injected gastrocnemius with similarly stained cytoplasmic morphologies (red), and collagen (blue) appearing more distinct in controls (both 9 weeks postoperatively, and scale bars: 2mm).

The intramuscular injection of Nanofat significantly increased the maximum force able to be generated at both the 9- and 12-week timepoints, as shown in **Figure 41**, presenting contraction force normalized to the rodent body mass giving units of N/kg. **Figure 41A,B** present the tetanic contraction forces over all seven frequencies used for stimulation. The force of the contralateral hindlimb was then plotted against the force of the injured hindlimb over both timepoints. At 50Hz, the contraction force generated by the contralateral gastrocnemii was at maximum relative to all other frequencies and was therefore used for analysis. **Figure 41C,D** present the forces generated. At both timepoints the contralateral hindlimbs were able to generate significantly greater force than their injured counterparts ( $p < 0.0001$ ). At both timepoints, the Nanofat-injected gastrocnemii were able to generate significantly greater force than controls ( $p < 0.0001$ ). **Figure 41E** presents a correlation plot where the strength of the Nanofat-injected gastrocnemii were better correlated to the strength of their contralateral gastrocnemii ( $R^2 = 0.938$ , strong correlation) relative to the control conditions and their contralateral gastrocnemii ( $R^2 = 0.527$ , moderate correlation).

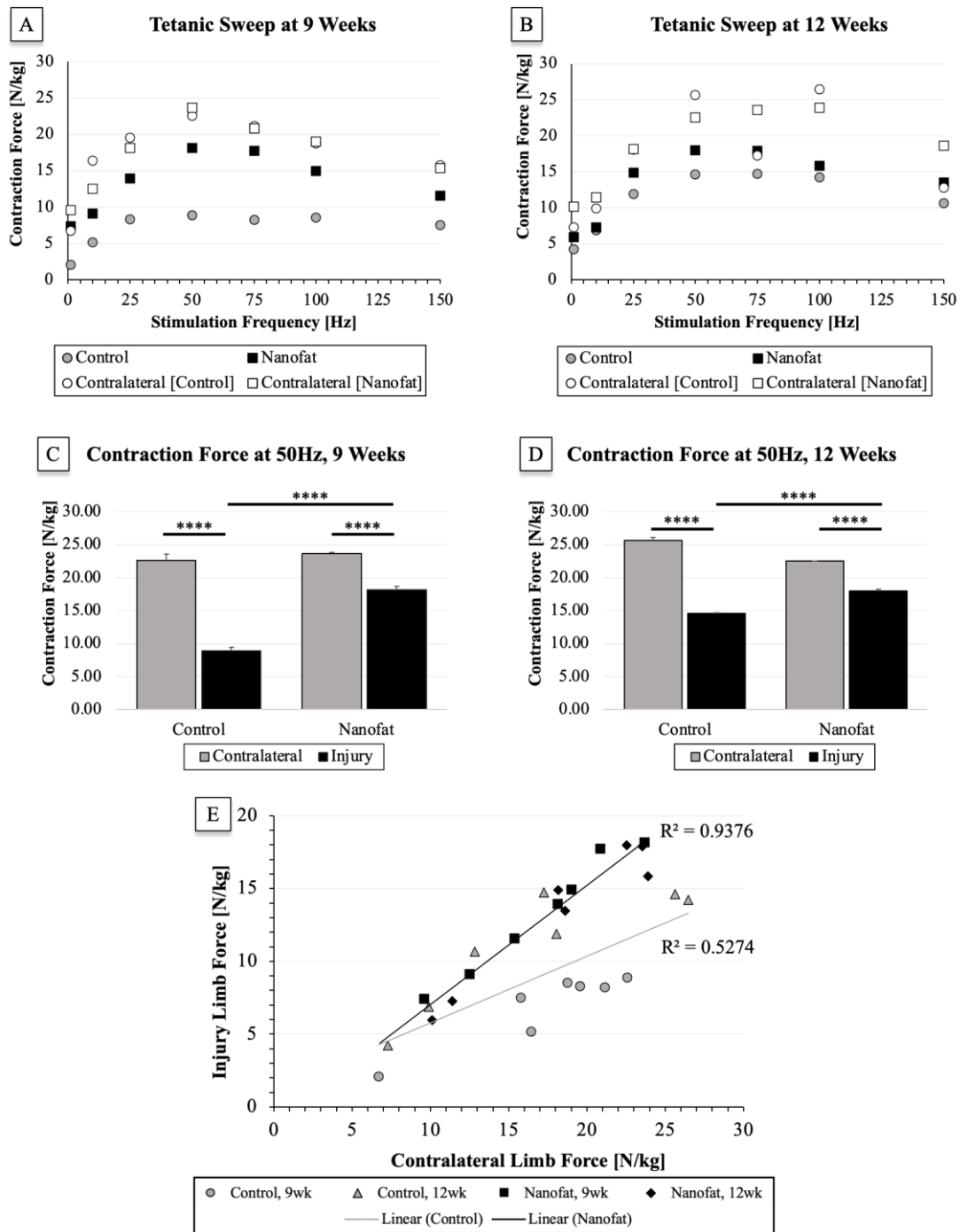


**Figure 41: Contraction Forces Generated Normalized by Rodent Body Mass [N/kg].**

**A.** Contraction force data plotted over all stimulation frequencies at 9 weeks, and **B.** at 12 weeks. **C.** Maximal contraction force generated at 50Hz stimulation at 9 weeks, and **D.** at 12 weeks. **E.** Linear correlation of injury force generated plotted against contralateral force generated.

Mean  $\pm$  SEM, \* $p < 0.05$ , \*\* $p < 0.01$ , \*\*\* $p < 0.001$ , \*\*\*\* $p < 0.0001$ .

The intramuscular injection of Nanofat significantly increased the maximum force able to be generated at 9 weeks relative to all comparisons, including the Contralateral, when contraction force was normalized to the gastrocnemius muscle mass giving units of N/g, as shown in **Figure 42**. **Figure 42A,B** present the tetanic contraction forces over all seven frequencies used for stimulation. At 50Hz, the contraction force generated by the Nanofat-treated gastrocnemii was at maximum relative to all other frequencies and was therefore used for analysis. **Figure 42C,D** present the forces generated. At 9-weeks the Nanofat-injected gastrocnemii were able to generate significantly more force relative to all other comparisons ( $p < 0.0001$ ). At 12 weeks, this trend did not persist, where Nanofat-injected gastrocnemii only outperformed the Contralateral limbs of Control animals ( $p < 0.0001$ ), a comparison not entirely relevant to drawing conclusions on the effect of the therapy.

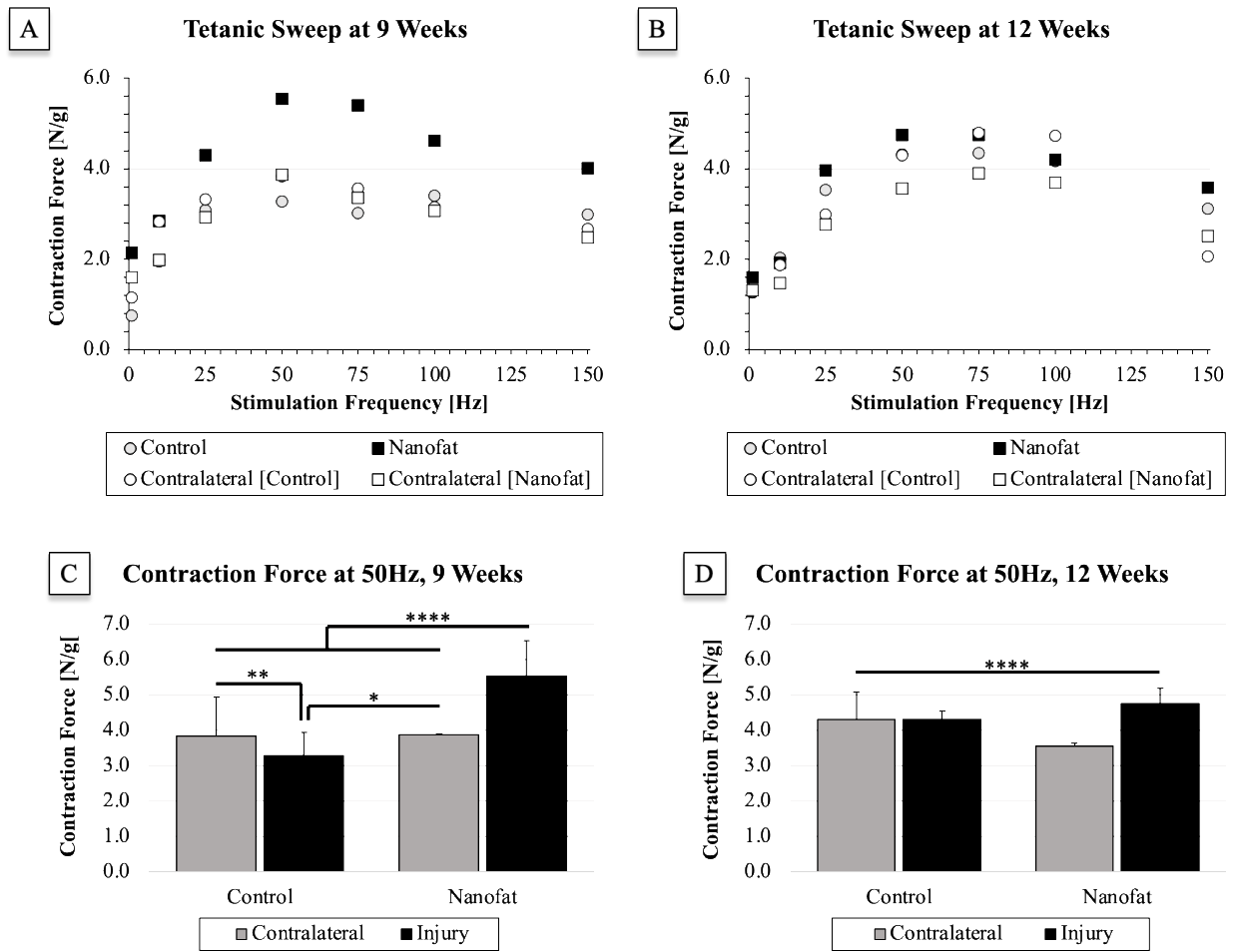


**Figure 42: Contraction Forces Generated Normalized by Gastrocnemius Mass [N/g].**

**A.** Contraction force data plotted over all stimulation frequencies at 9 weeks, and **B.** at 12 weeks.

**C.** Maximal contraction force generated at 50Hz stimulation at 9 weeks, and **D.** at 12 weeks.

Mean  $\pm$  SEM, \* $p < 0.05$ , \*\* $p < 0.01$ , \*\*\* $p < 0.001$ , \*\*\*\* $p < 0.0001$ .

### 3.3.4 Gene Expression in Nanofat-Injected Gastrocnemii

Expression of fifteen genes were quantified in gastrocnemii, each rat serving as its own control, normalizing injured muscle to contralateral. Significant upregulation of the inflammatory genes CD68 ( $p < 0.0001$ ) and iNOS ( $p < 0.05$ ) were present in Nanofat-treated gastrocnemii relative

to control. Significant upregulation of AdipoQ ( $p < 0.01$ ) and MyoD ( $p < 0.01$ ) were present in control gastrocnemii compared with Nanofat-treated (**Figure 43A-C**). All other expression comparisons were non-significant (**Figure 43D,E**).

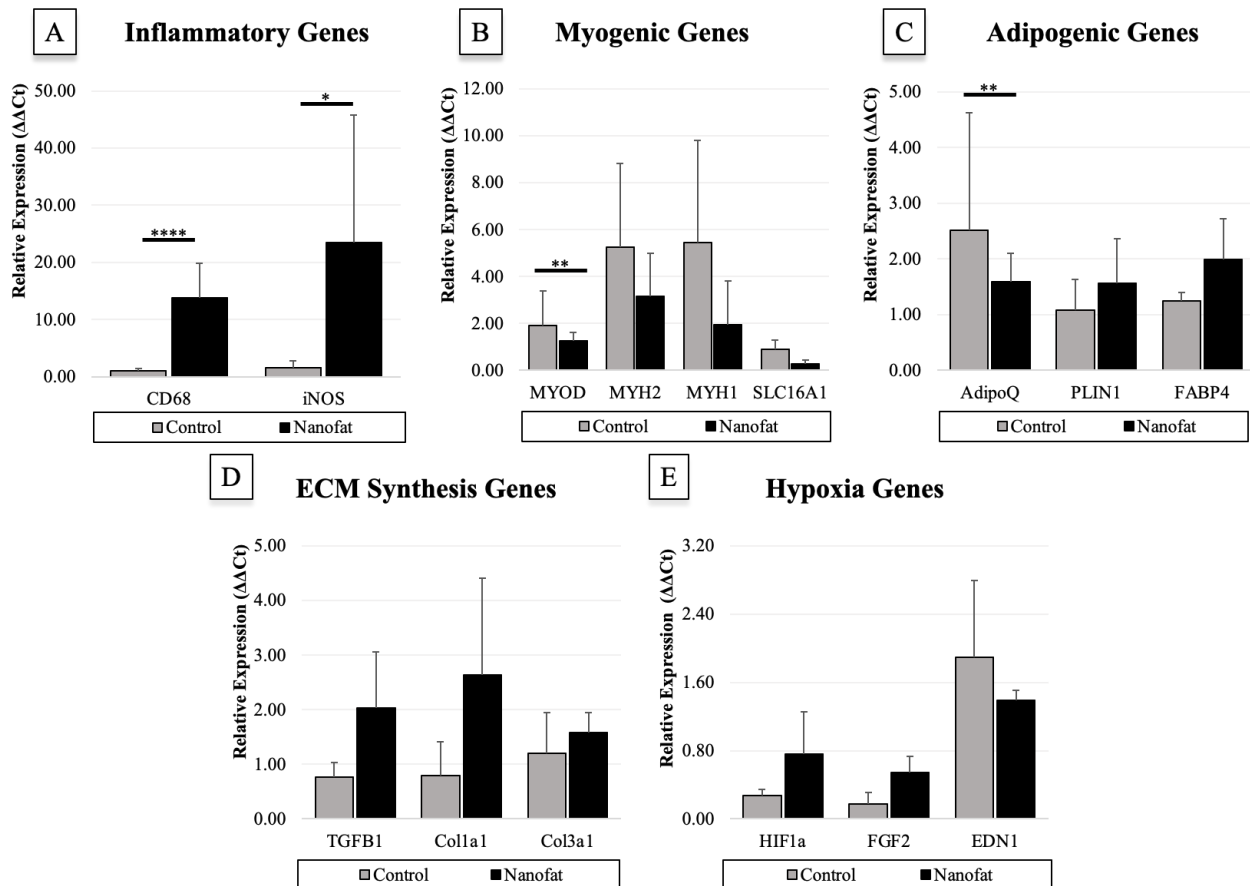


**Figure 43: Gene Transcription in Nanofat-Injected and Non-Treated Gastrocnemii.**

Relative expression of genes in the gastrocnemii responsible for A. Inflammation, B. Myogenesis, C. Adipogenesis, D. ECM Synthesis, and E. Hypoxia. All expressions were normalized to their respective contralateral, uninjured gastrocnemii. Mean  $\pm$  SEM, \* $p < 0.05$ , \*\* $p < 0.01$ , \*\*\* $p < 0.001$ , \*\*\*\* $p < 0.0001$ .

### 3.3.5 Cytokine Quantification in Nanofat-Injected Gastrocnemii and TAs

Eleven cytokines were analyzed with IL-1 $\beta$ , IL-18, VEGF, GC-MSF and TIMP-1 (**Figure 44**) being significantly higher in Nanofat-injected gastrocnemii. Contralateral gastrocnemii of the Nanofat-injected cohort expressed highest IL-1 $\beta$  (adjusted  $p < 0.0001$ ) compared to all groups, followed by the Nanofat-injected gastrocnemii, which expressed IL-1 $\beta$  significantly higher than control (adjusted  $p < 0.01$ ) (**Figure 44A**). Nanofat-injected gastrocnemii expressed highest IL-18 (adjusted  $p < 0.0001$ ); all remaining IL-18 comparisons were not significant (**Figure 44B**). VEGF expression was highest in the Contralateral gastrocnemii of the control cohort relative to all other conditions (adjusted  $p < 0.0001$  for all comparisons), followed by the Nanofat-injected gastrocnemii showing greater expression than its respective contralateral gastrocnemii (adjusted  $p < 0.001$ ) and control gastrocnemii (adjusted  $p < 0.0001$ ) (**Figure 44C**).

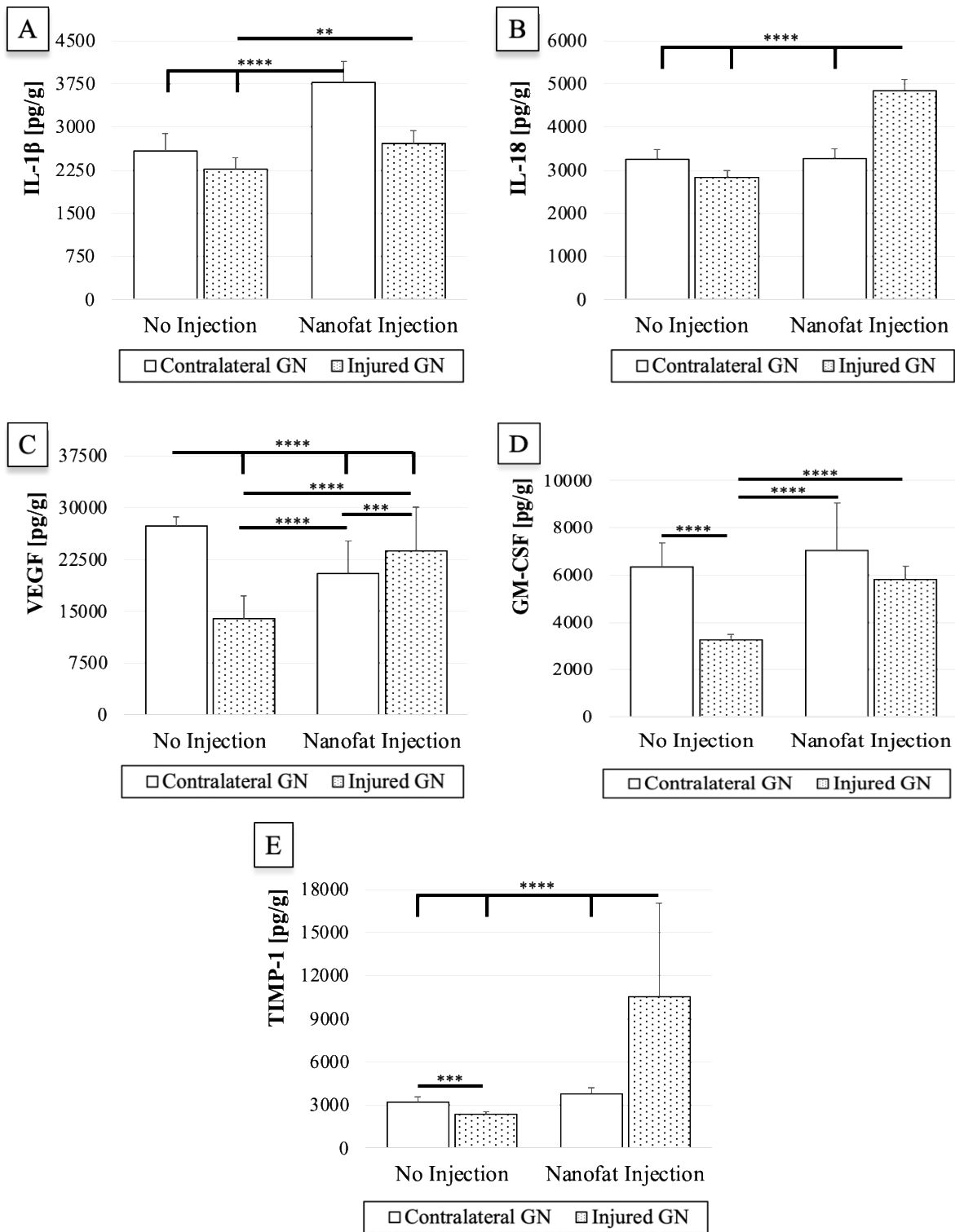


**Figure 44: Significantly-Expressed Cytokines in Gastrocnemii.**

**A. IL-1 $\beta$ , B. IL-18, C. VEGF, CM-CSF, and D. TIMP-1 in contralateral and injury gastrocnemii.**

**Mean  $\pm$  SEM,  $p < 0.05$ ,  $**p < 0.01$ ,  $***p < 0.001$ ,  $****p < 0.0001$ .**

### 3.4 Discussion for Intramuscular Nanofat for Treating Denervated Muscle

Sciatic nerve injury not only results in the dysfunction of the affected nerve, but also induces adverse changes in the muscular microenvironment, resulting in MA. Despite intervention to the nerve itself, the time needed for nerve restoration leaves the downstream musculature in the atrophying state. This induces significant stiffening due to collagenous deposition, shrinkage, and loss in muscle force generation (Burnett and Zager 2004, Corona, Wu et al. 2013). Intramuscular intervention to denervated muscle may be of substantial therapeutic benefit. Preclinically, it has been shown that an intramuscular injection of adipose-derived stem cells can increase gastrocnemius weight after peripheral nerve injury, perhaps through upregulation of IL-10 as assessed immunohistochemically (Schilling, Schusterman et al. 2019). In a clinical study, an intramuscular adipose graft enriched with stromal vascular fraction improved the functional outcome of muscular torticollis suggesting prospective therapeutic benefit of intramuscular injection (Monreal 2017).

Though intramuscular injection of Nanofat resulted in increased contraction force over both timepoints, there have been mixed reports of functional recovery in models of nerve injury and muscle denervation. Combined nerve laceration and ECM-based volumetric muscle repair did not result in significant recovery of contractile force (Merritt, Hammers et al. 2010), and a similar study without nerve injury revealed significant force return only when cells were added into the ECM (Kasukonis, Kim et al. 2016). Together, these studies suggest that a cellular component, perhaps in conjunction with a protein component, may be essential to the muscle healing process. Shown here, the force from gastrocnemii injected with Nanofat result in contraction forces that are better correlated, and therefore more predicable than, those gastrocnemii having not received treatment (**Figure 41E**). While correlative modeling in muscular strength is often performed in

*cross-education*, where inter-limb transfer of strength occurs during the rehabilitative phase of healing (Farthing, Krentz et al. 2011, Magnus, Arnold et al. 2013, Lepley and Palmieri-Smith 2014, Cirer-Sastre, Beltran-Garrido et al. 2017), pre/clinical correlations from intramuscular therapeutics are exceedingly limited and merit dedicated study. Despite greater contraction force (**Figure 41**), administration of Nanofat did not improve SFI-based gait kinematics, where gait function returned similarly over time (**Figure 37**). There has been criticism of the ink-pawprint method for SFI (Sarikcioglu, Demirel et al. 2009, Fricker, Penna et al. 2016), and it is possible that the true fidelity of the toe spread was underappreciated.

It is largely thought that the secretome of the injured muscle tissue, and specifically, the inflammatory cytokines, contribute substantially to its successful recovery postinjury (Butterfield, Best et al. 2006, Smith, Kruger et al. 2008, Yang and Hu 2018). Here, cytokine analyses revealed several significantly upregulated proteins in the Nanofat injected gastrocnemii. Skeletal muscle injury is accompanied by major changes in the ECM. Matrix metalloproteases (MMPs) are regulatory enzymes that function in ECM remodeling. TIMPs are responsible for inhibiting and controlling MMP activity, and specifically, an upregulation of TIMP-1 is involved in protection of skeletal muscle following injury (Mackey, Donnelly et al. 2004, Urso, Szelenyi et al. 2010). While it has been demonstrated in thermal injury that fat grafting increases revascularization and decreases fibrotic factors such as TIMP-1 (Sultan, Barr et al. 2012), optimal muscle ECM remodeling is dependent on tightly regulated activity of the MMP/TIMP system (Kjaer 2004), and therefore the Nanofat may have favorably promoted such remodeling here. Like TIMP-1, GM-CSF is active at sites of muscle inflammation and repair (Becher, Tugues et al. 2016), promoting neutrophil chemotaxis (Peterson and Pizza 2009). Neutrophils have been shown to facilitate muscle repair through removal of tissue debris, activation of satellite cells, and dampening fibrosis

(Butterfield, Best et al. 2006, Toumi, F'Guyer et al. 2006, Yang and Hu 2018), perhaps occurring before the 9-week time point suggested by a lack of significant expression from ECM synthesis genes (**Figure 43**). In fat grafting, GM-CSF has been shown to mobilize resident stromal cells and induce angiogenesis (Cai, Li et al. 2017), where perhaps some synergistic action between the Nanofat and the muscle inflammation promoted functional return.

VEGF plays a key role in skeletal muscle repair via its effect on angiogenesis and vascular permeability through endothelial cell activation and migration (Hoeben, Landuyt et al. 2004, Gianni-Barrera, Trani et al. 2011); it has been shown that adipose tissue grafting promotes secretome-mediated angiogenesis (Evans, Gronet et al. 2020). CD68-positivity is typically indicative of skeletal muscle-resident M1 macrophage phenotype, responsible for clearing necrotic muscular regions, and also have been shown in regenerating zones along injured fibers (Mackey and Kjaer 2017, Kosmac, Peck et al. 2018, Zuo, Wang et al. 2018). However, CD68 also presents in cells outside the monocyte/macrophage lineage, notably, in endothelial cells (Gottfried, Kunz-Schughart et al. 2008, Chistiakov, Killingsworth et al. 2017), where the elevated CD68 expression in the Nanofat-treated gastrocnemii (**Figure 43**) potentially contributed to the significantly increased presence of VEGF (**Figure 44**). Two preclinical rodent models using Nanofat preparations to treat podiatric ulcer (Chen, Wang et al. 2019) and to treat mild dermal irradiation injury (Xu, Yu et al. 2018), both showed increased presence of CD31-positive cells as well as upregulation of VEGF, both being implicated as the therapeutic benefit of Nanofat.

iNOS upregulation is well recognized as proinflammatory (Mantovani, Sica et al. 2004, Novak and Koh 2013), its expression has been implicated as a requirement for effective regeneration of muscle by modulating inflammatory cell recruitment (Rigamonti, Touvier et al. 2013). The upregulation of iNOS at the gene level may have acted as a driver for the

proinflammatory cytokines identified in multiplexing (IL-1 $\beta$ , IL-18). IL-1 $\beta$  is a proinflammatory cytokine involved in chemotaxis, recruitment of circulating macrophages to the site of muscle injury and activating endothelial cells to secrete GM-CSF (Dimauro, Grasso et al. 2014), which was also significantly upregulated here. IL-1 $\beta$  inhibits satellite cell differentiation to enhance proliferation (Smith, Kruger et al. 2008), potentially resulting in prolonged myofiber fusion as satellite cells continue to proliferate. IL-1 $\beta$  also induces prostaglandin synthesis, neutrophil influx and activation, and plays a role in angiogenesis by inducing VEGF production (Nakahara, Song et al. 2003) and having been upregulated as the Nanofat therapy is of a lipid-laden source tissue. To that end, AdipoQ promotes satellite muscle cell differentiation into adipocytes rather than into the myogenic lineage with overexpression of the AdipoQ gene resulting in increased intracellular lipid accumulation (Fu, Luo et al. 2005, Wang, Xue et al. 2018). AdipoQ can also act as a local protective mechanism to counteract cellular damage by weakening inflammation (Jortay, Senou et al. 2012), and because of this, perhaps having also causing a reduction of contraction force in controls. Both the upregulation of AdipoQ and MyoD in controls may suggest some competition between the myogenic and lipogenic pathways (Acosta, Jia et al. 2020), or distinct actions on separate cell types within the muscle. Unintuitively, the master regulator of muscle differentiation, MyoD (Aziz, Liu et al. 2010, Zammit 2017), was upregulated in the control cohort (**Figure 43**), though this could be from the lag in force return (compare control 9wk versus 12wk in **Figure 41** to Nanofat treatment).

### **3.4.1 Limitation of the Intramuscular Nanofat Study**

While rodents are often used to model adipose metabolism and fat grafting, it remains unclear whether rodent fat pads are the most suitable model of human adipose (Chusyd, Wang et

al. 2016). Further, secretome analysis of rat adipose tissues shows location-specific roles for each depot type (Roca-Rivada, Alonso et al. 2011), so the selection of the inguinal fat pad may not be the most ideal analog of a (Nano)fat therapeutic. Finally, obese adipose tissue releases more inflammatory and ECM molecules, collagens, and proteases than lean adipose tissue (Chen, Hunt et al. 2009), which may have serious implications when grafted into the intramuscular environment, and therefore obesity states merit investigation.

### 3.5 Chapter Conclusions

Here, it was shown that several inflammatory cytokines like IL-1 $\beta$ , IL-18, inflammatory genes like iNOS and CD68, and the angiogenic growth factor VEGF were significantly upregulated (**Figure 44**), where perhaps, prolonged upregulation of satellite cell proliferation combined with regulation of injury lipogenesis and inflammation contributed to the increased contraction. There is strong statistical evidence that an intramuscular injection of Nanofat provides substantial therapeutic benefit to the recovery of contractile force in denervated muscle. This phenomenon appears to be mediated, at least in part, by inflammation, and specifically by the cytokines IL-1 $\beta$ , IL-18, and their interacting effects. The findings here serve to potentially increase the therapeutic applications of Nanofat to include muscular recovery after nerve injury.

## **4.0 Acellular, Extracellular Matrix-Based Therapies for Mitigating Gastrocnemius Denervation Atrophy after Sciatic Nerve Transection**

Extracellular matrices (ECM) resulting from decellularized tissue have shown exceptional promise for repair and regeneration of many types of damaged tissue. To that end, over forty ECM-based products are registered, cleared, or approved for clinical use by FDA in the US alone (Parmaksiz, Dogan et al. 2016). Typically used for repair of homologous tissue, allogenic and xenogeneic decellularized ECMs span a plethora of therapeutic applications. Such applications include hernia repair (Shankaran, Weber et al. 2011, Primus and Harris 2013), breast reconstruction (Becker, Saint-Cyr et al. 2009, Sbitany and Serletti 2011), adipose regeneration (Kokai, Schilling et al. 2019), dental and orthopedic bone void repair (Grover, Kapoor et al. 2011, Shehadi and Elzein 2017), tendon reconstruction (Krych, Jackson et al. 2008), and wound care (Snyder 2005, Sheikh, Sheikh et al. 2014). Decellularized ECM therapies continue to be investigated through clinical trials, addressing a multitude of applications at anatomic sites including the trachea, heart valves, eye, and bladder, among many others (Porzionato, Stocco et al. 2018). Further, complex ECM scaffolds generated from perfusion decellularization, such as heart (Lu, Lin et al. 2013, Robertson, Dries-Devlin et al. 2014), lung (Gilpin, Ren et al. 2014), kidney (Pornejad, Buckmiller et al. 2017), or face (Duisit, Orlando et al. 2017) are within the foreseeable pipeline for future clinical translation.

## 4.1 Design of an Automation-Capable Perfusion Platform for Skeletal Muscle Tissue

### Decellularization

Perfusion decellularization for whole organ engineering requires additional hardware that a spinner flask or agitation decellularization does not, as well as similar, if not greater, requirements for solution exposure (Guyette, Gilpin et al. 2014). Initial attempts at automating decellularization processes have resulted in shorter decellularization periods with greater efficiency in removing DNA material; however, automation systems are often developed for a target tissue or organ and typically include several large, piecemeal components that limit or prevent mobility (Price, Godin et al. 2015). Here, a functional prototype of an integrated Tissue Infusion/Perfusion Device (TIPD) has been designed and fabricated using 3D printed parts coupled with commercially-available components. This device has been tested for proof of concept through infusion decellularization of porcine skeletal muscle, as well as perfusion decellularization of rodent epigastric free flaps and kidneys (**Appendix C: Perfusion Decellularization Using TIPD**). The 3D-printable components, software, and circuitry files have been made available along with the instructions for the device's assembly. These are intended to decrease the burden of entry into infusion or perfusion decellularization, increase the reproducibility of experimental designs, and to promote an open-source hardware (OSH) initiative in tissue engineering.

There were several target considerations in designing the TIPD: namely these design constraints included the integration of 3D printable-scaffolding coupled with the use of off-the-shelf, OSH components intended to maximize flexibility for parts replacement. For purposes of mobility, the total volume of the device was to be kept under 1 cubic foot. For fluidics, the integration of programmatic control of at two peristaltic pumps (to govern in-flow and out-flow, either into/out of a scaffold or chamber) and control of fluid selection through some valve

operation was necessitated. Finally, all components were to be unified into an automation-capable software platform.

#### **4.1.1 3D Printing Parameters for the TIPD**

Eighteen parts were designed for the assembly of the TIPD, organized into part families in **Table 7** through **Table 10**, all of which were designed in Solid Works CAD/CAM (Dassault Systems, Waltham, MA). Prior to 3D printing, all part files were converted into stereolithography (.stl) file format from Solid Works. All parts were sliced and 3D printed using the fused filament fabrication (FFF) technique via ideaMaker Slicing Engine and Raise3D N2+ printer (Irvine, CA). PLA filament (1.75mm diameter, Raise3D) was extruded through a 0.4mm nozzle at 205°C onto a heated bed with a BuildTak surface (Maplewood, NJ) set to 65°C. All parts were printed using a raft to facilitate bed adhesion, with a 0.30mm raft gap from each model. Parts were printed at a speed of 50mm/s with three shells, variable infills at 45% or greater (tabularized below, based on part), and with support structures at 10% infill where any overhang angle greater than 40° received support. Approximate print times and estimated part masses presented in the Tables are based on these slicing and printing parameters, however parameters will likely vary depending on the printer and filament being used.

#### **4.1.2 Machine Design and Assembly**

CAD/CAM renderings of the TIPD assemblies are presented in **Figure 45**. The TIPD was designed to include two peristaltic pumps, two 3-way valves, and to accommodate two styles of chambers. **Figure 46** presents the TIPDs after printing and assembling the requisite components

using basic hardware. All through-holes and junctions have been designed to accommodate M3 machine screws (McMaster-Carr, Aurora, OH). Tubing, coupling, motors, and electronics are presented in detail in **Appendix B**. For ease of repeat assembly, the TIPD can be segmented into four part families, which include the Device Scaffold subassembly, the Peristaltic Pump subassembly, the Valve Operation subassembly, and the Chamber Support subassembly.

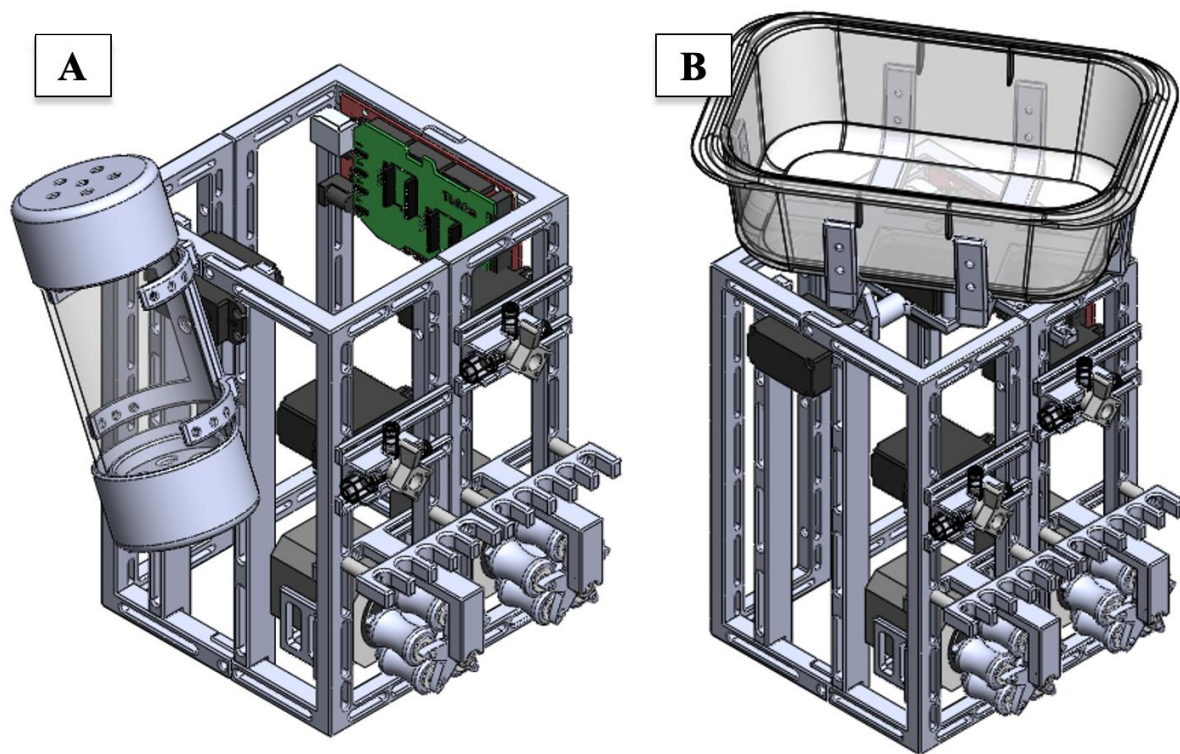


**Figure 45: CAD/CAM Renderings of the TIPD Assemblies.**

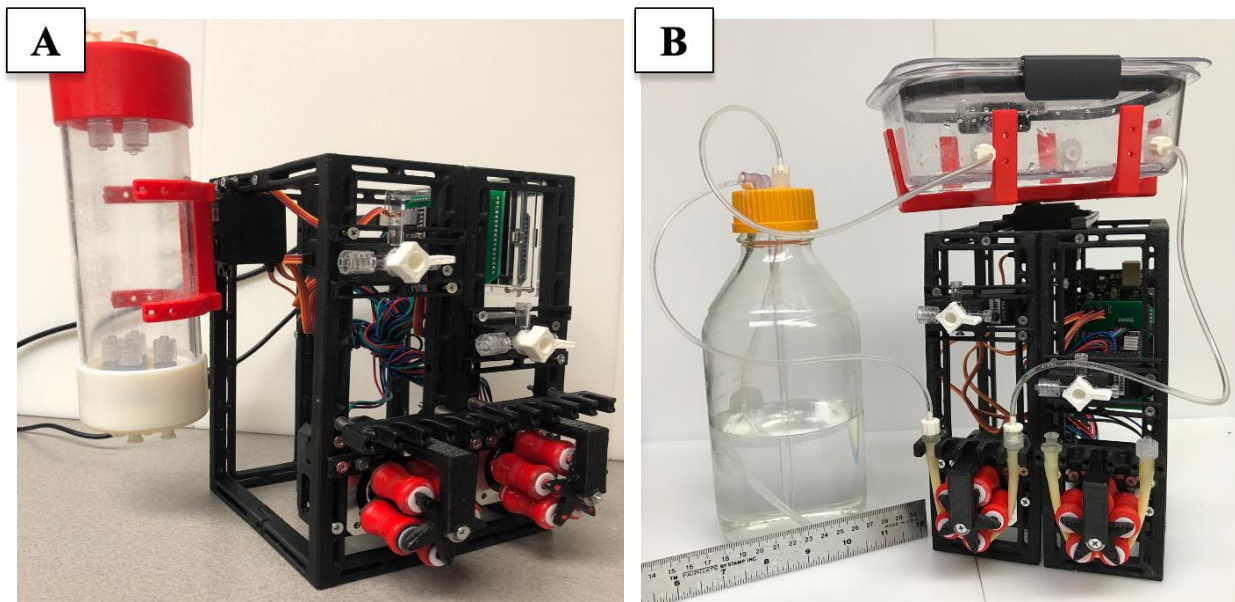


**Figure 46: TIPD after 3D Printing and Assembly.**

The Device Scaffold subassembly provides structural support for the remaining three subassemblies. **Table 7** presents the components necessary to create the Device Scaffold. Four Quarter Scaffold parts are organized such that a rectangular scaffold is made, occupying a footprint of 5.5in (14.0cm) wide by 5in (12.7cm) deep with a height of 8in (20.3cm). The Quarter Scaffold part has been designed with elongated through-holes allowing variable placement of the Pump and Valve subassemblies, designed to be affixed using M3 screws. Each Quarter Scaffold also possesses bores in which magnets can be press-fit (optional).

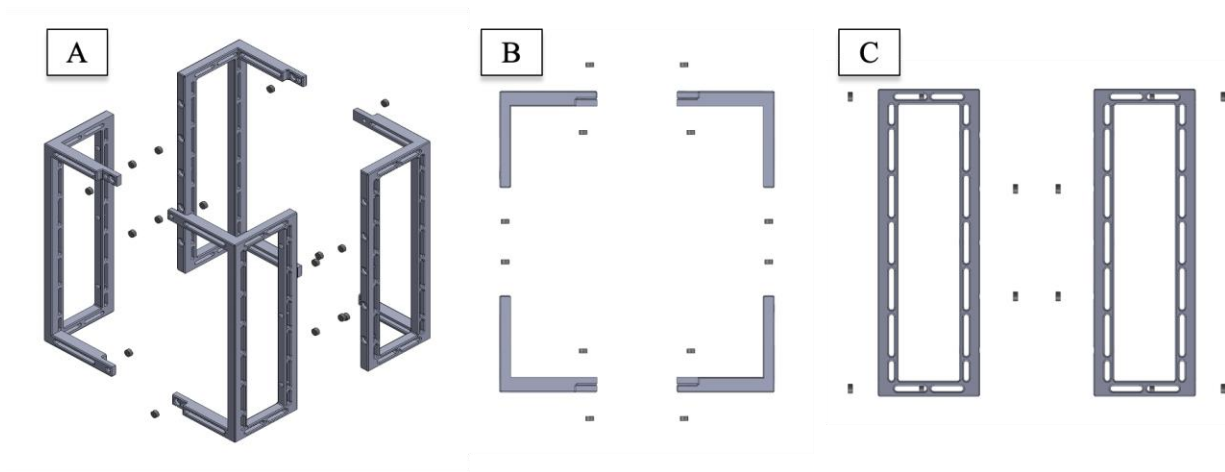
**Table 7: TIPD Quarter Scaffold Part Family.**

Thumbnails and information relevant to the 3D printed components of the Quarter Scaffold Part Family, which provides the overall support to the device.

Part Name	Thumbnail Image (Not to Scale)	Quantity Needed	Approximate Print Time	Estimated Mass [g]	Notes
Quarter Scaffold		4	9 hours 45 minutes	57.1	1
Scaffold Side Post		2	3 hours 32 minutes	19.2	None

*Note 1:* In-print support material recommended.

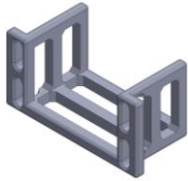
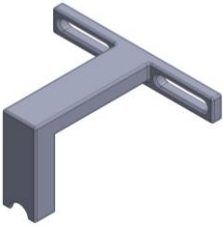
**Figure 47** demonstrates the subassembly in isometric (**Figure 47A**), top (**Figure 47B**), and front (**Figure 47C**) views. Sixteen magnets can be seen in this exploded view from each of the four Quarter Scaffold parts of the subassembly. Near each magnet bore is a through-hole for permanent fixation via machine screw. Note that **Figure 47** does not show the Scaffold Side Post; however, this structure is utilized to support a servomotor responsible for chamber motion, which is shown in the assemblies of **Figure 49**.



**Figure 47: Exploded Views of the TIPD Quarter Scaffold Family Assembly.**

**Exploded displays of isometric (A), top (B), and front (Figure 47C) views.**

**Table 8: TIPD Peristaltic Pump Part Family.**

<b>Part Name</b>	<b>Thumbnail Image (Not to Scale)</b>	<b>Quantity Needed</b>	<b>Approximate Print Time</b>	<b>Estimated Mass [g]</b>	<b>Notes</b>
<b>Stepper Chassis</b>		2	2 hours 20 minutes	12.2	1
<b>Stepper Fastener</b>		2	30 minutes	3.9	2
<b>Pump Carousel</b>		2	1 hour 50 minutes	6.5	2, 3, 4
<b>Post Collar</b>		10	1 hour 10 minutes	3.0	3, 4
<b>Carousel Cap</b>		2	35 minutes	3.6	None
<b>Carousel Stabilizer</b>		2	1 hour 40 minutes	6.4	1
<b>Luer-Lok Collar</b>		2	1 hour 20 minutes	5.8	None

Note 1: In-print support material recommended; Note 2: 100% infill density recommended;

Note 3: High-quality print recommended; Note 4: Part sanding and chemical polishing recommended.

The Peristaltic Pump subassembly creates the mechanism for driving fluid flow from a reservoir into the scaffold. **Table 8** details the 3D printed part family for creating this subassembly, which is comprised of a combination of 3D printed parts as well as commercially-available components. A NEMA 17 bipolar stepper motor (Stepper Online, Nanjing City, China) is used to generate the rotational movement of the pump. The Pump Carousel is designed to be press-fit onto the horn of the stepper motor, where a notch in the Pump Carousel will determine proper placement onto the motor. The Pump Carousel accommodates five Post Collars, which roll freely and creates the peristaltic action when a tube is pulled taut against the faces of the Post Collars. In an effort to reduce friction during operation, Post Collars and the Pump Carousel were printed using the highest quality print setting available on the N2+ as definable in ideaMaker; the posts of the Pump Carousel, as well as the outer surface of the Post Collars, were sanded with fine-grit sandpaper and then were chemically polished using ethyl acetate (Millipore-Sigma, St. Louis, MO), smoothing the posts of the Pump Carousel as well as the Post Collar surfaces. Additionally, an M5 unthreaded spacer (McMaster-Carr) inserts into each Post Collar, which further minimizes friction against the posts of the Pump Carousel during operation. Likewise, two M5 PTFE washers (McMaster-Carr) rest at the top and bottom of each Post Collar, separating it from the Carousel Cap and the base of the Pump Carousel. The Carousel Cap secures the Post Collars onto the Pump Carousel and is assembled with a ball bearing separated by a 3mm-long unthreaded spacer, holstered by the Carousel Stabilizer. Once all components within the subassembly are assembled, they are affixed to a Quarter Scaffold. **Figure 48A** presents these components in exploded view. Once the pump is assembled, the Stepper Fastener, Stepper Chassis, and the Carousel Stabilizer components are used to affix the stepper motor with the assembled carousel onto the Quarter Scaffold (refer to **Figure 47**). The Luer-Lok Collar is then affixed to a Quarter Scaffold, resting atop the Carousel Stabilizer.

A 10cm tube with Luer-Lok couplers may then be wrapped around the assembled carousel, held in tension by the Luer-Lok Collar. The TIPD was designed to integrate two sets of this subassembly yielding independent peristaltic pumps capable of programmatically driving fluid at a controlled rate.

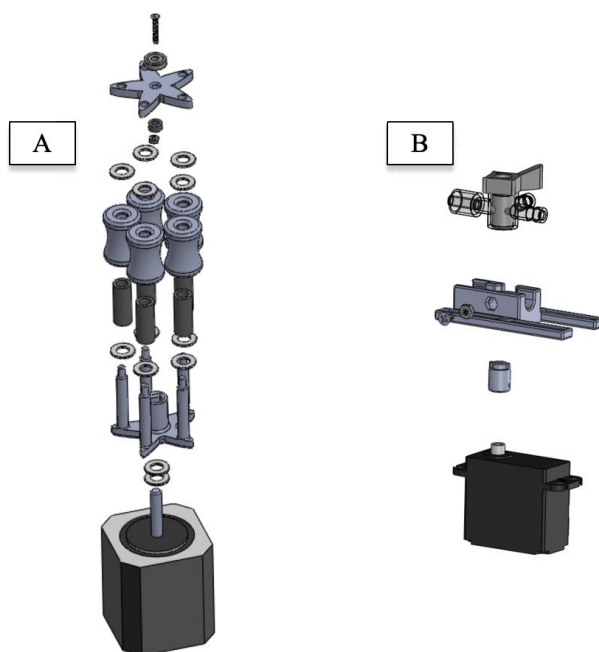


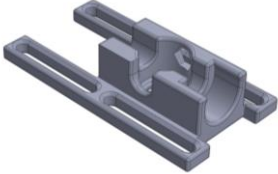
**Figure 48: TIPD Subassemblies of the Peristaltic Pump and Valve Rotator.**

(A) Exploded view of the Peristaltic Pump subassembly with a stepper motor at the base, driving the rotation of the pump once assembled. (B) Exploded view of the Valve Operation subassembly with a servomotor at the base, enabling valve selection within the 180° rotation range of the motor.

The Valve Operation subassembly is designed specifically for interfacing with a 4-Way Stopcock (Qosina, Ronkonkoma, NY, Part No. 88218). The 3D printed part family is presented in **Table 9**, and **Figure 48B** presents the exploded view of the subassembly. The Valve Chassis is responsible for holding the stopcock above the servomotor and has been designed for adhesive fixation of an M3 hex nut, which stabilizes the stopcock when light pressure is applied from a thumbscrew. The Valve Rotator has been designed with a through-hole that seats concentrically

with respect to the horn of a servomotor (DFRobot, Pudong, Shanghai, China) such that the Valve Rotator can be screwed directly into the servomotor. This minimizes the potential slippage of the Valve Rotator on the servomotor horn when turning the stopcock via servomotor control. For assembly onto a Quarter Scaffold, the servomotor with the affixed Valve Rotator is placed first, followed by the Valve Chassis. The top of the Valve Rotator interfaces directly with the bottom of the stopcock when seated within the Chassis.

**Table 9: TIPD Valve Operation Part Family.**

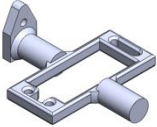
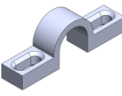
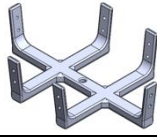
<b>Part Name</b>	<b>Thumbnail Image (Not to Scale)</b>	<b>Quantity Needed</b>	<b>Approximate Print Time</b>	<b>Estimated Mass [g]</b>	<b>Notes</b>
<b>Valve Chassis</b>		2	1 hour 40 minutes	9.8	1
<b>Valve Rotator</b>		2	20 minutes	0.9	1

*Note 1: In-print support material recommended.*

The Chamber Support subassembly can be constructed in one of two ways: a hanging-mount design (**Figure 45A** and **Figure 46A**) or a top-mount design (**Figure 45B** and **Figure 46B**). **Table 10** details the 3D printed components needed for each assembly. The hanging-mount design is constructed to hold a 2.25"-diameter tube which is cut to a 4in (10.2cm) length in the Figure but can cut to an application-specific length. The side-mount design couples a single servomotor with the Side-Chamber Chassis and allows oscillatory movement between 0° and 180°. The top-mount design has been constructed for use with a commercially available 750ml container (Rubbermaid),

and integrates additional complexity into its assembly allowing for movement in the roll and yaw directions. **Figure 49A**, **Figure 49B**, and **Figure 49C** present exploded views of the parts and hardware for creating the top-mount design. The Servo Roll Chassis (shown in **Figure 49B**) accommodates a servomotor, governing the roll direction; this servomotor is horizontally mounted onto Scaffold Side Posts and then the opposing, cylindrical end of the Servo Roll Chassis is supported by the mounting the subassembly shown in **Figure 49A** onto the top of the assembled Quarter Scaffolds. The Top-Chamber Chassis is secured into the servomotor using an M3 screw. The entire subassembly, including the 750ml chamber, is shown in **Figure 49D**.

**Table 10: TIPD Chamber Support Part Family**

<b>Part Name</b>	<b>Thumbnail Image (Not to Scale)</b>	<b>Quantity Needed</b>	<b>Approximate Print Time</b>	<b>Estimated Mass [g]</b>	<b>Notes</b>
<b>Yaw Chassis Bracket</b>		1	1 hour 39 minutes	11.1	1
<b>Servo Roll Chassis</b>		1	2 hours 40 minutes	19.6	1
<b>Roll Chassis Buckle</b>		1	21 minutes	3.3	1
<b>Servo Spacer</b>		2	34 minutes	2.9	None
<b>Top- Chamber Chassis</b>		1	7 hours 26 minutes	70.0	1
<b>Side- Chamber Chassis</b>		1	2 hours 34 minutes	15.8	1
<b>Cylindrical Chamber Cap</b>		2	12 hours 37 minutes	87.3	2, 3

*Note 1:* In-print support material recommended; *Note 2:* 100% infill density recommended;

*Note 3:* High-quality print recommended.

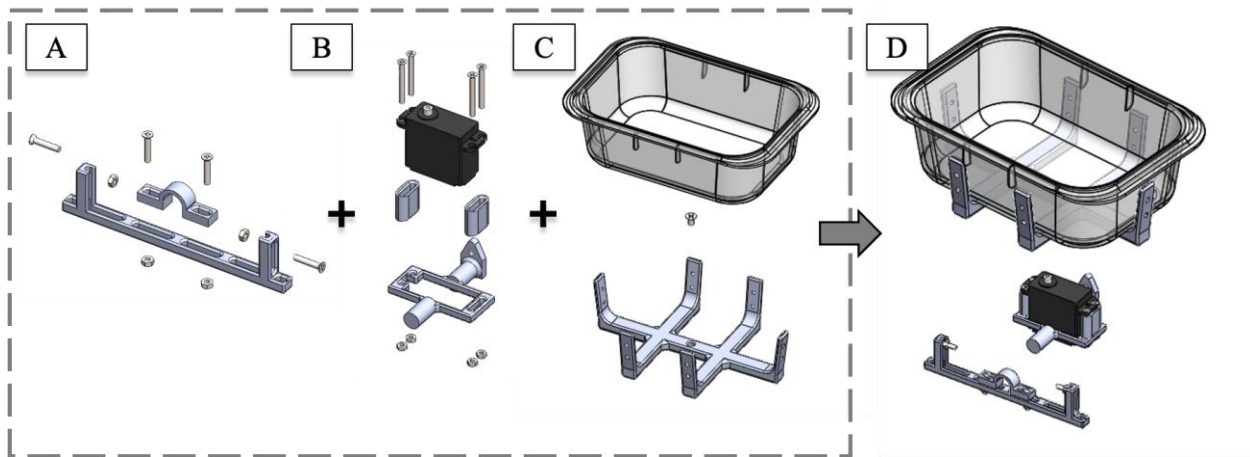


**Figure 49: TIPD Exploded Chamber Assembly.**

*Circuitry, Electronics, and Programmatic Control:* Logic-based control of the TIPD’s electronic components is based around an Arduino Mega2650 microcontroller (Ivrea, Italy) and a custom printed circuit board (PCB), which forms an Arduino shield once assembled. Layout of the PCB was designed in EasyEDA and fabricated by JLC PCB (Shenzhen, Guangdong, China). **Figure 50A** and **Figure 50B** present the front and back, respectively, of the PCB design in the EasyEDA environment. Structures are color-coded per **Table 11**. The top and bottom layers of the PCB are used to avoid crossing of the wires (red and blue) so as to avoid short-circuiting, and are physically separated. A zipped folder containing the respective GERBER files is provided in the Supplemental Content of the publication (Schilling, Lamberti et al. 2019), which can be uploaded directly into the JLC PCB portal.

**Table 11: Color Coding of PCB Objects and Layers from Figure 50.**

<b>Color</b>	<b>PCB Layer</b>	<b>Description</b>
Red	Top	Wire connecting solder pads (gray)
Blue	Bottom	Wire connecting solder pads (gray)
Yellow	Top (Silk)	Lettering atop topside solder mask
Pink	Bottom (Silk)	Lettering below bottom-side solder mask
Purple	Both	Outline of circuit board
Gray	Both	Solder pad with thru-hole for pin insertion

**Figure 50C** and **Figure 50D** show the unpopulated PCB and the PCB after soldering all components into place, respectively. From **Figure 50**, numeric labels 1-6 indicate “Components/Component Sets”: Component Set 1 denotes four sets of male pinouts for the servomotors (chamber movement and valve operation). Component Set 2 denotes two sets of male pinouts for the stepper motors (peristaltic pumps). Component Set 3 denotes two sets of DRV8825 Stepper Motor Drivers (Pololu, Las Vegas, NV), which are responsible for converting the logic received from the microcontroller into the appropriate rotational pump speed. Component 4 denotes a DC-DC step-down module that is adjusted to 5V (volt) output from 12V input, which powers both the stepper and servomotors. Component 5 is a 100 microfarad ( $\mu\text{F}$ ) capacitor and is used for smoothing the current of the stepper motors on startup. Finally, Component 6 denotes a 2.1mm barrel jack, which accommodates a 12V 5A (ampere) power supply that is responsible for powering the system independent of the microcontroller.

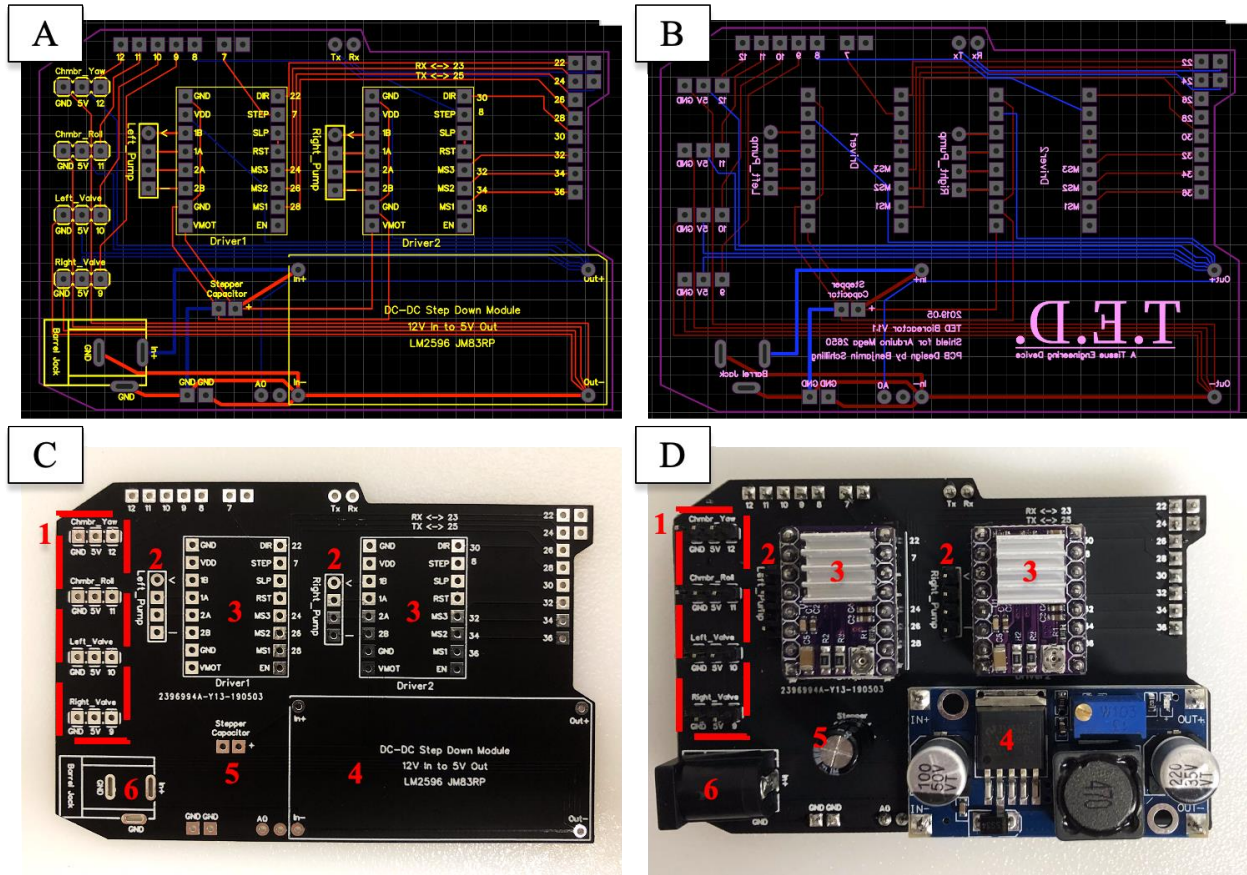


**Figure 50: TIPD Printed Circuit Board Design and Population.**

The Arduino integrated development environment (IDE) was downloaded, which includes the requisite drivers for running the microcontroller. All coding for the TIPD was done via Virtual Instrument (VI) in LabVIEW 2018 (National Instruments, Austin, TX) with the Digilent LINX package addon from the Virtual instrument Package Manager (VIPM, JKI, Lafayette, CA). The LINX prebuilt hex was installed onto the Arduino microcontroller prior to operation. Main and sub-VIs were saved as an Executable (.exe) file extension and are available in the Supplemental Content of the publication (Schilling, Lamberti et al. 2019). Note, for running the Executable, NI-VISA RunTime Engine 18.5 must be installed such that LabVIEW is able to recognize use of a

COM port by the microcontroller. Additionally, either the full version of LabVIEW or LabVIEW SP1 RunTime 18 must be installed. Windows OS was used throughout.

#### **4.1.3 TIPD Proof of Concept through Skeletal Muscle Infusion Decellularization**

Porcine skeletal quadriceps muscle from male Yorkshire pigs was obtained immediately after sacrifice and was stored at  $-80^{\circ}\text{C}$  prior to decellularization. Muscle was thawed and cut into contiguous segments of  $1.25\text{g} \pm 0.05\text{g}$  after which an 18G Precision Glide sharp-tip needle (BD, Franklin Lakes, NJ) was inserted into the muscle such that the needle opened at approximately the centroid of the segment. For infusion decellularization, 100ml 0.3% or 1% sodium dodecyl sulfate (SDS, Millipore-Sigma) was pumped for approximately 20 hours, where the SDS was recirculated after tissue contact (0.3% was only used for infusion decellularization). Next, 1000ml DI water was pumped through the tissue and was not recirculated. To further ensure clearance of the SDS, 100ml 1% Triton X-100 (Millipore-Sigma) was pumped and recirculated through the tissue for 20 hours, followed by an additional 1000ml DI water (non-recirculated). The pump was set to 1/8-step for all processes. Separately, muscle was decellularized in a spinner flask following previously-established protocols (DeQuach, Mezzano et al. 2010, DeQuach, Lin et al. 2012). Briefly, the spinner flask was set to 400RPM and a ratio of 1:10 muscle mass to solution volume was exposed to 1% SDS for 3 days. Residual SDS was removed using eight exchanges of DI water, followed by an additional exposure of 1% Triton X-100 overnight. Finally, the muscle was exposed to eight additional exchanges of DI water.

#### **4.1.3.1 H&E Staining of Skeletal Muscle**

After decellularization, soft tissues were fixed in 10% neutral buffer formalin (Fisher Scientific, Waltham, MA), paraffin-embedded, and mounted in 5 $\mu$ m sections on polarized glass slides. H&E staining was performed by removing paraffin at 60°C for 60 minutes and then rehydrating sections in serial washes of decreasing ethanol concentrations. Wiegert's hematoxylin and eosin were applied per manufacturer's instruction (Millipore-Sigma). Sections were then dehydrated and mounted with slide glass. A Keyence BZ-X was used for all histological imaging.

#### **4.1.3.2 DNA Quantification of Skeletal Muscle**

Muscle was frozen to -80°C and then freeze-dried (Labconco FreezeZone 2.5, Kansas City, MO). Dry samples of 25mg  $\pm$  5mg were digested in proteinase-k and purified following manufacturer's instructions (QIAamp, Qiagen, Germantown, MD). DNA was quantified using the QUANT-it PicoGreen dsDNA kit per manufacturer's instructions (Fisher Scientific).

#### **4.1.3.3 TIPD Study Statistical Analysis**

JMP Pro 14 was used for statistical analyses. DNA results were evaluated using a one-way ANOVA with Tukey-Kramer *post hoc* after testing for normality of residuals via Shapiro-Wilk W test and homoscedasticity via Levene's tests. Statistical significance was defined as  $p < 0.05$ .

#### **4.1.4 Results of TIPD Fabrication and Skeletal Muscle Decellularization**

##### **4.1.4.1 LabVIEW VI, Automation, and Fluid Flow Capabilities**

**Figure 51** and **Figure 52** display the graphical user interface (GUI) when running the VI in Control and Automation modes, respectively. Nineteen points of interest are displayed in the

Figure: (1) denotes the Communication Port “COM#” tethered to the PCB-shielded microcontroller, to be defined prior to running the VI; (2) displays the current time and date; (3) displays the total runtime of the VI; (4) is a notifier that changes based on operating state of the TIPD; (5) displays a resettable clock; (6) denotes a set of indicators that control the movement of the chamber, being either yaw movement if the top-mount chamber is affixed, or the oscillatory movement if the side-mount chamber is affixed; (7) denotes a set of indicators that control the roll movement of the top-mount chamber only (*note*: the Chamber Controls values dictate pulse widths sent from the microcontroller to the servomotor and are arbitrary with respect to the physical orientation of the servomotor horn); (8) indicates communication to the microcontroller when illuminated green; (9) displays three selectable panels being the Main Controls panel (**Figure 51**), the Automation panel (**Figure 52**), and the Settings panel, which allows additional user customization of servomotor boundaries; (10) denotes a push-button to stop one or both pumps if running; (11) displays an indicator light, which illuminates when the pump is active, along with a scale bar ranging from Off to Full that determines the spin-rate of the pump; (12) denotes a switch that reverses the pump direction; (13) denotes controls for the 3-way valve where “Timed” is a function controlling oscillation between the top or side port being open; (14) denotes another set of the controls and indicators explained in (11-13) for the opposing pump; (15) denotes the file selection window for running an automation protocol from a comma-separated (.csv) file; an Excel template for building custom automation protocols has been provided in the Supplemental Content of the publication (Schilling, Lamberti et al. 2019); (16) displays the Initiate Automation buttons, which will only become active when a protocol is defined in the selection window and the notifier as discussed in (4) is updated with the current step, step time, and the overall protocol time as shown; (17) displays the Abort Automation button, which will only become active when a protocol

is running; (18) displays a table of the entire protocol once Initiated; finally, (19) similar to (9) presents the selection tab but with the Automation panel active. Through manual control or via automation, the TIPD is capable of controlling fluid flow spanning the six-step motor range.

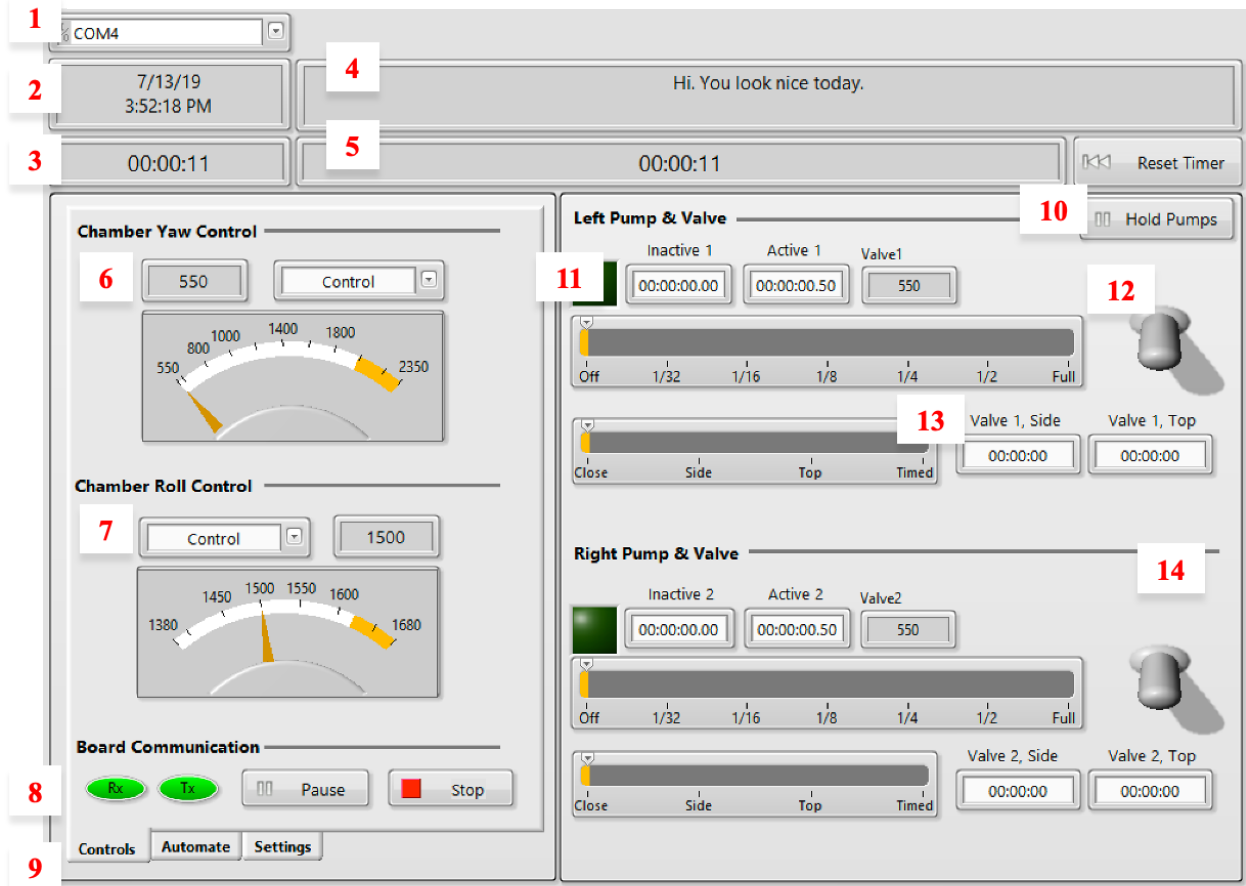
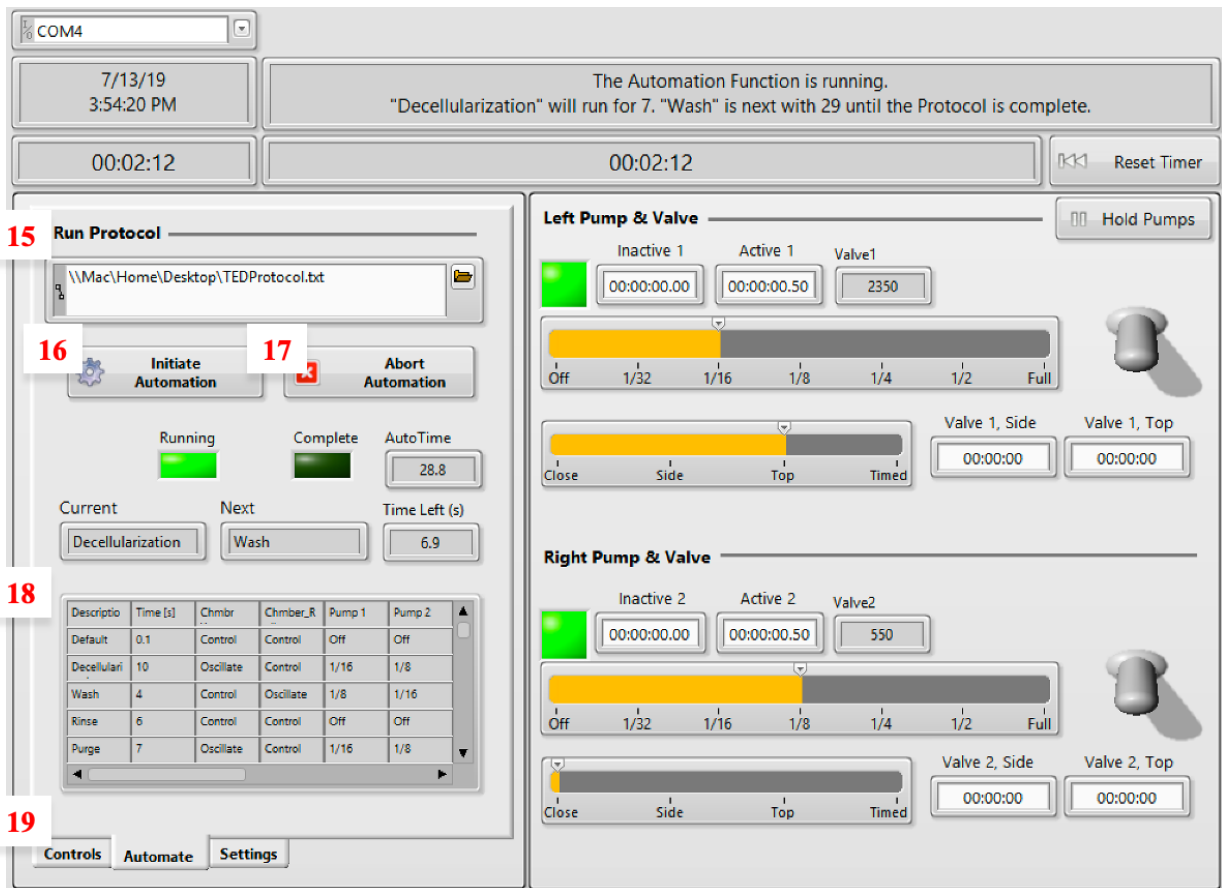


Figure 51: TIPD GUI of the Control Page VI.



**Figure 52: TIPD GUI in the Automation panel**

GUI in the Automation panel, where a protocol for the automation of a process has been selected and initiated as shown by the Notifier (Callout 4, Figure 51) and the Automation Matrix (Callout 18).

**Figure 53** presents the flow velocity by the step size and the flow velocity by the revolutions per minute and their fitted curves, respectively. As shown, the pumps are capable of achieving flow rate of up to 1.25mL/s (4.50L/hour) Intermittent flow rates can be achieved by utilizing the “Active”/“Inactive” setting in the VI.

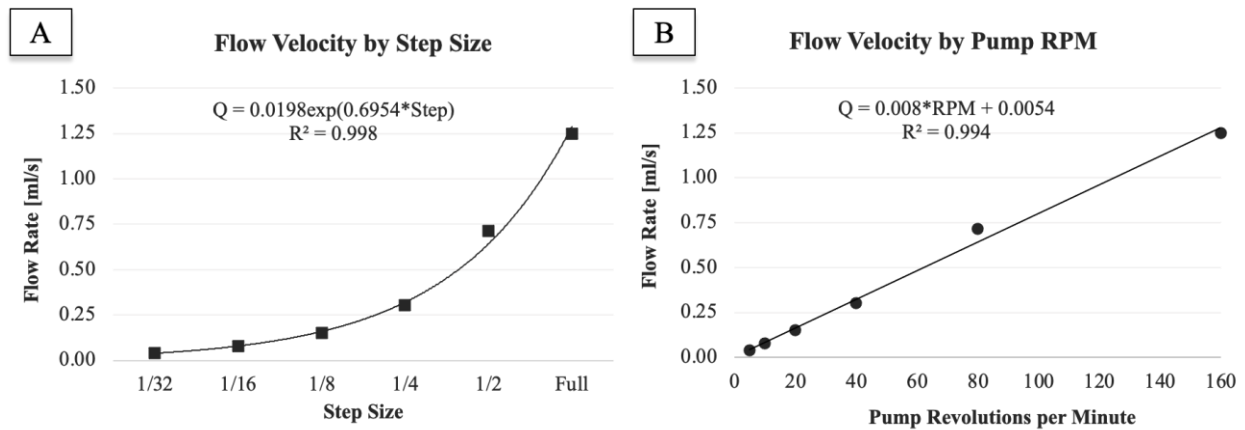


**Figure 53: TIPD Pump/Fluid Velocity Relationship.**

Fluid velocity characteristics of the over the range of peristaltic pumps governed by the step size of the motor; exponential and linear equations are shown for predicting flow rates at intermittent pump steps.

#### 4.1.4.2 TIPD Decellularization of Skeletal Muscle

On harvest, vascular access to some muscle cannot be established and hence the infusion method was utilized to similarly replicate perfusion decellularization. **Figure 54A-C** display setup for skeletal muscle infusion, infusion decellularization inside the side-mount chamber, and the resulting scaffold, respectively. The H&E image in **Figure 54D** shows native porcine skeletal muscle and **Figure 54E** presents H&E of the fibrous ultrastructure lacking nuclei after decellularization, which is confirmed by DNA quantification (**Figure 54F**). As shown, significant reduction of DNA was achieved in all decellularization processes with respect to native porcine skeletal muscle ( $p < 0.001$ ). No significant difference in DNA content was found when comparing 20-hour 0.3% or 1% SDS infusion processes against the 72-hour 1% SDS spinner flask process (adjusted  $p > 0.750$  for each comparison).

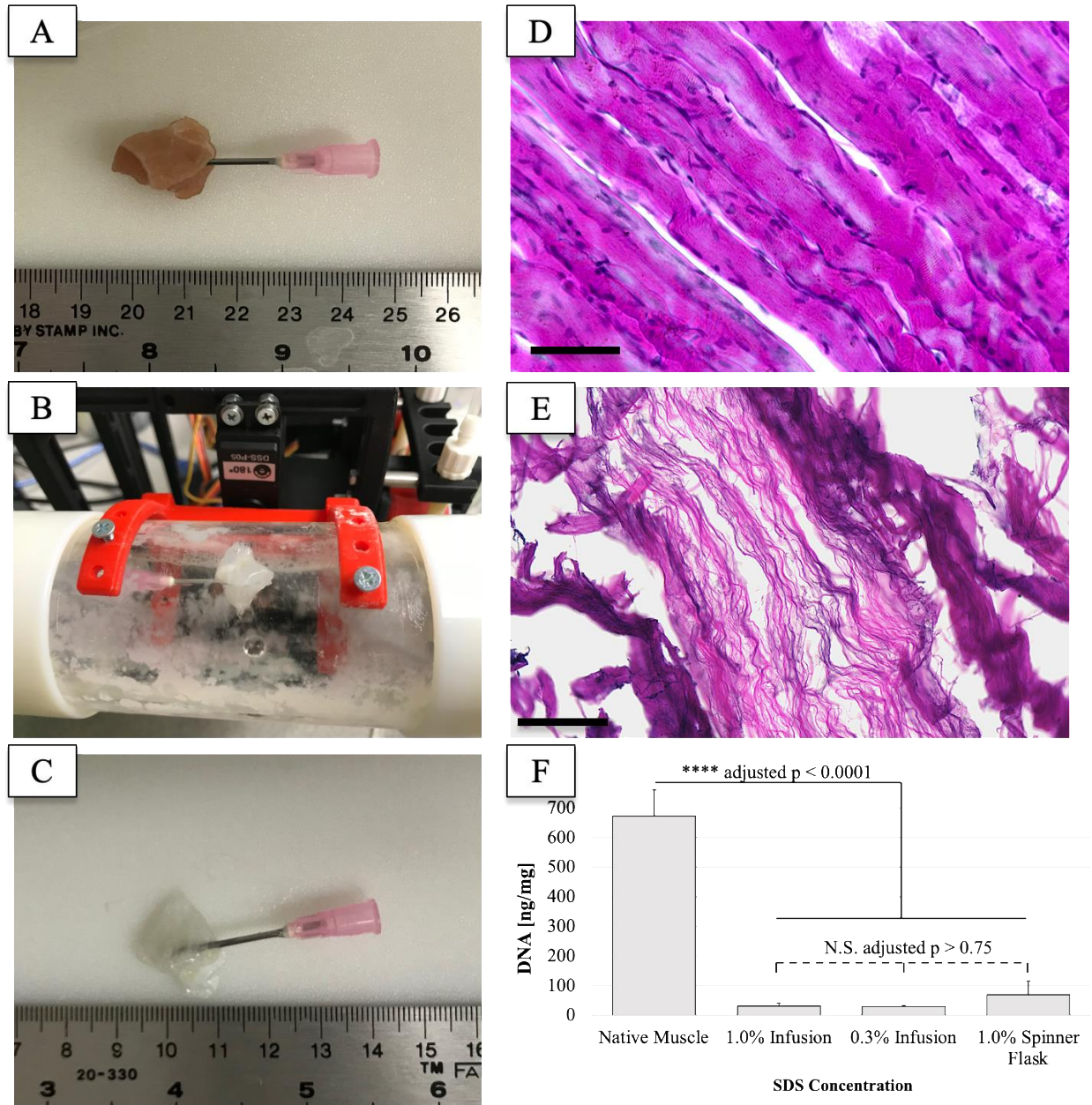


**Figure 54: Decellularization of Skeletal Muscle using the TIPD.**

A-C present the steps of skeletal muscle infusion decellularization, where a needle is inserted into the muscle body, the needle junction is affixed within the chamber, and after SDS-based infusion decellularization, the resulting muscle ECM becomes translucent. (D-F) H&E staining of native porcine muscle, confirmation of decellularization by H&E staining (scale bars: 100  $\mu$ m), and DNA quantification, respectively; compared with native porcine skeletal muscle, all decellularization processes resulted in significant DNA reduction, however, infusion decellularization was able to achieve this result in half the time and at a lower concentration of SDS.

#### 4.1.5 Discussion on Automated Systems for producing ECMs

Consistent with the open-source initiative (Pearce 2012), the TIPD has been designed as an OSH platform using components designed for replication via 3D printing (**Table 7, Table 8, Table 9, Table 10**) in conjunction with commercially-available hardware (see **Appendix B**). Two types of chambers are designed here, and though the Cylindrical Chamber is more easily constructed with 3D printed components, its leak-proof construction is nuanced. Though leak-proofing was achieved using the Raise3D printer, this required 100% infill and the highest quality print setting offered on the printer used. Since leak-proofing is an essential aspect of any fluidics devices, a commercially available and leak-proof component is offered here to avoid the potential difficulties when using FFF-printed components given the resolution and fusion variability between printers and filaments. Use of either chamber over the other for any given process or tissue type is discretionary since the critical component is the entrance and exit of fluid and not the vessel in which it is housed. Rotation of the two chamber types was integrated as a feature for the user to better control the posture of a tissue within a chamber. This is particularly relevant for preventing kinks or twists in tissue pedicles, which can induce thrombosis during perfusion (Zhan, Marre et al. 2016). If a user's application does not require such motion, these components can be subtracted from the system with no adverse effect on the function of the electronics or software. Driving these servomotors, the valve servomotors, and the stepper motors governing the peristaltic pumps, is an Arduino microcontroller, which was selected because it is an open-source electronics platform based on an IDE that allows for control of a myriad of devices capable of interacting with the external environment and shares a large developer community that has written, tested and published functional code (Margolis 2011, Oxaer and Blemings 2011). Though an Executable (.exe) has been formed from a LabVIEW VI file, the compilation of code and communication to the

hardware within the system is not limited to the provided VI alone. The VI that is provided, however, leverages integration of the components into a single GUI and transfers the processing from the microcontroller to a computer, which is more ideal for accomplishing non-repetitive tasks relative to a microcontroller.

Implementation of a peristaltic pump has been key for both infusion (Kasukonis, Kim et al. 2016) and perfusion tissue engineering bioreactors (Scarritt, Pashos et al. 2015). The TIPD is configurable such that either infusion directly into a tissue or perfusion of tissue vasculature can be achieved as shown through the decellularization of porcine skeletal muscle. The system was also used for the perfusion-based decellularization of rodent epigastric free flaps as well as a rodent kidney (**Appendix C**). Using the infusion technique, 48 hours less SDS exposure time was utilized to achieve similar residual DNA results, which could also be achieved with a lesser concentration of SDS. This may be of importance in the context of matrix preservation due to the cytotoxic nature of SDS (Caamano, Shiori et al. 2009), and its ability to denature collagenous fibrils of ECM in cases of prolonged exposure when assessed in decellularizing urinary bladder and tendon (Hwang, San et al. 2017). Since the muscle was frozen prior to decellularization (both spinner flask and infusion), the freeze/thaw cycle likely played a role in enhancing the decellularization processes at least somewhat; such mechanical disruption has been shown to assist decellularization when implemented repeatedly, though complete decellularization is only obtained with additional steps that include surfactant exposure (Gillies, Smith et al. 2011, Burk, Erbe et al. 2014, Roth, Glauche et al. 2017). In these instances of infusion decellularization of muscle tissue, the chamber was not filled with fluid to appreciate the infusion process and compare it to spinner flask decellularization. It is conceivable that infusion decellularization coupled with a fluid-filled chamber may facilitate increasingly rapid decellularization; this, however, requires further investigation.

Perfusion through the renal artery of a rodent kidney was achieved to show proof of concept for perfusion decellularization, where the resulting scaffold and H&E staining resulted in a translucent scaffold. Conceptually, the method of arterial cannulation and perfusion-based flow can be achieved in any vascular structure able to accommodate a port, but doing so in this specific system requires further investigation. Additionally, understanding the effects that fluidic shear imposes on the integrity or directionality of residual fiber alignment within a scaffold warrants additional investigation. Integration of infusion and perfusion capabilities into a single platform allows programmatic decellularization of tissue and organ types beyond what has been explored here. Decellularization of many tissue types do not establish vascular access, and therefore use spinner flask-based processes; such tissue types have included tendon (Lovati, Bottagisio et al. 2016), peripheral nerve (Choi, Kim et al. 2018), or cartilage (Duisit, Amiel et al. 2018), where an infusion process similar to what was done here with muscle segments could be used. While muscle was infused with an 18G needle punctured into the centroid of the scaffold, optimization to facilitate decellularization of additional tissue types would likely require adjusting needle size as the tissue segments change in size. Further, the addition of multiple points of entry would likely enhance infusion decellularization. Utilizing the same device, perfusion decellularization of solid organs via pedicle access is achievable, though the device would likely be better suited to have anatomically relevant outflows present (i.e., for the kidney, inflow into the artery and independent outflows from the vein and ureter). This could allow more direct control over the intra-scaffold pressure, and speculatively, may better maintain the scaffold architecture if drawing fluid from the outflow(s) using one or a series of peristaltic pumps.

#### 4.1.6 Limitations of the TIPD Design

While this innovation is promising, there are several limitations with the platform at hand. Additional complexity could be integrated into the device that more accurately controls flow rates or intra-scaffold pressures, which may increase the efficacy of decellularization and overall preservation of the vasculature network embedded within the matrix (Momtahan, Poornejad et al. 2015). Notably, it has been shown that intra-scaffold pressures better dictate successes in recellularization relative to constant flow velocities that do not adjust for pressure (Lichtenberg, Cebotari et al. 2006). Cold-perfusion decellularization of pancreatic tissue has shown improved retention of the vascular network relative to its ambient temperature counterpart (Elebring, Kuna et al. 2017). Modifying the device to include a cooling element within the chamber may function to achieve similar results, or alternatively the unit is of an appropriate footprint to fit inside a standard laboratory refrigerator. A paramount challenge in tissue engineering has been the development of a single, modular system that allows the versatility to decellularize tissues in the same device in which the tissues will be recellularized, tested, and subsequently transported for providing a functional tissue-engineered therapy at the point of care (Martin, Simmons et al. 2014). To do so, the unit as it stands will require modifications in terms of additional fluid handling capabilities, on-board monitoring of relevant quality characteristics, and pre-implantation metrics able to ensure that a scaffold is suitable for *in vivo* use. Additionally, the scale of this prototype as designed is best suited for applications in small organ and tissue decellularization and is therefore ill-suited for large animal/adult human organ engineering at present. This can largely be remedied by the reconstruction of the chambers to accommodate larger volumes as the pumps are able to achieve physiologically relevant flow velocities for larger organs. Despite its limitations, the platform described here is suitable for creating repeatable decellularization processes and is readily

expandable with the litany of components that are commercially available for significantly expanding the current capabilities of the device.

## **4.2 Application of Intramuscular Skeletal Muscle Derived ECM for Mitigating Denervation Atrophy**

The 6-week pilot study comparing various muscle and nerve therapies showed gastrocnemii injected with d-skECM were able to recover significantly more force than any other intramuscular injection. Additionally, the d-skECM cohort showed in gait analysis by SFI, a positive linear trend towards healing, where the regression (slope) was strongest relative to all other conditions receiving an intramuscular injection (see **Section 2.5.3.3 Contraction Force Analysis**). Leveraging the denervation model by sciatic nerve transection and immediate repair, two unique preparations of skECM were compared to Control (nerve repair only). These preparations of skECM were a micronized, particulate format (p-skECM) and the other was a pepsin-digested format (d-skECM). The process for rendering skECM was based on previously published protocols (Ungerleider, Johnson et al. 2015), though a peracetic acid (PAA, 1% [v/v]) disinfection step is added to the process after decellularization given the sterility requirement of FDA-regulated ECMs, being medical devices (Yoganarasimha, Trahan et al. 2014). Further, the process of making a particulate skECM reduces time in the overall process, and lessens the handling time of the preparation, reducing the probability of contamination after the disinfection process. These skECM preparations will elucidate homologous use cases of skECM, that is, an ECM of skeletal muscle being injected into skeletal muscle rather than an ECM of some other tissue-based origin.

## 4.2.1 Methods

### 4.2.1.1 Decellularization of Porcine Skeletal Muscle

**Figure 55** displays the flow process to create skECM. Skeletal muscle was harvested from the hindlimbs of recently-deceased Yorkshire pigs, aliquoted into 20-gram batches, and then frozen at  $-80^{\circ}\text{C}$  until processing. Prior to chemical exposure, all muscle was cut into segments approximately of  $1\text{cm}^3$ . Muscle segments were processed in an Erlenmeyer flask at a mass to solution ratio of 1g tissue to 10ml solution; this mass-to-solution ratio was maintained throughout the decellularization process. All processes through disinfection were performed under constant rotation of a spinner flask. SDS, Triton X-100, and PAA solutions were all 1% concentration in DI water [ $w/v$ ] (all chemicals, Millipore Sigma, St. Louis, MO). PAA-based disinfection and all subsequent processes were performed aseptically, in a biosafety cabinet, to maintain sterility. After disinfection rinses of 1xPBS and DI water ensued, where PAA was considered sufficiently removed when colorimetric PAA test paper no longer reacted with rinsate (MQuant, 5-50 mg/L PAA, Millipore Sigma), typically after four rinses in 1xPBS and an additional two to four rinses in DI water.

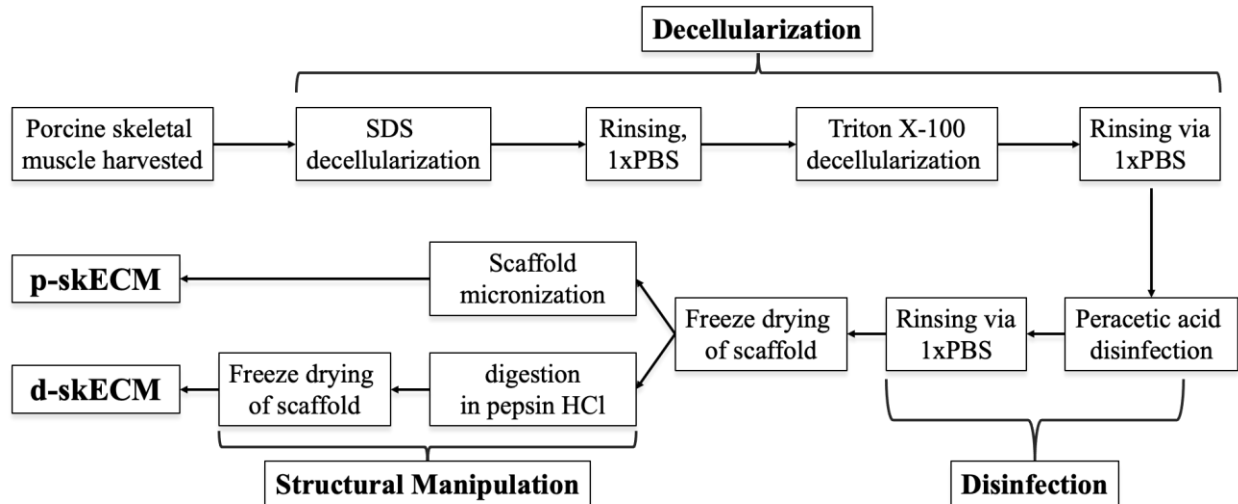


**Figure 55: Flow Diagram to for Production of skECM.**

After thoroughly rinsing the skECM, it was frozen overnight at  $-80^{\circ}\text{C}$  in preparation for freeze drying, which was performed for 20-24 hours (FreeZone 2.5 Liter Benchtop Freeze Dryer, Labconco, Kansas City, MO). The freeze-dried skECM then diverged for preparing either p-skECM or d-skECM. For p-skECM, the freeze-dried skECM was milled into a fine particulate (A11 Basic Analytical Mill, IKA, Wilmington, NC). For preparing d-skECM, the freeze-dried skECM was digested in a pepsin hydrochloride solution (HCl), being 10mg pepsin per 1mg tissue dry weight in 1N HCl; the digestion process occurred under constant spinning in an Erlenmeyer flask for 72 hours, after which the d-skECM was titrated to neutral with 10xPBS and again frozen at  $-80^{\circ}\text{C}$  and freeze dried. Both skECM preparations were sealed and stored at ambient temperature until rehydration and injection. Rehydration was performed at 8% [w/v], that is 8mg d-skECM to 92mg USP injectable saline. The process of making the d-skECM is identical to the process as shown in **Figure 26**.

#### **4.2.1.2 Scanning Electron Microscopy**

skECM samples were prepared for scanning electron microscopy (SEM) via hydration to their target injection concentration of 8% [w/v]. All samples were then frozen at -80°C at which point they could be cryo-sectioned at 8µm onto glass slides. The mounted samples were then fixed in 10% neutral buffered formalin, rinsed in 95% ethanol and then rinsed with water (via 60-second submersions). Slides were dried at ambient temperature prior to sputter coating. Sputter coating and SEM were performed on native porcine muscle and both preparations of skECM at the Nanoscale Fabrication and Characterization Facility (NFCF, University of Pittsburgh, Pittsburgh, PA). Cryo-sectioned samples were sputter coated with a gold/palladium mixture for 60 seconds at 20 milliamperes (Desk V TSC Turbo Molecular-Pumped Sputter Coater, Denton Vacuum, Moorestown, NJ). SEM was performed on coated samples at 200x and 500x magnifications (Zeiss Sigma VP, Oberkochen, Germany).

#### **4.2.1.3 Transection Injury to the Sciatic Nerve and Intramuscular skECM Injection**

To induce injury to the sciatic nerve (n=24), the surgical site was prepared by shaving the fur with an electric razor. The sciatic nerve was accessed via 2 cm transverse incision at the inguinal region of the right hindlimb (all injuries were performed on the right hindlimb and the left hindlimb was left as the uninjured contralateral). The gluteus muscle was dissected to expose the sciatic nerve, and injury was induced by transecting the nerve approximately 0.5cm from the bifurcation. The transection was repaired with 9-0 nylon microsuture (Microsurgery Instruments, Inc., Bellaire, TX) and the wound opening was then closed with 5-0 absorbable suture (Ethicon, Somerville, NJ).

Rodents received one of two intramuscular therapies, being either p-skECM (n=8) or d-skECM (n=8). Approximately 0.50cc of either skECM preparation was injected into the

gastrocnemius immediately after closure of the wound. The needle was inserted through skin at the base of the Achilles tendon, extending proximally on the hindlimb and therapy was injected over approximately five passes. **Figure 56** illustrates relevant anatomy of the rodent hindlimbs, where all rats had one limb (Contralateral) unoperated and the other transected (Injury). The Control limbs (n=8) were not manipulated.

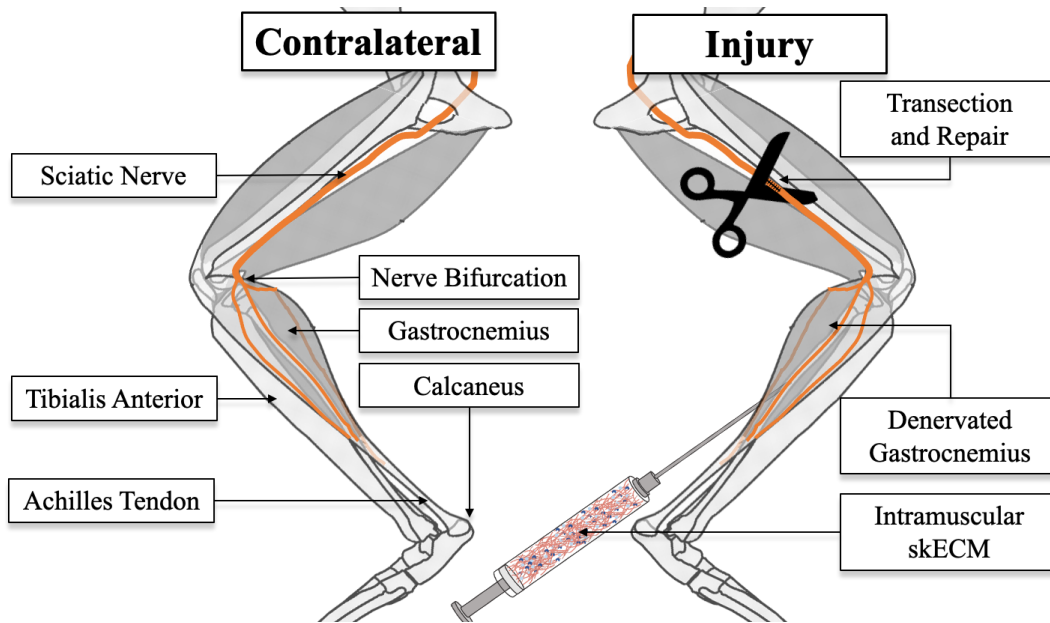


**Figure 56: Illustration of Anatomy and skECM Injection Therapies Rendered.**

#### 4.2.1.4 Walking Track Analysis

SFI was performed consistent with the previous methods described here with the fabricated walking track described in **Section 2.3**. Briefly, each rodent's hind-feet were coated with water-soluble paint, which imprinted footprints onto the paper laid into the track. Six footprints per walk were used to calculate SFI. Evaluators were blinded to groups prior to walking. Unfortunately, due

to closures and facility restrictions prompted by COVID-19, only two points of gait analysis were collected, being at the start of the study (Week 1) and at the end of the study (Week 20).

#### **4.2.1.5 Contraction Force Measurement**

Each rodent was sedated in 2% isoflurane in oxygen, the gastrocnemius was dissected by cutting the calcaneus, and then securing the bone to a load cell. A custom gantry was used to secure the knee. Briefly, nerve cuffs (1cm length) were fabricated from 1/16" ID Tygon tubing (McMaster-Carr 5155T12); two de-insulated wires (Cooner Wire AS-631) were inserted through tubing and glued into place 5mm apart (see **2.4.2 Fabrication of Stimulation Cuffs** for additional details). Stimulation was induced by stimulus isolator at 0.50mA (A320, World Precision Instruments, Sarasota, FL), and the contraction force of the load cell was read via MyDAQ coded in LabVIEW (NI, Austin, TX). Optimum fiber length was established by tensioning gastrocnemii until the highest twitch force was established. Tetanic force generation was induced via stimulations of 1Hz, 10Hz, 20Hz, 30Hz, 40Hz, 50Hz, 60Hz, 70Hz, 80Hz, 100Hz, and 150Hz over a 1 second duration. After stimulations of  $\leq 80$ Hz, 40 seconds of rest was allocated, and at 100Hz and 150Hz, 60 seconds were allocated (see **2.4 Development of an Electrophysiology System Capable of Measuring Contraction Force** for additional details). Animals were euthanized via CO<sub>2</sub> asphyxiation on completion of electrophysiology, and their gastrocnemii and TA muscle harvested from both hindlimbs for mass measurements, protein quantification and histological staining.

#### **4.2.1.6 Histology**

After sacrifice at 20-weeks postoperatively, the gastrocnemii were isolated and removed from both hindlimbs, weighed, and then stored at -80°C. For histology, 8 $\mu$ m cryo-sections were

cut and mounted from frozen blocks. Slides were stained with Masson's trichrome (American MasterTech, Lodi, CA), and Oil Red O (O0625, Millipore Sigma), each per manufacturer's instructions. All images were captured on using BZ-X800 Biological Microscope (Keyence, Itasca, IL).

#### **4.2.1.7 Protein Quantification**

Samples were minced with fine surgical scissors and then were extracted in 4M guanidine HCl in 0.05M Trizma Base (both Millipore Sigma, St. Louis, MO) at an approximate ratio of 1 gram tissue per 5ml extractant over three days, inverting constantly. Samples were exposed to 2.5ml extractant over the first 24 hours and then an additional 2.5ml extractant over the following 48 hours. Extractants were combined, purified using 15k MWCO filtration columns (4,200 RPM for 30 minutes at 4°C), and then reconstituted in 1xPBS (diluted 1:4). Quantification of GM-CSF, IFN- $\gamma$ , IL-1 $\beta$ , IL-4, IL-6, IL-10, IL-13, IL-18, TIMP-1, TNF- $\alpha$ , and VEGF was performed using a Luminex assay (LXSARM-12, R&D Systems, Minneapolis, MN) via Bio-Plex 200 (Bio-Rad, Hercules, CA). Enzyme-linked immunosorbent assays (ELISA) were used to quantify IGF-1 (MG100, R&D Systems) and muscle skeletal receptor tyrosine-protein kinase (MuSK, MBS943725, MyBioSource, San Diego, CA). Absorbance from both ELISAs were measured using a Tecan Infinite 200 Pro (Switzerland) plate reader at 450nm with wavelength correction at 570nm.

#### **4.2.1.8 Statistical Analysis**

JMP Pro (Cary, NC) was used for all analyses. Robust ANOVA with Bonferroni *post hoc* corrections were used for comparing SFI measurements as well as for comparing muscle masses. Repeated Measures ANOVA with Tukey HSD *post hoc* was used to compare force output. In both

uses of ANOVA, normality of residuals were verified with a Shapiro-Wilk W test prior to analyses. Comparisons were considered significant at  $p < 0.05$ . For goodness of fit, correlations above  $R^2 > 0.75$  were considered strong, correlations within  $0.75 \geq R^2 \geq 0.25$  were considered moderate, and correlations with  $R^2 < 0.25$  were considered weak.

## **4.2.2 Results from skECM**

### **4.2.2.1 Ultrastructure of Porcine Muscle and skECM**

**Figure 57** displays the surface topography and structure of native porcine muscle, p-skECM and d-skECM via SEM at 200x and 500x magnifications. The myofiber striations can be appreciated in the native porcine muscle, indicative of the normal skeletal muscle structure. Both p-skECM and d-skECM image sets occur after substantial chemical exposure through the decellularization, disinfection, and digestion (d-skECM) processes. From these, it can be seen that the resulting p-skECM is a porous scaffold with few loose fibrillar strands; conversely, the d-skECM scaffold is shown as increasingly weblike relative to the p-skECM, where the pores are more akin to a collagenous meshwork.

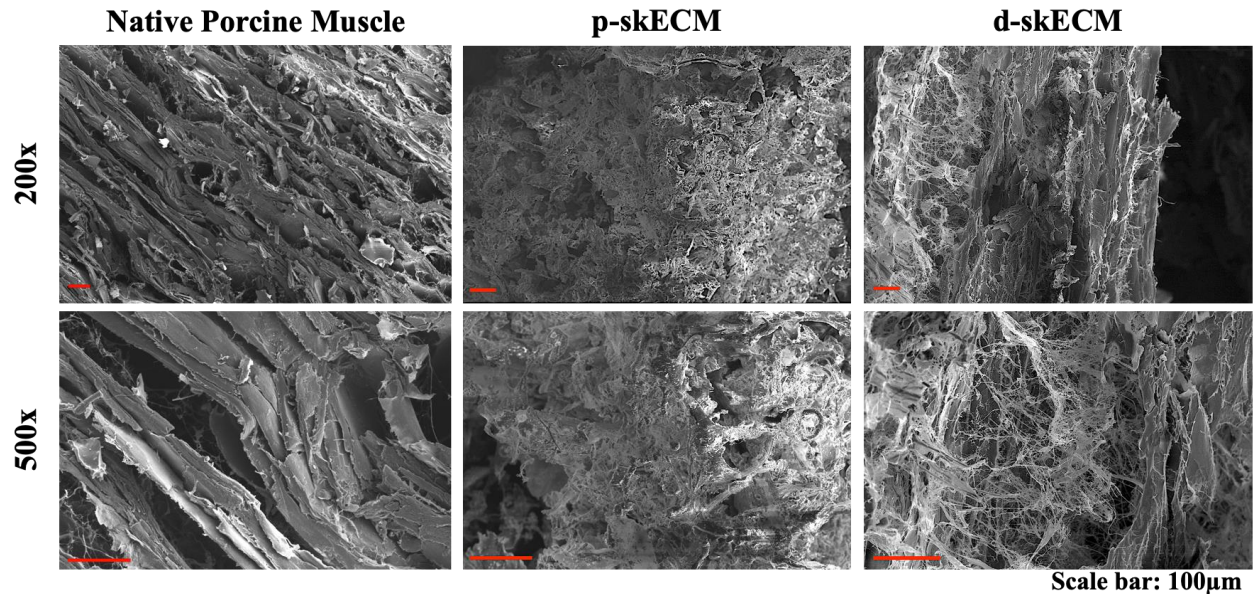


**Figure 57: SEM of Native Muscle, p-skECM, and d-skECM.**

#### 4.2.2.2 Walking Track Analysis

Results of the walking track analysis are presented in **Figure 58**, displaying representative pawprints from the Contralateral and Injury Conditions at Weeks 1 and 20. In all cohorts, there was improvement of SFI within each Cohort over the 20-week study, with the control showing the least significant increase ( $p=0.049$ ) relative to the skECM Cohorts, where both showed more significant recovery (both,  $p<0.0001$ ). Both skECM preparations resulted in significantly higher SFI values at 20 weeks when compared to Control at 20 weeks, (both,  $p<0.001$ ). Resulting SFI from the skECM preparations were not significantly different from one another ( $p=0.573$ ), where the fidelity in toe-spread can be appreciated in the representative images at 20 weeks, especially when compared to that of the Control. Additionally,  $R^2$  values trend better toward linear correlation in the skECM Cohorts (both moderately correlated, that is  $0.75 \geq R^2 \geq 0.25$ ) relative to control (weakly correlated, that is  $R^2 < 0.25$ ).

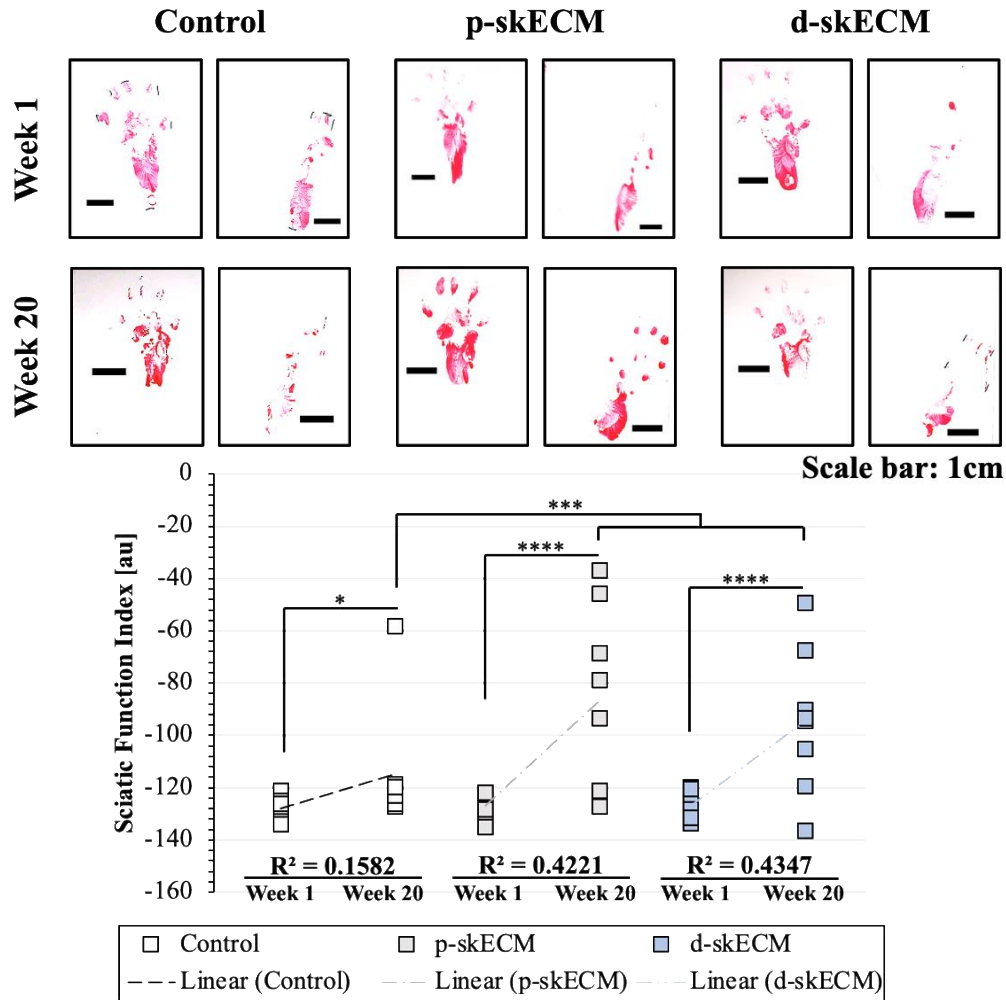


Figure 58: Representative Pawprints and Resulting SFI Analysis.

Ink-imprinted pawprints at Week 1 and Week 20 (top) with results from SFI across Cohorts.

Boxes are individual measurements, \* $p < 0.05$ , \*\* $p < 0.01$ , \*\*\* $p < 0.001$ , \*\*\*\* $p < 0.0001$ .

#### 4.2.2.3 Gastrocnemii and TA Muscle Mass Analysis

Figure 59 presents the gastrocnemii and TA masses, where the injured muscle is normalized to the contralateral (left) as well as normalized to the overall rodent body mass (right). As shown, there is statistical difference in cohorts' gastrocnemii when normalizing either by the contralateral or the body mass; animals treated with d-skECM were shown to have significantly higher massed gastrocnemii relative to control ( $p < 0.01$ ) when normalizing by the contralateral

gastrocnemius mass, though this comparison does not hold when normalizing to the body mass of the rodent (no significance when comparing groups). When comparing TA normalizations however, the trends are not affected; as shown in both normalizations of the TAs downstream of the sciatic nerve transection, both cohorts receiving an skECM injection into the gastrocnemius resulted in larger TA muscles than the Control (all,  $p < 0.001$ ). No statistical differences were shown between the two cohorts receiving skECM preparations regardless of normalization. Note that no manipulation was performed on the TA muscles, and the skECM preparations were injected into the gastrocnemius only.

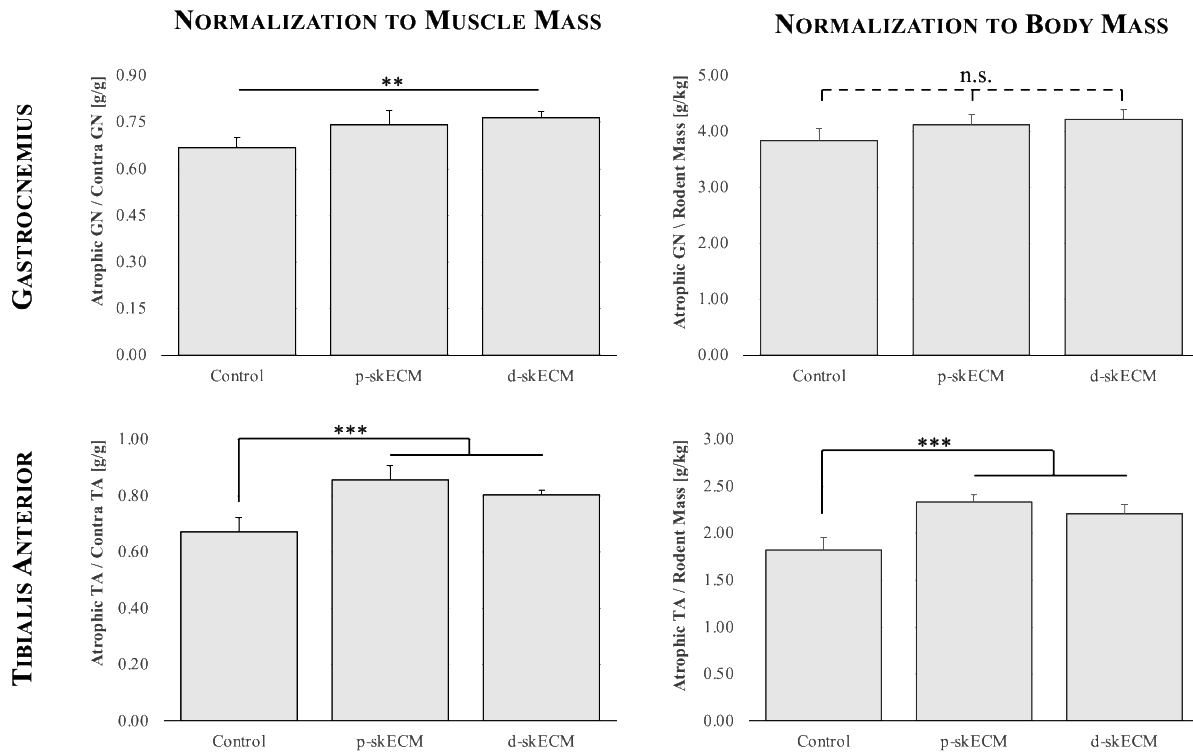


**Figure 59: Gastrocnemii and TA Mass Normalizations.**

Denervated (injured) Gastrocnemii or (top) TA (bottom) normalizations are to the respective contralateral muscle (left) or to the rodent body mass (right). Mean  $\pm$  SEM, \* $p < 0.05$ , \*\* $p < 0.01$ , \*\*\* $p < 0.001$ , \*\*\*\* $p < 0.0001$ .

#### 4.2.2.4 Muscle Contraction Force

**Figure 60** and **Figure 61** present the force outputted by gastrocnemii normalized by the rodent body mass as well as normalization based on the mass of the gastrocnemius, respectively. In both figures, frequency sweeps (left) and the tetanic contraction forces (right) are shown, where stimulation of the sciatic nerve at 100Hz induced the strongest contraction force of the contralateral, uninjured gastrocnemii. When normalized to the rodent body mass (**Figure 60**), it can be seen in the frequency sweep that the Contralateral gastrocnemii were able to generate more force compared to any other group. In the chart breaking out the force generated at 100Hz

stimulation, the contraction force generated by Contralateral gastrocnemii was significantly greater than Injury Control ( $p < 0.0001$ ) and p-skECM-treated ( $p = 0.030$ ) gastrocnemii. Body mass-normalized force *was not* different, however, from d-skECM-treated ( $p = 0.105$ ) gastrocnemii.

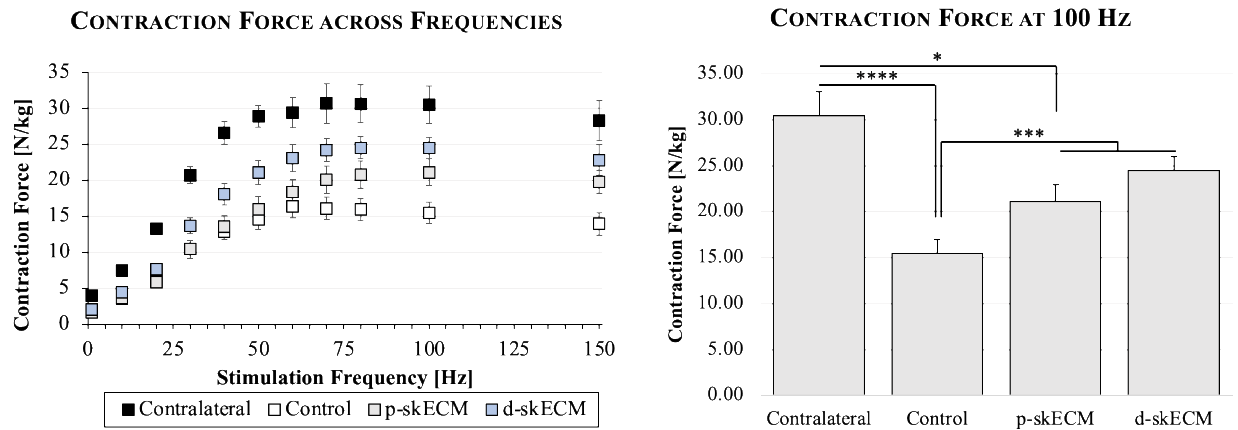


**Figure 60: Gastrocnemii Contraction Force Normalized to Rodent Body Mass.**

Force generated across all stimulation frequencies (left) and force generated at maximum (right).

Mean  $\pm$  SEM, \* $p < 0.05$ , \*\* $p < 0.01$ , \*\*\* $p < 0.001$ , \*\*\*\* $p < 0.0001$ .

In contrast to the frequency sweep shown in **Figure 60**, the frequency sweep in **Figure 61** shows the maximum gastrocnemius-normalized force is not generated by Contralateral muscles, but rather is generated by gastrocnemii having been treated with d-skECM, albeit not significantly greater. At the maximum contraction force, only d-skECM-treated gastrocnemii showed significantly greater force generation relative Control ( $p = 0.033$ ). No differences were presented in any other comparisons ( $p \geq 0.133$  for each comparison).

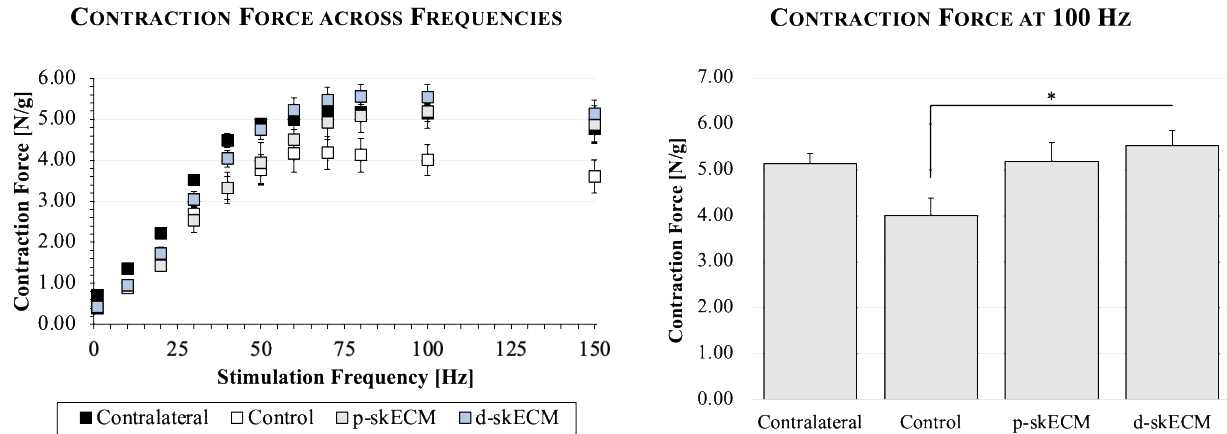


**Figure 61: Gastrocnemii Contraction Force Normalized to the Gastrocnemius Muscle.**

Force generated across all stimulation frequencies (left) and force generated at maximum (right).

Mean  $\pm$  SEM, \* $p < 0.05$ , \*\* $p < 0.01$ , \*\*\* $p < 0.001$ , \*\*\*\* $p < 0.0001$ .

#### 4.2.2.5 skECM Histology

**Figure 62** displays representative Masson's Trichrome staining of gastrocnemii. Imaging of the entire field is presented for each Condition, as well as magnified images of areas of interest. In trichrome staining, healthy muscle appears as red with degenerating fibers staining a lighter red relative to the healthy muscle. Collagens/fibrous tissue appear blue with necrotic tissue staining a deeper blue relative to normal fibrous tissue, and nuclei appear as deep purple/black puncta. From the images, it can be seen that the muscle fibers appear of a similar red color across all groups, with perhaps the Control cohort appearing a slightly deeper red than the other conditions. Stranding fibrosis was present most abundantly in the Control cohort. The p-skECM conditions presented blue staining atop, and perhaps with the myofibers; this may be remnants of the injected skECM, though in the d-skECM cohort, this architecture was not observed as pervasively.

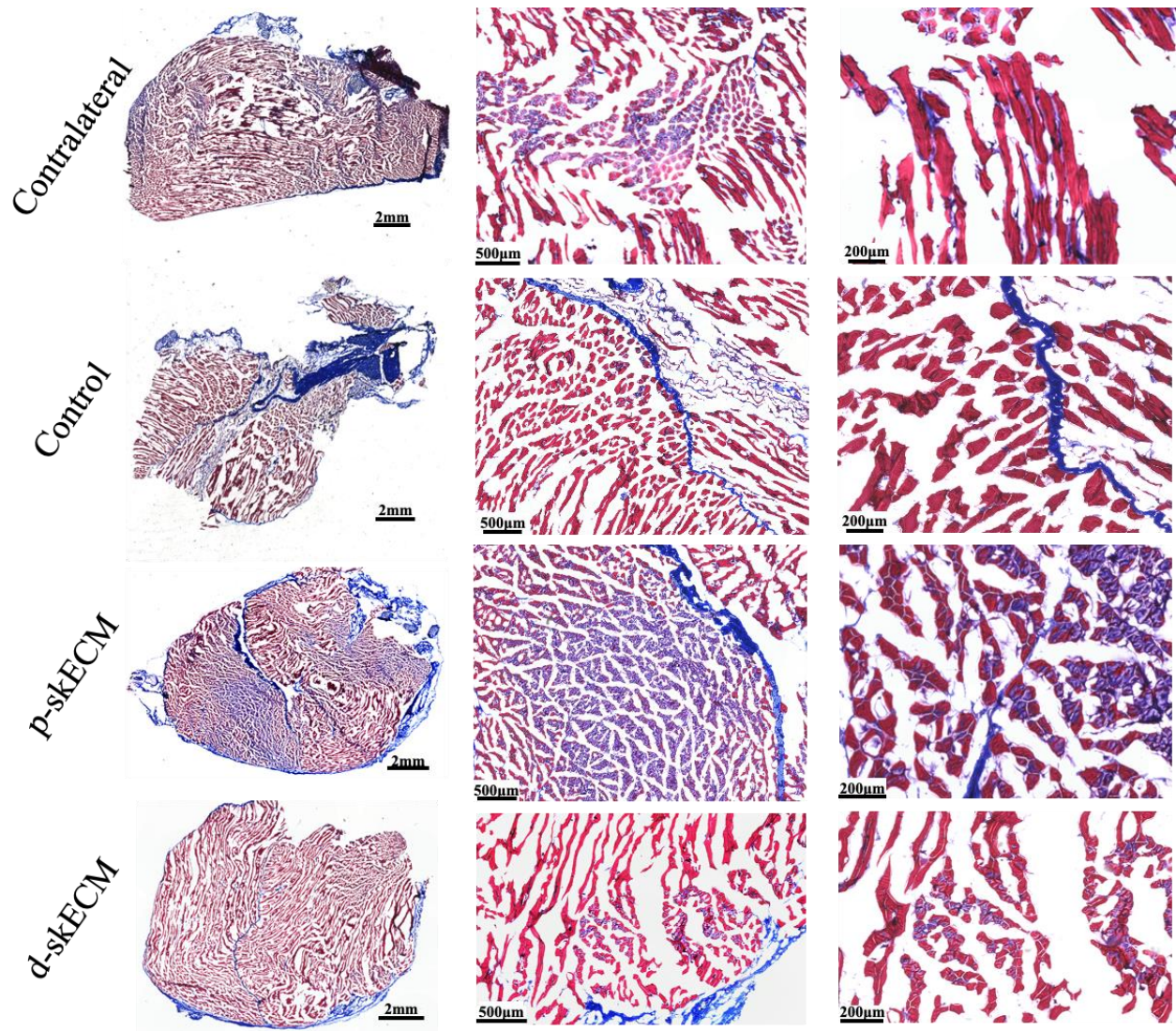


**Figure 62: Masson's Trichrome Staining of Gastrocnemii.**

**Figure 63** displays representative Oil Red O (red) staining for lipid content accumulated in the gastrocnemii. The Contralateral gastrocnemii and those gastrocnemii injected with d-skECM appeared similar in their lipid content, where Oil Red O-positivity can be seen at the periphery of the muscle; lipid deposits, however, were not totally eliminated by the treatment of gastrocnemii with d-skECM, as shown in the magnified section. Both the p-skECM and Control cohorts presented significantly more lipid accumulation relative to the d-skECM cohort. These lipid

deposits were present both at the periphery of the muscle segment as well as within the muscle itself.

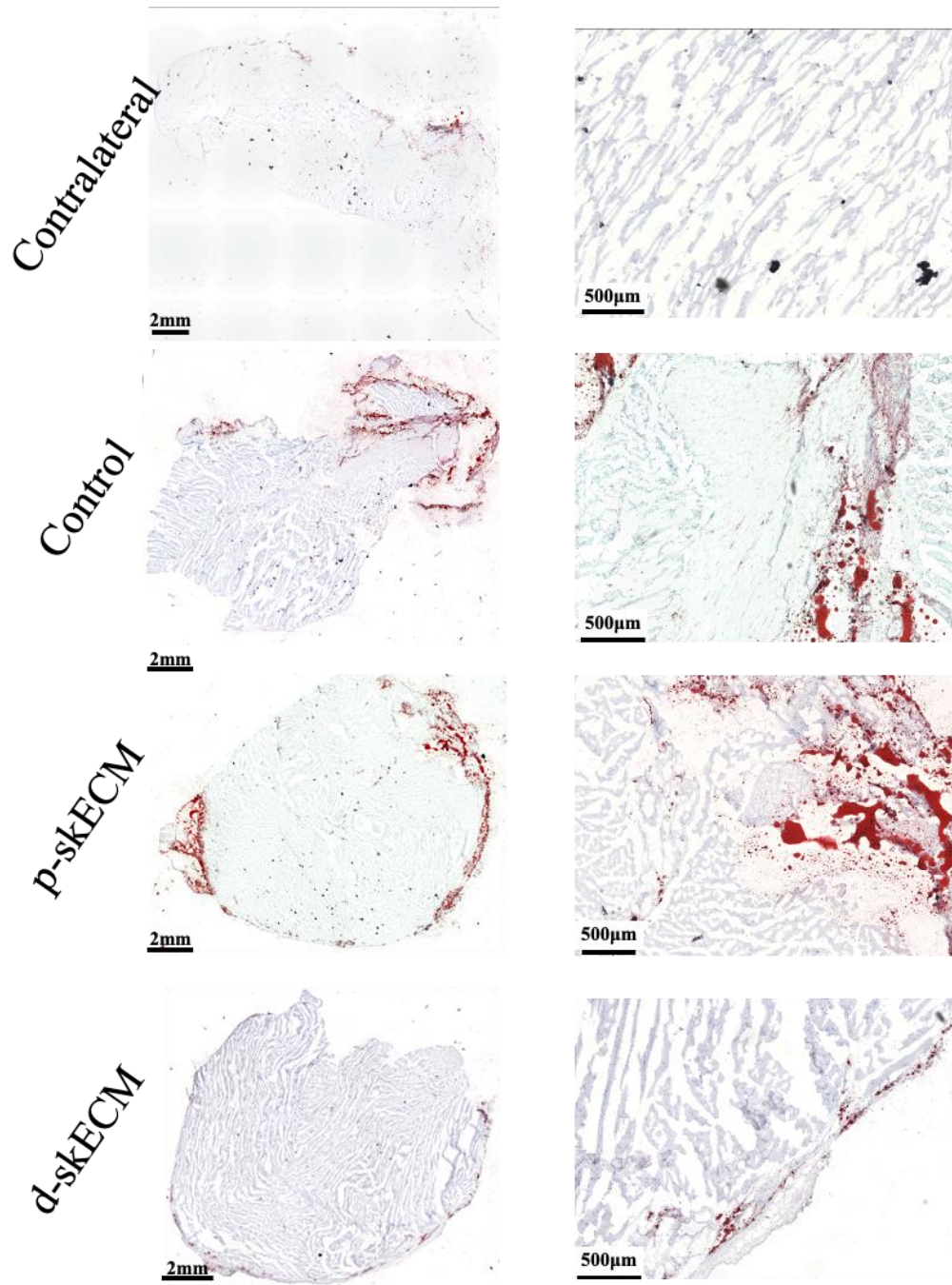
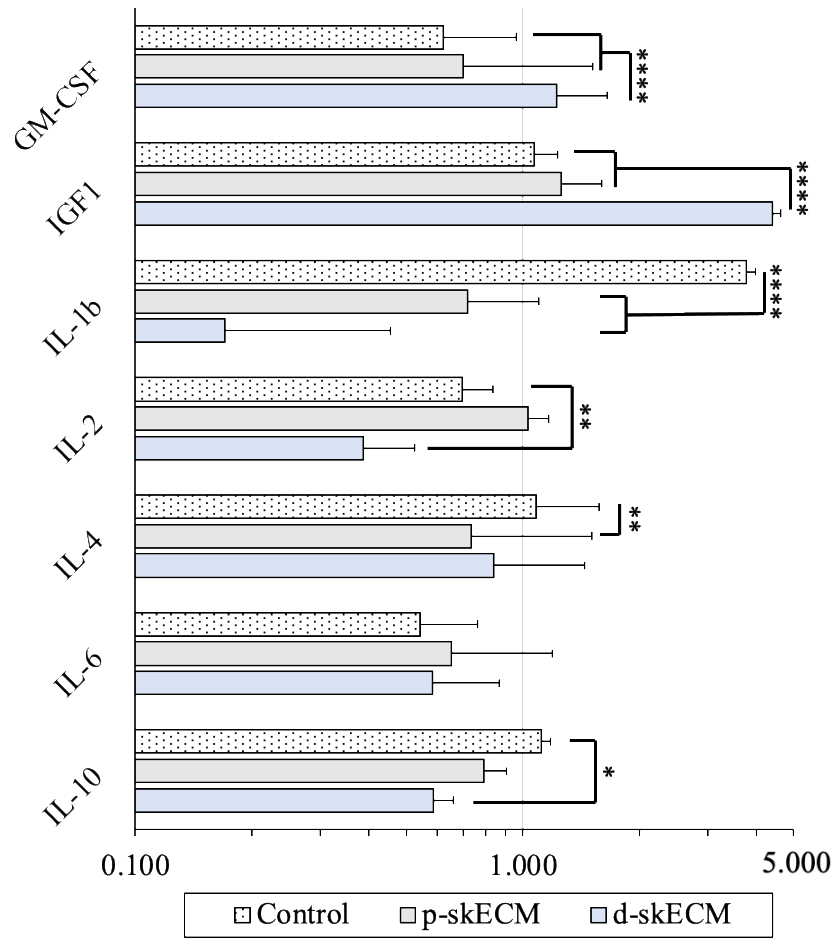


Figure 63: Oil Red O Staining of Gastrocnemii.

#### 4.2.2.6 Quantified Proteins in Gastrocnemii

**Figure 64** and **Figure 65** present growth factors and cytokines quantified in the gastrocnemii, ordered alphabetically between the two figures. The values are shown as normalizations to the protein concentration of the respective cohorts' contralateral gastrocnemii. **Figure 64** and **Figure 65** show the cohort injected with d-skECM having significantly higher expression of GM-CSF and IGF-1 relative to both Control and p-skECM cohorts. Control gastrocnemii showed significantly higher expression of IL-1 $\beta$ , IL-18, IFN $\gamma$ , TIMP-1, and TNF $\alpha$  relative to both p-skECM and d-skECM. Control gastrocnemii showed significantly higher expression of IL-4 and IL-13 compared to the p-skECM cohort only; Control gastrocnemii showed significantly higher expression of IL-2 and IL-10 compared to the d-skECM cohort only. Significant differences in relative expressions between p-skECM and d-skECM cohorts were shown in with GM-CSF and IGF-1 only.



**Figure 64: Cytokines in skECM-Injected Gastrocnemii (Set 1 of 2).**

**Mean ± SEM, \*p<0.05, \*\*p<0.01, \*\*\*p<0.001, \*\*\*\*p<0.0001.**

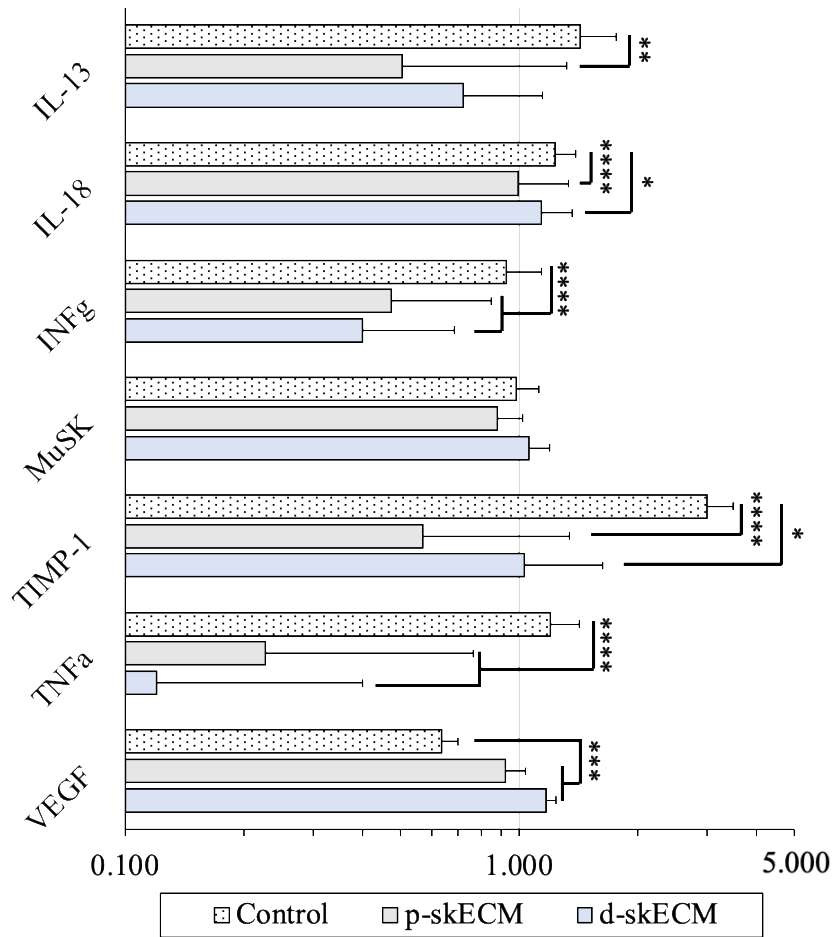


**Figure 65: Cytokines in skECM-Injected Gastrocnemii (Set 2 of 2).**

Mean ± SEM, \*p<0.05, \*\*p<0.01, \*\*\*p<0.001, \*\*\*\*p<0.0001.

### 4.2.3 Discussion

Atrophic muscle after a denervation injury can be physically characterized by a reduction in bulk mass due to shrinkage of individual muscle fibers (Wang and Pessin 2013). This is accompanied by a loss in muscle power, which may be accompanied by and accelerated from collagenous deposition (Lieber and Ward 2013). Concomitantly, these phenomena cause

significantly altered mechanical and biochemical properties relative to the pre-atrophied state. Normal muscle possesses a stiffness of approximately 12 kPa and several groups have shown that varying substrate stiffness outside the 5-20 kPa range significantly decreases satellite cell capacity for both proliferation and differentiation (Engler, Griffin et al. 2004, Cosgrove, Sacco et al. 2009). Additionally, fibrotic muscle can reach stiffnesses up to 30 kPa (Yong, Li et al. 2016), adversely impairing the ability of satellite cells to regenerate the atrophic muscle and decreasing its contractile potential (Lacraz, Rouleau et al. 2015). Based on this, it is perhaps unsurprising that poor myoblast survival in the damaged muscular environment has been attributed to damaged ECM (Sacco, Doyonnas et al. 2008), even though the ECM only comprises approximately 5% of the overall muscle mass relative to its other constituents, predominantly the muscle fibers, and to a lesser extent, vasculature and resident cells (Light and Champion 1984).

In an effort to restore properties of the normal mechanical environment within the atrophic muscular environment, two preparations of injectable skECM were created and injected into the gastrocnemii of rodents having undergone a sciatic nerve transection, inducing denervation atrophy. Porcine skeletal muscle was prepared in a particulate and a digested preparation per **Figure 55**, where the principal differences is the exposure of particulate skECM to a pepsin-based solution for three days, titrating the solution to neutral, and then freeze-drying the preparation. While d-skECM has been shown to increase angiogenesis and cell survival in a rodent ischemia model (Rao, Agmon et al. 2017) and increase satellite cell differentiation (Zhang, Zhang et al. 2017), a digested preparation has not been examined against its non-digested counterpart. Comparison between ECM preparations is exceedingly important, particularly from a regulatory and translational perspectives. Though particulate or powdered ECMs are clinically marketed currently (Edgar, Altamimi et al. 2018), digested ECMs enjoy the majority of academic focus

(Saldin, Cramer et al. 2017). In fact, studies directly comparing particulate ECM to a digested ECM are exceedingly rare, having been performed in bone ECM, and shown to attenuate the M1/M2 macrophage infiltrate *in vivo* (Wu, He et al. 2019).

Throughout the skECM process, the ultrastructure of the protein structure changes substantially. **Figure 57** displays SEM of native muscle as well as of both preparations of skECM. The skECM loses the striated, myofibrillar appearance in both cases relative to the structure of native muscle, which is unsurprising given the processes as a whole. The appearance of the skECM preparations are increasingly porous relative to the native muscle, where p-skECM exhibits porous similar to a collagenous sponge and the d-skECM exhibits fibrillar strands, both being consistent with the structures of other skECM prepared similarly (Gillies, Smith et al. 2011, Lee, Ju et al. 2020). Despite differences in morphology, both were wetttable materials, readily hydrating in saline prior to their injection.

Gait analysis via SFI, showed significant differences between the groups, compared both in terms of their linear fit ( $R^2$ ) as well as using robust ANOVA. Though previous studies involving intramuscular Nanofat and d-skECM injections after sciatic nerve laceration did not show significance in SFI (see **Figure 29** and **Figure 37**) between cohorts, both skECM preparations showed significantly improved SFI relative to Control (**Figure 58**,  $p < 0.001$ ). There are at least two possibilities for this result in significant SFI, being statistical analysis type (robust ANOVA) and duration of the study. The robust ANOVA was used here to reduce the effect of outliers within the data; this method also reduces the influence of large coefficients of variation when comparing means. Historically, SFI calculation has been prone to large discrepancies between animals, illustrated in both skECM cohorts in the scatter plot of **Figure 58**, where approximately half of the animals in each group healed well, but deviated largely from those that did not. This study was

also 8 weeks longer than the Nanofat study, where the healing time alone may have favorably impacted restoration of SFI. Time alone as the contributing factor to increasing SFI seems unlikely, however, given the continued impairment shown in the Control cohort relative to those injected with either skECM preparation.

Analyzing contraction force resulted in two distinctly different trends when normalizing by the overall mass of the rodent (**Figure 60**) versus the mass of the gastrocnemius responsible for the force generation (**Figure 61**). Based on normalization by rodent body mass, the force generated by contralateral gastrocnemii differed from Control ( $p < 0.0001$ ) and p-skECM ( $p = 0.0490$ ) cohorts but did not differ from the d-skECM cohort ( $p = 0.1050$ ). In a study leveraging a muscle defect to the gastrocnemius with a bulk skECM repair, approximately 80% of the gastrocnemius force was returned relative to contralateral gastrocnemii at 6 weeks (Merritt, Hammers et al. 2010). A similar return to function which is confirmed in this skECM study, as well as in the previous study using Nanofat (see **Figure 32**); notably, there was no defect rendered to the nerve, rather only a partial laceration to the gastrocnemii themselves. Full lacerations damaging the muscle as well as the local nerve showed more variable returns of force, being approximately 40%-80% of the contralateral (Pereira, Tan et al. 2006, Crow, Haltom et al. 2007).

Interestingly, the contraction force normalization based on the gastrocnemius mass does not maintain the statistical trend that is shown when normalizing by the body mass (**Figure 61**). This discrepancy was shown even most distinctly at the 9-week time point in the intramuscular Nanofat injection study (**Figure 42**), where the Nanofat-injected gastrocnemii were able to generate significantly more force than all other comparisons, including the contralateral gastrocnemii. This phenomenon appeared to diminish as regeneration continued, perhaps reaching stasis (e.g., 12 weeks to 20 weeks, **Figure 42B,D** and **Figure 61**, respectively).

Despite the discrepancies in ultrastructure morphology shown in SEM, both skECM preparations performed similarly in restoring force generation as well as with the relative expressions in growth factors/cytokines (**Figure 64** and **Figure 65**), only differing significantly in the relative concentrations of GM-CSF and IGF-1, where GM-CSF is responsible for recruitment of M1-like macrophages responsible for healing damaged muscle (Martins, Gallo et al. 2020), and IGF-1 has a direct and well-established role in muscle hypertrophy (Glass 2003). Since digestion will produce a unique profile of cryptic molecules, some of which possess bioactive properties, it is possible that these unique properties of the d-skECM were increasingly available to have paracrine effects on the local cellular environment (Agrawal, Kelly et al. 2011, Agrawal, Tottey et al. 2011). Alternatively, the host-material interface has been shown to be a mediator of paracrine signaling as well based on the topography of the biomaterial being implanted (Su, Gao et al. 2017, Zhang, Hwang et al. 2017), where perhaps the reduced lipid expression result from continued expression of GM-CSF and IGF-1 in the d-skECM cohort relative to the p-skECM cohort. In the canonical PI3K/AKT/IGF-1 pathway, binding of IGF-1 excreted from damaged myoblasts activates AKT phosphorylation for continued protein synthesis from myofibers. SCs asymmetrically divide, either self-renewing or differentiating and fusing into new myofibers, restoring damaged muscle and therefore limiting lipogenesis (Mourkioti and Rosenthal 2005). Despite IGF-1 being more significantly expressed in the d-skECM-injected cohort, however, the return of force was not returned substantially.

Gastrocnemii injected with skECM preparations showed significantly higher expression of VEGF relative to the Control cohort. VEGF is well known as an important molecule in angiogenesis. VEGF overexpression has been used as a therapy for tissue ischemia. Muscle-specific VEGF knockout in mouse skeletal muscle reduces the presence of intramuscular

capillaries by approximately 50%, significantly decreases endurance time by approximately 80% (in the context of exercise), and dampens the angiogenic-specific response to exercise training (Wagner 2011). The d-skECM cohort expressed GM-CSF more significantly than all other comparisons. GM-CSF is a cytokine that stimulates hematopoietic stem cell mobilization, myelopoiesis, as well as the production and activation of neutrophils (Wright, Brown et al. 2014). It has been shown that GM-CSF elevates VEGF (Okazaki, Ebihara et al. 2005), an interesting correlation since VEGF was more highly expressed in skECM preparations relative to control. With specificity to muscle, GM-CSF promotes neutrophil chemotaxis after injury (Peterson and Pizza 2009), improves recovery of force, activates satellite cells, and has been shown to increase muscle mass (Stratos, Rotter et al. 2007). GM-CSF has also been shown as an antifibrotic cytokine (Moore, Coffey et al. 2000, Hu, Zhang et al. 2020), perhaps contributing to the lessened collagenous deposition as shown in the Masson's Trichrome imaging of the d-skECM relative to Control and p-skECM (**Figure 62**).

Control gastrocnemii showed significantly higher expression of IL-1 $\beta$ , IL-18, IFN $\gamma$ , TIMP-1, and TNF $\alpha$  relative to both p-skECM and d-skECM, where it is perhaps the case that the skECM preparations are acting to downregulate these cytokines. IL-1 $\beta$  has been implicated in metabolic adaptations of skeletal muscle occurring in response to stresses (Cannon, Fielding et al. 1989). IL-18 is overexpressed in inflammatory myopathies (Helmers, Bruton et al. 2018), and may be involved in muscle wasting (Petersen, Penkowa et al. 2007). IL-18 has been implicated in intramuscular lipid metabolism (Lindgaard, Hvid et al. 2018), potentially resulting in the lipid deposition seen in the Control and p-skECM cohorts (**Figure 63**). Inhibition of muscle-specific genes, including myogenin, has been shown when myoblasts are presented with supraphysiological levels IFN $\gamma$ , though administration of exogenous IFN $\gamma$  has been shown to

hasten skeletal muscle regeneration while limiting fibrosis (Foster, Li et al. 2003). Taken together, this upregulation in and of itself may not necessarily be detrimental, but in the context of the upregulated cytokines collective in the Control cohort, may be adversely affecting force (re)generation.

TNF $\alpha$  has been well recognized as a proinflammatory cytokine and is produced by activated macrophages. TNF $\alpha$  induces muscle satellite cells to enter the cell cycle and accelerates G1-to-S phase transition (Li 2003). TNF $\alpha$  is a polypeptide cytokine that has been associated with muscle wasting and weakness in inflammatory disease (Reid and Li 2001). TNF $\alpha$  may play a role in inflammatory-status mediated muscle mass loss (McMahon, Morse et al. 2019). Additionally, TIMP-1 is elevated in the serum, plasma, and muscle biopsies of Duchenne's Muscle Dystrophy patients, a population where dystrophin dysfunction is marked, resulting in muscle malfunction including loss of strength (von Moers, Zwirner et al. 2005). While study in denervation injury is limited, the pathogenesis of upregulated TNF $\alpha$  and TIMP-1 likely are not acting in a regenerative manner.

While the quality of the nerve healing at the coaptation site was not investigated explicitly, each cohort expressed MuSK similarly. Since MuSK is a receptor tyrosine kinase essential in the formation of neuromuscular junctions (NMJ) (Hubbard and Gnanasambandan 2013), this finding suggests that reinnervation at the NMJ occurred similarly in all conditions. Denervation injury models have shown NMJ disruption resulting in the loss of nerve-evoked muscle force (Pratt, Shah et al. 2015). Since all nerve repairs were performed in the same manner, this hypothesis seems rationale. Whether either skECM preparation played a role in hastening NMJ recovery requires additional study, with investigation likely at a much earlier timepoint.

#### 4.2.3.1 Regulatory Considerations of skECM

Homologous use cases have a history of specific regulation by FDA, and specifically, 21 CFR 1271.10(a)(1) details the statutory requirements of packaging and labeling a Human Cell/Tissue Product (HCT/P) that is being marketed for homologous use in the clinic. In this context, the marketing of an HCT/P is discussed with respect to Section 361 of the Public Health & Safety Act as it pertains to homologous use, and not to Section 351, which is oriented to cell and tissue products that are either non-homologous use or do not meet the requirements for minimal manipulation (e.g., cell therapies, biologics). While HCT/Ps are human in origin, the process of making skECM, and p-skECM in particular is essentially identical to current processing methods being employed commercially for HCT/Ps today. In the event that the origin tissue was human rather than porcine, the regulatory burden may potentially be significantly mitigated since HCT/Ps do not require the more rigorous standards that traditional medical devices, drugs, or biologics require, where registration with FDA is the prerequisite rather than a clearance or an approval.

Despite this, the FDA is moving toward more stringent requirements of 361 HCT/Ps, where FDA's July 2020 Guidance for Industry: "Regulatory Considerations for Human Cells, Tissues, and Cellular and Tissue-Based Products: Minimal Manipulation and Homologous Use", where the Agency makes specific note of 21 CFR 1271.3(ff) *Processing*, and that a means of decellularization does indeed constitute "processing", and therefore falls out of the interpretation of minimal manipulation. This is a large departure from the historical interpretation as many decellularized products are marketed under the HCT/P umbrella, particularly acellular dermal matrices (Macadam and Lennox 2012) and bone void fillers (Zhang, Yang et al. 2019). This interpretation does, however, enable the potential for a porcine-derived ECM, highly similar to the

ones created here to be regulated as a medical device, and perhaps through 510(k) pathway as micronized porcine urinary bladder matrix (see submission K153754 via fda.gov).

#### **4.2.4 Limitations of the skECM in the Gastrocnemii Study**

Unfortunately, the COVID-19 pandemic detracted significantly from work being performed physically in the laboratories and animal facility, which was concurrent with this study. though multiple timepoints were planned in this study (e.g., 8, 16), restrictions on animal ordering and husbandry precluded the expansion of the study. While contraction force is a highly relevant and commonly-utilized measure of muscle function, additions of EMG and nerve conduction velocity would also have been ideal; MuSK was shown without difference across all three groups, though a biophysical confirmation by nerve conduction would make an increasingly robust case that the nerves did indeed heal similarly across cohorts, and therefore did not impede the healing of the muscle. Finally, though downregulations of a series of cytokines is shown, IHC, or ideally, multi-labelled IF for inflammatory-specific cells would be ideal for better elucidating the mechanisms of healing.

### **4.3 Chapter Conclusion**

The TIPD designed is a compact, integrated system capable of automated decellularization of multiple tissue types via fluid infusion or perfusion. The TIPD has been created with OSH and using 3D printed components that are replaceable if damaged and easily replicated across laboratories. The code governing the TIPD allows a user to define an automation protocol, creating

an opportunity to greatly enhance the repeatability between instances of decellularization with a program capable of precisely specifying when solution changes are to occur in a given process. The system has been designed with the intention of increasing reproducibility and repeatability throughout decellularization and ideally can be implemented readily across many niches of tissue engineering.

The TIPD was also used to decellularize skECM and was shown to be capable of doing so with similar efficacy in the context of DNA removal. This decellularized muscle was then made into two preparations being a particulate format and a digested format, each having distinct ultrastructure. These skECM preparations were able to produce significantly more force when injected into gastrocnemii after a sciatic nerve laceration injury relative to control. Gastrocnemii injected with d-skECM also showed marked less intramuscular lipid accumulation relative. Cytokines of the gastrocnemii revealed significant expression of VEGF in both skECM cohorts relative to Control, and downregulation of several inflammatory cytokines: IL-1 $\beta$ , IL-18, IFN $\gamma$ , TIMP-1, and TNF $\alpha$  relative to Control.

## **5.0 Statistical Correlations of Muscle Mass, Contraction Force, and Measured Proteins**

While relative values and statistical significance relating categorical to continuous variables (e.g., ANOVA) is indeed essential to drawing conclusions and additional hypotheses of mechanisms, it typically does not directly correlate across results. Though many cytokines have been implicated in detail about their impacts throughout muscle regeneration at large, specific modeling of intramuscular protein concentration as against contraction force has been limited. Based on the force and cytokine data collected from the studies involving intramuscular injection of therapies post-PNI, linear modeling was performed to study the contributions individual and interacting cytokine have on predicting force measures.

### **5.1 Statistical Methods for Correlation Analyses**

JMP Pro (Cary, NC) was used for all correlation and multivariate analyses. Prior to analyses, distributions were assessed for goodness of fit based on their relative Akaike information criterion (AIC), which is an estimator of the prediction error within a given dataset, providing probabilistic weight on whether a sample originates from a given distribution. Generalized Regression based on the assessed distribution were used to determine significant predictors of the mean, being either categorical and/or continuous variables using maximum likelihood or least-squares methods. The distribution hypothesis was tested using Anderson-Darling. Significance was assessed at  $p < 0.05$  for all hypothesis testing. For multivariate modeling,

correlations above  $R^2 > 0.75$  were considered strong, correlations within  $0.75 \geq R^2 \geq 0.25$  were considered moderate, and correlations with  $R^2 < 0.25$  were considered weak.

## 5.2 Predicting Force Generation by Intramuscular Cytokine Concentration

### 5.2.1 Cytokine Analysis of Nanofat-Injected Rodent Gastrocnemii and their Correlation to Contraction Force

For extraction methods for quantitation of cytokines, refer to **3.2.6 Multiplexing**. Using multivariate mapping and linear regression analyses, the significantly-expressed cytokines were used to predict maximal contraction forces. The multivariate map is presented in **Figure 66** presents correlations of the significant cytokines (IL-1 $\beta$ , IL-18, GM-CSF, VEGF, TIMP-1) and the forces measured at their highest values, being at the stimulation frequencies of 50Hz, 75Hz, and 100Hz. In the figure, correlations with density ellipses and their linear trend lines are shown toward the bottom left, and a visual representation of the correlation parameters (colored circles) are shown toward top right. Positive correlations (i.e., upward slope) are represented with red circles and negative correlations (i.e., downward slope) are represented with blue circles. As the circle size increases, its correlation ( $R^2$ ) approaches 1.00 or -1.00. As shown, the contraction forces are all well correlated. Despite significances of the raw cytokine concentration in muscle,

Where the multivariate analysis is non-discriminant its comparisons, correlating every variable to the next, standard least squares regression was then used (**Figure 67**), specifically for modeling the behavior the significant cytokines to predict contraction force; this modeling technique would also allow multiple factors to contribute significantly to a prediction variable,

unlike multivariate analysis, where only two variables are compared in an instance. From standard least squares modeling, only IL-1 $\beta$  was shown as significantly correlated to contraction force (Figure 66), and as a significant predictor of contraction force (Figure 67).

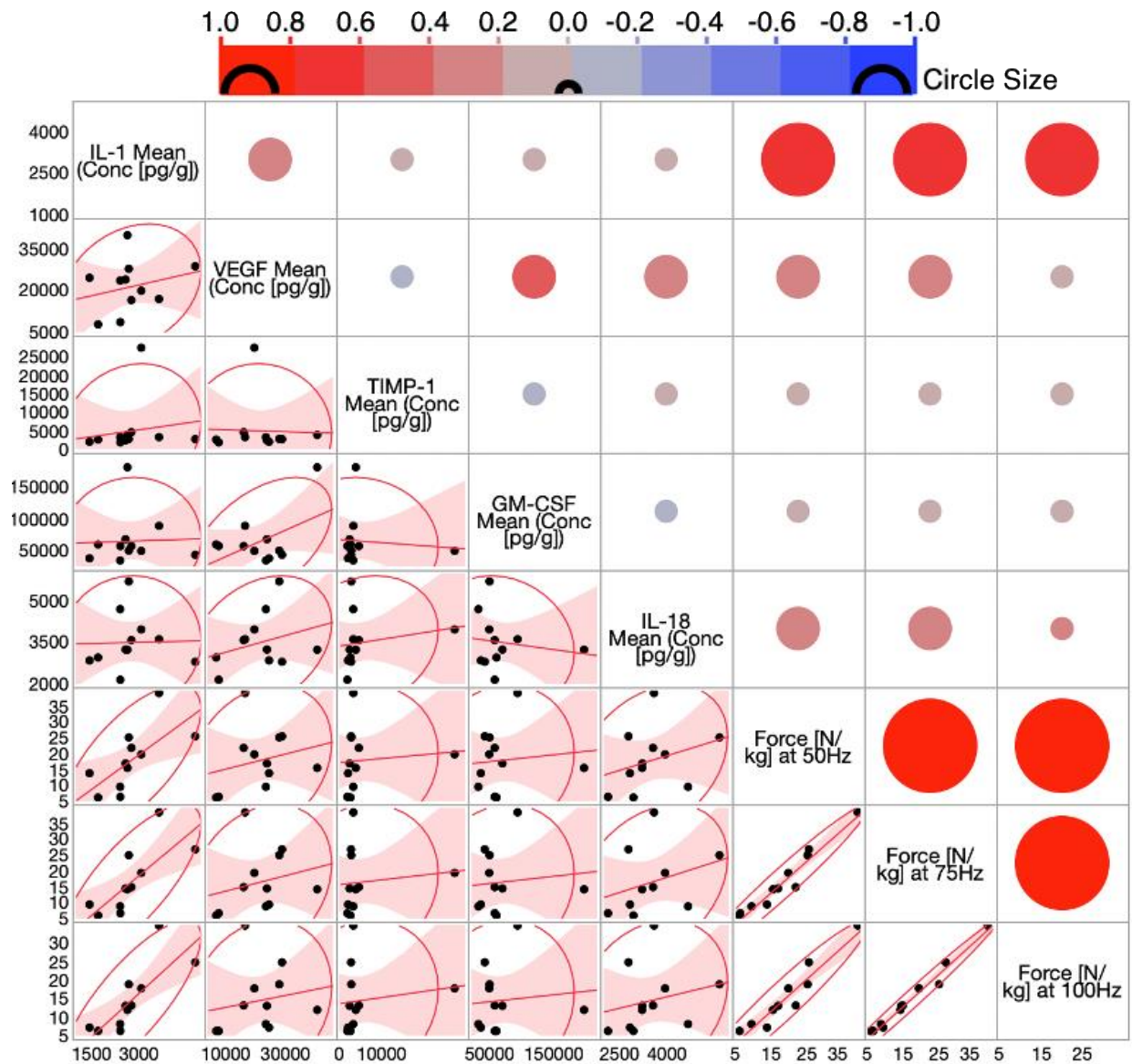
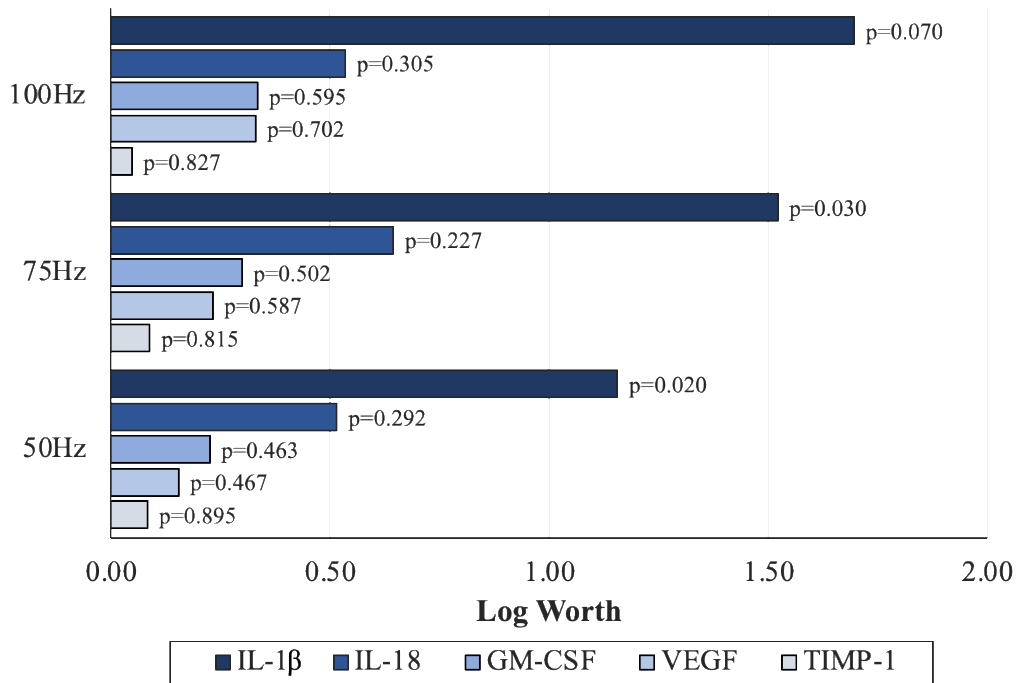


Figure 66: Multivariate Analysis Correlating Cytokines and Contraction Force [N/kg].



**Figure 67: Contribution of Cytokine Concentration to Tetanic Force.**

**Log-worth contribution to the linearized model for predicting maximal tetanic contraction force from each of the five significant cytokines.**

In removing the three least significant cytokines from the regression (GM-CSF, VEGF, TIMP-1), IL-1 $\beta$ , IL-18, and their interaction effect were modeled resulting in each being a significant predictor of contraction force (**Figure 68**).

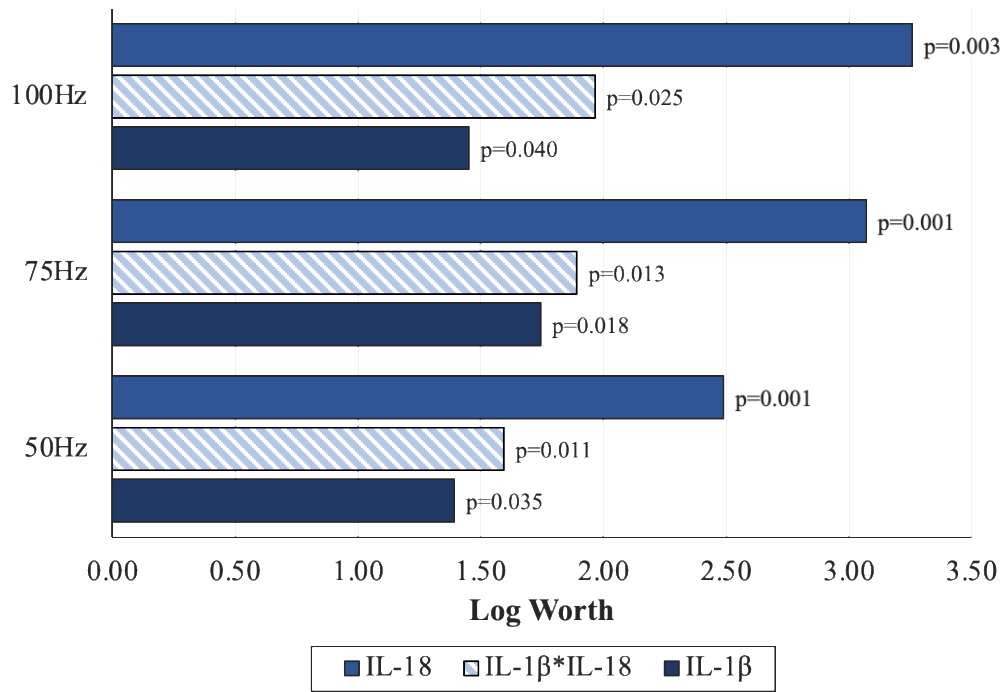


**Figure 68: Contribution of IL-1β and IL-18 to Predict Force in Correlative Modeling.**

The prediction equations of the force generation based on IL-1β, IL-18, and their interacting effect are shown across the three highest force-generating frequencies being 50 Hz (**Equation 5-1**,  $R^2=0.788$ ), 75 Hz (**Equation 5-2**,  $R^2=0.865$ ), and 100 Hz (**Equation 5-3**,  $R^2=0.879$ ) where  $\bar{c}$  denotes the average concentration of a given cytokine.

**Equation 5-1: Linear Correlation of Force [N/kg] at 50 Hz to IL-1β and IL-18**

$$\begin{aligned}
 F_{50Hz} = & -43.1776 + 0.0163\bar{c}_{IL1\beta} \\
 & + 0.0046\bar{c}_{IL18}(\bar{c}_{IL1\beta} - 2759.9655) \\
 & + 0.000016(\bar{c}_{IL18} - 3526.5463)
 \end{aligned}
 \tag{Equation 5-1}$$

**Equation 5-2: Linear Correlation of Force [N/kg] at 75 Hz to IL-1 $\beta$  and IL-18**

$$\begin{aligned}
 F_{75\text{Hz}} = & -46.6588 + 0.0170\bar{c}_{IL1\beta} \\
 & + 0.0046\bar{c}_{IL18}(\bar{c}_{IL1\beta} - 2759.9655) \\
 & + 0.000015(\bar{c}_{IL18} - 3526.5463)
 \end{aligned}
 \tag{Equation 5-2}$$

**Equation 5-3: Linear Correlation of Force [N/kg] at 100 Hz to IL-1 $\beta$  and IL-18**

$$\begin{aligned}
 F_{100\text{Hz}} = & -39.4690 + 0.0154\bar{c}_{IL1\beta} \\
 & + 0.0032\bar{c}_{IL18}(\bar{c}_{IL1\beta} - 2759.9655) \\
 & + 0.000013(\bar{c}_{IL18} - 3526.5463)
 \end{aligned}
 \tag{Equation 5-3}$$

Based on the  $R^2$  values of the linear equations above, each is strongly predictive of force the force being generated at their respective stimulation frequencies ( $R^2 > 0.75$  for each). This relationship is visually represented in **Figure 69**.

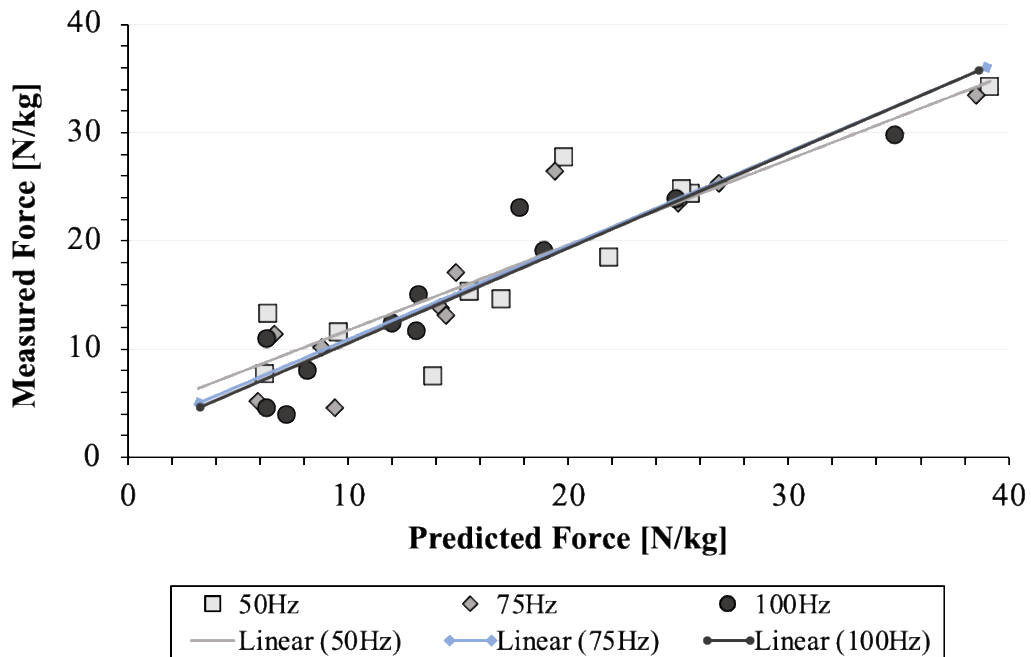


**Figure 69: Force Predicted from IL-1 $\beta$  and IL-18 against Measured Force.**

Despite the significant correlation between IL-1 $\beta$  and Contraction Force when it was normalized to the overall rodent body mass, this correlation did not hold when normalizing force by the gastrocnemius muscle mass as shown in **Figure 70**.

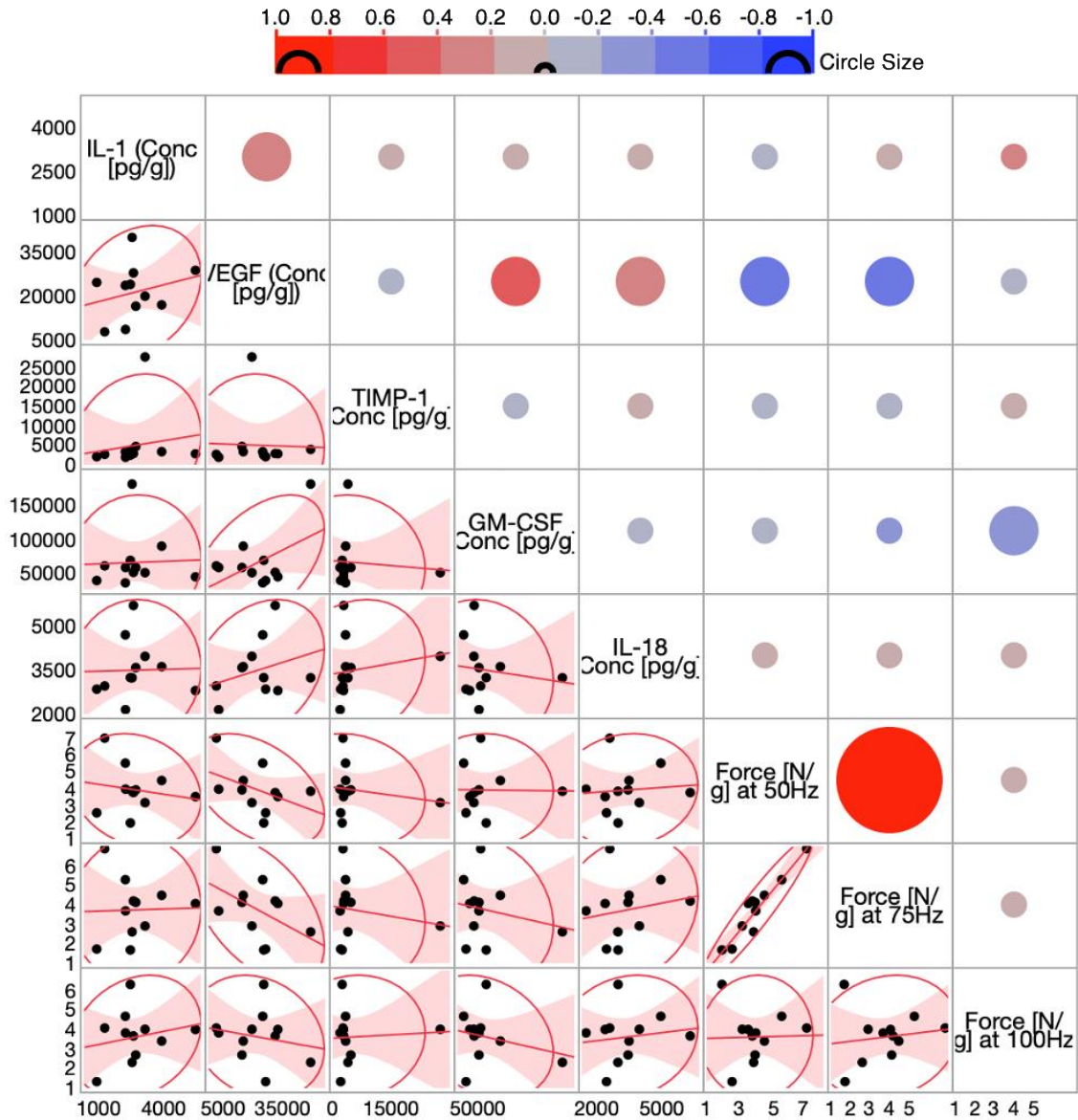


**Figure 70: Multivariate Analysis Correlating Cytokines and Contraction Force [N/g].**

Stimulation at 50Hz was shown to achieve the largest muscle contraction, both when normalizing by the rodent body mass (**Figure 41**) and when normalizing by gastrocnemius muscle mass (**Figure 42**), thus **Figure 71** models the correlation of the significantly-upregulated cytokines to the contraction force generated at the 50Hz stimulation frequency. As is shown in correlations plot of **Figure 70**, no significant predictors exist, also holding true when leveraging all cytokines in a standard least squares model for force prediction. **Figure 71A** the model itself is moderately correlated ( $R^2=0.415$ ), where the Predicted Force values of the x-axis were derived from **Equation 5-4** and plotted against the actual measure contraction force values.

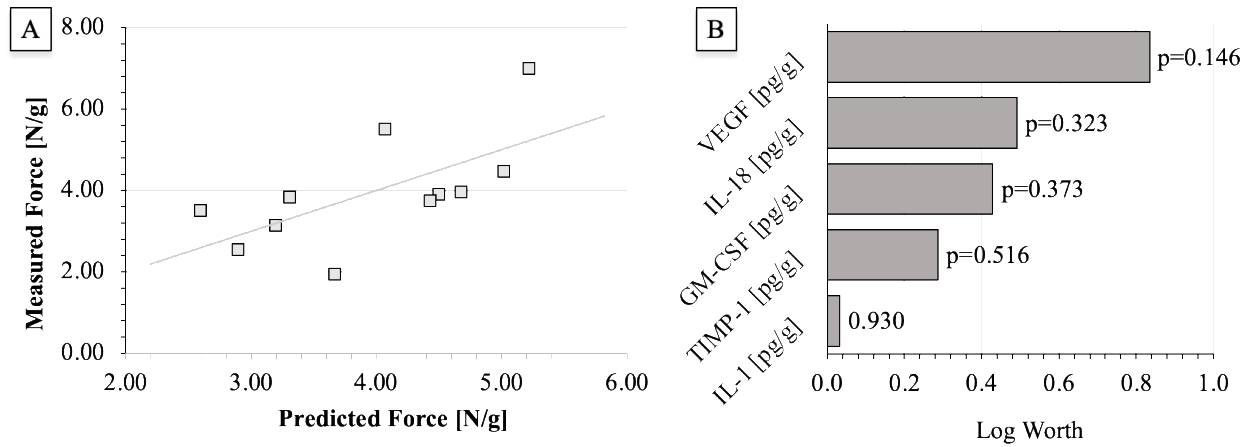


**Figure 71: Regression of Contraction Force [N/g] at 50Hz predicted by Cytokines.**

**A. Displays the linear regression from standard least squares prediction modeling of cytokines to predict contraction force [N/g], where the predicted force is calculated from Equation 5-4, and B. displays the contribution of each cytokine to the prediction of the contraction force [N/g].**

**Equation 5-4: Linear Correlation of Force [N/g] at 50 Hz by Significantly-Expressed Cytokines.**

$$\begin{aligned}
 F_{50\text{Hz,predicted}} &= 5.08 \\
 &\times 10^{-5} (\bar{c}_{IL1\beta} - 2.303\bar{c}_{VEGF} - 0.902\bar{c}_{TIMP1} + 0.274\bar{c}_{GM-CSF} \\
 &+ 11.860\bar{c}_{IL18} + 69,878)
 \end{aligned}
 \quad \text{Equation 5-4) }$$

## 5.2.2 Cytokine Analysis of skECM-Injected Rodent Gastrocnemii and their Correlation to Contraction Force

**Figure 72** displays a correlation plot of each of the fourteen cytokines quantified as well as the muscle force when normalized by both body mass and gastrocnemius mass. Sizes of circles denote their relative correlation, where larger circles are increasingly correlated; the colors of the circles indicate positive or negative correlation, red and blue, respectively. As the size of a circle increases, its likelihood for being a predictor with statistical significance increases. These significances are mapped in **Figure 73**. As shown in both figures, the only cytokine significantly correlated to force was IFN $\gamma$  ( $p=0.0088$ ), though VEGF did trend toward the threshold of significance ( $p=0.0864$ ).

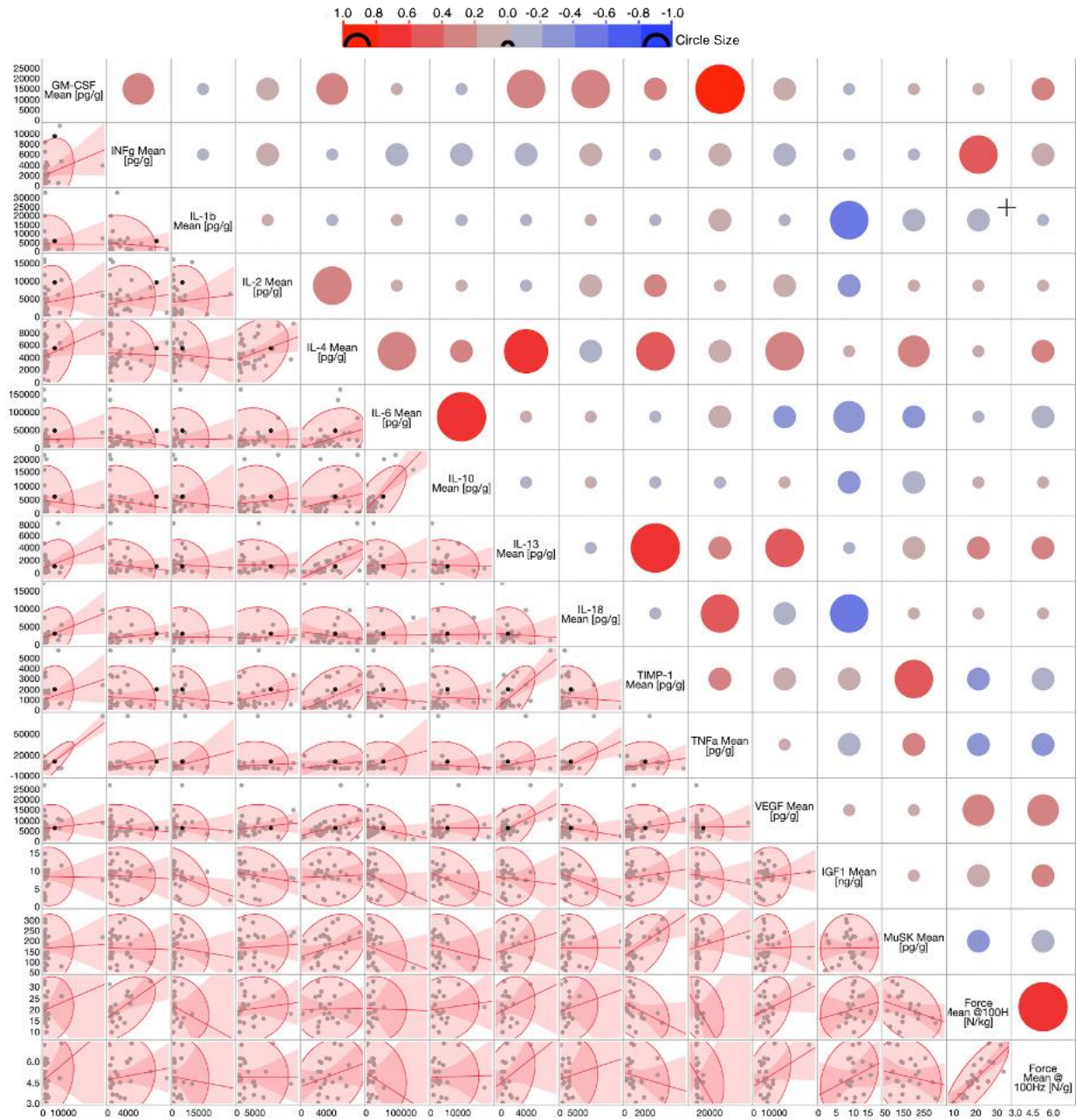


**Figure 72: Multivariate Analysis Correlating Cytokines and Contraction Force.**

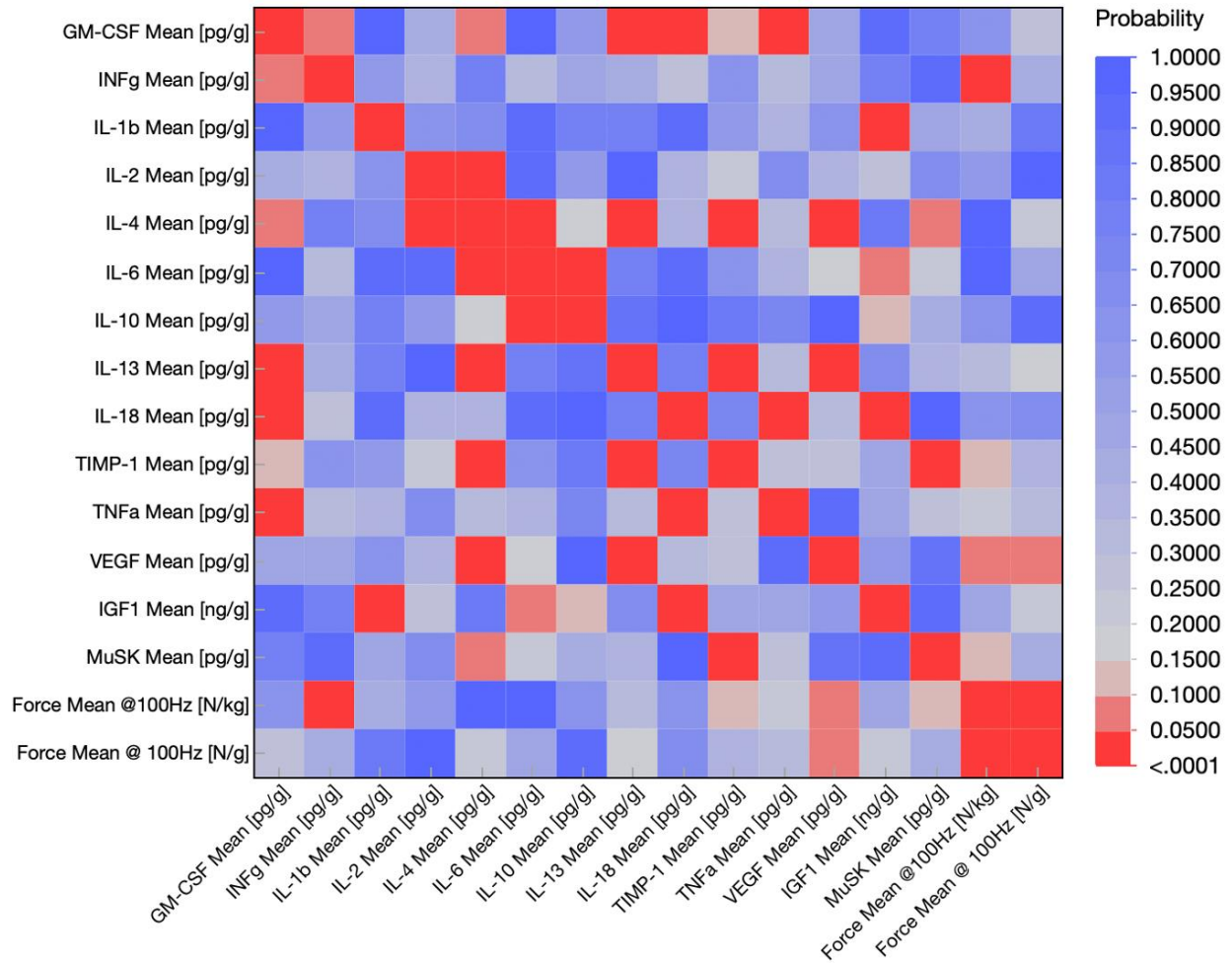


**Figure 73: Color Map of p-values for Correlations based on skECM Multivariate Assessment (Figure 72).**

### 5.2.2.1 Relation of Force, $IFN\gamma$ , $IL-1\beta$ , and $IL-18$

**Figure 74A** presents the correlation of the measured contraction force [ $N/kg$ ] to the intramuscular concentration of  $IFN\gamma$ , a moderately correlated regression ( $R^2=0.2966$ ). The regression equation is presented as **Equation 5-5**.

**Equation 5-5: Linear Correlation of Force by IFN $\gamma$ .**

$$F_{100Hz} = 16.882 + 0.0016 \bar{c}_{IFN\gamma} \quad \text{Equation 5-5)}$$

Though not explicitly predictive of contraction force here, the cytokines IL-1 $\beta$  and IL-18 were used to predict force in a full factorial model. IL-1 $\beta$  and IL-18 were chosen given their statistically significant correlation to force previously (**Figure 68** and **Figure 69**). Results from the full factorial correlation model are presented in **Figure 74B**, and the regression was shown as having a high correlation to force ( $R^2=0.8674$ ). The predicted force values (x-axis) were generated from **Equation 5-6** and **Equation 5-7**, linear equations of the factors and their interactions, respectively.

**Equation 5-6: Linear Correlation of Force based on Full Factorial Model with IFN $\gamma$ , IL-1 $\beta$ , and IL-18.**

$$F_{pred,100Hz} = 0.0139\bar{c}_{IL18} + 0.0059\bar{c}_{IL1\beta} + 0.0049\bar{c}_{IFN\gamma} + k_{F_{pred,100Hz}} \quad \text{Equation 5-6)}$$

Where the variable  $k_{F_{pred, 100Hz}}$  is the interacting effects as function of the three cytokines, as shown in **Equation 5-7**.

**Equation 5-7: Interacting Effects of IFN $\gamma$ , IL-1 $\beta$ , and IL-18.**

$$k_{F_{pred,100Hz}} = -6.807 \times 10^{-6} \bar{c}_{IL1\beta}\bar{c}_{IL18} - 2.982 \times 10^{-6} \bar{c}_{IFN\gamma}\bar{c}_{IL18} - 1.320 \times 10^{-6} \bar{c}_{IL1\beta}\bar{c}_{IL18} + 1.540 \times 10^{-9} \bar{c}_{IFN\gamma}\bar{c}_{IL1\beta}\bar{c}_{IL18} \quad \text{Equation 5-7)}$$

**Figure 74C** presents the log worth plot for all of the factors and their interactions, and their *worth* in terms of their contribution to force prediction. All factors and their interactions are

significant predictors of force *except* IL-18 and then interacting effect between IL-18 and IFN $\gamma$ . In contrast, IL-18 reaches significance is its interactions with IL-1 $\beta$  and the three-way interaction between IL-1 $\beta$ , IL-18, and IFN $\gamma$ . Interestingly, as a standalone variable IFN $\gamma$  was most predictive of force (**Figure 73**), however in the context of the broader model, IL-1 $\beta$  becomes most predictive.

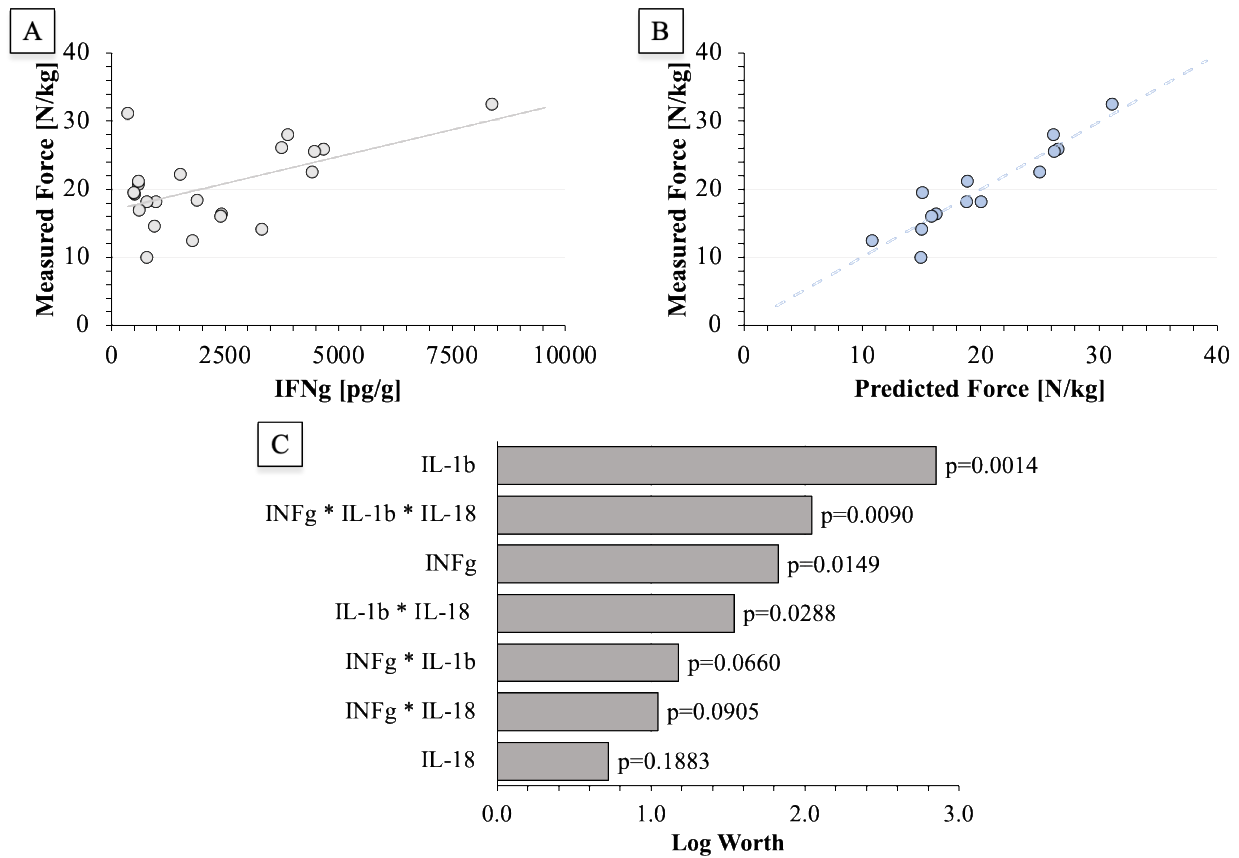


**Figure 74: Contraction Force as Predicted by IFN $\gamma$ , IL-1 $\beta$ , and IL-18.**

### 5.2.2.2 Relation of IL-4, IL-6, and MuSK

Based on the Color Map of p-values corresponding to correlative significance, IL-4 was shown to have the most factors significantly correlated (**Figure 73**). Five factors were shown to

be significantly correlated and two were shown to be nearly correlated; these factors, in order of correlation significance, were: IL-13 (p=0.0002), TIMP-1 (p=0.0038), IL-2 (p=0.0227), VEGF (p=0.0244), IL-6 (p=0.0477), GM-CSF (p=0.0577), and MuSK (p=0.0834). From this, a standard least squares regression used to model which of the proteins were most correlated to the concentration of IL-4, displayed in **Figure 75**. Factors were removed sequentially in order of their worth in an effort to best show what cytokines predict intramuscular IL-4 with significance, resulting in two additional linear model. **Figure 75A** presents the regressions from each of the three linear models, where the model involving all seven cytokines (“7 Factors”) was shown to be highly correlated ( $R^2=0.8237$ ), having prediction values derived from **Equation 5-8**.

**Equation 5-8: Linear Correlation of IL-4 to Significant and Near-Significant Proteins.**

$$P_{IL4} = -924.8 + 0.109\bar{c}_{IL2} + 0.048\bar{c}_{IL6} + 0.446\bar{c}_{TIMP1} + 0.240\bar{c}_{VEGF} + 8.550\bar{c}_{MuSK} - 0.030\bar{c}_{IL13} + 0.044\bar{c}_{GM-CSF} \quad \text{Equation 5-8)}$$

This correlation resulted in only two of the seven factors significantly contributing to the intramuscular IL-4 concentration, being VEGF (p=0.0065) and MuSK (p=0.0429), with IL-6 approaching the threshold of significance, and therefore likely significantly in a model involving fewer predictors. All other cytokines were not significantly correlated (p>0.11), as shown in **Figure 75B**.

To reduce the potential of overfitting the model and therefore artificially inflating the correlation, the four least-contributing factors were removed (see **Figure 75A**, “3 Factors”). This resulted in a moderately correlated regression ( $R^2=0.6346$ ) whose predicted force values were obtained from **Equation 5-9**. **Figure 75C** displays the log worth chart for the three cytokines, all

significantly correlated to intramuscular IL-4, being VEGF (p<0.0001), MuSK (p=0.0003), and IL-6 (p=0.0014).

**Equation 5-9: Linear Correlation of IL-4 to VEGF, MuSK, and IL-6.**

$$P_{IL4} = -1056.4 + 0.109\bar{c}_{IL6} + 0.048\bar{c}_{VEGF} + 0.446\bar{c}_{MuSK} \quad \text{Equation 5-9)}$$

These three factors were then modeled in as partial factorials, to the second degree (see **Figure 75A**, “Interacting Factors”) resulting in six predictors of intramuscular IL-4. This resulted in a moderately correlated regression ( $R^2=0.7056$ ) whose predicted force values were obtained from **Equation 5-10** and **Equation 5-11**.

**Equation 5-10: Linear Correlation of IL-4 to VEGF, MuSK, and IL-6 and their Interactions.**

$$P_{IL4} = 2688 - 0.014 \bar{c}_{IL6} - 11.847\bar{c}_{MuSK} - 0.071\bar{c}_{VEGF} + k_{P,IL4} \quad \text{Equation 5-10)}$$

Where the variable  $k_{P,IL4}$  is the interacting effects as function of the three cytokines, as shown in **Equation 5-11**.

**Equation 5-11: Interacting Effects of IL-6, MuSK, and IL-6.**

$$k_{p,IL4} = 7.258 \times 10^{-4}\bar{c}_{IL6}\bar{c}_{MuSK} - 7.117 \times 10^{-6}\bar{c}_{IL6}\bar{c}_{VEGF} + 2.486 \times 10^{-3}\bar{c}_{MuSK}\bar{c}_{VEGF} \quad \text{Equation 5-11)}$$

**Figure 75** displays the log worth chart for the three cytokines and their interactions. VEGF ( $p < 0.0001$ ), MuSK ( $p = 0.0003$ ), and IL-6 ( $p = 0.0014$ ) remain significantly correlated to intramuscular IL-4, though none of their interactions are significant ( $p > 0.06$ ).

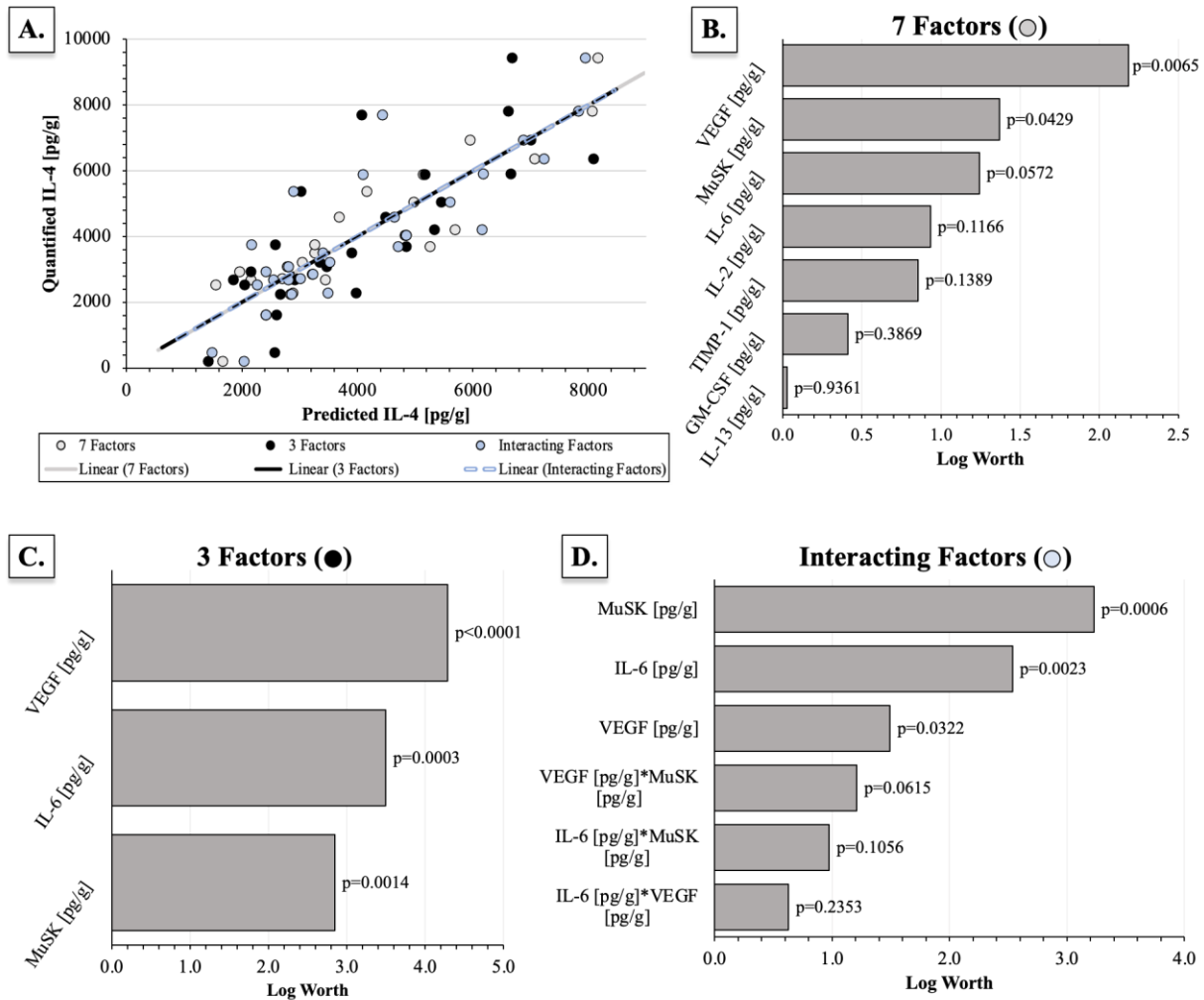


**Figure 75: IL-4 Concentration Predicted by Concentration of Intramuscular Cytokines.**

### 5.3 Discussion on Correlations Data

Linear regression analyses correlating cytokines in plasma to muscular function has been performed, though it is not clear whether regression of quantified intramuscular cytokines and force has been performed to date. Blood plasma regression analysis showed that IL-6 was significantly and negatively correlated to handgrip strength (Kim, Choi et al. 2014). In a similar correlation analysis, IL-6 blood levels were shown significantly and negatively correlated to muscle mass and muscle strength in the elderly, exacerbated by presence of TNF $\alpha$  (Visser, Pahor et al. 2002). In intramuscular injection studies involving both Nanofat and skECM, significant, positive, and moderate to strong correlations were made to force production by measurement of the intramuscular cytokine concentrations (**Figure 69** and **Figure 74**). Additionally, both of these studies implicate IL-1 $\beta$  and IL-18 as having a highly correlated effect with respect to force generation when force is normalized by the rodent body mass. In Nanofat-treated conditions, it was shown that the inflammatory cytokines IL-1 $\beta$ , IL-18, and their interacting effects are significantly and positively correlated to contraction force measured at 9 weeks postoperatively. Similarly, in the skECM-treated conditions at 20 weeks postoperatively, IL-1 $\beta$  and IL-18, and their interactions were again correlated to contraction force generation, though also with the effect of IFN $\gamma$  as well as its interacting effects.

It is known that the inflammatory process has profound impact on the regenerating or degenerating muscle, affecting its function (Tidball 2017). The effects of IL-1 $\beta$  and IFN $\gamma$  on the regenerating muscle has been mixed, and the contributions of IL-18 to muscle regeneration have not been well studied to date. It has been reported that IL-1 $\beta$ -positive neutrophils support physical performance by potentially alleviating fatigue (Tsuchiya, Sekiai et al. 2018). In masseter muscles,

locally increased IL-1 $\alpha/\beta$  supports functional activity by maintaining glucose homeostasis, which also involved IL-6; IL-1 $\alpha/\beta$  with IL-6 were shown to have direct involvement in muscle performance and fatigability (Chiba, Tsuchiya et al. 2015, Cohen, Many et al. 2015), with concentration trends here corroborating these findings. IL-1 $\beta$ -polarized macrophages have been reported to reduce intramuscular lipid (Moratal, Raffort et al. 2018), though this finding seems to be at odds with the visual lipid deposits found in the Control and p-skECM-treated gastrocnemii (**Figure 63**). Intramuscular lipid accumulation and force generation may not be mutually exclusive, however, given reports that moderately upregulated intramuscular lipid accumulation does not affect contractile force (Watt and Hoy 2012).

It has been shown that IFN $\gamma$  is required for efficient muscle regeneration. IFN $\gamma$  administration can hasten skeletal muscle repair and limit fibrosis. IFN $\gamma$  also regulates macrophage phenotype in muscle from dystrophic (*mdx*) mice during the period of acute muscle damage and the following regenerative stage (Villalta, Deng et al. 2011). Despite these findings, it has also been shown that IFN $\gamma$  inhibits muscle-specific gene upregulation, including myogenin, when myoblasts are presented with supraphysiological IFN $\gamma$  levels (Foster, Li et al. 2003), consistent with what is shown here (**Figure 65**). It has been demonstrated by linear correlation that IL-1 $\beta$  and IFN $\gamma$  were able to induce iNOS gene expression in skeletal muscle (Adams, Nehrhoff et al. 2002), where significantly upregulated iNOS was shown in muscle at 9 weeks (**Figure 43A**). By coordinating the initial inflammation and activating satellite cells to express MYOD, IFN $\gamma$  has been suggested to be an early regulator of myogenesis (Cheng, Nguyen et al. 2008), and seemingly continues to impact repair with respect to muscle power through 20 weeks.

IL-18 has an interesting role in these models. At 9 weeks, IL-18 is shown to have the most significant contribution to predicting muscle contraction force (**Figure 68**), with is lone

contribution dwindling at the 20-week timepoint. Rather, at 20-weeks, the interaction of IL-18 with IL-1 $\beta$ , and the three-way interaction between IL-18 with IL-1 $\beta$  and IFN $\gamma$  are significant predictors of contraction force (**Figure 74C**). IL-18 may be involved in regulating intramuscular lipid metabolism and hypertriglyceridemia, controlling local access to energy stores (Lindegaard, Hvid et al. 2018). While high intramuscular expression of IL-18 has been reported in inflammatory diseases and myopathies (Tucci, Quatraro et al. 2006), like with IL-1 $\beta$  and its lipid association, the IL-18 concentrations did not appear to follow the trends in the Oil Red O staining (**Figure 63**). IL-18 also has a role in maintaining healthy skeletal muscle, with expression in type-II muscle fibers (Plomgaard, Penkowa et al. 2005, Bruun, Stallknecht et al. 2007). Type-II muscle fibers are predominant in rat gastrocnemii (Cornachione, Benedini-Elias et al. 2011), and perhaps a stasis was reached due to the relatively long postoperative timepoints (9 and 20 weeks), leading to significant IL-18 correlation in force. Taken together, perhaps the effects and interactions of IL-1 $\beta$ , IL-18, and IFN $\gamma$  prolonged upregulation of satellite cell proliferation combined with regulation of injury lipogenesis and inflammation contributed to the increased contraction force.

IL-4 and the proteins correlated to it were investigated in more depth relative to other protein interactions for two reasons: (i) it showed the most significant ( $p < 0.05$ ) and near-significant ( $p < 0.09$ ) correlations in the analysis, five and two respectively, and (ii) the none of factors that were correlated force (IL-1 $\beta$ , IL-18, IFN $\gamma$ ) were correlated to IL-4; rather, each cytokine correlated to force was weakly correlated to IL-4,  $r(\text{IL-1}\beta) = -0.0460$ ,  $r(\text{IL-18}) = -0.0825$ , and  $r(\text{IFN}\gamma) = -0.1641$  (**Figure 72**), respectively, suggesting that IL-4 may be regulating some type of regenerative mechanics that not obviously correlated to force generation. Though an abundance of literature surrounds IL-6 and its impacts on muscle, here IL-4 showed to correlate to an abundance of cytokines relative to IL-6. While IL-1 $\beta$  has been implicated in upregulating IL-6 *in*

*vitro* (Luo, Hershko et al. 2003), the correlation between these cytokines was not seen in the denervation atrophy model here ( $r=0.0102$ ). With IL-6 acting as a significant predictor of IL-4, perhaps latent IL-6 mechanisms responsible for producing IL-4 are at work (Heijink, Vellenga et al. 2002), but are not perceptibly correlated to force generation in regression. The impact of IL-4 on VEGF has been mixed, with studies showing VEGF-induced angiogenesis being dependent on IL-4 (Fukushi, Ono et al. 2000), and others showing IL-4 preventing VEGF (Hong, Cho et al. 2007). Literature relating IL-4 and NMJ (MuSK) is not abundant, though there are implications of increased IL-4 causing dysfunction at NMJ in patients exhibiting the myasthenia gravis disease state.

### **5.3.1 Correlations Studies Limitations**

These correlations studies have several limitations. Foremost, increasing the animal numbers and early time-points would serve to better elucidate variability and time-based changes, especially in cytokine expressions. Increased animal numbers would also serve to increase the statistical power in performing any statistical method, but particularly for correlations, increasing cohort number would allow for additional interactions to be compared without losing degrees of freedom. Analyses here needed to be performed without sufficient freedom to parse therapies from one another; rather correlations of cytokines needed to be taken as a whole. While achieving statistical significance with disparate treatment conditions only serve to strength the case of the cytokines' contributions, the ability to control for individual injury cohorts would strength, and even perhaps quantify similar correlations in increasingly greater detail. In searching the literature for similar studies, several publications correlating functional muscle force to levels of cytokines in the blood plasma. Any future investigation repeating the work would greatly benefit from the

additional insight that could be provide when comparing systemic to local cytokines and then perform multivariate analyses.

#### **5.4 Chapter Conclusions**

When correlating contraction force to intramuscular cytokine concentration, the literature contains limited, and appears to be even absent of, similar studies. Cytokine analyses at 9 weeks postoperatively implicated IL-1 $\beta$ , IL-18, and their interacting effects as significant predictors of gastrocnemius contraction force. Analysis at and 20 weeks postoperatively corroborated those cytokines as predictors, but did so in presence of IFN $\gamma$  and its interacting effects in the model. This method of analysis may provide a powerful tool for establishing increasingly explicit mechanisms responsible for translating intramuscular concentration of proteins to function muscle force during regeneration.

## 6.0 Dissertation Conclusions and Contemplations

The status of relevant data to nerve injury and muscle atrophy are unfavorably staggering. Currently about 20 million Americans are dealing with PNI/MA-related ailments, or about 6 out of every 100 people (Lundborg 2003). Annually, 3 out of every 100 admittances to a trauma center are specific to a nerve injury (Huckhagel, Nuchtern et al. 2018). Though admittances for PNI affects males disproportionately, with rates being 85% men of  $39.9 \pm 14.2$  years of age (Bergmeister, Grosse-Hartlage et al. 2020), slower healing of poorer quality in the aging population is well reported (Verdu, Ceballos et al. 2000, He, Yadgarov et al. 2012). Patients who experience nerve injury become amongst the highest probability to be diagnosed with chronic pain, and as muscle atrophy progresses, this patient population is exceedingly likely to require physical therapy and/or occupational therapy services for more than 3 months post-injury (Padovano, Dengler et al. 2020). Surveys of this patient population one year post-injury report 40% unable to return to work due to residual complications (Jaquet, Luijsterburg et al. 2001, Bruyns, Jaquet et al. 2003). Taken together, the annual United States expenditure on PNI/MA is approximated to be \$150 billion annually (Taylor, Braza et al. 2008), or when considering the totality of annual US health-related spending, \$3.5 trillion (Conway 2017), PNI/MA occupies about 4.3%.

In an effort to address this profound clinical and socioeconomic challenge, several intramuscular therapies were studied in a nerve injury model with the aim of mitigating denervation atrophy. The rodent sciatic nerve injury model was leveraged for inducing atrophy of distal muscle, which included denervation and the eventual atrophy of the gastrocnemius. Both cellular and acellular therapies were administered directly into gastrocnemii, being adipose-derived stem cells (ASCs), a preparation of emulsified adipose tissue (“Nanofat”), and a skeletal

muscle-derived extracellular matrix (skECM). Additionally, in select conditions a polycaprolactone nerve wrap was applied at the nerve injury site to assess cotreatment of muscle and nerve. Two automated devices were created to produce neuromuscular therapies: An automated dip coating device was used fabricate nerve wraps and an automated perfusion machine was used to produce skECM. Studies were conducted with postoperative analysis performed at 6, 9, 12, and 20 weeks, which included gait analysis, force production, cytokine quantification, and histological analysis. Intramuscular therapies, particularly skECM, were shown to be superior against non-injected muscle controls across all time points and showed no difference to uninjured muscle at 20 weeks. Cytokines IL-1 $\beta$ , IL-18, and VEGF appeared to mediate regeneration throughout. Statistical regression implicated IL-1 $\beta$ , IL-18, and their interacting effects, as strong predictors of muscle contraction force at 9 weeks with IFN $\gamma$  along with IL-1 $\beta$  and IL-18 showing significant correlation at 20 weeks. The studies here implicate these intramuscular treatments as lucrative co-therapies in the PNI patient population.

## 6.1 Future Work

Developed here are prototypes for the fabrication of neuromuscular therapies, being the Automated Dip Coating Machine for nerve wrap fabrication (See **Section 2.5.1.1**), and the TIPD for skECM processing (see **Section 4.1**). While the ultimate goal of these tools is to provide repeatable fabrication platforms for the respective therapies, further validation is required. For both systems, more research is warranted into the tolerancing of the device, that is, what the maxima and minima are in terms of processing times for each fabrication step and how such variability affects the resulting material. For instance, the study of PCL tensile strength as it relates to dip

coating duration is one of the myriad studies required for validating a process. Industry performs Installation and Operation Qualifications (IOQ or IQ/OQ) for equipment to be used in a regulatable process. These are verification processes that explicitly document that a piece of equipment has been properly delivered, installed, and configured. Such metrics and standards are typically set cooperatively, by manufacturer of the equipment in terms of the device specifications, and then by an installation checklist determined by whoever is using that device, tailored to a specific purpose or process. Authorship and provision of an IOQ with these machines would be an ideal inclusion toward adoption and consistency when using such automated platforms.

Though postoperative timepoints of 6-, 9-, 12-, and 20 weeks were studied here, they differed in the therapies administered to gastrocnemii after a nerve injury. Ideally, the Nanofat and p-/d-skECM studies would be repeated across each of these timepoints, with a recommended n=6 animals per group per timepoint. It would also be ideal to study cytokine response at each of these timepoints as well as the functional outcomes of force and EMG in each hindlimb, including contralateral muscle. This would serve to make the statistical analyses, and particularly the correlations, more robust and illustrative as a time series. Further characterization of the injected materials, specifically rheological and proteomic characterizations, may serve to better elucidate the mechanisms by which the therapies produce their effect on the regenerating muscle. Additionally, a return to investigate cotreatment of the injured nerve site with an intramuscular injection deserves further study; particularly in the 1.5cm defect model; where atrophy was increasingly progressive relative to the transection model, the benefits of treatment to denervated distal muscle may be amplified in a more challenging model. Finally, as the future should influence the present just as much as the past, considerations for the anticipated regulatory and scale-for-

manufacturing are increasingly essential in therapeutic development and are briefly considered below.

### **6.1.1 Regulatory Considerations for Nanofat, ECMs, and ASCs**

The United States Food & Drug Administration (FDA) seeks to regulate most stem cell therapies under the 21 CFR 601 with a Biologics License Applications (BLA) process, where an ASCs therapy would likely fall into that category. BLAs are evaluated and regulated by the Center for Biological Evaluation and Research (CBER), which is one of the six main FDA centers. CBER regulates such products as vaccines, some xenografts, and therapies whose mechanism of action depends on metabolism rather than molecular binding. This Center will most likely regulate the emerging field of whole organ engineering (e.g., a decellularized and recellularized organ) when commercial translation becomes viable. Under federal provisions, the BLA allows a commercial entity to introduce a biological product into interstate commerce per 21 CFR 601. Several key requirements must be met to fulfill the BLA process toward clinical readiness. Some of these factors include intended indication, product and manufacturing information (verification and validation matrices, failure mode and effects analysis, Good Manufacturing Practices (GMP) compliance), and preclinical investigation, study designs and results with and an ongoing post-market surveillance strategy. With therapeutics of increasing complexity, mechanism of action can also be a constituent of the regulatory process, and therefore studies must be designed that best elucidate not only safety and efficacy, but the means by which that efficacy is achieved.

Decellularized tissue matrices, like the skECM preparations studied here, have more of nebulous regulatory pathway. As discussed in **Section 4.2.3**, an skECM may fall into the HCT/P category, provided the source tissue origin is human, exclusively. HCT/Ps provide somewhat of

an amalgamated Class I/II pathway as would be regulated by CDRH, though tissue banks processing such material must register with and inform FDA of marketing prior to doing so, but do not necessarily require a premarket clearance or approval (see 21 CFR 1271). Processing of tissue is subject to Good Tissue Practices (Hatcher, Atala et al. 2015), where cleanroom management and quality systems are regulated under parts of 21 CFR 211, and as such, are still subject to FDA audit, Warning or Untitled Letters. A recent addition of clinically-marketed human tissues has been an allograft adipose matrix. Pre- and clinical studies have evaluated the safety and efficacy of the ECM derived from adipose tissue (allograft adipose matrix, AAM processed by MTF Biologics, Edison, NJ), demonstrating the ability of the material to form new adipose tissue in immunocompromised and immunocompetent mouse models and when injected into the subdermal or subcutaneous compartments in humans (Giatsidis, Succar et al. 2019, Kokai, Schilling et al. 2019, Kokai, Sivak et al. 2020). Recent guidance from FDA, however, has cited processes of decellularization and disinfection of human tissue as falling outside of the 361 HCT/P pathway, though it is not immediately clear what Center would lead.

For applications specific to skeletal muscle in the context of regulated ECMs, porcine urinary bladder matrix (UBM) was administered to muscle in a volumetric injury (MatriStem, processed by ACell Inc., Columbia, MD), yielding favorable results (Sicari, Rubin et al. 2014). MatriStem is a 510(k)-cleared medical device (K112409), to be marketed as a collagen wound dressing (FDA device classification code: KGN), intended for the management of wounds including partial and full-thickness wounds, pressure ulcers, venous ulcers, diabetic ulcers, chronic vascular ulcers, tunnel/undermined wounds, surgical wounds, trauma wounds, and draining wounds. While the potential to establish substantial equivalence, and thus apply for 510(k) clearance, for an skECM is certainly possible under the wound care pretext, it likely limits the

indications to those aforementioned, precluding direct application into denervated muscle. Indeed, muscle-specific treatment regulated under CDRH are exceedingly rare. 21 CFR Parts 862 to 892 define all product codes assigned to medical devices, and in the context of device development, the term “muscle” is only specifically called out as an antibody test system (§866.5120), as an obstetrical/gynecological device (§884.5940, requiring PMA), and as physical medicine devices, being muscle stimulators (§890.1850, §890.5850, §890.5860).

In the absence of HCT/P or 510(k), it would seem that the likely pathway for skECM is either *de novo* or PMA via CDHR, or BLA via CBER. To determine the appropriate Center, 21 CFR 3 directs assignment based on currently-marketed products of similar type, safety, and effectiveness. If such a produce does not exist currently, a risk-based approach is taken, where the Agency defers to the Center having the broadest expertise to evaluate the most significant safety and effectiveness concerns. Concerning implantable or injectable therapies, like the skECM preparations that were used here, the biomedical industry, inclusive of both manufactures and regulatory bodies alike, have looked to standardized testing strategies like ISO 10993 and its panel of biocompatibility tests. This testing regimen has been highly successful for supplementing regulatory approval with well-known *in vitro* and *in vivo* analyses. Where these tests particularly excelled was with materials eliciting limited biological activity such as metals, ceramics, or inert plastics. Additionally, some of the more inert ECM-derived materials, like the purified collagens, have also had successes with this battery of tests, but increasingly complex biomaterials have presented challenges, raising questions of both patient safety and the validity of the tests regarding biologically active materials. In order to begin the standardization process in the cellular therapeutics space, high levels of collaboration will be necessary from regulatory bodies and

researchers, both industrial and academic. Advancements to cell-based standardization will come as considerable benefit to the field as a whole.

In stark contrast, the use of Nanofat clinically is considered the *practice of medicine*. The FTC Act establishes the scope of FDA's regulation and generally limits its jurisdiction to marketed products, though there is a growing litigation on whether FDA is overstepping its bounds and infringing on medical practice (Freeman and Fuerst 2012, Aicher 2013). The tools used to emulsify the adipose tissue are defined as surgical tools, and thus regulated medical devices through CDRH, the Nanofat produced is not regulated and as such, and neither are its applications. The interest in studying Nanofat here stems from this highest level of translatability, where a clinician, using her own discretion, may choose to render a Nanofat therapy to denervated muscle, provided patient consent.

### **6.1.2 Scaling for Manufacturing in ASCs and ECMs**

The potential downside of using Nanofat is the forfeiture of strict material controls that would be necessary for marketing a regulated medical product. There is inherent variability that exists between humans, and that has been studied at length in the fat grafting literature for graft survivability and effect on the local environment, particular when grafting occurs in post-cancerous breast (Rigotti, Marchi et al. 2010, Fisher, Grahovac et al. 2013, Largo, Tchang et al. 2014, Evans, Gronet et al. 2020). Further, the adipose tissue differs in pathology states like obesity, diabetes, and cardiovascular disease, all of which change the ECM and stroma (Chait and den Hartigh 2020). Since stromal cells and ECMs are key constituents of Nanofat, there may be implications in rendering an intramuscular therapy post-PNI in a patient population with a comorbidity affecting the adipose tissue. While potential issues arising from such disease states in

Nanofat are speculative, further investigation is merited to understand potential augmentations to the prospective therapy.

Since and ASC/cell therapy and an skECM therapy would need some premarket clearance/approval prior to clinical availability, by definition it must meet quality and consistency requirements as defined by the manufacturer and approved by FDA. A therapy of either ASCs or skECM has the potential to originate from a single source. Though it is likely that ASCs at first would originate from an autogenetic source with controls around surface markers as proliferation to the desired scale occurs, there are reports that passaged ASCs do not elicit T cell response and suppress mixed leukocyte reaction (McIntosh, Zvonic et al. 2006), suggesting the possibility of additional control through single-batch autologous culture. Cellular yield will be an essential challenge to overcome, not only for ASC-based therapies, but for any cell-based therapy, particularly if that therapy is most efficacious as autogenic. Closed-system reactors will be required for the culture, expansion, and protection of ASCs, all while maintaining an environment that is auditable for quality parameters. Some investigations have pointed to phenotypical changes resulting from increased passaging, resulting in changes of ASC mechanical properties (Gonzalez-Cruz and Darling 2013). Confluency may also be a concern, where increasing cell proximity downregulates proliferative gene expression and upregulates immunogenic expressions (Kim, Lee et al. 2014). In addition to cell growth metrics, sterility will be a requisite test of ASCs coming into and going out of an expansion facility, along with monitoring other culture conditions (temperature, oxygen content, CO<sub>2</sub> content, pH) for quality control.

In a sense, the manufacture of ECMs is indeed simpler. Though strict sterility standards must be maintained (i.e., cGMP Production), the selection of the source material can be broader and the processing of material more lenient with respect to logistical flow. Manufacture of an

skECM may be either allogeneic (cadaveric human) or xenogeneic (e.g., bovine, porcine). A major advantage to xenogeneic grafts is the control that is offered over the originating tissue material. Unlike grafts originating from humans, scaffolds of xenogeneic origin have regulated dietary and in-life activities, as well as genetic screening throughout the lifespan of the animal; additionally, precise research can be conducted with regard to times and conditions of sacrifice, optimizing them for graft size, integrity, and function. Further, the animal strain can be controlled and maintained increasing the level reproducibility that cannot be achieved with allogeneic technologies (Cooper, Gollackner et al. 2002). The processes of decellularization and disinfection need to be approached as a balance between ridding cellular content to avoid immunogenicity and preserving endogenous scaffold proteins that create the therapeutic effect *in situ*. Decellularization can be performed using either chemical and/or enzymatic solutions, mechanical disruption, and/or thermal (Gilbert 2012). As shown in the skECM process here (see **Section 4.1.3.2**), the ionic surfactant SDS has been particularly effective for decellularization (O'Neill, Anfang et al. 2013, Gilpin, Ren et al. 2014, Guyette, Gilpin et al. 2014, Fu, Fan et al. 2016); however, SDS is highly cytotoxic requiring extensive washing post-treatment (Syed, Walters et al. 2014), is capable of solubilizing whole growth factors, and alters the microstructure of fibrillar proteins (Zhou, Fritze et al. 2010). Non-ionic surfactants like Triton X-100 have been shown to be gentler on proteins, but are simultaneously less effective at decellularization, requiring increased exposure times relative to SDS (Mendoza-Novelo, Avila et al. 2011). Disinfection of the scaffold can be performed using different agents like peracetic acid (PAA), gamma irradiation (GI), or ethylene oxide (EtO) gas (Hodde, Janis et al. 2007). GI and EtO treatment will require freeze-drying before disinfection (Lee, Chang et al. 2013). Note that xenogeneic materials (as regulated, implantable

medical products) require terminal disinfection, which can be detrimental to the structure and biophysical properties of a scaffold (Matuska and McFetridge 2015).

Establishing and maintaining validations and tolerances for purity, stability, potency, and safety are the most challenging requirement for scale-up as they may be therapy/indication-dependent but are critical for ensure the safety and quality of a medical product. For cell therapies, batch investigations into surface markers, select secretome proteins, and differentiation capabilities can be performed. Similarly, post-production quality control on growth factors retained, porosity, and rheological characteristics of an ECM can be performed to bolster confidence in product performance. The complexity of the manufacturing and the quality-based analyses must be balanced with the resulting cost of the therapy. It is exceedingly important that therapies be competitive not only with standards of care, but also work lessen the overall healthcare burden and to ensure equity of treatment across socioeconomic status.

## Appendix A ASCs in Nerve Injury Models

Series of tables summarizing models and results from in vivo application of ASCs onto peripheral nerve injuries. Tables are organized alphabetically by nerve and then by duration of the investigation.

**Appendix Table 1 Studies of Cavernous Nerve Injury.**

Reference	Nerve	Injury Type	Animal	Duration	Results	Proposed Mechanisms
(Lin, Albersen et al. 2011)	Cavernous	Crush	Rat	1 week	Substantial recovery of erectile function when ASCs seeded into decellularized adipose	Downregulation of inflammation with nervous tissue ingrowth
(Chen, Yang et al. 2016)	Cavernous	Crush	Rat	4 weeks	ASC injection increased intracavernous pressure and presence of Schwann cells at dorsal stump	ASC-mediated increases in early pigment epithelium-derived factor (PEDF), followed by elevated nitric oxide synthase and phosphorylated Akt
(Fandel, Albersen et al. 2012)	Cavernous	Crush	Rat	4 weeks	Intracavernous, but not perineural, ASC injection significantly improved erectile function	Injury-induced upregulation of stromal cell-derived factor-1 recruited injected ASCs, which neuro-regenerative effects
(Qiu, Fandel et al. 2012)	Cavernous	Crush	Rat	4 weeks	Immediate and delayed ASC injection increased neuronal nitric oxide synthase and neurofilament; increased smooth muscle-to-collagen ratio	Increase of spontaneous nerve regeneration in ASC-treated conditions, producing pro-survival, anti-apoptotic and neurotrophic factors

**Appendix Table 1 (continued)**

<b>Reference</b>	<b>Nerve</b>	<b>Injury Type</b>	<b>Animal</b>	<b>Duration</b>	<b>Results</b>	<b>Proposed Mechanisms</b>
(Yang, Fang et al. 2015)	Cavernous	Crush	Rat	4 weeks	ASC injection improved erectile function via neuronal (n)NOS-positive nerve regeneration	ASCs may promote neurite outgrowth without direct contact through the neurturin–GFR $\alpha$ 2 pathway
(Ying, Yang et al. 2019)	Cavernous	Crush	Rat	4 weeks	SC-ASC injection increased intracavernous pressure, myelinated axons and dorsal neuronal nitric oxide synthase-positive fibers	SC-ASC-mediated production of neuronal growth factors; protection against hemorrhage-induced apoptosis
(You, Jang et al. 2013)	Cavernous	Crush	Rat	4 weeks	ASC injection significantly improved erectile, though smooth muscle content was similar to controls	Possible mediation of neuronal nitric oxide synthase by injected ASCs
(You, Jang et al. 2015)	Cavernous	Crush	Rat	4 weeks	ASC injection increase maximal and mean intracavernous pressures, and increase erectile function	Increased expression of von Willebrand, thus, angiogenesis, may accelerate healing cascades
(Ying, Yang et al. 2013)	Cavernous	Crush	Rat	12 weeks	ASC injection increased mean arterial and intracavernous pressures; increased smooth muscle/collagen ratio in the corpus cavernosum	ASC secretome of VEGF, BDNF, and CXCL5 upregulated nNOS and acted on Janus kinase (JAK)/signal transducer and activator of transcription (STAT) pathway

**Appendix Table 2: Studies of Facial Nerve Injury.**

<b>Reference</b>	<b>Nerve</b>	<b>Injury Type</b>	<b>Animal</b>	<b>Duration</b>	<b>Results</b>	<b>Proposed Mechanisms</b>
(Sun, Zhou et al. 2011)	Facial	Defect, 8mm	Rat	8 weeks	SC-ASCs in decellularized artery conduit were involved in the axonal regeneration and remyelination more so than ASCs	SC-ASCs interact with endogenous Schwann cells to stimulate nerve regeneration
(Abbas, Borman et al. 2016)	Facial	Transection	Rat	12 weeks	Significant ASC-mediated axonal regeneration quantified by electrophysiology and histology	SC-ASC transdifferentiation suspected
(Ghoreishian, Rezaei et al. 2013)	Facial	Defect, 7mm	Dog	12 weeks	ASCs in an ePTFE conduit increased nerve conduction velocity; no appreciable histological change between groups	Possible ASC-mediated acceleration of axonal regeneration through ePTFE tube
(Watanabe, Sasaki et al. 2017)	Facial	Defect, 7mm	Rat	13 weeks	ASCs or SC-ASCs in collagen conduits performed to near-autologous metrics with facial palsy scoring system	Secretion of neurotrophic factors (NGF, BDNF, GDNF); hypoxia induced upregulation of angiogenic and anti-apoptotic factors (VEGF, HGF, bFGF)

**Appendix Table 3: Studies of Laryngeal Nerve Injury.**

<b>Reference</b>	<b>Nerve</b>	<b>Injury Type</b>	<b>Animal</b>	<b>Duration</b>	<b>Results</b>	<b>Proposed Mechanisms</b>
(Li, Xu et al. 2017)	Laryngeal	Crush	Rat	6 weeks	ASCs injection hastened vocal fold movement regeneration, compared to SC-ASCs and ECM injections	ASCs secretion of trophic factors, stabilization of the microenvironment

**Appendix Table 4: Studies of Peroneal Nerve Injury.**

<b>Reference</b>	<b>Nerve</b>	<b>Injury Type</b>	<b>Animal</b>	<b>Duration</b>	<b>Results</b>	<b>Proposed Mechanisms</b>
(Tomita, Madura et al. 2012)	Peroneal	Defect, 10mm	Rat	10 weeks	SC-ASC increased nerve regeneration and motor functional recovery	SC-ASC associated with neurites and provided trophic support to existing and regenerating axons
(Passipieri, Dienes et al. 2019)	Peroneal	Defect, 6mm	Rat	12 weeks	ASC in PCL conduit increased neurofilament and Schwann cell presence with enhanced recovery of muscular contraction	ASC-mediated repair at the distal stump promoted re-functionalization of neuromuscular junctions

**Appendix Table 5: Studies of Sciatic Nerve Injury.**

Reference	Nerve	Injury Type	Animal	Duration	Results	Proposed Mechanisms
(di Summa, Kingham et al. 2010)	Sciatic	Defect, 10mm	Rat	2 weeks	SC-ASC in fibrin conduit increased axonal regeneration and Schwann cell presence relative to sham	Likely similar mechanisms between SC-ASC and Schwann cells in regeneration
(Erba, Mantovani et al. 2010)	Sciatic	Defect, 10mm	Rat	2 weeks	ASCs in a conduit stimulate proximal axonal outgrowth; upregulate Schwann cell proliferation in distal stump	Regenerative paracrine secretome of ASCs; ASC downregulation of SRY gene
(Kingham, Kolar et al. 2014)	Sciatic	Defect, 10mm	Rat	2 weeks	ASCs in fibrin conduit enhanced overall axon growth	ASCs increase intraneural angiogenesis, enhance GAP-43, and activate transcription factor (ATF)-3 expression
(Suganuma, Tada et al. 2013)	Sciatic	Defect, 10mm	Rat	2 weeks	ASCs in collagen conduit promoted significantly faster nerve regeneration per protein gene product 9.5	Likely secretion of some humoral factor like Neu-1 and/or VEGF, with Schwann cell transdifferentiation not observed
(Marconi, Castiglione et al. 2012)	Sciatic	Crush	Mouse	3 weeks	Significant improvement in fiber sprouting and the reduction of inflammatory infiltrates	ASCs induced a local production of GDNF through Schwann cells activation
(Jiang, Chen et al. 2015)	Sciatic	Defect, 20mm	Rat	4 weeks	ASCs in decellularized nerve did not elicit an immune response	ASCs mediate CD3 <sup>+</sup> , CD4 <sup>+</sup> , and CD8 <sup>+</sup> subsets in a manner similar to autograft
(Kappos, Baenziger-Sieber et al. 2018)	Sciatic	Crush	Rat	4 weeks	ASC injection resulted in no significant differences in G-ratio or relative muscle mass compared to controls	Perhaps insufficiently severe model and/or insufficient stimulation by neuronal factors

**Appendix Table 5 (continued)**

Reference	Nerve	Injury Type	Animal	Duration	Results	Proposed Mechanisms
(Luo, Zhang et al. 2012)	Sciatic	Defect, 50mm	Dog	4 weeks	ASCs with TGFβ in decellularized nerve ECM increased nerve regeneration more so than control	VEGF significantly increased in TGFβ-exposed ASCs; reduced inflammatory response; ASCs reduction of apoptosis
(Masgutov, Masgutova et al. 2018)	Sciatic	Defect, 10mm	Rat	4 weeks	ASCs increased survival of ganglia neurons, improved vascularization, increased distal myelination	ASC-mediated angiogenesis; possible SC-ASC transdifferentiation
(Rodriguez Sanchez, de Lima Resende et al. 2019)	Sciatic	Crush	Rat	4 weeks	ASC-mediated normalization of EMG amplitude and gait recovery, though no differences in muscle mass	Concentration of pro-regenerative molecules in the microenvironment like BDNF, neurotrophin-3/4, VEGF, IGF1
(Sowa, Imura et al. 2012)	Sciatic	Defect, 5mm	Mice	4 weeks	ASCs in gelatin conduits promoted axonal regeneration and myelin formation, comparable to Schwann cell control	No evidence of transdifferentiation suggesting naive mechanisms of ASC mediation
(Trempe, Meyer Zu Schwabedissen et al. 2015)	Sciatic	Defect, 10mm	Rat	4 weeks	Syngeneic ASCs in fibrin conduit increased axonal regenerated relative to xenogeneic ASCs	Transdifferentiation of transplanted ASC; immunosuppressive properties of inhibiting mixed lymphocyte proliferation
(Allbright, Bliley et al. 2018)	Sciatic	Defect, 15mm	Rat	6 weeks	ASCs in poloxamer conduit increased axonal regrowth	Trophic and ASC-macrophage mediation promote regeneration over inflammation
(Hsieh, Chang et al. 2016)	Sciatic	Defect, 10mm	Rat	6 weeks	ASCs on external wall of PLA conduit increased regenerated nerve and number of myelinated axons	ASC migration into conduit toward injury site acted as epineural-like support; possible local Schwann cell interactions

Appendix Table 5 (continued)

Reference	Nerve	Injury Type	Animal	Duration	Results	Proposed Mechanisms
(Hsueh, Chang et al. 2014)	Sciatic	Defect, 10mm	Rat	6 weeks	ASCs in chitosan-coated silicone conduit increased myelinated axons density, muscle fiber diameter, and gait stride lengths	ASC-mediated inhibition of IL-1 $\beta$ and leukotriene B4 receptor-1; conversion into neurosphere morphology from ASCs
(Dai, Huang et al. 2013)	Sciatic	Defect 15mm	Rat	8 weeks	Combination of SCs and ASCs had the greatest functional gait recovery and nerve conduction velocity	Synergistic effects of occulting ASCs with Schwann cells, with emphasis on NGF production
(Georgiou, Golding et al. 2015)	Sciatic	Defect, 15mm	Rat	8 weeks	SC-ASCs in collagen conduit increased axon presence in distal, but not proximal, stump	SC-ASCs enhanced neurite outgrowth <i>in situ</i> ; increased growth factor mRNAs possibly due to cell-ECM interaction
(Liu, Yang et al. 2014)	Sciatic	Defect, 10mm	Rat	8 weeks	ASCs in gelatin-ceramic conduit increased gait function and CMAP relative to autograft	Dampening of inflammatory and foreign body response, being both ASC and conduit mediated
(Masgutov, Masgutova et al. 2016)	Sciatic	Defect, 10mm	Rat	8 weeks	ASCs increased glial cell presence	ASC-mediated neurotrophic factor transport
(Carriel, Garzon et al. 2017)	Sciatic	Defect, 10mm	Rat	12 weeks	ASC-filled conduit upregulated neurofilament and growth associated protein (GAP-43)	Potential temporal regulation of nerve sprouting via neurofilament and GAP-43 mediation
(Chato-Astrain, Campos et al. 2018)	Sciatic	Defect, 10mm	Rat	12 weeks	ASCs increased nerve regeneration and functional recovery	Insufficient evidence for ASC-specific contribution when inside nerve conduit
(Hernandez-Cortes, Toledo-Romero et al. 2017)	Sciatic	Defect, 10mm	Rat	12 weeks	ASCs in a PCL conduit increased nerve area, myelin area, myelinated fibers	ASC-mediated enhancement of mid and distal regeneration zones
(Kappos, Engels et al. 2015)	Sciatic	Defect, 10mm	Rat	12 weeks	SC-ASCs in fibrin conduit showed less muscle atrophy and superior functional gait results	SC-ASC more closely mimicked the Schwann cell phenotype promoting the intrinsic regeneration cascade

**Appendix Table 5 (continued)**

<b>Reference</b>	<b>Nerve</b>	<b>Injury Type</b>	<b>Animal</b>	<b>Duration</b>	<b>Results</b>	<b>Proposed Mechanisms</b>
(Mohammadi, Azizi et al. 2013)	Sciatic	Defect, 10mm	Rat	12 weeks	ASCs in silicone conduit increased nerve fiber area, functional recovery, and gastrocnemius mass	Possible ASC-macrophage interactions promoting enhanced nerve regeneration via IL-1
(Mohammadi, Asadollahi et al. 2014)	Sciatic	Defect, 10mm	Rat	12 weeks	ASCs in artery graft increased myelination, toe spread, and gastrocnemius muscle mass	ASC interaction with axons and Schwann cell-like cells assisting remyelination and structural recovery
(Santiago, Clavijo-Alvarez et al. 2009)	Sciatic	Defect, 6mm	Rat	12 weeks	ASCs in PCL conduit increased gastrocnemius muscle mass, but diminishing difference in gait relative to control	Likely ASC-mediate paracrine effects and not Schwann cell transdifferentiation at the sites of injury
(Xu, Zhang et al. 2016)	Sciatic	Defect, 10mm	Rat	12 weeks	ASCs and Schwann cells in silk-collagen conduit similar to autograft with considerably reduced local inflammation	ASCs transdifferentiate more quickly when in contact with Schwann cells, accelerating axonal growth
(Saller, Huettl et al. 2018)	Sciatic	Defect, 20mm	Rat	16 weeks	ASCs applied at coaptation sites with reverse polarity autograft improved remyelination, axon ingrowth, and gait	ASC-mediated retrograde tracing of reestablished axonal tracts from the distal stump

**Appendix Table 5 (continued)**

<b>Reference</b>	<b>Nerve</b>	<b>Injury Type</b>	<b>Animal</b>	<b>Duration</b>	<b>Results</b>	<b>Proposed Mechanisms</b>
(Klein, Vykoukal et al. 2016)	Sciatic	Defect, 10mm	Rat	24 weeks	ASCs in collagen tube showed higher motor and sensory nerve conduction velocities, and increased Schwann cell presence	ASC-mediated organization of axonal arrangement throughout the conduit
(Orbay, Uysal et al. 2012)	Sciatic	Defect, 10mm	Rat	24 weeks	ASCs or SC-ASCs in silicone conduits increase myelination; ASCs in silicone conduit increased gait function	Paracrine effects of ASCs/SC-ASCs; native architecture (use of decellularized nerve) likely not relevant to myelination
(Wei, Gong et al. 2011)	Sciatic	Defect, 10mm	Rat	24 weeks	ASCs in chitosan/silk fibroin conduit enhanced nerve continuity, gait recovery, and better reinnervated the gastrocnemius	ASC-mediated and immediate prevention or reduction of axonal dieback

## Appendix B TIPD Construction Parts Details

PART NAME	PART DETAILS (VENDOR, CODE)	QUANTITY NEEDED
<i><u>MOTION COMPONENTS</u></i>		
Stepper Motor	NEMA 17 Stepper Motor, Bipolar: 2A, 59Ncm, 48mm body, 4-lead (Stepper Online, 17HS19-2004S1)	2
Stepper Driver	DRV8825 Stepper Motor Driver Module, six micro-step resolutions	2
Servomotor	DSS-P05 Standard Servomotor, 5kg (DFRobot, SER0020)	4
<i><u>ELECTRONICS &amp; CIRCUITRY</u></i>		
Microcontroller	Mega 2560 (Arduino, A000067)	1
DC Barrel to PCB	DC Power Jack/Connector 2.1mm x 5.5mm (Gravitech, CON-SOCJ-2155)	1
DC-DC Step Down Module	LM2596 DC to DC Buck Converter (eBoot, EXPSFD005794)	1
Power Supply	12V 5A 60W Power Supply Adapter, barrel jack 5.5mm x 2.1mm (SUPERNIGHT, ABC044)	1
<i><u>HARDWARE</u></i>		
Side Chamber (body)	Clear Cast Acrylic Tube, 2-1/4" OD x 2" ID (McMaster-Carr, 8486K345)	1
Top Chamber	Brilliance Storage Container, 750ml (Rubbermaid, 2024352)	1
Scaffold Magnets	6mm x 3mm Brushed Nickel Pawn Style Magnets (FINDMAG B077K364Z7)	
Ball Bearing	Stainless Steel Ball Bearing for 3 mm Shaft Diameter (McMaster-Carr, 7804K128)	2
Bearing Spacer	Aluminum Unthreaded Spacer, 6 mm OD, 3 mm Long, for M3 Size (McMaster-Carr, 94669A003)	
Post Collar Inserts	Aluminum Unthreaded Spacer, 8 mm OD, 20 mm Long, M5 Screw (McMaster-Carr, 94669A063)	10
Post Collar Washers	Chemical-Resistant PTFE Plastic Washer for M5 Screw Size (McMaster-Carr, 95630A640)	10

<b>PART NAME</b>	<b>PART DETAILS (VENDOR, CODE)</b>	<b>QUANTITY NEEDED</b>
<u><i>COUPLERS &amp; TUBING</i></u>		
Tubing	Tygon PVC Tubing for Chemicals, 1/16" ID, 1/8" OD (McMaster-Carr, 5155T12)	8
	Super-Soft Latex Rubber Tubing, Semi-Clear, 3/16" ID, 1/4" OD (McMaster-Carr, 5234K971)	2
Couplers	Luer-Lok x 3/16" ID Hose, Barb Adaptor (McMaster-Carr, 51525K271 [male] & 51525K285 [female])	4
	Luer-Lok for 1/16" ID Hose, Barb Adaptor (McMaster-Carr, 51525K275 [male] & 51525K281 [female])	2
	4-Way Stopcock, 2 Female Luer-Lok, Swivel Male Luer-Lok (Qosina, 88218)	2

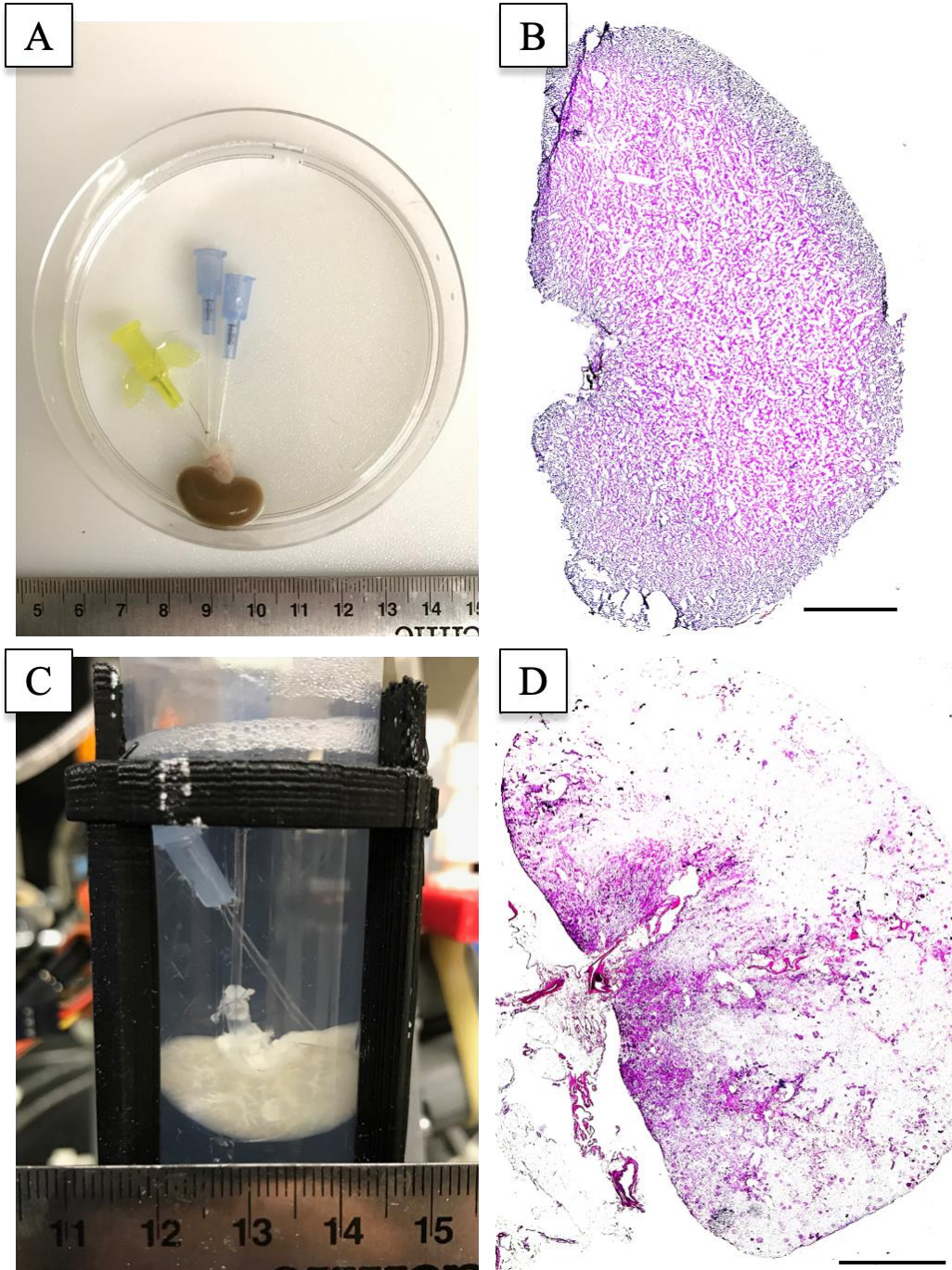
## **Appendix C Perfusion Decellularization Using TIPD**

Decellularization of vascularized composite tissues can be achieved using perfusion in the TIPD, though requires cannulation of at least one vessel for successful perfusion.

### **Appendix C.1 Kidney Perfusion Decellularization**

Rodent kidneys from recently-deceased Lewis rats were obtained, where the vascular and ureter pedicle was cannulated using 20G Introcan IV catheters for the renal artery and ureter and a 24G Introcan IV catheter (B. Braun, Bethlehem, PA) for the renal vein. The kidney was flushed with 10ml heparinized saline prior to decellularization. For perfusion decellularization, 100ml 1% sodium dodecyl sulfate (SDS, Millipore-Sigma) was pumped for approximately 20 hours, where the SDS was recirculated after tissue contact (0.3% was only used for infusion decellularization). Next, 1000ml DI water was pumped through the tissue and was not recirculated. To further ensure clearance of the SDS, 100ml 1% Triton X-100 (Millipore-Sigma) was pumped and recirculated through the tissue for 20 hours, followed by an additional 1000ml DI water (non-recirculated). The pump was set to 1/8-step for kidney perfusion.

**Appendix Figure 1A,C** displays a rodent kidney cannulated IV catheters, where the artery is affixed to a luer-lok junction for establishing fluid flow and subsequent decellularization. **Appendix Figure 1B** displays H&E of a native rodent kidney, presenting nuclei prominently about the periphery. **Appendix Figure 1D** displays H&E of the kidney after decellularization showing preservation of the ultrastructure nearest to the pedicle and lacking visible nuclei.



**Appendix Figure 1: Rodent Kidney Perfusion Decellularization using the TIPD.**

Perfusion through the renal artery of a rodent kidney was achieved to show proof of concept for perfusion decellularization, where the resulting scaffold and H&E staining resulted in a

translucent scaffold. Conceptually, the method of arterial cannulation and perfusion-based flow can be achieved in any vascular structure able to accommodate a port but doing so in this specific system requires further investigation. Additionally, understanding the effects that fluidic shear imposes on the integrity or directionality of residual fiber alignment within a scaffold warrants additional investigation. Further, the addition of multiple points of entry would likely enhance infusion decellularization. Utilizing the same device, perfusion decellularization of solid organs via pedicle access is achievable, though the device would likely be better suited to have anatomically relevant outflows present (i.e., for the kidney, inflow into the artery and independent outflows from the vein and ureter). This could allow more direct control over the intra-scaffold pressure, and speculatively, may better maintain the scaffold architecture if drawing fluid from the outflow(s) using one or a series of peristaltic pumps.

### **Appendix C.2 Perfusion Decellularization of the Rodent Free Flap**

Traumatic wounds are a significant source of morbidity and mortality for military personnel and the civilian populations. High energy injuries such as blast, ballistic, and motor vehicle often result in complex wounds (extremities, craniofacial, genitourinary, trunk) with exposed critical structures such as bone, tendon, blood vessels, nerve, and hardware. Grafts and local tissue flap reconstruction are often inadequate to provide durable coverage for these structures (Hallock 1991).

Microvascular free tissue transfer (free flaps) are required for such complex reconstructions. This entails transferring tissue (e.g., skin, fascia, muscle or bone) with its blood supply from the patient's own body to the distant area of injury using microsurgical technique to

reattach vessels and restore blood flow to the transferred tissue. Raising these free flaps are lengthy operations can result in significant donor site morbidity, a summary of which is presented in

**Appendix Table 6.**

**Appendix Table 6: Free Flap Donor Site Morbidities.**

<b>Donor Free Flap Site</b>	<b>Donor Site Morbidity</b>	<b>Incidence</b>	<b>Total Patients</b>	<b>Median Follow Up</b>	<b>Reference</b>
Radial forearm	Aesthetic deformity	30%	20	17 mos.	(Huang, Chen et al. 2004)
		45%	20	24 mos.	(Liu, Li et al. 2011)
	Hematoma	2%	113	12 mos.	(Knott, Seth et al. 2016)
		0%	30	3 mos.	(Riecke, Assaf et al. 2015)
	Infection	30%	113	12 mos.	(Knott, Seth et al. 2016)
		0%	30	3 mos.	(Riecke, Assaf et al. 2015)
	Musculoskeletal dysfunction	35%	20	24 mos.	(Liu, Li et al. 2011)
		3%	40	1.5 mos.	(Schwarzer, Mucke et al. 2016)
	Sensory Disturbance	80%	20	17 mos.	(Huang, Chen et al. 2004)
	(numbness, tingling)	0%	30	3 mos.	(Riecke, Assaf et al. 2015)
		30%	20	24 mos.	(Liu, Li et al. 2011)
		68%	40	1.5 mos.	(Schwarzer, Mucke et al. 2016)
	Seroma	1%	113	12 mos.	(Knott, Seth et al. 2016)
		3%	30	3 mos.	(Riecke, Assaf et al. 2015)
	Wound Reopening	3%	113	12 mos.	(Knott, Seth et al. 2016)
		0%	30	3 mos.	(Riecke, Assaf et al. 2015)
		14%	41	3 mos.	(Schwarzer, Mucke et al. 2016)

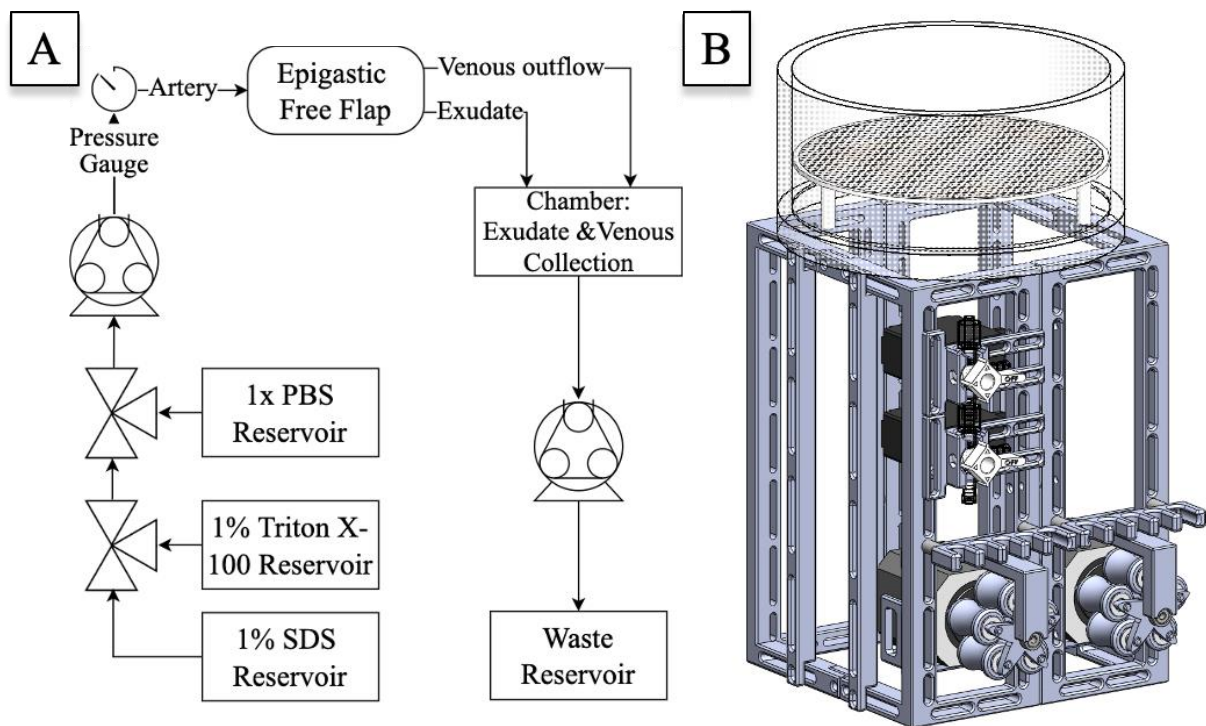
**Appendix Table 6 (continued)**

<b>Donor Free Flap Site</b>	<b>Donor Site Morbidity</b>	<b>Incidence</b>	<b>Total Patients</b>	<b>Median Follow Up</b>	<b>Reference</b>
Anterolateral thigh	Aesthetic deformity	38%	21	13 mos.	(Huang, Chen et al. 2004)
		43%	14	24 mos.	(Liu, Li et al. 2011)
	Hematoma	5%	113	12 mos.	(Knott, Seth et al. 2016)
	Infection	5%	113	12 mos.	(Knott, Seth et al. 2016)
	Musculoskeletal dysfunction	88%	32	19 mos.	(Kimata, Uchiyama et al. 2000)
		0%	14	24 mos.	(Liu, Li et al. 2011)
	Sensory Disturbance	88%	32	19 mos.	(Kimata, Uchiyama et al. 2000)
		43%	14	24 mos.	(Liu, Li et al. 2011)
		100%	1	13 mos.	(Huang, Chen et al. 2004)
	Seroma	0%	113	12 mos.	(Knott, Seth et al. 2016)
	Wound Reopening	2%	113	12 mos.	(Knott, Seth et al. 2016)

Though researchers have attempted to develop alternatives to autologous free flaps to mitigate these complications, but have been unable to produce results that are both amply viable, possessing sufficient cell lining to contain blood flow within the vasculature of the graft, and sufficiently durable, withstanding the physiological rigors of reperfusion (Zhang, Johnson et al. 2016). Furthermore, the field of tissue engineering lacks some of the requisite technologies to fulfill the translation from concept to commercialization, particularly as it pertains to a functionally-cellularized construct.

Perfusion-based tissue engineering has shown exceptional promise in the literature for scaffold decellularization (Guyette, Gilpin et al. 2014), and so the TIPD from **4.1** was redesigned with a larger chamber to accommodate the length of an entire free flap (**Appendix Figure 2** and **Appendix Figure 3**). The use of a tissue’s own vascular network coupled with shearing fluid

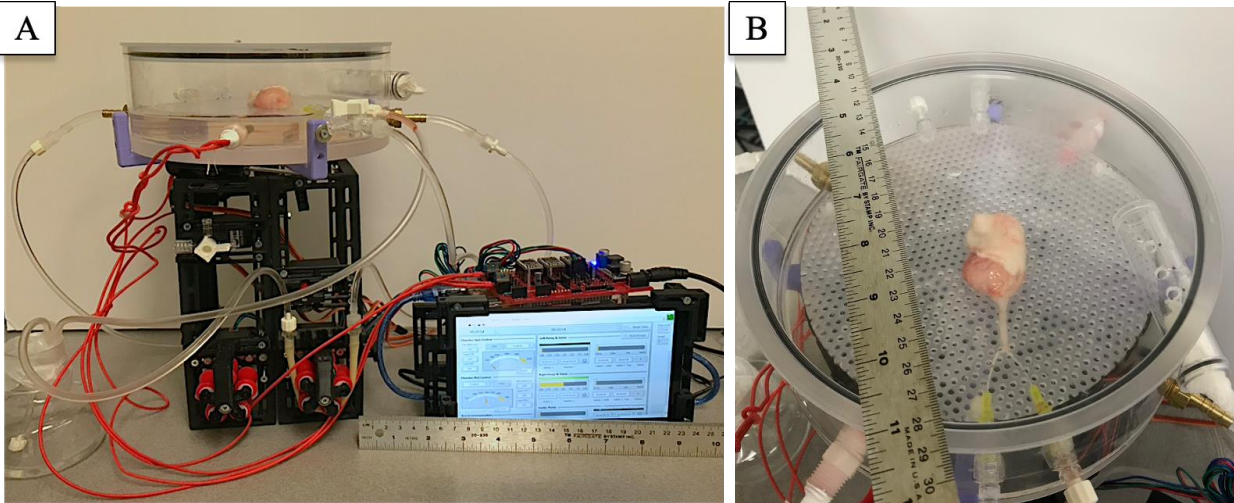
forces removes whole cells and debris, while preserving the vasculature, if performed correctly. It is the eventual goal that the perfusion system can also offer unique capabilities for recellularization, introducing cells directly into the scaffold by means of the scaffold's own vasculature while also controlling the fluid mechanics by which the cells are deposited.



**Appendix Figure 2: Schematic and CAD/CAM Rendering of TIPD (Modified from Figure 45).**

**A. Diagram depicting solution flow into and out of the free flap via perfusion device.**

**B. CAD/CAM rendering of the perfusion device used for free flap decellularization.**



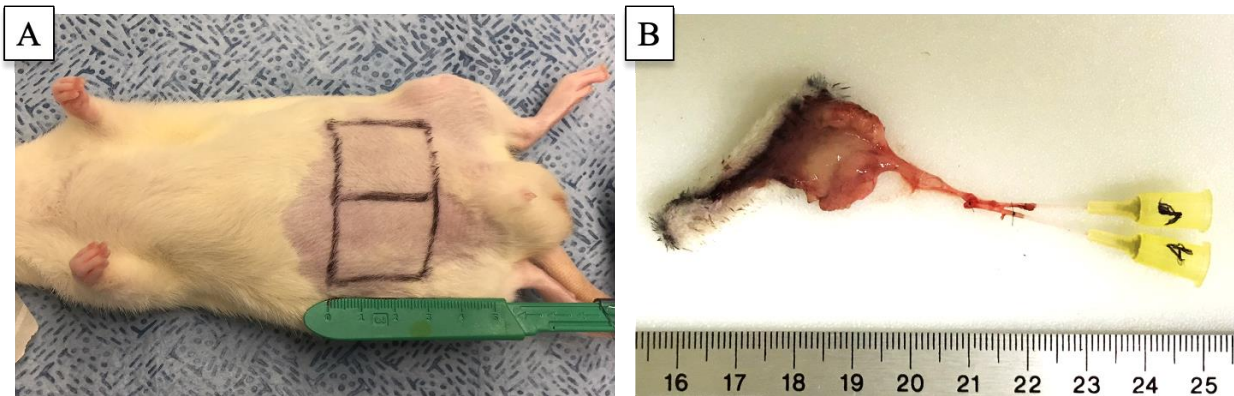
**Appendix Figure 3: Rodent Free Flap in TIPD Chamber Prior to Decellularization.**

### **Appendix C.2.1 Methods for Harvesting Rodent Epigastric Free Flaps**

Epigastric free flaps were harvested from Sprague Dawley rats (6-8 weeks, Charles River Laboratories, Wilmington, MA). All surgeries were performed under sterile conditions by a single surgeon. Rats were anesthetized using 2.5% isoflurane in pure oxygen, followed by an intraperitoneal combination injection of ketamine (Ketaset, 50mg/kg), xylazine (AnaSed, 2.5mg/kg), and acepromazine (AceproJect, 1.25mg/kg) immediately prior to the procedure so that the nosecone could be removed from the surgical field (all anesthetics: Henry Schein, Melville, NY). In the supine position, the harvest site was identified as a section approximately  $10 \times 8$  cm on the abdominal wall. The harvest region was further defined as between the anterior axillary lines, from the xiphoid process and costal arch to the pubic tubercle and inguinal ligaments. The fur was shaved, and skin was prepared with alternating wipes with 70% alcohol and chlorohexidine followed by marking prior to incision (**Appendix Figure 4A**).

A full-thickness incision, which included the skin and subcutaneous tissue above the fascia, was made into the abdominal wall, following the marked perimeter (approximately  $3 \times 8$  cm). A

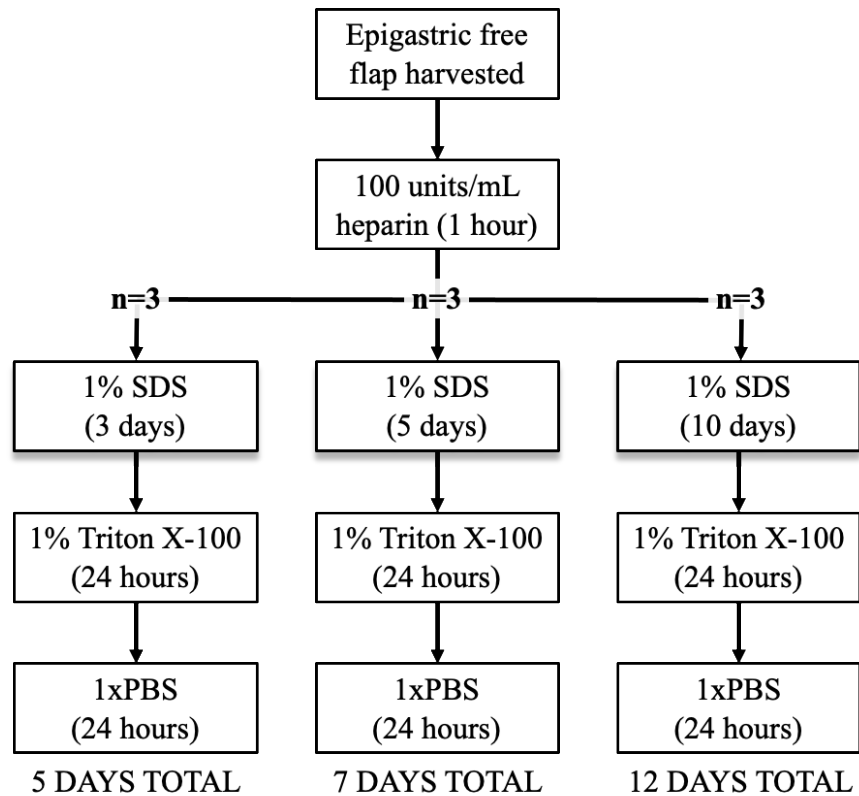
bilateral incision along linea alba yielded two independent tissue flaps. The superficial inferior epigastric vessels were be exposed and preserved. Distal to the origin of the superficial inferior epigastric vessels, the femoral vessels were dissected, ligated, and divided. The flap was then raised in a superior-to-inferior direction and everted caudally. The femoral vessels were ligated, cut at the groin and a 24G catheter (B. Braun Medical, Bethlehem, PA) was inserted into femoral artery and vein, and secured with 7-0 nylon suture (Microsurgery Instruments, Bellaire, TX) resulting in free tissue as shown in **Appendix Figure 4B**. The epigastric flap was irrigated with heparinized saline (100 U/ml). Additional details on this free flap harvesting method have been previously published (Casal, Pais et al. 2017). Animals were euthanized following procurement of the graft. Animal procedures were approved by the University of Pittsburgh IACUC prior to any experimentation.



**Appendix Figure 4: Harvest of the Rodent Epigastric Free Flap.**

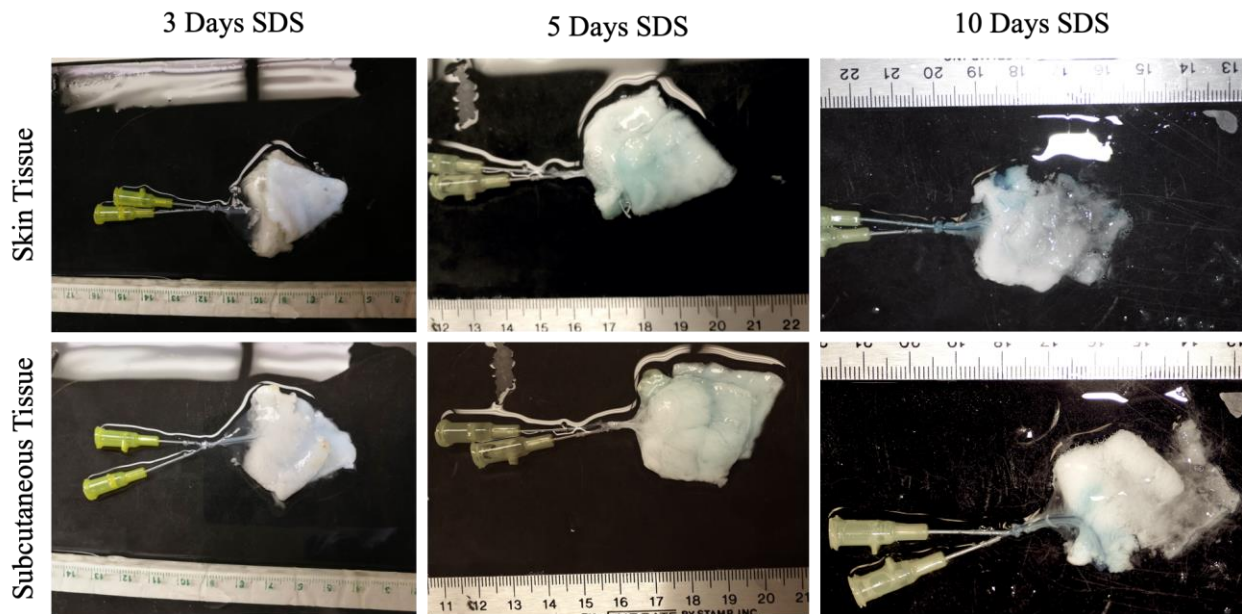
## Appendix C.2.2 Methods for Decellularizing Epigastric Free Flaps

Free flaps were perfused with heparinized saline (10U/ml) by hand immediately after harvest. The flap was then connected to the TIPD by catheterized artery. For all perfusion, the peristaltic pump speed was set at 1/32 step throughout (refer to **Figure 53** for fluid flow characteristics). Then the one of three decellularization procedure were performed by first perfusing the flap with 10U/ml heparinized saline (1 hour), and then 1% Sodium dodecyl sulfate was perfused either for 3 days, 5 days, or 10 days, followed by 1% Triton X-100 and 1xPBS, each for 24 hours. A flow diagram of the decellularization procedures is presented in **Appendix Figure 5**.



**Appendix Figure 5: Flow Diagram of Free Flap Perfusion Scheme.**

The gross appearance of the free flaps after each of the decellularization processes are shown are **Appendix Figure 6**.



**Appendix Figure 6: Skin and Subcutaneous View of Decellularized Free Flaps.**

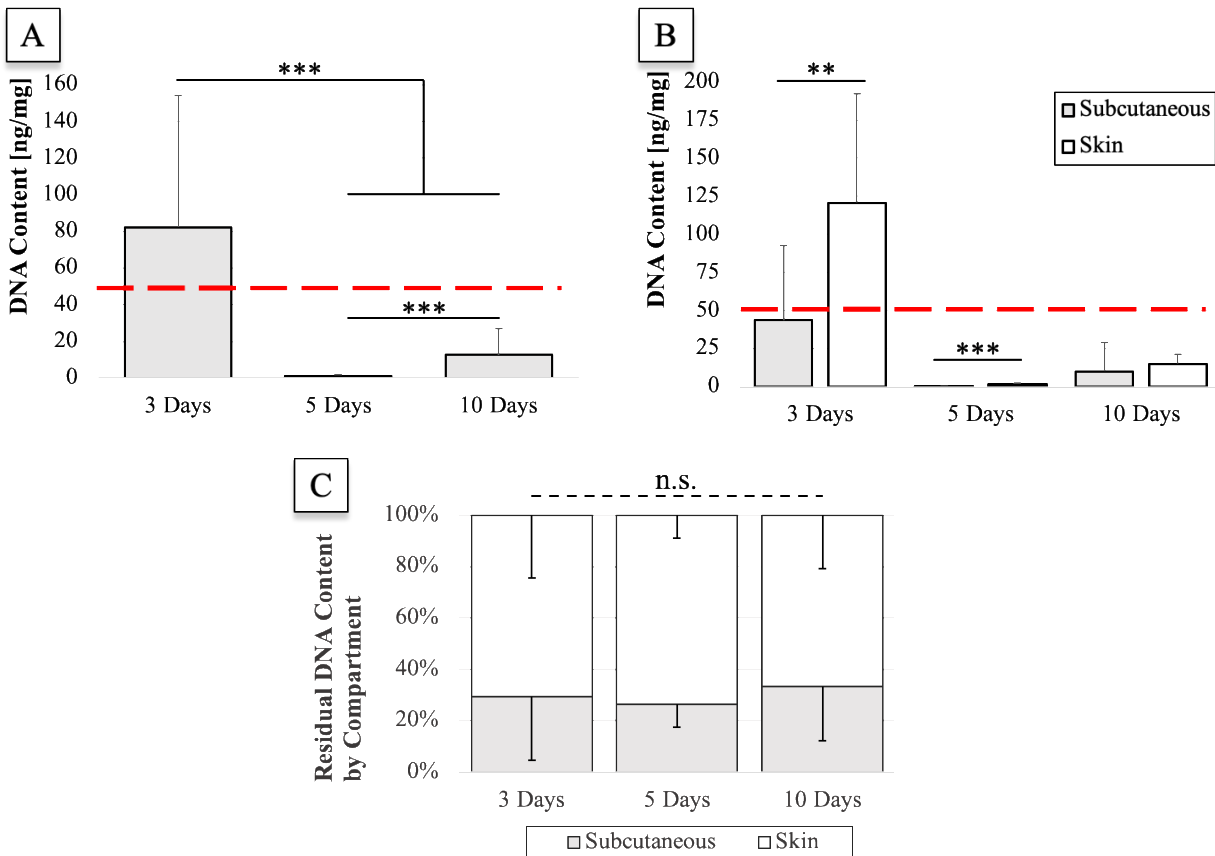
Resulting appearance of scaffolds after each decellularization process. The top row presents the epigastric flap with the skin oriented superficially, and the bottom row presents the epigastric flap with the subcutaneous tissue oriented superficially.

### **Appendix C.2.3 DNA Quantification and Analyses After Free Flap Decellularization**

For DNA quantification, each decellularized free flap was divided into four sections based on the overall length of the flap, where the length dimension was oriented parallel to the pedicle. AllPrep DNA/RNA/Protein Mini Kit (Qiagen, Germany) was used to extract DNA from tissues

and Quant-iT PicoGreen dsDNA assay kit (P7589, Invitrogen, Waltham, Massachusetts, USA) was used to for quantification. Briefly, native and decellularized samples (n=3 in all groups) were freeze-dried for 24 hours and weighed before homogenization. Then tissues were mixed with 600  $\mu$ L RLT buffer and homogenized for 30 seconds. Supernatants were moved wells of a 96-well plate, and diluted Quant-iT PicoGreen dsDNA reagent (1:200). Fluorescence intensity was measured to quantify DNA (Tecan Infinite 200 Pro, Switzerland), and the measured DNA content was normalized to the initial dry weight of the tissue and then was normalized further based on “Compartment” being either skin tissue or subcutaneous tissue, and then one of four “Regions” being Prx (Proximal), Prx-Dst, Dst-Prx, and Dst (Distal). Regions are illustrated in **Appendix Figure 8A**.

**Appendix Figure 7** displays DNA quantification by Process and Compartment. The dashed red line denotes the accepted quasi-standard of 50ng DNA per milligram tissue as the threshold for acceptability (ASTM: F3354 – 19). As shown the 3-Day Process contained the most DNA content relative to the other two processes, followed by the 10-Day Process, and then the 5-Day Process. It is then shown that in the 3-Day and 5-Day Processes, the skin contains significantly more residual DNA content, though the residual DNA content in the skin of the 10-Day Process is higher than its subcutaneous counterpart. When normalizing by percentage DNA within each Compartment (**Appendix Figure 7C**), there is no difference between the three processes despite the large differences in overall residual DNA, suggesting that the Process functions to decellularize the Compartments similarly over time.



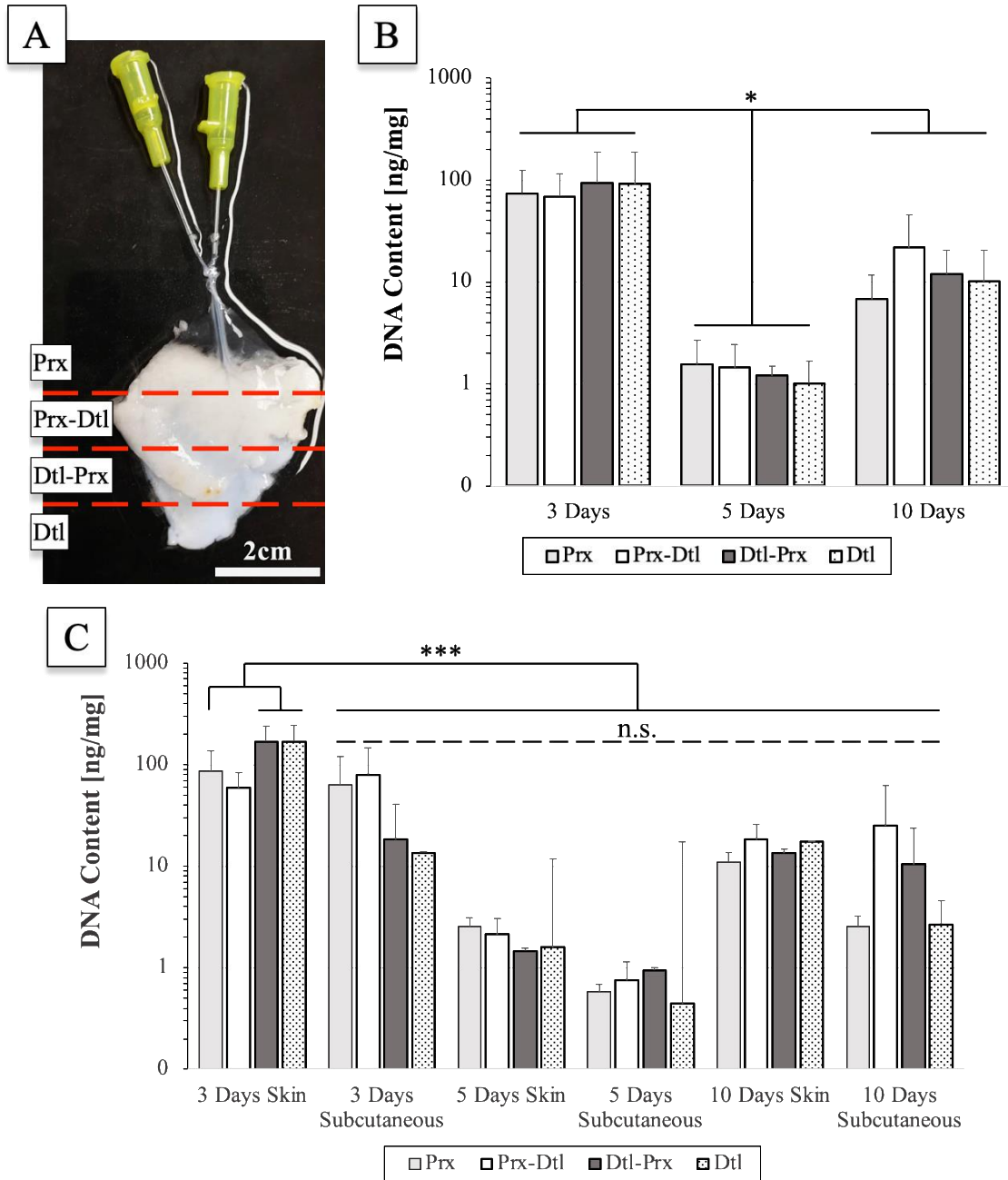
**Appendix Figure 7: Decellularization Efficiency based on Process and Compartment.**

**A.** DNA quantification grouped by SDS perfusion time. **B.** DNA quantification grouped by SDS perfusion time and compartment; **NOTE:** comparisons are between skin and subcutaneous compartments within a process only (i.e., not across compartments of processes). Dashed lines denote 50 ng DNA. **C.** DNA content of each compartments normalized to total DNA in each sample. \*\*  $p < 0.01$  and \*\*\*  $p < 0.001$ .

**Appendix Figure 8** displays the DNA quantification results with maximal normalization, that is, normalized with respect to all Compartments and Regions. Despite the differences in aggregate means across Processes shown in **Appendix Figure 7A**, **Appendix Figure 8B** begins to shown that the distillation of residual DNA by Region begins to negate those differences, where the 3-Day and the 10-Day Process are not significantly from one another in any of the four Regions.

Further distillation by both Compartment and Region, and thus, 8 quantifications per Process, and their comparisons is presented in **Appendix Figure 8C**. As shown, the majority of comparisons are not significant, and of particular relevance are those comparisons between the 5-Day and 10-Day Processes, as, logically, it would follow that a longer decellularization process should remove at least as much DNA content as a process of shorter duration.

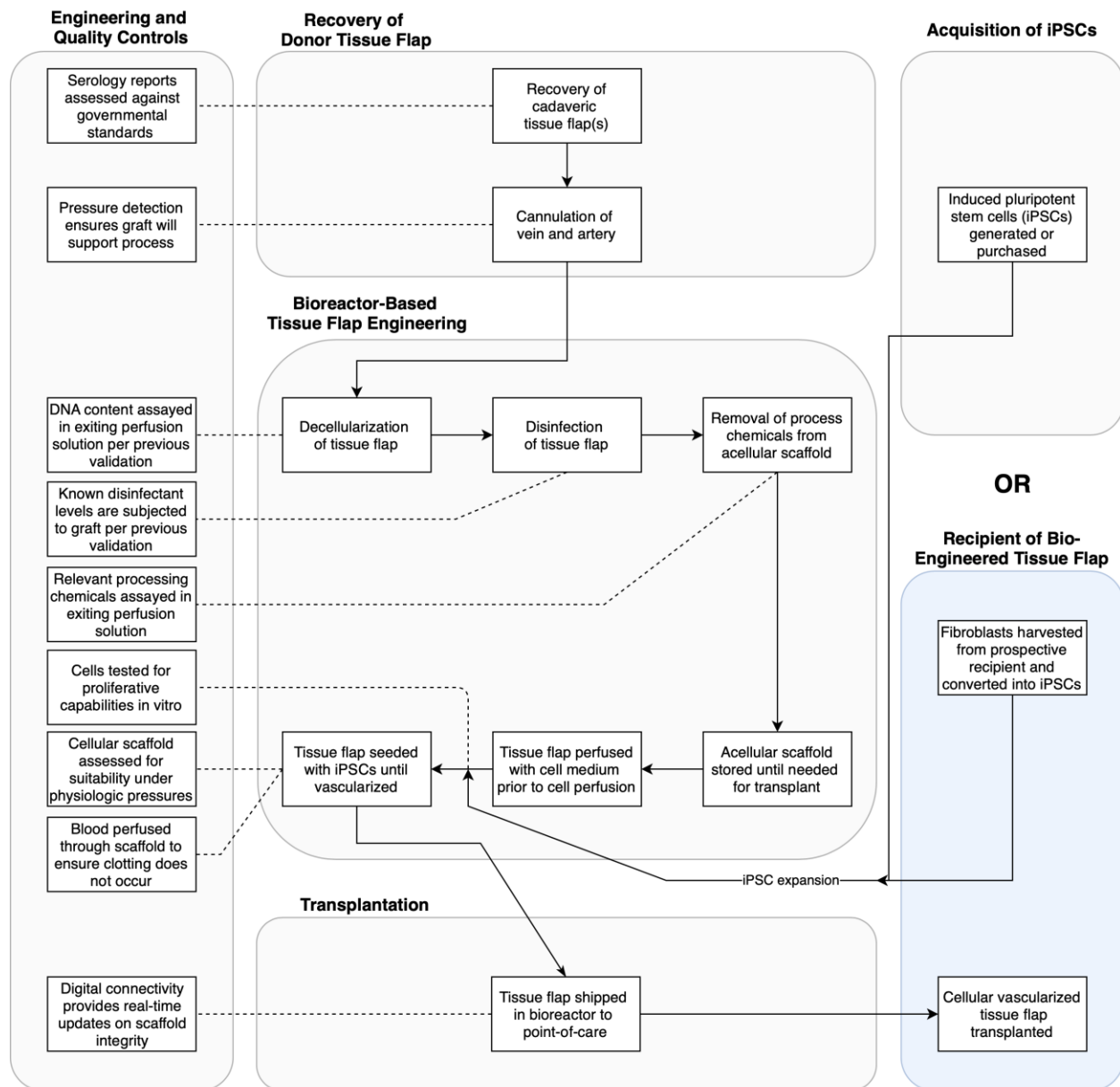
It is possible however, that a process of longer duration (e.g., 10 days) continues to remove DNA from the skin compartment, but due to the damage caused by the decellularization process itself to the vasculature, such solubilized DNA begins to deposit into the subcutaneous tissue, and therefore increases the aggregate DNA content. Perhaps too, such destruction of the hinders the rinsing processes that are comprised of the surfactant Triton X-100 and PBS; if the SDS is functioning only to solubilize cells out of their constituent membranes but requires the subsequent flushing of the rinsing solutions, the damaged vascular structure may prevent such flushing, and therefore result in the increased residual DNA content shown in **Appendix Figure 7**. These statements are, however, speculative and merit additional investigation with particular respect to the preservation of the vascular network.



**Appendix Figure 8: Decellularization Efficiency based on Process, Compartment, and Region.**

**A.** Segmentation of free flap into eight compartments, being skin compartment and the subcutaneous compartment, each subdivided into the four regions shown. **B.** DNA quantification grouped by SDS perfusion time and subdivision. DNA quantification grouped by SDS perfusion time and compartment and subdivision.

\*  $p < 0.05$  and \*\*\*  $p < 0.001$ .



Appendix Figure 9: Conceptual Flow of Free Flap Engineering in TIPD.

## **Appendix D Individual Biocontainment Unit for Preventing Spread of Infectious Respiratory Air during the COVID-19 Pandemic**

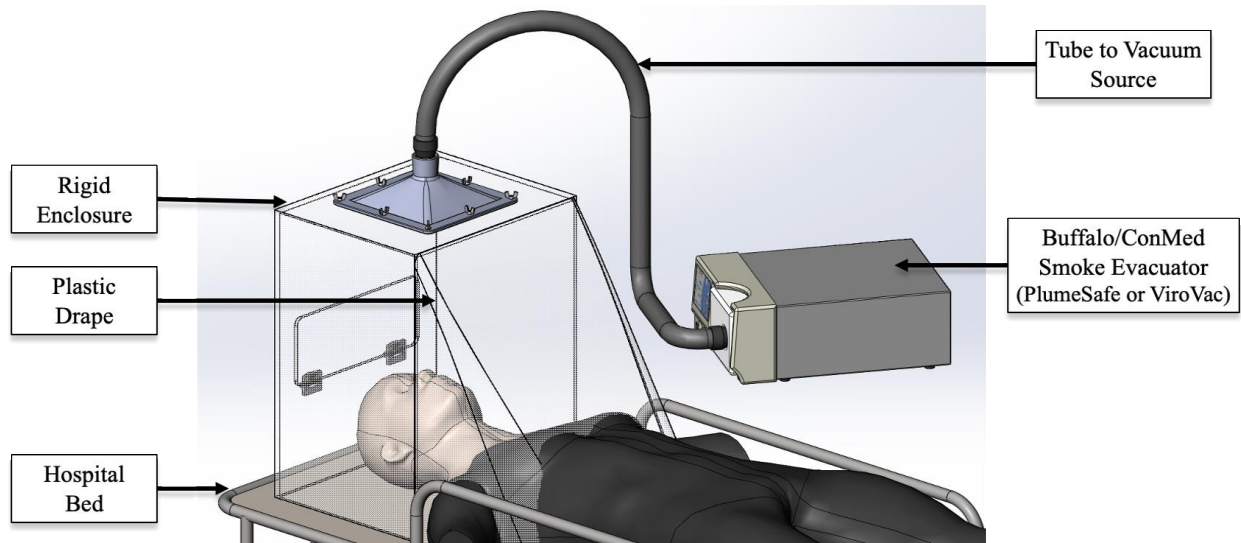
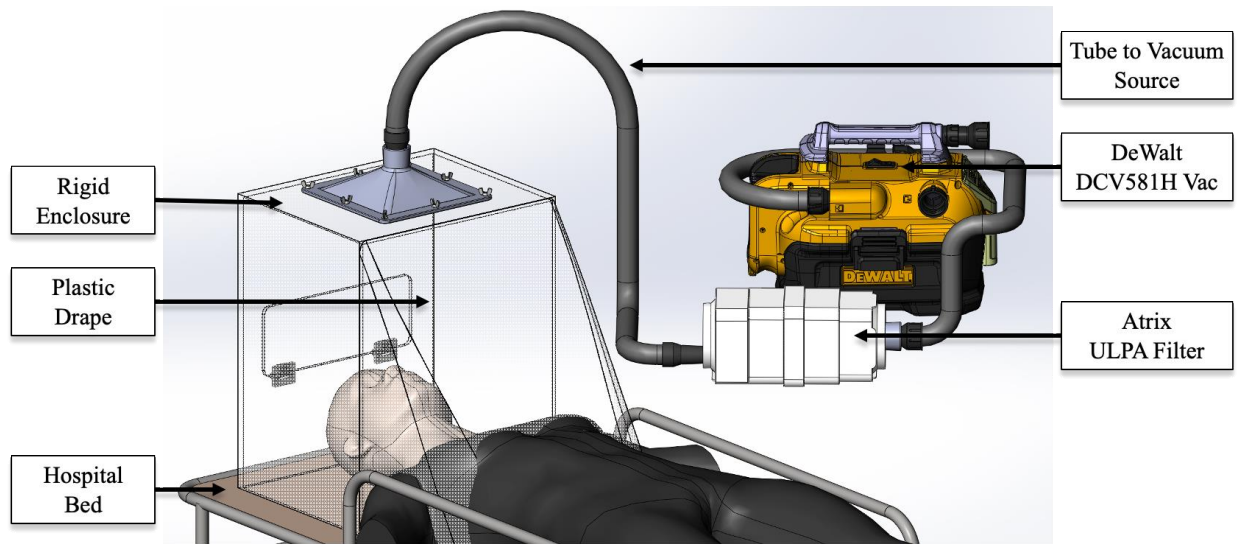
Aerosol-generating respiratory procedures that are performed on patients infected with SARS-CoV-2 virus (COVID-19) have been shown to increase the risk of transmission (Tran, Cimon et al. 2012). While personal protective equipment (PPE) including N95 masks and powered air-purified respirators (PAPR) can protect healthcare workers, the demand for specialized PPE has outstripped supply in many areas, prompting researchers and clinicians to design new protective devices (Mead and Johnson 2004).

Rigid plastic barrier enclosures, better known as “intubation boxes” or “intubation hoods”, have been put into use while performing Aerosol-generating respiratory procedures (Fang, Lin et al. 2020, Martel and Reardon 2020). The concept of physical containment is simple and does indeed ease provider anxiety; however, the lack of rigorous safety testing seriously raises concerns about their efficacy in actually reducing transmission, particularly with respiratory diseases. In current forms, these devices are a splash shield, but the effect on containing aerosol spread is unclear (Canelli, Connor et al. 2020).

Given the novelty of these devices, no explicit framework for testing or validation exists to ensure their safety and appropriateness of use. However, other fields use well-established standards for similar devices. For example, biosafety cabinets (laboratory hoods) protect their users from aerosolized pathogens and undergo a regimen of highly standardized testing. Per NSF/ANSI 49-2018, biosafety cabinets must demonstrate three performance characteristics in order to pass inspection: 1) contaminated air must not escape from within the hood during normal operation, 2) contaminated air must pass through a filter to remove the pathogens (< 0.01%

penetration through the filter or enclosure), and 3) a vacuum system must pull enough air into the hood to prevent pathogens from escaping (>75 feet per minute, fpm).

To meet the need of an “active” intubation hood, that is, a device capable of protecting healthcare workers dealing immediately with an airway of a patient as well as any bystanders who may also be affected, the Individual Biocontainment Unit (IBU) was conceptualized, fabricated, iterated, and validated, the data from which was published (Turer, Good et al. 2021) and Emergency Use Authorization (EUA) filed to FDA such that the system could be deployed clinically. The IBU is a single-patient isolation system that produces negative pressure, drawing air away from the head, face, and neck of a patient, and through an ultra-low particulate air (ULPA) filter. In doing so, potentially contaminated air is also redirected away from healthcare providers in the immediate vicinity of an infected or potentially infected patient. Therefore, the mechanism of action of this device is particulate filtration via negative pressure. See **Appendix Figure 10** for a CAD rendering of the IBU for its use with a commercially-available DeWalt Wet/Dry vacuum or surgical smoke evacuator.



**Appendix Figure 10: IBU Configurations with Multiple Vacuum Sources.**

### **Appendix D.1 Abridged Content from Submission for EUA**

The intended use of the IBU is to remove airborne particles and allergens, such as dust, smoke, pollen, mold spores, animal hair and dander, dust mites and harmful fibers, that may lead to allergic reactions. This intended use is based on our intention to show substantial equivalence

(SE) to the RespirAid Ltd. Mobile Air Filtration System (K981841), per Sec. 880.5045 Medical Recirculating Air Cleaner (Product Code: FRF).

In the context of the Emergency Use Authorization (EUA) for SARS-CoV-19, the anticipated users and use cases for this device include deployment over a patient’s head, neck, and torso regions. Anticipated users and use cases are summarized in **Appendix Table 7**.

**Appendix Table 7: Anticipated Uses and Use Cases of the IBU.**

Users	Use Cases
Anesthesiology	<ul style="list-style-type: none"> <li>• Intubation and extubation</li> <li>• Patient transportation</li> </ul>
Emergency Medicine Critical Care	<ul style="list-style-type: none"> <li>• High flow nasal cannula oxygenation</li> <li>• Bilateral Positive airway pressure (BIPAP)</li> <li>• Continuous positive airway pressure (CPAP)</li> <li>• Intubation and extubation</li> <li>• Patient transportation</li> </ul>
Pulmonology Gastroenterology Otolaryngology	<ul style="list-style-type: none"> <li>• Bronchoscopy</li> <li>• Endoscopy</li> <li>• Patient transportation</li> </ul>
Nurses and Nursing Staff	<ul style="list-style-type: none"> <li>• Patient staging if no room is available</li> <li>• Patient transportation</li> </ul>
Dentistry and Dental Hygienics	<ul style="list-style-type: none"> <li>• All cleaning and orthodontics procedures</li> </ul>
Nursing Homes	<ul style="list-style-type: none"> <li>• Administering contact-based patient care</li> </ul>
Ambulance and Medical Transport	<ul style="list-style-type: none"> <li>• During care and transport</li> </ul>
Mobile and Auxiliary Testing Centers	<ul style="list-style-type: none"> <li>• While performing nasopharyngeal swabs</li> </ul>

### **Appendix D.1.1 Detailed Product and Component Description**

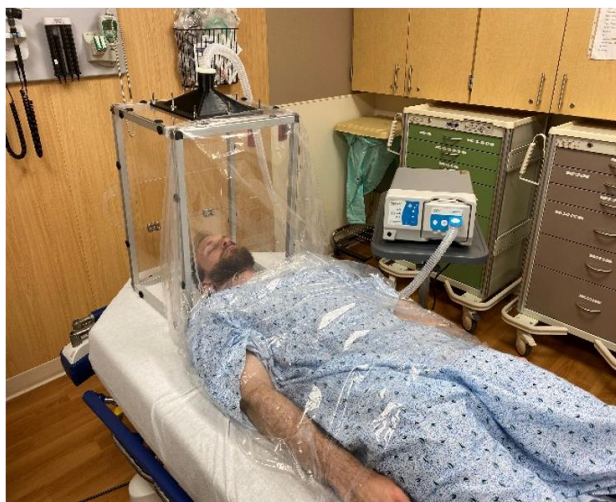
The Individual Biocontainment Device has been designed using similar principles to a Class I Biological Safety Cabinet (Alados, Alcaraz et al. 2010), but in a portable and versatile form (i.e. is deployable and able to be fastened to hospital beds, gurneys, and stretchers, and during

patient transportation either in an ambulance or throughout the hospital). The device consists of a rigid enclosure, which is placed over the head, face, and neck of a patient laying in a hospital bed (supine, prone, or upright) creating a physical barrier between the patient and the healthcare worker. There is a single window in the enclosure which allows access to the patient and may also be closed and sealed to facilitate long-term patient isolation. The enclosure is coupled to a vacuum source which provides continuous negative pressure inside the enclosure; a battery-powered version of the vacuum source allows for patient transport while maintaining negative pressure within the enclosure. An inline filter, e.g., high efficiency particulate air (HEPA) or ultra-low particulate air (ULPA), is included between the enclosure and the vacuum source to continuously filter the air and trap any aerosol or particulates, which can be changed between uses. A seal over the patient can be created using a disposable clear plastic drape, which can be lifted for access to the patient and to manipulate equipment (ventilator tubing, bag-valve-mask, etc.). The drape facilitates higher air velocity through the window, protecting the operator during aerosol-generating procedures. For longer-term isolation, the plastic drape is supported around the patient's torso and can be closed or left open on the bottom to allow for cranially directed airflow. The walls of the enclosure are made from a clear material to allow for visualization of the patient from all directions. The device may include a rigid underlying support structure as well.

The device can function in multiple modes of operation. In one, "Procedure Mode" (**Appendix Figure 11**), the device is used for acute aerosol generating procedures including intubation, extubation, bronchoscopy, or other endoscopic procedures. In this mode of operation, the procedure window is open, and the bottom is sealed around the patient with a disposable plastic drape. The patient is accessed through the single window in the enclosure, being more ergonomic for procedures like intubation as it allows a broader range of motion that is not possible using two

arm ports. If necessary, an assistant can reach under the drape to assist from below and the negative pressure protects them from contamination. Single-use sterile versions of the device in a variety of form factors could be used for surgical procedures, where replacing the vacuum source itself is not needed, but replacing any potential patient-contacting surfaces is possible.

### Procedure Mode



### Isolation Mode, Bed at 60°



Individual shown is 5'11", 170 lbs.

**Appendix Figure 11: Demonstrations of IBU Modes of Use.**

In another mode of operation, “Isolation Mode” (**Appendix Figure 11**), the device can be used for more long-term negative pressure isolation of a single patient. In this mode of operation, the window at the top of the enclosure is closed and sealed. The plastic drape can be supported by a separate structure, or by supports extending from the enclosure itself. The drape could be either closed or left open with airflow moving cranially towards the patient’s face. When the device is used for isolation, it will be secured to the bed with tape or straps, allowing for the head of the bed to be elevated for improved patient comfort. This mode of operations can facilitate the use of adjunct respiratory procedures including high flow nasal cannula, continuous positive pressure

airway pressure devices, bilevel positive airway pressure devices, or nebulizer use. These features are based on preliminary user requirements and iterative feedback from Emergency Medicine doctors and are outlined in a Traceability Matrix (**Appendix Table 8**).

**Appendix Table 8: IBU Traceability Matrix**

User Specification	Engineering Requirement(s)	Design Features	Testing Required/ Performed
Must protect operator from aerosolized particulates	<ul style="list-style-type: none"> <li>• Must sufficiently redirect and capture aerosolized particulates within the containment vessel such that a 4-log reduction in penetration is achieved during use at the procedure window</li> <li>• Must exchange air at least 400 times per hour based on previously established 510(k) devices (i.e. RespirAir)</li> </ul>	<ul style="list-style-type: none"> <li>• Procedure Window designed such that it may be closed and latched</li> <li>• Collector designed to minimize flow turbulence within the containment enclosure as air flows toward the vacuum source</li> <li>• Use of high suction, low pressure vacuums</li> </ul>	<ul style="list-style-type: none"> <li>• HEPA Leak Test per ISO 14644</li> <li>• Aerosol Penetration Test</li> <li>• Smoke Pattern Analysis</li> </ul>
Must protect bystanders from aerosolized particulates	<ul style="list-style-type: none"> <li>• Must sufficiently redirect and capture aerosolized particulates within the containment vessel such that a 4-log reduction in penetration is achieved when device is in use</li> </ul>	<ul style="list-style-type: none"> <li>• Mounting clips at front of Biocontainment Box use to affix drape</li> <li>• Plastic Drape (≥4 ft x ≥4 ft) affixes, tucks under patient’s torso</li> </ul>	<ul style="list-style-type: none"> <li>• HEPA Leak Test per ISO 14644</li> <li>• Aerosol Penetration Test</li> <li>• Smoke Pattern Analysis</li> </ul>
Must be sturdy and stable on hospital bed	<ul style="list-style-type: none"> <li>• Internal framework of Biocontainment Box shall be reinforced by aluminum crossbar</li> <li>• When secured to a bed/gurney with hospital tape or straps, the structural shall remain in place during procedures</li> <li>• When secured to a bed/gurney with hospital tape or straps, the structural shall remain in place when the bed is pitched up to 60°</li> </ul>	<ul style="list-style-type: none"> <li>• Biocontainment Box comprised of aluminum framing</li> <li>• Polycarbonate siding affixed with removable rivets, providing additional rigidity</li> <li>• Entire structure able to be secured to gurney or bed using integrated handles</li> </ul>	<i>In situ</i> testing for intubation and extubation
Must not impede common hospital procedures	<ul style="list-style-type: none"> <li>• Must include an opening not less than one inch plus the diameter forearm diameter of a male in the 99<sup>th</sup> percentile.</li> <li>• A provider must be able to perform intubation and extubation without impediment based on time to completion.</li> </ul>	<ul style="list-style-type: none"> <li>• Single, hinged access window that opens to patient</li> <li>• Rigid form factor that fits over the head and neck only, with plastic drape covering the patient’s torso</li> </ul>	<i>In situ</i> testing for intubation and extubation

**Appendix Table 8 (continued)**

<b>User Specification</b>	<b>Engineering Requirement(s)</b>	<b>Design Features</b>	<b>Testing Required/ Performed</b>
Must be quickly and easily removable when in use	<ul style="list-style-type: none"> <li>• Must be able to be removed from patient in 30 seconds or less</li> <li>• Must integrate handgrips</li> </ul>	<ul style="list-style-type: none"> <li>• Handgrips integrated onto side of housing</li> <li>• Push-click fasteners provide rigidity to aluminum/ polycarbonate structure</li> </ul>	Has <u>not</u> been completed to date
Must not result in additional harm to patient	<ul style="list-style-type: none"> <li>• Must be comprised of non-irritating materials</li> <li>• Must be able to be removed from patient in 30 seconds or less</li> </ul>	<ul style="list-style-type: none"> <li>• Polycarbonate and aluminum structure are primarily non-contacting</li> </ul>	See composition materials
Should be reusable	<ul style="list-style-type: none"> <li>• Biocontainment Box is comprised of materials (polycarbonate, aluminum) that will withstand chemical disinfection via commonly used agents (isopropyl alcohol or bleach)</li> <li>• Filter tubing is single-use and is disposable</li> <li>• ULPA filter is disposable upon completion of its lifecycle</li> </ul>	<ul style="list-style-type: none"> <li>• ULPA filter cartridge is sealed and can be removed and disposed of</li> <li>• Materials comprising Biocontainment Box are suitable for common hospital cleaning procedures</li> </ul>	Defer to hospital cleaning protocols
Should be usable over duration of hospital stay	<ul style="list-style-type: none"> <li>• Life of filter must last at least 15 days, or, filter must be changeable to last said 15-day duration</li> <li>• Efficacy of aerosol filtration must not be affected when the bed is pitched up to 60°</li> </ul>	<ul style="list-style-type: none"> <li>• Filters can be removed and replaced when functional life is depleted without adversely impeding overall device function</li> <li>• Biocontainment Box may be fastened to the bed such that it may accommodate a bed pitch up to 60°</li> </ul>	<ul style="list-style-type: none"> <li>• HEPA Leak Test per ISO 14644</li> <li>• Aerosol Penetration Test</li> <li>• Smoke Pattern Analysis</li> </ul>

Based on the specification listed in **Appendix Table 8** the device was tested with, and met specifications as defined for HEPA Leak Test per ISO 14644 Penetration Test, and Smoke Pattern Analysis, using three unique negative pressure sources, each coupled with inline ULPA filters (NOTE: the Biocontainment Box in each of the configurations remains the same). Amongst them, the recent Guidance for Industry and Food and Drug Administration Staff, “Enforcement Policy for Sterilizers, Disinfectant Devices, and Air Purifiers During the Coronavirus Disease 2019 (COVID-19) Public Health Emergency” (March 2020), was defined as the essential design criteria,

and testing showed each device configuration to demonstrate a log-4 reduction capture of particulates.

### Appendix D.1.2 FDA’s Approval Status and Adequacy of Current Technologies

This product is currently not cleared or approved for use by FDA, nor is it under an IDE or approved in a foreign country. Appendix Table 9 presents a comparison matrix of approved devices and their respective adequacies and Availabilities.

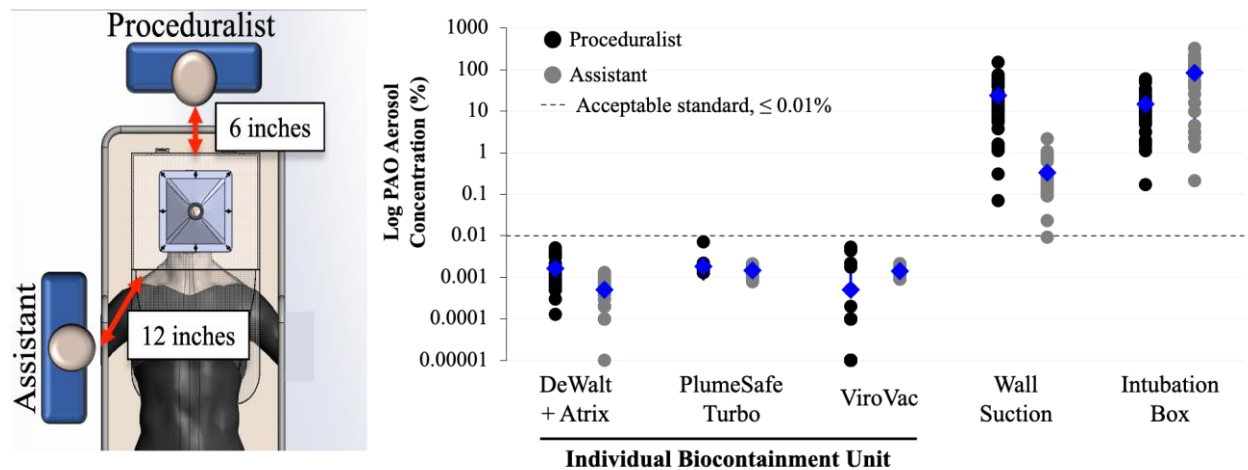
**Appendix Table 9: Comparison of Approved Technologies.**

<b>Currently Approved Alternatives</b>	<b>Adequacy (Relative Level of Protection)</b>	<b>Adequacy (Reusable per Label)</b>	<b>Availability (Approximate Cost)</b>	<b>General Availability</b>
Air Purifiers	Low	No	\$1,000 per unit	Moderate
Surgical Masks	Low	No	\$0.50 each	Low
N95 Respirator	Moderate	No	\$1.50 each	Low
Face Shields	Moderate	Yes	\$10 each	Low
Ventilators	High	Yes	\$30,000 per unit	Low
Negative Pressure Isolation Room	Highest	Yes	\$26,000 per construction	Lowest
Smoke Evacuator	Unknown	Yes	\$2,000k per unit	Moderate

Device testing has been conducted at the Winter Institute for Simulation, Education, and Research (WISER Institute, Pittsburgh, PA) with an attending emergency medicine physician performing simulated laryngoscopy, intubations, and extubations while the device is deployed in its intended use case. Testing was performed by an independent third party (Filtech Inc., Homestead, PA) using a combination of ISO 14644-3 and IEST test standards and procedures. Polyalphaolefin (PAO) was used in conjunction with a Laskin-nozzle aerosol generator to create

a poly-dispersed range of particles from 0.1µm to 10µm, serving as a surrogate for SARS-CoV-2, for particle containment testing (Liu, Ning et al. 2020).

Negative pressure was generated with each of the three vacuum sources as well as with wall suction (i.e., negative pressure source currently available in all hospitals), which was used as a comparison; additionally, a passive intubation box with two access holes at the rear of the structure was also tested. Testing on these configurations included smoke pattern testing, filtration efficiency, air flow face velocities at the Access Window and at the patient’s foot (as illustrated in **Appendix Figure 12**), as well as mean and maximum aerosol penetration measure as a concentration of PAO. IBU functionality for longer-term patient isolation was tested by placing an open, plastic tent suspended across the front with the access window closed. Repeat the testing battery confirmed containment at 60° of bed elevation. **Appendix Figure 12** and **Appendix Table 10** displays these results, which suggest adequate negative pressure to facilitate the use of high flow nasal cannula, CPAP, BiPAP, and nebulizers.



**Appendix Figure 12: PAO Monitoring Positions and Capture Results.**

**Appendix Table 10: Tabularized PAO Capture Results and Face Velocities.**

	Smoke Pattern Analysis (Pass/Fail)	Filtration Efficiency	Mean Penetration (Window)	Mean Penetration (Assistant)	Maximum Penetration (Window)	Maximum Penetration (Assistant)	Window Mean Face Velocity (FPM)	Foot Mean Face Velocity (FPM)
DeWalt Shop Vacuum + Atrix Filter	Pass	99.9988%	0.002%	0.001%	0.005%	0.001%	69	N/A
Buffalo ViroVac	Pass	99.9883%	0.001%	0.001%	0.005%	0.002%	52	14
Buffalo PlumeSafe Turbo	Pass	99.9936%	0.002%	0.001%	0.007%	0.002%	127	36
Passive Intubation Box	Fail	N/A	14.6%	83.4%	76%	330%	N/A	N/A
Wall Suction	Fail	N/A	23.8%	0.34%	148%	2.18%	2	N/A

Aerosol containment in a static enclosure that replicated previously described barrier enclosures (Canelli, Connor et al. 2020) was also quantified for comparison. Particle penetration values from **Appendix Figure 12** and **Appendix Table 10** demonstrate a lack of aerosol containment near the healthcare worker performing the procedure. This exhibits the lack of safety afforded by these enclosures in the studied scenarios, which is also visually represented in **Appendix Figure 13**. **Appendix Figure 13** displays stills from videography of a smoke testing comparing the vacuum-based IBU system (bottom) to the Passive Intubation Box (top). It is shown that considerable smoke is released from the containment of the passive device toward the face area of the provider performing the intubation. In contrast, constant negative pressure of the IBU redirects smoke from though filtration such that the care provider is not exposed to air from within the containment vicinity.



**Appendix Figure 13: Stills from Videography of Smoke Testing.**

**Appendix Table 11** provides a risk-based assessment in accordance with ISO 10993 biocompatibility.

**Appendix Table 11: Components, Materials, and Biocompatibility.**

Component	Patient Contacting	Material(s)	Biocompatibility
Biocontainment Box (custom)	Indirect	Polycarbonate	FDA-compliant
	Indirect	Aluminum	FDA-compliant
	Indirect	Nylon	GRAS*
Pyramidal Collector (custom)	Indirect	Polycarbonate	FDA-compliant
Drape (Allen Medical)	Direct	Polyethylene	FDA-compliant; CE marked; packaged sterile
Filter (Atrix)	No	Cellulose (ULPA filter)	N/A
	No	Fiberglass (ULPA filter)	N/A
	No	ABS (housing)	GRAS*
Vacuum Tube (Atrix)	No	PVC	GRAS*
Vacuum Source (DeWalt)	No	ABS (external housing)	GRAS*
Filter (Buffalo)	No	ABS (external housing)	GRAS*
Vacuum Source (Buffalo Turbo)	No	ABS (external housing)	GRAS*
Vacuum Source (Buffalo ViroVac)	No	ABS (external housing)	GRAS*

\* GRAS: generally recognized as safe (food-contacting materials)

Based on the materials from which the device is comprised, and on the minimal contact a patient will have with the device (i.e., minimal surface contact), the risk of any contact-based adverse reaction is negligible.

### **Appendix D.1.3 Risks & Usability Hazards, and Controls & Mitigations**

For assessing risks, establishing mitigations and risk controls, **Appendix Tables Appendix Table 12, Appendix Table 13, Appendix Table 14, and Appendix Table 15** follow guidance from ISO 14971:2007.

**Appendix Table 12: IBU Risks and Risk Controls**

<b>Component</b>	<b>Hazard (Risk ID*)</b>	<b>Inherent safe design</b>	<b>Protective measure</b>	<b>Information for safety</b>
Vacuum Source	Motor burnout (R1)	Vacuum is audible when functioning	Extensive field testing (DeWalt)	Instructions on approximate time to failure
	Motor fire (R2)	Motor within insulated material	UL testing prior to release	Instructions against heating and overuse
	Internal contamination (R3)	Filter in line with vacuum source	Obvious biohazard indication sticker	Warning to take proper precautions when disposing
Vacuum Tubing	Puncture in tubing (R4)	Rigid plastic design	Provide pre-use check sheet	Instructions to perform device inspection prior to use
	Internal contamination (R5)	Filter in line with vacuum tubing	Obvious biohazard indication sticker	Warning to take proper precautions when disposing
Filter Housing	Puncture in pyramidal adapter (R6)	Rigid plastic design	Provide pre-use check sheet	Instructions to perform device inspection prior to use
Filter	Does not scavenge particulates (R7)	Filter sealed in line with vacuum	Vacuum redirects particulates	Instructions on filter proper placement
	Use beyond end of useful life (R8)	Large-capacity ULPA filter	Replacement requirement	Instruction to replace filter based on ship-date
	Internal contamination (R9)	ULPA filter holds captured particles	Obvious biohazard indication sticker	Warning to take proper precautions when disposing
Biocontainment Box	Collapse of container (R10)	Dimensioned to standard gurney	Strengthened adjoining points	Recommendation to strap down device will be obvious
	Cross-contamination (R11)	Device use is non-patient contacting	Ability of material to be disinfected	Instructions on decontamination to be provided
	Puncture in pyramidal adapter (R6)	Rigid plastic design	Provide pre-use check sheet	Instructions to perform device inspection prior to use
	Failure at/of connection joint(s) (R12)	Rigid plastic design	Provide pre-use check sheet	Instructions to perform device inspection prior to use

\* Risk ID corresponds to **Appendix Table 16: Semi-Quantitative Risk Assessment.**

**Appendix Table 13** summarizes hazards (failure of device) and the foreseeable situations that may cause them, which would result in some harm (injury to person).

**Appendix Table 13: IBU Usability Hazards.**

<b>Hazard</b>	<b>Foreseeable Sequence of Events</b>	<b>Hazardous Situation</b>	<b>Harm</b>
<i>Biological:</i> Contaminated Filter	(1) Filter is not changed with sufficient frequency (2) Filter does not capture particulates	Potential for contagion(s) to be expelled within the exhaust of the vacuum	<ul style="list-style-type: none"> <li>• Exposure to potential contagion</li> </ul>
<i>Biological:</i> Contaminated Box	(1) Box not sufficiently decontaminated between patients	Potentially cross-contaminating particulates reside on surface of Box	<ul style="list-style-type: none"> <li>• Exposure to potential contagion</li> </ul>
<i>Functional:</i> Improper Box Setup	(1) Box not securely fastened together or to gurney (2) Instability of structure	Box falls or collapses during procedure	<ul style="list-style-type: none"> <li>• Delay, interruption, or failure of medical procedure</li> <li>• Physical, blunt trauma to patient or bystander</li> <li>• Exposure to potential contagion</li> </ul>
<i>Functional:</i> Improper Drape Placement	(1) Drape not sufficiently covering box opening	Insufficient negative pressure is generated within the box	<ul style="list-style-type: none"> <li>• Exposure to potential contagion</li> </ul>
<i>Functional:</i> Improper Tubing Connections	(1) Tubing not properly fastened into vacuum, housing, or combination	Potential leakage of infectious air from device tubing circuit	<ul style="list-style-type: none"> <li>• Delay or interruption of medical procedure</li> <li>• Exposure to potential contagion</li> </ul>
<i>Functional:</i> Motor Failure	(1) Motor is run excessively (2) Vacuum motor failure (3) Vacuum ceases within Box	Potentially contaminating particulates remain near facial area of patient	<ul style="list-style-type: none"> <li>• Delay or interruption of medical procedure</li> <li>• Exposure to potential contagion</li> </ul>

**Appendix Table 14** is common summarization of severity and its corresponding description.

**Appendix Table 14: Severity Rating and Description.**

<b>Severity Rating</b>	<b>Description</b>
Critical	Loss of limb; life-threatening injury or infection
Major	Severe, long-term injury; potential disability
Serious	Short-term injury or impairment requiring additional medical intervention to correct (e.g. reoperation)
Minor	Slight user/patient inconvenience; little to no effect on product performance, non-vital fault
Negligible	No or negligible risk to patient and/or user

**Appendix Table 15** is common summarization of probability ratings and their corresponding numerical probability.

**Appendix Table 15: Probability Rating and Frequency.**

<b>Probability Rating</b>	<b>Frequency</b>
Frequent	1 in 100
Probable	1 in 1,000
Occasional	1 in 10,000
Remote	1 in 100,000
Improbable	1 in 1,000,000

**Appendix Table 16** compiles the Probability Ratings from **Appendix Table 15** (y-axis) and the Severity Ratings from **Appendix Table 14** (x-axis) and then plots the IBU-specific hazards detailed in **Appendix Table 13**. Risks in dark gray denote risks that are unacceptable, risks in light gray denote the need to investigate further mitigation, and white denotes insignificant risks.

**Appendix Table 16: Semi-Quantitative Risk Assessment.**

	<b>Negligible</b>	<b>Minor</b>	<b>Serious</b>	<b>Major</b>	<b>Critical</b>
<b>Frequent</b>					
<b>Probable</b>					
<b>Occasional</b>		R9			
<b>Remote</b>	R1				
<b>Improbable</b>	R4		R6, R12	R2, R3, R10	R7, R8, R11

#### **Appendix D.1.4 Benefits of IBU Usage**

**Appendix Table 17** has been constructed under advice from the document Guidance for Industry and FDA Staff, “Factors to Consider Regarding Benefit-Risk in Medical Device Product Availability, Compliance, and Enforcement Decisions” (December 27<sup>th</sup>, 2016).

**Appendix Table 17: IBU Industry Guidance-Based Benefit Analysis.**

	<b>Description &amp; Rationale of Specific Benefit</b>
Types of Benefit	Implementation of the IBU is anticipated to significantly lessen the need for use of a ventilator and is intended to increase the protection of healthcare workers dealing with infectious or potentially infectious patients. With regular use of the device, the IBU may completely prevent healthcare workers from contracting COVID-19. Clinicians may find unanticipated ways to utilize the IBU giving rise to additional types of benefit. Such practice-based evidence may lead to clearance of new uses, thus increasing the types of benefit.
Magnitude of Benefit	As of late April 2020, over one million cases of COVID-19 have been confirmed in the United States with an approximate hospitalization rate of 19%. This device is intended to target those individuals needing to be transported and/or hospitalized.
Likelihood of Multiple Benefits	Based on testing penetration indicative of aerosolize particulate capture, the likelihood that this device can and will be used for during treatment of other respiratory diseases beyond COVID-19 is high.
Duration of Effects	The protective effects rendered by the device are anticipated to last for its duration of use. However, the protection of the healthcare worker from respiratory illness has effects that impact the overall wellbeing of the community more deeply, and therefore the protective effects are greater than that of its usage time only.
Patient & Care Provider Perspectives on Benefit	This device will improve the experience and protection of healthcare professionals and/or caregivers when caring for patients. This will directly improve clinical practice and therein, will likely also improve patient outcomes. Benefits for healthcare workers and/or caregivers include improvements in overall personal protection, and increased utility for various procedures. These benefits impact individuals of broad training, specialty, and skill levels, protecting against respiratory illness. By enhancing protection to healthcare workers and caregivers, a greater patient population may be served.
Medical Necessity	Table 4 summarizes the currently-available devices that may be used in substitution of, or in conjunction with, the IBU. The current state of COVID-19 has placed considerable strains on healthcare worker, supporting personnel, and the PPE supply chain. The IBU is a medical necessity for lessening the burden on the supply chain, as well as for mitigating the spread of COVID-19 to healthcare personnel.

**Appendix D.1.5 Summary of Risk-Benefit Analysis Limitations, Uncertainty, and Data Gaps**

The current limitations, uncertainties, and data gaps have been identified as the following:

(1) Validated use life of the Atrix filter, and (2) Exact recommendation for cyclic cleaning until device or device components warrant replacement. Based on the clinical data regarding SARS-CoV-19, the need for PPE, current data regarding this device in conjunction with the risk-mitigating strategies employed and to be employed throughout the product lifecycle, the benefits outweigh the risks.

### Appendix D.2 Manufacturing and Controls

Information on chemistry (as applicable), manufacturing, and controls; a list of each site where the product, if authorized, is or would be manufactured, and the current cGMP status of the manufacturing site(s).

**Appendix Table 18: Manufacturer and Sourcing Information.**

Component	Manufacturer	Address	cGMP Status
Containment Bin, Pyramidal Collector	Visions Group	1 Visions Pkwy Celina, OH 45822	ISO 9001:2015 Certified
Drape	Allen Medical	100 Discovery Way Acton, MA 01720	ISO 14385 Certified
Filter and Pre-Filter Tube	Atrix	1350 Larc Industrial Blvd. Burnsville, MN 55337, USA	General controls per manufacturer (non-GMP)
Wet/dry vacuum	Stanley Black & Decker Corp.	4041 Pleasant Rd, Fort Mill, SC 29708, USA	Underwriters Laboratories (UL) listed; General controls per manufacturer (non-GMP)
Filters and Smoke Evacuators	Buffalo Filter, LLC	5900 Genesee Street Lancaster, New York 14086 USA	ISO 14385 Certified; UL listed
<b>Final Product</b>	Innovative Electronics Corporation	750 Trumbull Drive Pittsburgh, PA 15205, USA	ISO 14385 Certified

### **Appendix D.2.1 Assembly of Final Product**

Manufacturing/assembly will take place at Innovative Electronics Corporation. This facility is cGMP per ISO 13485. Innovative Electronics Corporation regularly evaluates each current and prospective supplier, certifies and files these results to ensure compliance to their set quality standards. Prior to initiating device assembly, and with direct and specific assistance from Innovative Electronics Corporation, a test plan will be prepared which will include in-process testing and final testing (Quality Control in Appendix D.3) as per the design requirements. Innovative Electronics Corporation has established audits systems to ensure that the final Individual Biocontainment Unit devices meet engineering and performance standards. Complete system is audited from component parts, assembly instructions, in process and final testing, labeling and final packaging to ensure it meets customer requirements.

### **Appendix D.3 Quality Control, Shipping and Adverse Event Tracking & Reporting**

Innovative Electronics Corporation has procedures for Quality Control, Packaging & Labeling, Inventory Control, and Adverse Events Reporting. Innovative Electronics Corporation will source materials, and then will perform and incoming inspection on receipt of the materials. Innovative Electronics Corporation will then assemble each and perform Quality Control testing on each unit after is it built. Quality Control testing will ensure that:

- The vacuum is functional.
- The filter fits into the custom housing, and that housing can be securely affixed to the vacuum source.

- The container can be assembled as it would be in its Use Case, being securely mated to all other components.
- Once assembled, that ensure adequate vacuum pressure and particle capture is achieved.

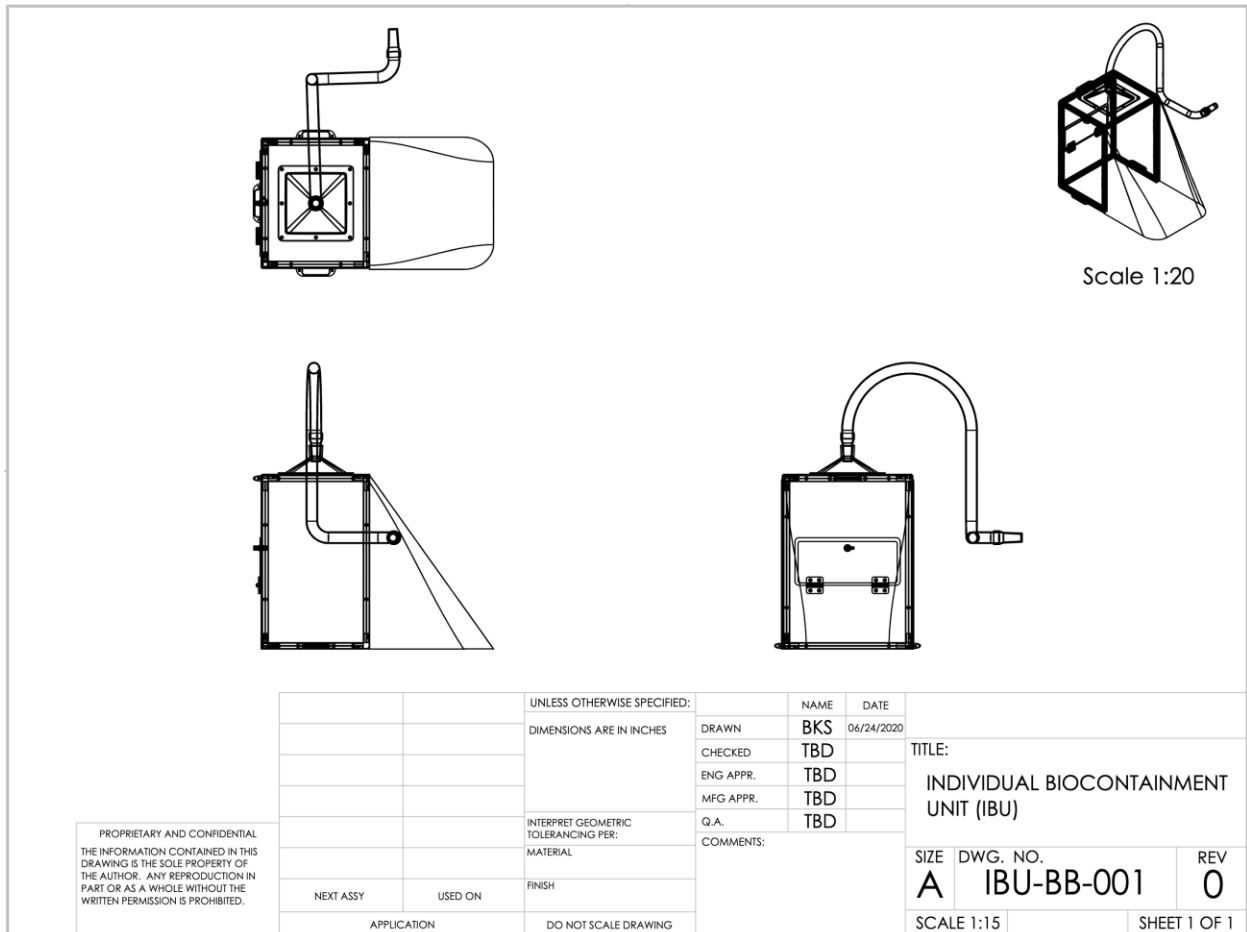
All records will be documented for on a per-unit basis. After Quality Control and documentation, Innovative Electronics Corporation will package, label, queue, and ship the units. Finally, Innovative Electronics Corporation has in place a digital repository for Field Tracking and Reporting; in the event that a user encounters a malfunction, a direct report can be filed with Innovative Electronics Corporation. The correspondence to whom an event shall be sent will be included on the device label as well as in the instruction for use.

### **Appendix D.3.1 Quantity and Scale-up Considerations**

Currently, the manufacturer and all respective components have been contacted for supply. One-thousand replicate of each component are presently available, has been confirmed as ready for shipment if ordered. Innovative Electronics Corporation has approximated 30-60 minutes for assembly of each device, with an additional 60-90 minutes of quality control testing, packaging, labeling, and assignment into inventory.

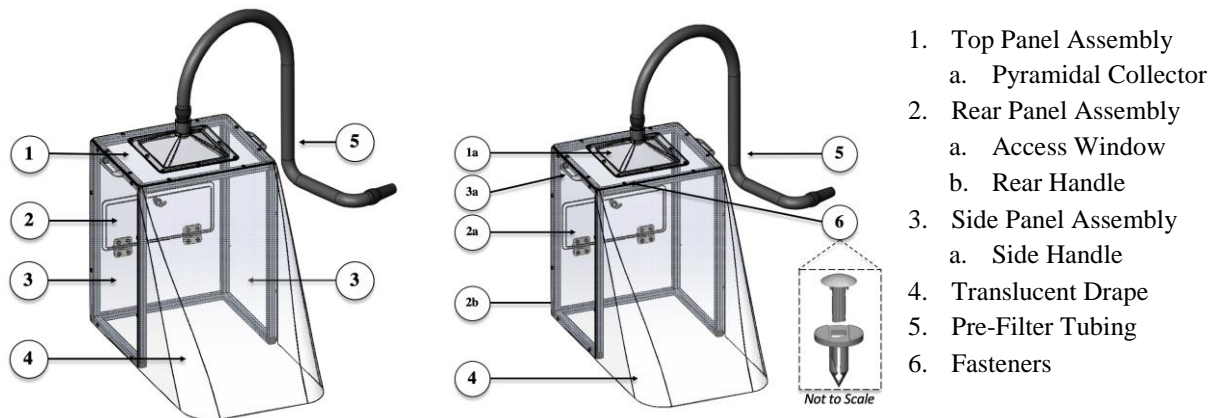
## Appendix D.4 Instructions for Healthcare Facilities and Cleaning Instructions

The IBU is a novel product. Therefore, the product is manufactured in conformance with the design in IBU Drawing Number IBU-BB-001. **Appendix Figure 14** is an assembly drawing that is to be provided with the IBU documentation to healthcare providers, depicting the formfactor of the assembled device. Care providers are to be outfitted with standard electrical outlets conforming to applicable US Federal, State, and Local Codes.



**Appendix Figure 14: IBU General Assembly Drawing.**

For cleaning, **Appendix Figure 15** displays a CAD rendering of the Biocontainment Box and the respective Assemblies needed for its proper function. The instructions for cleaning the IBU are as follows:



**Appendix Figure 15: Breakdown of IBU Components.**

The instructions for cleaning the IBU are as follows:

1. **Put on clean gloves and appropriate PPE** before beginning the cleaning and disinfection procedure.
2. Ensure the negative pressure source is turned off and unplugged.
3. Ensure patient and any suction hoses are removed from the device.
4. Remove and discard the pre-filter tubing from the collector and the negative pressure source.  
**NOTE:** This component is potentially biohazardous and should be disposed of accordingly.
5. Remove and discard the translucent drape. **NOTE:** This component is potentially biohazardous and should be disposed of accordingly.
6. If the device needs to be moved prior to cleaning,

- a. Close and secure the access window at the rear of the IBU,
  - b. Remove any straps and/or tie-downs that are affixed to the IBU,
  - c. Pick up device with handles on the lateral side and move to the final cleaning location.
  - d. **Handle the IBU with care.** Do not drop, strike, or place heavy objects onto the IBU.
  - e. Continue cleaning procedure.
7. Establish a checklist to track the cleaning of the individual components and subassemblies of the IBU – the complete list of components are presented in Appendix Table 19.
  8. Disassemble each of the panel assemblies by removing the Fasteners from their insertions into the frame. Consult the Parts List to ensure all parts are cleaned.
    - a. Remove the thirty-two (32) Fasteners from the each of the Panel Assemblies. This may be done by wedging a flathead screwdriver in between the two nylon components and applying a gentle force to remove the inner Nylon fastening piece. Once the inner-most piece of the fastener is removed, the outer spike of the fastener that contacts the polycarbonate can then be pulled out.
    - b. Remove the polycarbonate panels from the aluminum scaffold and disassemble the scaffold connector pieces.
    - c. Remove the eight (8) screws securing the Pyramidal collector to the Top Panel Assembly using a screwdriver.
  9. For cleaning, dispense a towelette of Cavicide wipe or other hospital-approved EPA-registered quaternary ammonium compound/isopropyl alcohol-based hospital disinfectant wipe. Wipe clean the inner and outer surfaces of each of the Assemblies and their respective components to remove soiling. Use at least one wipe per inner and outer surfaces.

10. If visible soiling remains, repeat the procedure. **Let all parts sit visibly wet for at least 2 minutes.** Allow all parts to air dry. Remove and discard gloves.
11. For disinfection, spray all disassembled parts with a hospital-approved EPA-registered isopropyl alcohol-based disinfectant, such as Cavicide. **Let all parts sit visibly wet for at least the contact time indicated on the disinfectant labeling** (i.e., 2 minutes for Cavicide) before allowing all parts to air dry. See List N: Disinfectants for Use Against SARS-CoV-2, <https://www.epa.gov/pesticide-registration/list-n-disinfectants-use-against-sars-cov-2>.
12. If visible soiling remains, repeat the cleaning and disinfection procedures.
13. Reassemble the IBU and inspect it as described below under System Maintenance and Routine Inspection.
14. Do not use harsh chemicals or abrasives to clean. Do not apply heat. Do not use high concentrations of ammonium in excess of 20% as this may degrade components.
15. Store device at room temperature and a relative humidity between 40-60%. Store in a container, if possible, to avoid foreign contaminants (e.g., dust, grease) from accumulating on the device.
16. **All external surfaces of the negative pressure-generating source should be cleaned and disinfected. If the negative pressure-generating sources require cleaning and/or disinfection (i.e., if the negative pressure source is suspected of collecting liquids):**
  - a. For cleaning and/disinfection of the Buffalo PlumeSafe, Buffalo ViroVac, and the Stryker Neptune, refer to their respective instructional information for appropriate procedures

For cleaning the *outer surfaces* of the DeWalt DCV581H and/or the Atrix ULPA filter, repeat the cleaning and disinfection steps listed above. **NOTE: DO NOT expose any internal compartments of either the DeWalt DCV581H or the Atrix Filter to chemical cleaners or disinfectants.**

**Appendix Table 19: IBU Full Components List.**

<b>App. Fig. 15 Ref Number</b>	<b>Description</b>	<b>Quantity</b>	<b>Material</b>
1	Top Panel Assembly		
	Top Panel	1	Polycarbonate
1a	Pyramidal Collector	1	Polycarbonate
	Fastening Bolt (Pyramidal Collector)	8	Stainless Steel
	Fastening Nut (Pyramidal Collector)	8	Stainless Steel
	Scaffolding Parts	4	Aluminum
2	Rear Panel Assembly		Polycarbonate; aluminum
	Rear Panel	1	Polycarbonate
	3-Way Connector	4	Nylon
2b	Handle	1	(ABS) Acrylonitrile butadiene styrene
	Handle Bolt	2	Stainless Steel
	Scaffolding Parts	4	Aluminum
	Access Window	1	Polycarbonate
	Window Hinge	2	Stainless Steel
	Fastening Bolts (for Window Hinge)	8	Stainless Steel
	Acorn Nuts (for Window Hinge)	4	Stainless Steel
	Window Hinge Spacer	2	Polycarbonate
	Window Latch	1	Stainless Steel
3	Side panel assembly		Polycarbonate; aluminum
	Side Panel	2	Polycarbonate
	3-Way Connector	2	Nylon
	2-Way Connector	2	Nylon
3b	Handle	2	(ABS) Acrylonitrile butadiene styrene
	Handle Bolt	4	Stainless Steel
	Scaffolding Parts	8	Aluminum
4	Translucent Drape	1	Polyethylene
5	Pre-Filter Tubing	1	PVC (polyvinyl chloride)
	Tubing Adapter, (for 7/8" tubing)	1	Polycarbonate
6	Fasteners	17	Nylon

## Appendix D.5 Packaging and Labeling

Per ISO 15223-1:2016, the device label will be furnished with the symbols presented in **Appendix Table 20**, along with the statement that the device is authorized for use per Emergency Use Authorization.

**Appendix Table 20: Symbols to be Printed on IBU Label.**

Symbol	Label information
	<i>Manufacturer:</i> Symbol will be followed by the name and address of the manufacture at the rear of the device and on sterility barrier of components and solutions
	<i>Date of Manufacture:</i> Symbol indicates the date (day, month, year) of the device was manufactured.
	<i>Serial Number:</i> Symbol will be followed by the serial number of the device at the rear of the device and on sterility barrier of components and solutions.
	<i>Not for General Waste:</i> Symbol indicates that the device can be reused, and must be disposed of in accordance with local, state, and federal regulations.
	<i>Alternating Current:</i> Symbol indicates that the each installation of vacuum component operates with alternating current.
	<i>Radio Frequency Transmission:</i> Symbol indicates emission of non-ionizing radiation.
	<i>Grounding (Earth):</i> Symbol indicates electrical grounding.
<b>IPX1</b>	<i>Water Ingress:</i> Symbol indicates that the vacuum source is protected against vertically falling water drops ( <i>Buffalo Smoke Evacuators only</i> ).
	<i>Biohazard:</i> Symbol indicates potentially biohazardous material after usage, which will be placed on the vacuum, the vacuum tubing, and the filter.
	<i>Non-Sterile:</i> Symbol indicates that the device is <i>not</i> provided sterile.
	<i>Consult Instructions:</i> Symbol will be placed on physical interface of the filter housing. Instructions will detail the setup, use, and clearing of the device.

## **Appendix D.6 Current EUA Status of the IBU**

As of March 4<sup>th</sup>, 2021, the FDA is reviewing the submission and the device remains pending Authorization (PEUA201146).

## Bibliography

- (2011). Chimpanzees in Biomedical and Behavioral Research: Assessing the Necessity. B. M. Altevogt, D. E. Pankevich, M. K. Shelton-Davenport and J. P. Kahn. Washington (DC).
- Abbas, O. L., Borman, H., Uysal, C. A., Gonen, Z. B., Aydin, L., Helvacioğlu, F., Ilhan, S. and Yazici, A. C. (2016). "Adipose-Derived Stem Cells Enhance Axonal Regeneration through Cross-Facial Nerve Grafting in a Rat Model of Facial Paralysis." Plast Reconstr Surg **138**(2): 387-396.
- Acosta, F. M., Jia, U. A., Stojkova, K., Pacelli, S., Brey, E. M. and Rathbone, C. (2020). "Divergent effects of myogenic differentiation and diabetes on the capacity for muscle precursor cell adipogenic differentiation in a fibrin matrix." Biochem Biophys Res Commun **526**(1): 21-28.
- Adams, V., Nehrhoff, B., Spate, U., Linke, A., Schulze, P. C., Baur, A., Gielen, S., Hambrecht, R. and Schuler, G. (2002). "Induction of iNOS expression in skeletal muscle by IL-1beta and NFkappaB activation: an in vitro and in vivo study." Cardiovasc Res **54**(1): 95-104.
- Afshari, A., Nguyen, L., Kelm, N. D., Kim, J. S., Cardwell, N. L., Pollins, A. C., Bamba, R., Shack, R. B., Does, M. D. and Thayer, W. P. (2018). "Assessment of the Effect of Autograft Orientation on Peripheral Nerve Regeneration Using Diffusion Tensor Imaging." Ann Plast Surg **80**(4): 384-390.
- Agrawal, V., Kelly, J., Tottey, S., Daly, K. A., Johnson, S. A., Siu, B. F., Reing, J. and Badylak, S. F. (2011). "An isolated cryptic peptide influences osteogenesis and bone remodeling in an adult mammalian model of digit amputation." Tissue Eng Part A **17**(23-24): 3033-3044.
- Agrawal, V., Tottey, S., Johnson, S. A., Freund, J. M., Siu, B. F. and Badylak, S. F. (2011). "Recruitment of progenitor cells by an extracellular matrix cryptic peptide in a mouse model of digit amputation." Tissue Eng Part A **17**(19-20): 2435-2443.
- Aicher, R. H. (2013). "Is the FDA regulating the practice of medicine?" Aesthet Surg J **33**(3): 452-455.
- Alados, J. C., Alcaraz, M. J., Aller, A. I., Miranda, C., Perez, J. L. and Romero, P. A. (2010). "[Designing a clinical microbiology laboratory]." Enferm Infecc Microbiol Clin **28**(7): 453-460.
- Allbright, K. O., Bliley, J. M., Havis, E., Kim, D. Y., Dibernardo, G. A., Grybowski, D., Waldner, M., James, I. B., Sivak, W. N., Rubin, J. P. and Marra, K. G. (2018). "Delivery of adipose-derived stem cells in poloxamer hydrogel improves peripheral nerve regeneration." Muscle Nerve.

- Alvites, R., Rita Caseiro, A., Santos Pedrosa, S., Vieira Branquinho, M., Ronchi, G., Geuna, S., Varejão, A. S. P. and Colette Maurício, A. (2018). "Peripheral nerve injury and axonotmesis: State of the art and recent advances." Cogent Medicine **5**(1): 1466404.
- Angius, D., Wang, H., Spinner, R. J., Gutierrez-Cotto, Y., Yaszemski, M. J. and Windebank, A. J. (2012). "A systematic review of animal models used to study nerve regeneration in tissue-engineered scaffolds." Biomaterials **33**(32): 8034-8039.
- Arnold, W. D., Sheth, K. A., Wier, C. G., Kissel, J. T., Burghes, A. H. and Kolb, S. J. (2015). "Electrophysiological Motor Unit Number Estimation (MUNE) Measuring Compound Muscle Action Potential (CMAP) in Mouse Hindlimb Muscles." J Vis Exp(103).
- Arslantunali, D., Dursun, T., Yucel, D., Hasirci, N. and Hasirci, V. (2014). "Peripheral nerve conduits: technology update." Med Devices (Auckl) **7**: 405-424.
- Asensio-Pinilla, E., Udina, E., Jaramillo, J. and Navarro, X. (2009). "Electrical stimulation combined with exercise increase axonal regeneration after peripheral nerve injury." Exp Neurol **219**(1): 258-265.
- Aziz, A., Liu, Q. C. and Dilworth, F. J. (2010). "Regulating a master regulator: establishing tissue-specific gene expression in skeletal muscle." Epigenetics **5**(8): 691-695.
- Becher, B., Tugues, S. and Greter, M. (2016). "GM-CSF: From Growth Factor to Central Mediator of Tissue Inflammation." Immunity **45**(5): 963-973.
- Becker, S., Saint-Cyr, M., Wong, C., Dauwe, P., Nagarkar, P., Thornton, J. F. and Peng, Y. (2009). "AlloDerm versus DermaMatrix in immediate expander-based breast reconstruction: a preliminary comparison of complication profiles and material compliance." Plast Reconstr Surg **123**(1): 1-6; discussion 107-108.
- Beekman, C., Sipkens, J. A., Testerink, J., Giannakopoulos, S., Kreuger, D., van Deutekom, J. C., Campion, G. V., de Kimpe, S. J. and Loubakos, A. (2014). "A sensitive, reproducible and objective immunofluorescence analysis method of dystrophin in individual fibers in samples from patients with duchenne muscular dystrophy." PLoS One **9**(9): e107494.
- Bellini, E., Grieco, M. P. and Raposio, E. (2017). "The science behind autologous fat grafting." Ann Med Surg (Lond) **24**: 65-73.
- Bergmeister, K. D., Grosse-Hartlage, L., Daeschler, S. C., Rhodius, P., Bocker, A., Beyersdorff, M., Kern, A. O., Kneser, U. and Harhaus, L. (2020). "Acute and long-term costs of 268 peripheral nerve injuries in the upper extremity." PLoS One **15**(4): e0229530.
- Borrelli, M. R., Patel, R. A., Sokol, J., Nguyen, D., Momeni, A., Longaker, M. T. and Wan, D. C. (2019). "Fat Chance: The Rejuvenation of Irradiated Skin." Plast Reconstr Surg Glob Open **7**(2): e2092.

- Bosurgi, L., Manfredi, A. A. and Rovere-Querini, P. (2011). "Macrophages in injured skeletal muscle: a perpetuum mobile causing and limiting fibrosis, prompting or restricting resolution and regeneration." Front Immunol **2**: 62.
- Brown, J. C., Shang, H., Yang, N., Pierson, J., Ratliff, C. R., Prince, N., Roney, N., Chan, R., Hatem, V. and Gittleman, H. (2020). "Autologous Fat Transfer for Scar Prevention and Remodeling: A Randomized, Blinded, Placebo-controlled Trial." Plastic and Reconstructive Surgery–Global Open **8**(5): e2830.
- Brown, K. J., Marathi, R., Fiorillo, A. A., Ciccimaro, E. F., Sharma, S., Rowlands, D. S., Rayavarapu, S., Nagaraju, K., Hoffman, E. P. and Hathout, Y. (2012). "Accurate Quantitation of Dystrophin Protein in Human Skeletal Muscle Using Mass Spectrometry." J Bioanal Biomed **Suppl 7**.
- Brull, R., Hadzic, A., Reina, M. A. and Barrington, M. J. (2015). "Pathophysiology and Etiology of Nerve Injury Following Peripheral Nerve Blockade." Reg Anesth Pain Med **40**(5): 479-490.
- Bruun, J. M., Stallknecht, B., Helge, J. W. and Richelsen, B. (2007). "Interleukin-18 in plasma and adipose tissue: effects of obesity, insulin resistance, and weight loss." Eur J Endocrinol **157**(4): 465-471.
- Bruyns, C. N., Jaquet, J. B., Schreuders, T. A., Kalmijn, S., Kuypers, P. D. and Hovius, S. E. (2003). "Predictors for return to work in patients with median and ulnar nerve injuries." J Hand Surg Am **28**(1): 28-34.
- Buck, M. and Chojkier, M. (1996). "Muscle wasting and dedifferentiation induced by oxidative stress in a murine model of cachexia is prevented by inhibitors of nitric oxide synthesis and antioxidants." EMBO J **15**(8): 1753-1765.
- Bunge, M. B., Bunge, R. P., Kleitman, N. and Dean, A. C. (1989). "Role of peripheral nerve extracellular matrix in Schwann cell function and in neurite regeneration." Dev Neurosci **11**(4-5): 348-360.
- Burk, J., Erbe, I., Berner, D., Kacza, J., Kasper, C., Pfeiffer, B., Winter, K. and Brehm, W. (2014). "Freeze-thaw cycles enhance decellularization of large tendons." Tissue Eng Part C Methods **20**(4): 276-284.
- Burnett, M. G. and Zager, E. L. (2004). "Pathophysiology of peripheral nerve injury: a brief review." Neurosurg Focus **16**(5): E1.
- Burnham, R., McNeil, S., Hegedus, C. and Gray, D. S. (2006). "Fibrous myopathy as a complication of repeated intramuscular injections for chronic headache." Pain Res Manag **11**(4): 249-252.
- Butterfield, T. A., Best, T. M. and Merrick, M. A. (2006). "The dual roles of neutrophils and macrophages in inflammation: a critical balance between tissue damage and repair." J Athl Train **41**(4): 457-465.

- Caamano, S., Shiori, A., Strauss, S. H. and Orton, E. C. (2009). "Does sodium dodecyl sulfate wash out of detergent-treated bovine pericardium at cytotoxic concentrations?" J Heart Valve Dis **18**(1): 101-105.
- Cabaud, H. E., Rodkey, W. G. and McCarroll, H. R., Jr. (1980). "Peripheral nerve injuries: studies in higher nonhuman primates." J Hand Surg Am **5**(3): 201-206.
- Cai, J., Li, B., Liu, K., Feng, J., Gao, K. and Lu, F. (2017). "Low-dose G-CSF improves fat graft retention by mobilizing endogenous stem cells and inducing angiogenesis, whereas high-dose G-CSF inhibits adipogenesis with prolonged inflammation and severe fibrosis." Biochem Biophys Res Commun **491**(3): 662-667.
- Canelli, R., Connor, C. W., Gonzalez, M., Nozari, A. and Ortega, R. (2020). "Barrier Enclosure during Endotracheal Intubation." N Engl J Med.
- Cannon, J. G., Fielding, R. A., Fiatarone, M. A., Orencole, S. F., Dinarello, C. A. and Evans, W. J. (1989). "Increased interleukin 1 beta in human skeletal muscle after exercise." Am J Physiol **257**(2 Pt 2): R451-455.
- Carmeli, E., Moas, M., Reznick, A. Z. and Coleman, R. (2004). "Matrix metalloproteinases and skeletal muscle: a brief review." Muscle Nerve **29**(2): 191-197.
- Carriel, V., Garzon, I., Campos, A., Cornelissen, M. and Alaminos, M. (2017). "Differential expression of GAP-43 and neurofilament during peripheral nerve regeneration through bio-artificial conduits." J Tissue Eng Regen Med **11**(2): 553-563.
- Casal, D., Pais, D., Iria, I., Mota-Silva, E., Almeida, M. A., Alves, S., Pen, C., Farinho, A., Mascarenhas-Lemos, L., Ferreira-Silva, J., Ferraz-Oliveira, M., Vassilenko, V., Videira, P. A. and Gory O'Neill, J. (2017). "A Model of Free Tissue Transfer: The Rat Epigastric Free Flap." J Vis Exp(119).
- Caviggioli, F., Maione, L., Forcellini, D., Klinger, F. and Klinger, M. (2011). "Autologous fat graft in postmastectomy pain syndrome." Plastic and reconstructive surgery **128**(2): 349-352.
- Ceglia, L., Niramitmahapanya, S., Price, L. L., Harris, S. S., Fielding, R. A. and Dawson-Hughes, B. (2013). "An evaluation of the reliability of muscle fiber cross-sectional area and fiber number measurements in rat skeletal muscle." Biol Proced Online **15**(1): 6.
- Chait, A. and den Hartigh, L. J. (2020). "Adipose Tissue Distribution, Inflammation and Its Metabolic Consequences, Including Diabetes and Cardiovascular Disease." Front Cardiovasc Med **7**: 22.
- Chato-Astrain, J., Campos, F., Roda, O., Miralles, E., Durand-Herrera, D., Saez-Moreno, J. A., Garcia-Garcia, S., Alaminos, M., Campos, A. and Carriel, V. (2018). "In vivo Evaluation of Nanostructured Fibrin-Agarose Hydrogels With Mesenchymal Stem Cells for Peripheral Nerve Repair." Front Cell Neurosci **12**: 501.

- Chen, L., Wang, Z.-C., Ma, J.-J., Sun, W.-J., Wang, S.-W., Gu, Z.-C. and Yang, X. (2019). "Autologous nanofat transplantation accelerates foot wound healing in diabetic rats." Regenerative medicine **14**(3): 231-241.
- Chen, X., Hunt, D., Cushman, S. W. and Hess, S. (2009). "Proteomic characterization of thiazolidinedione regulation of obese adipose secretome in Zucker obese rats." Proteomics Clin Appl **3**(9): 1099-1111.
- Chen, X., Yang, Q., Zheng, T., Bian, J., Sun, X., Shi, Y., Liang, X., Gao, G., Liu, G. and Deng, C. (2016). "Neurotrophic Effect of Adipose Tissue-Derived Stem Cells on Erectile Function Recovery by Pigment Epithelium-Derived Factor Secretion in a Rat Model of Cavernous Nerve Injury." Stem Cells Int **2016**: 5161248.
- Cheng, M., Nguyen, M. H., Fantuzzi, G. and Koh, T. J. (2008). "Endogenous interferon-gamma is required for efficient skeletal muscle regeneration." Am J Physiol Cell Physiol **294**(5): C1183-1191.
- Chhabra, A., Ahlawat, S., Belzberg, A. and Andreseik, G. (2014). "Peripheral nerve injury grading simplified on MR neurography: As referenced to Seddon and Sunderland classifications." Indian J Radiol Imaging **24**(3): 217-224.
- Chiba, K., Tsuchiya, M., Koide, M., Hagiwara, Y., Sasaki, K., Hattori, Y., Watanabe, M., Sugawara, S., Kanzaki, M. and Endo, Y. (2015). "Involvement of IL-1 in the Maintenance of Masseter Muscle Activity and Glucose Homeostasis." PLoS One **10**(11): e0143635.
- Chistiakov, D. A., Killingsworth, M. C., Myasoedova, V. A., Orekhov, A. N. and Bobryshev, Y. V. (2017). "CD68/macrosialin: not just a histochemical marker." Lab Invest **97**(1): 4-13.
- Choi, J., Kim, J. H., Jang, J. W., Kim, H. J., Choi, S. H. and Kwon, S. W. (2018). "Decellularized sciatic nerve matrix as a biodegradable conduit for peripheral nerve regeneration." Neural Regen Res **13**(10): 1796-1803.
- Cholok, D., Lee, E., Lisiecki, J., Agarwal, S., Loder, S., Ranganathan, K., Qureshi, A. T., Davis, T. A. and Levi, B. (2017). "Traumatic muscle fibrosis: From pathway to prevention." J Trauma Acute Care Surg **82**(1): 174-184.
- Chusyd, D. E., Wang, D., Huffman, D. M. and Nagy, T. R. (2016). "Relationships between Rodent White Adipose Fat Pads and Human White Adipose Fat Depots." Front Nutr **3**: 10.
- Cinteza, D., Persinaru, I., Maciuceanu Zarnescu, B. M., Ionescu, D. and Lascar, I. (2015). "Peripheral Nerve Regeneration - an Appraisal of the Current Treatment Options." Maedica (Buchar) **10**(1): 65-68.
- Cirer-Sastre, R., Beltran-Garrido, J. V. and Corbi, F. (2017). "Contralateral Effects After Unilateral Strength Training: A Meta-Analysis Comparing Training Loads." J Sports Sci Med **16**(2): 180-186.

- Clavijo-Alvarez, J. A., Nguyen, V. T., Santiago, L. Y., Doctor, J. S., Lee, W. P. and Marra, K. G. (2007). "Comparison of biodegradable conduits within aged rat sciatic nerve defects." Plast Reconstr Surg **119**(6): 1839-1851.
- Cohen, T. V., Many, G. M., Fleming, B. D., Gnocchi, V. F., Ghimbovschi, S., Mosser, D. M., Hoffman, E. P. and Partridge, T. A. (2015). "Upregulated IL-1beta in dysferlin-deficient muscle attenuates regeneration by blunting the response to pro-inflammatory macrophages." Skelet Muscle **5**: 24.
- Conway, P. H. (2017). "Factors Associated With Increased US Health Care Spending: Implications for Controlling Health Care Costs." JAMA **318**(17): 1657-1658.
- Cooper, D. K., Gollackner, B. and Sachs, D. H. (2002). "Will the pig solve the transplantation backlog?" Annu Rev Med **53**: 133-147.
- Cornachione, A. S., Benedini-Elias, P. C., Polizello, J. C., Carvalho, L. C. and Mattiello-Sverzut, A. C. (2011). "Characterization of fiber types in different muscles of the hindlimb in female weanling and adult Wistar rats." Acta Histochem Cytochem **44**(2): 43-50.
- Corona, B. T., Wu, X., Ward, C. L., McDaniel, J. S., Rathbone, C. R. and Walters, T. J. (2013). "The promotion of a functional fibrosis in skeletal muscle with volumetric muscle loss injury following the transplantation of muscle-ECM." Biomaterials **34**(13): 3324-3335.
- Cosgrove, B. D., Sacco, A., Gilbert, P. M. and Blau, H. M. (2009). "A home away from home: challenges and opportunities in engineering in vitro muscle satellite cell niches." Differentiation **78**(2-3): 185-194.
- Crow, B. D., Haltom, J. D., Carson, W. L., Greene, W. B. and Cook, J. L. (2007). "Evaluation of a novel biomaterial for intrasubstance muscle laceration repair." J Orthop Res **25**(3): 396-403.
- Dai, L. G., Huang, G. S. and Hsu, S. H. (2013). "Sciatic nerve regeneration by cocultured Schwann cells and stem cells on microporous nerve conduits." Cell Transplant **22**(11): 2029-2039.
- Daumas, A., Magalon, J., Delaunay, F., Abellan, M., Philandrianos, C., Sabatier, F., Granel, B. and Magalon, G. (2020). "Fat Grafting for Treatment of Facial Scleroderma." Clin Plast Surg **47**(1): 155-163.
- Del Vecchio, D. A., Villanueva, N. L., Mohan, R., Johnson, B., Wan, D., Venkataram, A. and Rohrich, R. J. (2018). "Clinical Implications of Gluteal Fat Graft Migration: A Dynamic Anatomical Study." Plast Reconstr Surg **142**(5): 1180-1192.
- Deng, B., Wehling-Henricks, M., Villalta, S. A., Wang, Y. and Tidball, J. G. (2012). "IL-10 triggers changes in macrophage phenotype that promote muscle growth and regeneration." J Immunol **189**(7): 3669-3680.

- Deng, C., Yao, Y., Liu, Z., Li, H., Yang, Z., Wang, D. and Wei, Z. (2019). "Chronic wound treatment with high-density nanofat grafting combined with negative pressure wound therapy." Int J Clin Exp Med **12**(2): 1402-1411.
- DeQuach, J. A., Lin, J. E., Cam, C., Hu, D., Salvatore, M. A., Sheikh, F. and Christman, K. L. (2012). "Injectable skeletal muscle matrix hydrogel promotes neovascularization and muscle cell infiltration in a hindlimb ischemia model." Eur Cell Mater **23**: 400-412; discussion 412.
- DeQuach, J. A., Mezzano, V., Miglani, A., Lange, S., Keller, G. M., Sheikh, F. and Christman, K. L. (2010). "Simple and high yielding method for preparing tissue specific extracellular matrix coatings for cell culture." PLoS One **5**(9): e13039.
- Di Rocco, G., Iachininoto, M. G., Tritarelli, A., Straino, S., Zacheo, A., Germani, A., Crea, F. and Capogrossi, M. C. (2006). "Myogenic potential of adipose-tissue-derived cells." J Cell Sci **119**(Pt 14): 2945-2952.
- di Summa, P. G., Kingham, P. J., Raffoul, W., Wiberg, M., Terenghi, G. and Kalbermatten, D. F. (2010). "Adipose-derived stem cells enhance peripheral nerve regeneration." J Plast Reconstr Aesthet Surg **63**(9): 1544-1552.
- Dimauro, I., Grasso, L., Fittipaldi, S., Fantini, C., Mercatelli, N., Racca, S., Geuna, S., Di Gianfrancesco, A., Caporossi, D., Pigozzi, F. and Borriero, P. (2014). "Platelet-rich plasma and skeletal muscle healing: a molecular analysis of the early phases of the regeneration process in an experimental animal model." PLoS One **9**(7): e102993.
- Dinh, P., Hazel, A., Palispis, W., Suryadevara, S. and Gupta, R. (2009). "Functional assessment after sciatic nerve injury in a rat model." Microsurgery **29**(8): 644-649.
- Dowdall, T., Robinson, I. and Meert, T. F. (2005). "Comparison of five different rat models of peripheral nerve injury." Pharmacol Biochem Behav **80**(1): 93-108.
- Duisit, J., Amiel, H., Wuthrich, T., Taddeo, A., Dedriche, A., Destoop, V., Pardoën, T., Bouzin, C., Joris, V., Magee, D., Vogelin, E., Harriman, D., Dessy, C., Orlando, G., Behets, C., Rieben, R., Gianello, P. and Lengele, B. (2018). "Perfusion-decellularization of human ear grafts enables ECM-based scaffolds for auricular vascularized composite tissue engineering." Acta Biomater **73**: 339-354.
- Duisit, J., Orlando, G., Debluts, D., Maistriaux, L., Xhema, D., de Bisthoven, Y. J., Galli, C., Peloso, A., Behets, C., Lengele, B. and Gianello, P. (2017). "Decellularization of the Porcine Ear Generates a Biocompatible, Nonimmunogenic Extracellular Matrix Platform for Face Subunit Bioengineering." Ann Surg.
- Dumont, N. and Frenette, J. (2010). "Macrophages protect against muscle atrophy and promote muscle recovery in vivo and in vitro: a mechanism partly dependent on the insulin-like growth factor-1 signaling molecule." Am J Pathol **176**(5): 2228-2235.

- Edgar, L., Altamimi, A., García Sánchez, M., Tamburrinia, R., Asthana, A., Gazia, C. and Orlando, G. (2018). "Utility of extracellular matrix powders in tissue engineering." Organogenesis **14**(4): 172-186.
- Elebring, E., Kuna, V. K., Kvarnstrom, N. and Sumitran-Holgersson, S. (2017). "Cold-perfusion decellularization of whole-organ porcine pancreas supports human fetal pancreatic cell attachment and expression of endocrine and exocrine markers." J Tissue Eng **8**: 2041731417738145.
- Engler, A. J., Griffin, M. A., Sen, S., Bonnemann, C. G., Sweeney, H. L. and Discher, D. E. (2004). "Myotubes differentiate optimally on substrates with tissue-like stiffness: pathological implications for soft or stiff microenvironments." J Cell Biol **166**(6): 877-887.
- Erba, P., Mantovani, C., Kalbermatten, D. F., Pierer, G., Terenghi, G. and Kingham, P. J. (2010). "Regeneration potential and survival of transplanted undifferentiated adipose tissue-derived stem cells in peripheral nerve conduits." J Plast Reconstr Aesthet Surg **63**(12): e811-817.
- Evans, B. G. A., Gronet, E. M. and Saint-Cyr, M. H. (2020). "How Fat Grafting Works." Plast Reconstr Surg Glob Open **8**(7): e2705.
- Evans, G. R. (2001). "Peripheral nerve injury: a review and approach to tissue engineered constructs." Anat Rec **263**(4): 396-404.
- Fandel, T. M., Albersen, M., Lin, G., Qiu, X., Ning, H., Banie, L., Lue, T. F. and Lin, C. S. (2012). "Recruitment of intracavernously injected adipose-derived stem cells to the major pelvic ganglion improves erectile function in a rat model of cavernous nerve injury." Eur Urol **61**(1): 201-210.
- Fang, P. H., Lin, Y. Y. and Lin, C. H. (2020). "A Protection Tent for Airway Management in Patients With COVID-19 Infection." Ann Emerg Med **75**(6): 787-788.
- Farthing, J. P., Krentz, J. R., Magnus, C. R., Barss, T. S., Lanovaz, J. L., Cummine, J., Esopenko, C., Sarty, G. E. and Borowsky, R. (2011). "Changes in functional magnetic resonance imaging cortical activation with cross education to an immobilized limb." Med Sci Sports Exerc **43**(8): 1394-1405.
- Fisher, C., Grahovac, T. L., Schafer, M. E., Shippert, R. D., Marra, K. G. and Rubin, J. P. (2013). "Comparison of harvest and processing techniques for fat grafting and adipose stem cell isolation." Plast Reconstr Surg **132**(2): 351-361.
- Foster, W., Li, Y., Usas, A., Somogyi, G. and Huard, J. (2003). "Gamma interferon as an antifibrosis agent in skeletal muscle." J Orthop Res **21**(5): 798-804.
- Fredman, R., Edkins, R. E. and Hultman, C. S. (2016). "Fat grafting for neuropathic pain after severe burns." Annals of plastic surgery **76**: S298-S303.

- Freeman, M. and Fuerst, M. (2012). "Does the FDA have regulatory authority over adult autologous stem cell therapies? 21 CFR 1271 and the emperor's new clothes." J Transl Med **10**: 60.
- Fricker, L., Penna, V., Lampert, F., Stark, G. B., Witzel, C. and Koulaxouzidis, G. (2016). "A self-made, low-cost infrared system for evaluating the sciatic functional index in mice." Neural Regen Res **11**(5): 829-834.
- Frostick, S. P., Yin, Q. and Kemp, G. J. (1998). "Schwann cells, neurotrophic factors, and peripheral nerve regeneration." Microsurgery **18**(7): 397-405.
- Fu, Y., Fan, X., Tian, C., Luo, J., Zhang, Y., Deng, L., Qin, T. and Lv, Q. (2016). "Decellularization of porcine skeletal muscle extracellular matrix for the formulation of a matrix hydrogel: a preliminary study." J Cell Mol Med **20**(4): 740-749.
- Fu, Y., Luo, N., Klein, R. L. and Garvey, W. T. (2005). "Adiponectin promotes adipocyte differentiation, insulin sensitivity, and lipid accumulation." J Lipid Res **46**(7): 1369-1379.
- Fukuba, M., Uozaki, H. and Komuro, Y. (2020). "Effectiveness of the combination of fat grafting and injection on radiation ulcer healing." Journal of Plastic Surgery and Hand Surgery **54**(1): 24-28.
- Fukushi, J., Ono, M., Morikawa, W., Iwamoto, Y. and Kuwano, M. (2000). "The activity of soluble VCAM-1 in angiogenesis stimulated by IL-4 and IL-13." J Immunol **165**(5): 2818-2823.
- Fukushima, K., Nakamura, A., Ueda, H., Yuasa, K., Yoshida, K., Takeda, S. and Ikeda, S. (2007). "Activation and localization of matrix metalloproteinase-2 and -9 in the skeletal muscle of the muscular dystrophy dog (CXMDJ)." BMC Musculoskelet Disord **8**: 54.
- Gallo, G. (2011). "The cytoskeletal and signaling mechanisms of axon collateral branching." Dev Neurobiol **71**(3): 201-220.
- Gaudet, A. D., Popovich, P. G. and Ramer, M. S. (2011). "Wallerian degeneration: gaining perspective on inflammatory events after peripheral nerve injury." J Neuroinflammation **8**: 110.
- Geere, J., Chester, R., Kale, S. and Jerosch-Herold, C. (2007). "Power grip, pinch grip, manual muscle testing or thenar atrophy - which should be assessed as a motor outcome after carpal tunnel decompression? A systematic review." BMC Musculoskelet Disord **8**: 114.
- George, R. and Griffin, J. W. (1994). "The proximo-distal spread of axonal degeneration in the dorsal columns of the rat." J Neurocytol **23**(11): 657-667.
- Georgiou, M., Golding, J. P., Loughlin, A. J., Kingham, P. J. and Phillips, J. B. (2015). "Engineered neural tissue with aligned, differentiated adipose-derived stem cells promotes peripheral nerve regeneration across a critical sized defect in rat sciatic nerve." Biomaterials **37**: 242-251.

- Geuna, S. (2015). "The sciatic nerve injury model in pre-clinical research." J Neurosci Methods **243**: 39-46.
- Ghoreishian, M., Rezaei, M., Beni, B. H., Javanmard, S. H., Attar, B. M. and Zalzali, H. (2013). "Facial nerve repair with Gore-Tex tube and adipose-derived stem cells: an animal study in dogs." J Oral Maxillofac Surg **71**(3): 577-587.
- Gianni-Barrera, R., Trani, M., Reginato, S. and Banfi, A. (2011). "To sprout or to split? VEGF, Notch and vascular morphogenesis." Biochem Soc Trans **39**(6): 1644-1648.
- Giatsidis, G., Succar, J., Haddad, A., Lago, G., Schaffer, C., Wang, X., Schilling, B., Chnari, E., Matsumine, H. and Orgill, D. P. (2019). "Preclinical Optimization of a Shelf-Ready, Injectable, Human-Derived, Decellularized Allograft Adipose Matrix." Tissue Eng Part A **25**(3-4): 271-287.
- Gibson, D. A. and Ma, L. (2011). "Developmental regulation of axon branching in the vertebrate nervous system." Development **138**(2): 183-195.
- Gilbert, T. W. (2012). "Strategies for tissue and organ decellularization." J Cell Biochem **113**(7): 2217-2222.
- Gillies, A. R., Smith, L. R., Lieber, R. L. and Varghese, S. (2011). "Method for decellularizing skeletal muscle without detergents or proteolytic enzymes." Tissue Eng Part C Methods **17**(4): 383-389.
- Gilpin, S. E., Ren, X., Okamoto, T., Guyette, J. P., Mou, H., Rajagopal, J., Mathisen, D. J., Vacanti, J. P. and Ott, H. C. (2014). "Enhanced lung epithelial specification of human induced pluripotent stem cells on decellularized lung matrix." Ann Thorac Surg **98**(5): 1721-1729; discussion 1729.
- Gimble, J. M., Katz, A. J. and Bunnell, B. A. (2007). "Adipose-derived stem cells for regenerative medicine." Circ Res **100**(9): 1249-1260.
- Glass, D. J. (2003). "Signalling pathways that mediate skeletal muscle hypertrophy and atrophy." Nat Cell Biol **5**(2): 87-90.
- Godoy, P. M. and Munhoz, A. M. (2018). "Intramuscular gluteal augmentation with implants associated with immediate fat grafting." Clinics in plastic surgery **45**(2): 203-215.
- Gonzalez-Cruz, R. D. and Darling, E. M. (2013). "Adipose-derived stem cell fate is predicted by cellular mechanical properties." Adipocyte **2**(2): 87-91.
- Gordon, T. and English, A. W. (2016). "Strategies to promote peripheral nerve regeneration: electrical stimulation and/or exercise." Eur J Neurosci **43**(3): 336-350.
- Gordon, T., Tyreman, N. and Raji, M. A. (2011). "The basis for diminished functional recovery after delayed peripheral nerve repair." J Neurosci **31**(14): 5325-5334.

- Gottfried, E., Kunz-Schughart, L. A., Weber, A., Rehli, M., Peuker, A., Muller, A., Kastenberger, M., Brockhoff, G., Andreesen, R. and Kreutz, M. (2008). "Expression of CD68 in non-myeloid cell types." Scand J Immunol **67**(5): 453-463.
- Gramsbergen, A., J, I. J.-P. and Meek, M. F. (2000). "Sciatic nerve transection in the adult rat: abnormal EMG patterns during locomotion by aberrant innervation of hindleg muscles." Exp Neurol **161**(1): 183-193.
- Grinsell, D. and Keating, C. P. (2014). "Peripheral nerve reconstruction after injury: a review of clinical and experimental therapies." Biomed Res Int **2014**: 698256.
- Grover, V., Kapoor, A., Malhotra, R. and Sachdeva, S. (2011). "Bone allografts: a review of safety and efficacy." Indian J Dent Res **22**(3): 496.
- Gumucio, J. P., Flood, M. D., Roche, S. M., Sugg, K. B., Momoh, A. O., Kosnik, P. E., Bedi, A. and Mendias, C. L. (2016). "Stromal vascular stem cell treatment decreases muscle fibrosis following chronic rotator cuff tear." Int Orthop **40**(4): 759-764.
- Guyette, J. P., Gilpin, S. E., Charest, J. M., Tapias, L. F., Ren, X. and Ott, H. C. (2014). "Perfusion decellularization of whole organs." Nat Protoc **9**(6): 1451-1468.
- Hall, J. K., Banks, G. B., Chamberlain, J. S. and Olwin, B. B. (2010). "Prevention of muscle aging by myofiber-associated satellite cell transplantation." Sci Transl Med **2**(57): 57ra83.
- Hallock, G. G. (1991). "Complications of 100 consecutive local fasciocutaneous flaps." Plast Reconstr Surg **88**(2): 264-268.
- Hamrick, M. W., McGee-Lawrence, M. E. and Frechette, D. M. (2016). "Fatty Infiltration of Skeletal Muscle: Mechanisms and Comparisons with Bone Marrow Adiposity." Front Endocrinol (Lausanne) **7**: 69.
- Harris, M. A. and Steudel, K. (2002). "The relationship between maximum jumping performance and hind limb morphology/physiology in domestic cats (*Felis silvestris catus*)." J Exp Biol **205**(Pt 24): 3877-3889.
- Hatcher, H. C., Atala, A. and Allickson, J. G. (2015). Chapter 2 - Landscape of Cell Banking. Translational Regenerative Medicine. A. Atala and J. G. Allickson. Boston, Academic Press: 13-19.
- He, L., Yadgarov, A., Sharif, S. and McCluskey, L. P. (2012). "Aging profoundly delays functional recovery from gustatory nerve injury." Neuroscience **209**: 208-218.
- Heijink, I. H., Vellenga, E., Borger, P., Postma, D. S., de Monchy, J. G. and Kauffman, H. F. (2002). "Interleukin-6 promotes the production of interleukin-4 and interleukin-5 by interleukin-2-dependent and -independent mechanisms in freshly isolated human T cells." Immunology **107**(3): 316-324.

- Helmers, S. B., Bruton, M., Loell, I., Ulfgren, A. K., Gracie, A. J., McInnes, I. B. and Lundberg, I. E. (2018). "Expression of interleukin-18 in muscle tissue of patients with polymyositis or dermatomyositis and effects of conventional immunosuppressive treatment." Rheumatology (Oxford) **57**(12): 2149-2157.
- Herbison, G. J., Jaweed, M. M. and Ditunno, J. F. (1980). "Effect of activity and inactivity on reinnervating rat skeletal muscle contractility." Exp Neurol **70**(3): 498-506.
- Hernandez-Cortes, P., Toledo-Romero, M. A., Delgado, M., Gonzalez-Rey, E., Gomez Sanchez, R., Prados-Olleta, N., Aneiros-Fernandez, J., Crespo-Lora, V., Aguilar, M., Galindo-Moreno, P. and O'Valle, F. (2017). "Ghrelin and adipose-derived mesenchymal stromal cells improve nerve regeneration in a rat model of epsilon-caprolactone conduit reconstruction." Histol Histopathol **32**(6): 627-637.
- Hodde, J., Janis, A. and Hiles, M. (2007). "Effects of sterilization on an extracellular matrix scaffold: part II. Bioactivity and matrix interaction." J Mater Sci Mater Med **18**(4): 545-550.
- Hoeben, A., Landuyt, B., Highley, M. S., Wildiers, H., Van Oosterom, A. T. and De Bruijn, E. A. (2004). "Vascular endothelial growth factor and angiogenesis." Pharmacol Rev **56**(4): 549-580.
- Hoke, A. (2006). "Mechanisms of Disease: what factors limit the success of peripheral nerve regeneration in humans?" Nat Clin Pract Neurol **2**(8): 448-454.
- Hong, K. H., Cho, M. L., Min, S. Y., Shin, Y. J., Yoo, S. A., Choi, J. J., Kim, W. U., Song, S. W. and Cho, C. S. (2007). "Effect of interleukin-4 on vascular endothelial growth factor production in rheumatoid synovial fibroblasts." Clin Exp Immunol **147**(3): 573-579.
- Hsieh, S. C., Chang, C. J., Cheng, W. T., Tseng, T. C. and Hsu, S. H. (2016). "Effect of an Epineurial-Like Biohybrid Nerve Conduit on Nerve Regeneration." Cell Transplant **25**(3): 559-574.
- Hsueh, Y. Y., Chang, Y. J., Huang, T. C., Fan, S. C., Wang, D. H., Chen, J. J., Wu, C. C. and Lin, S. C. (2014). "Functional recoveries of sciatic nerve regeneration by combining chitosan-coated conduit and neurosphere cells induced from adipose-derived stem cells." Biomaterials **35**(7): 2234-2244.
- Hu, D., Zhang, Y., Cao, R., Hao, Y., Yang, X., Tian, T. and Zhang, J. (2020). "The protective effects of granulocyte-macrophage colony-stimulating factor against radiation-induced lung injury." Transl Lung Cancer Res **9**(6): 2440-2459.
- Huang, C. H., Chen, H. C., Huang, Y. L., Mardini, S. and Feng, G. M. (2004). "Comparison of the radial forearm flap and the thinned anterolateral thigh cutaneous flap for reconstruction of tongue defects: an evaluation of donor-site morbidity." Plast Reconstr Surg **114**(7): 1704-1710.

- Hubbard, S. R. and Gnanasambandan, K. (2013). "Structure and activation of MuSK, a receptor tyrosine kinase central to neuromuscular junction formation." Biochim Biophys Acta **1834**(10): 2166-2169.
- Huckhagel, T., Nuchtern, J., Regelsberger, J., Lefering, R. and TraumaRegister, D. G. U. (2018). "Nerve injury in severe trauma with upper extremity involvement: evaluation of 49,382 patients from the TraumaRegister DGU(R) between 2002 and 2015." Scand J Trauma Resusc Emerg Med **26**(1): 76.
- Huebner, E. A. and Strittmatter, S. M. (2009). "Axon regeneration in the peripheral and central nervous systems." Results Probl Cell Differ **48**: 339-351.
- Hwang, J., San, B. H., Turner, N. J., White, L. J., Faulk, D. M., Badylak, S. F., Li, Y. and Yu, S. M. (2017). "Molecular assessment of collagen denaturation in decellularized tissues using a collagen hybridizing peptide." Acta Biomater **53**: 268-278.
- Jan, S. N., Bashir, M. M., Khan, F. A., Hidayat, Z., Ansari, H. H., Sohail, M., Bajwa, A. B., Shami, H. B., Hanif, A. and Aziz, F. (2019). "Unfiltered nanofat injections rejuvenate postburn scars of face." Annals of plastic surgery **82**(1): 28-33.
- Jaquet, J. B., Luijsterburg, A. J., Kalmijn, S., Kuypers, P. D., Hofman, A. and Hovius, S. E. (2001). "Median, ulnar, and combined median-ulnar nerve injuries: functional outcome and return to productivity." J Trauma **51**(4): 687-692.
- Jeong, W., Kung, H., Cheng, C. C., Lim, C., Jung, M. J., Lee, J., Kim, D. S. and Shin, Y. (2017). "Dexmedetomidine to Help Nerve Regeneration in a Rat Sciatic Nerve Injury Model." Pain Res Manag **2017**: 9045608.
- Jessen, K. R. and Mirsky, R. (2016). "The repair Schwann cell and its function in regenerating nerves." J Physiol **594**(13): 3521-3531.
- Jiang, L. F., Chen, O., Chu, T. G., Ding, J. and Yu, Q. (2015). "T Lymphocyte Subsets and Cytokines in Rats Transplanted with Adipose-Derived Mesenchymal Stem Cells and Acellular Nerve for Repairing the Nerve Defects." J Korean Neurosurg Soc **58**(2): 101-106.
- Jin, R., Shen, M., Yu, L., Wang, X. and Lin, X. (2017). "Adipose-Derived Stem Cells Suppress Inflammation Induced by IL-1beta through Down-Regulation of P2X7R Mediated by miR-373 in Chondrocytes of Osteoarthritis." Mol Cells **40**(3): 222-229.
- Jonsson, S., Wiberg, R., McGrath, A. M., Novikov, L. N., Wiberg, M., Novikova, L. N. and Kingham, P. J. (2013). "Effect of delayed peripheral nerve repair on nerve regeneration, Schwann cell function and target muscle recovery." PLoS One **8**(2): e56484.
- Jortay, J., Senou, M., Abou-Samra, M., Noel, L., Robert, A., Many, M. C. and Brichard, S. M. (2012). "Adiponectin and skeletal muscle: pathophysiological implications in metabolic stress." Am J Pathol **181**(1): 245-256.

- Jortner, B. S. (2000). "Mechanisms of toxic injury in the peripheral nervous system: neuropathologic considerations." Toxicol Pathol **28**(1): 54-69.
- Kalil, K., Li, L. and Hutchins, B. I. (2011). "Signaling mechanisms in cortical axon growth, guidance, and branching." Front Neuroanat **5**: 62.
- Kanaya, F., Firrell, J. C. and Breidenbach, W. C. (1996). "Sciatic function index, nerve conduction tests, muscle contraction, and axon morphometry as indicators of regeneration." Plast Reconstr Surg **98**(7): 1264-1271, discussion 1272-1264.
- Kandarian, S. C. and Jackman, R. W. (2006). "Intracellular signaling during skeletal muscle atrophy." Muscle Nerve **33**(2): 155-165.
- Kappos, E. A., Baenziger-Sieber, P., Tremp, M., Engels, P. E., Thommen, S., Sprenger, L., Benz, R. M., Schaefer, D. J., Schaeren, S. and Kalbermatten, D. F. (2018). "Epineural adipose-derived stem cell injection in a sciatic rodent model." Brain Behav **8**(7): e01027.
- Kappos, E. A., Engels, P. E., Tremp, M., Meyer zu Schwabedissen, M., di Summa, P., Fischmann, A., von Felten, S., Scherberich, A., Schaefer, D. J. and Kalbermatten, D. F. (2015). "Peripheral Nerve Repair: Multimodal Comparison of the Long-Term Regenerative Potential of Adipose Tissue-Derived Cells in a Biodegradable Conduit." Stem Cells Dev **24**(18): 2127-2141.
- Kappos, E. A., Sieber, P. K., Engels, P. E., Mariolo, A. V., D'Arpa, S., Schaefer, D. J. and Kalbermatten, D. F. (2017). "Validity and reliability of the CatWalk system as a static and dynamic gait analysis tool for the assessment of functional nerve recovery in small animal models." Brain Behav **7**(7): e00723.
- Kasukonis, B., Kim, J., Brown, L., Jones, J., Ahmadi, S., Washington, T. and Wolchok, J. (2016). "Codelivery of Infusion Decellularized Skeletal Muscle with Minced Muscle Autografts Improved Recovery from Volumetric Muscle Loss Injury in a Rat Model." Tissue Eng Part A **22**(19-20): 1151-1163.
- Kim, D. S., Lee, M. W., Yoo, K. H., Lee, T. H., Kim, H. J., Jang, I. K., Chun, Y. H., Kim, H. J., Park, S. J., Lee, S. H., Son, M. H., Jung, H. L., Sung, K. W. and Koo, H. H. (2014). "Gene expression profiles of human adipose tissue-derived mesenchymal stem cells are modified by cell culture density." PLoS One **9**(1): e83363.
- Kim, J. K., Choi, S. R., Choi, M. J., Kim, S. G., Lee, Y. K., Noh, J. W., Kim, H. J. and Song, Y. R. (2014). "Prevalence of and factors associated with sarcopenia in elderly patients with end-stage renal disease." Clin Nutr **33**(1): 64-68.
- Kim, Y. K., Yun, P. Y., Kim, J. H., Lee, J. Y. and Lee, W. (2015). "The quantitative sensory testing is an efficient objective method for assessment of nerve injury." Maxillofac Plast Reconstr Surg **37**(1): 13.

- Kimata, Y., Uchiyama, K., Ebihara, S., Sakuraba, M., Iida, H., Nakatsuka, T. and Harii, K. (2000). "Anterolateral thigh flap donor-site complications and morbidity." Plast Reconstr Surg **106**(3): 584-589.
- Kingham, P. J., Kolar, M. K., Novikova, L. N., Novikov, L. N. and Wiberg, M. (2014). "Stimulating the neurotrophic and angiogenic properties of human adipose-derived stem cells enhances nerve repair." Stem Cells Dev **23**(7): 741-754.
- Kjaer, M. (2004). "Role of extracellular matrix in adaptation of tendon and skeletal muscle to mechanical loading." Physiol Rev **84**(2): 649-698.
- Klein, S. M., Vykoukal, J., Li, D. P., Pan, H. L., Zeitler, K., Alt, E., Geis, S., Felthaus, O. and Prantl, L. (2016). "Peripheral Motor and Sensory Nerve Conduction following Transplantation of Undifferentiated Autologous Adipose Tissue-Derived Stem Cells in a Biodegradable U.S. Food and Drug Administration-Approved Nerve Conduit." Plast Reconstr Surg **138**(1): 132-139.
- Klinger, M., Caviggioli, F., Klinger, F. M., Giannasi, S., Bandi, V., Banzatti, B., Forcellini, D., Maione, L., Catania, B. and Vinci, V. (2013). "Autologous fat graft in scar treatment." J Craniofac Surg **24**(5): 1610-1615.
- Klinger, M., Klinger, F., Caviggioli, F., Maione, L., Catania, B., Veronesi, A., Giannasi, S., Bandi, V., Giaccone, M. and Siliprandi, M. (2020). "Fat grafting for treatment of facial scars." Clinics in plastic surgery **47**(1): 131-138.
- Knott, P. D., Seth, R., Waters, H. H., Revenaugh, P. C., Alam, D., Scharpf, J., Meltzer, N. E. and Fritz, M. A. (2016). "Short-term donor site morbidity: A comparison of the anterolateral thigh and radial forearm fasciocutaneous free flaps." Head Neck **38 Suppl 1**: E945-948.
- Kokai, L. E., Bourbeau, D., Weber, D., McAtee, J. and Marra, K. G. (2011). "Sustained growth factor delivery promotes axonal regeneration in long gap peripheral nerve repair." Tissue Eng Part A **17**(9-10): 1263-1275.
- Kokai, L. E., Schilling, B. K., Chnari, E., Huang, Y. C., Imming, E. A., Karunamurthy, A., Khouri, R. K., D'Amico, R. A., Coleman, S. R., Marra, K. G. and Rubin, J. P. (2019). "Injectable Allograft Adipose Matrix Supports Adipogenic Tissue Remodeling in the Nude Mouse and Human." Plast Reconstr Surg **143**(2): 299e-309e.
- Kokai, L. E., Sivak, W. N., Schilling, B. K., Karunamurthy, A., Egro, F. M., Schusterman, M. A., Minter, D. M., Simon, P., D'Amico, R. A. and Rubin, J. P. (2020). "Clinical Evaluation of an Off-the-Shelf Allogeneic Adipose Matrix for Soft Tissue Reconstruction." Plast Reconstr Surg Glob Open **8**(1): e2574.
- Kolle, S. F., Fischer-Nielsen, A., Mathiasen, A. B., Elberg, J. J., Oliveri, R. S., Glovinski, P. V., Kastrup, J., Kirchhoff, M., Rasmussen, B. S., Talman, M. L., Thomsen, C., Dickmeiss, E. and Drzewiecki, K. T. (2013). "Enrichment of autologous fat grafts with ex-vivo expanded adipose tissue-derived stem cells for graft survival: a randomised placebo-controlled trial." Lancet **382**(9898): 1113-1120.

- Kosmac, K., Peck, B. D., Walton, R. G., Mula, J., Kern, P. A., Bamman, M. M., Dennis, R. A., Jacobs, C. A., Lattermann, C., Johnson, D. L. and Peterson, C. A. (2018). "Immunohistochemical Identification of Human Skeletal Muscle Macrophages." Bio Protoc **8**(12).
- Krastev, T. K., Schop, S. J., Hommes, J., Piatkowski, A. and van der Hulst, R. R. (2020). "Autologous fat transfer to treat fibrosis and scar-related conditions: a systematic review and meta-analysis." Journal of Plastic, Reconstructive & Aesthetic Surgery.
- Krych, A. J., Jackson, J. D., Hoskin, T. L. and Dahm, D. L. (2008). "A meta-analysis of patellar tendon autograft versus patellar tendon allograft in anterior cruciate ligament reconstruction." Arthroscopy **24**(3): 292-298.
- Lacraz, G., Rouleau, A. J., Couture, V., Sollrard, T., Drouin, G., Veillette, N., Grandbois, M. and Grenier, G. (2015). "Increased Stiffness in Aged Skeletal Muscle Impairs Muscle Progenitor Cell Proliferative Activity." PLoS One **10**(8): e0136217.
- Largo, R. D., Tchang, L. A., Mele, V., Scherberich, A., Harder, Y., Wettstein, R. and Schaefer, D. J. (2014). "Efficacy, safety and complications of autologous fat grafting to healthy breast tissue: a systematic review." J Plast Reconstr Aesthet Surg **67**(4): 437-448.
- Lee, H., Ju, Y. M., Kim, I., Elsangeedy, E., Lee, J. H., Yoo, J. J., Atala, A. and Lee, S. J. (2020). "A novel decellularized skeletal muscle-derived ECM scaffolding system for in situ muscle regeneration." Methods **171**: 77-85.
- Lee, J. H., Chang, C. H., Seo, S. W. and Kim, J. K. (2013). "The effects of sterilization methods on lyophilized cartilage grafts in an experimental model." J Craniofac Surg **24**(4): 1436-1440.
- Lepley, L. K. and Palmieri-Smith, R. M. (2014). "Cross-education strength and activation after eccentric exercise." J Athl Train **49**(5): 582-589.
- Leto Barone, A. A., Khalifian, S., Lee, W. P. and Brandacher, G. (2013). "Immunomodulatory effects of adipose-derived stem cells: fact or fiction?" Biomed Res Int **2013**: 383685.
- Li, Y., Xu, W. and Cheng, L. Y. (2017). "Adipose-derived mesenchymal stem cells accelerate nerve regeneration and functional recovery in a rat model of recurrent laryngeal nerve injury." Neural Regen Res **12**(9): 1544-1550.
- Li, Y. P. (2003). "TNF-alpha is a mitogen in skeletal muscle." Am J Physiol Cell Physiol **285**(2): C370-376.
- Lichtenberg, A., Cebotari, S., Tudorache, I., Sturz, G., Winterhalter, M., Hilfiker, A. and Haverich, A. (2006). "Flow-dependent re-endothelialization of tissue-engineered heart valves." J Heart Valve Dis **15**(2): 287-293; discussion 293-284.

- Lieber, R. L. and Ward, S. R. (2013). "Cellular mechanisms of tissue fibrosis. 4. Structural and functional consequences of skeletal muscle fibrosis." Am J Physiol Cell Physiol **305**(3): C241-252.
- Light, N. and Champion, A. E. (1984). "Characterization of muscle epimysium, perimysium and endomysium collagens." Biochem J **219**(3): 1017-1026.
- Lim, T. K., Shi, X. Q., Johnson, J. M., Rone, M. B., Antel, J. P., David, S. and Zhang, J. (2015). "Peripheral nerve injury induces persistent vascular dysfunction and endoneurial hypoxia, contributing to the genesis of neuropathic pain." J Neurosci **35**(8): 3346-3359.
- Lin, G., Albersen, M., Harraz, A. M., Fandel, T. M., Garcia, M., McGrath, M. H., Konety, B. R., Lue, T. F. and Lin, C. S. (2011). "Cavernous nerve repair with allogenic adipose matrix and autologous adipose-derived stem cells." Urology **77**(6): 1509 e1501-1508.
- Lindegaard, B., Hvid, T., Wolsk Mygind, H., Mortensen, O. H., Grondal, T., Abildgaard, J., Gerstoft, J., Pedersen, B. K. and Baranowski, M. (2018). "Low expression of IL-18 and IL-18 receptor in human skeletal muscle is associated with systemic and intramuscular lipid metabolism-Role of HIV lipodystrophy." PLoS One **13**(1): e0186755.
- Lisa, A., Murolo, M., Maione, L., Vinci, V., Bandi, V., Klinger, F. and Klinger, M. (2016). "Painful scar neuropathy: principles of diagnosis and treatment." Plastic and Aesthetic Research **3**(2): 68.
- Liu, B. S., Yang, Y. C. and Shen, C. C. (2014). "Regenerative effect of adipose tissue-derived stem cells transplantation using nerve conduit therapy on sciatic nerve injury in rats." J Tissue Eng Regen Med **8**(5): 337-350.
- Liu, J., Saul, D., Boker, K. O., Ernst, J., Lehman, W. and Schilling, A. F. (2018). "Current Methods for Skeletal Muscle Tissue Repair and Regeneration." Biomed Res Int **2018**: 1984879.
- Liu, Q. Y., Miao, Y., Wang, X. H., Wang, P., Cheng, Z. C. and Qian, T. M. (2019). "Increased levels of miR-3099 induced by peripheral nerve injury promote Schwann cell proliferation and migration." Neural Regen Res **14**(3): 525-531.
- Liu, W. W., Li, H., Guo, Z. M., Zhang, Q., Yang, A. K., Liu, X. K. and Song, M. (2011). "Reconstruction of soft-tissue defects of the head and neck: radial forearm flap or anterolateral thigh flap?" Eur Arch Otorhinolaryngol **268**(12): 1809-1812.
- Liu, Y., Ning, Z., Chen, Y., Guo, M., Liu, Y., Gali, N. K., Sun, L., Duan, Y., Cai, J., Westerdahl, D., Liu, X., Ho, K.-f., Kan, H., Fu, Q. and Lan, K. (2020). "Aerodynamic Characteristics and RNA Concentration of SARS-CoV-2 Aerosol in Wuhan Hospitals during COVID-19 Outbreak." bioRxiv: 2020.2003.2008.982637.
- Liu, Y., Shi, J., Lu, C. C., Wang, Z. B., Lyuksyutova, A. I., Song, X. J. and Zou, Y. (2005). "Ryk-mediated Wnt repulsion regulates posterior-directed growth of corticospinal tract." Nat Neurosci **8**(9): 1151-1159.

- Liu, Z. Y., Chen, Z. B. and Chen, J. H. (2018). "A novel chronic nerve compression model in the rat." Neural Regen Res **13**(8): 1477-1485.
- Llobet Rosell, A. and Neukomm, L. J. (2019). "Axon death signalling in Wallerian degeneration among species and in disease." Open Biol **9**(8): 190118.
- Lopez, J., Xin, K., Quan, A., Xinan, K., Leto, A. A., Budihardjo, J., Ibrahim, Z., Mao, H.-Q., Lee, W. A. and Brandacher, G. (2018). "Abstract 128: Poly-caprolactone Nanofiber Nerve Wrap Improves Nerve Regeneration and Rodent Functional Outcomes after Delayed Nerve Repair." Plastic and Reconstructive Surgery Global Open **6**(4 Suppl): 100-101.
- Lovati, A. B., Bottagisio, M. and Moretti, M. (2016). "Decellularized and Engineered Tendons as Biological Substitutes: A Critical Review." Stem Cells Int **2016**: 7276150.
- Lu, T. Y., Lin, B., Kim, J., Sullivan, M., Tobita, K., Salama, G. and Yang, L. (2013). "Repopulation of decellularized mouse heart with human induced pluripotent stem cell-derived cardiovascular progenitor cells." Nat Commun **4**: 2307.
- Lundborg, G. (2003). "Nerve injury and repair—a challenge to the plastic brain." Journal of the Peripheral Nervous System **8**(4): 209-226.
- Lunn, E. R., Brown, M. C. and Perry, V. H. (1990). "The pattern of axonal degeneration in the peripheral nervous system varies with different types of lesion." Neuroscience **35**(1): 157-165.
- Luo, G., Hershko, D. D., Robb, B. W., Wray, C. J. and Hasselgren, P. O. (2003). "IL-1beta stimulates IL-6 production in cultured skeletal muscle cells through activation of MAP kinase signaling pathway and NF-kappa B." Am J Physiol Regul Integr Comp Physiol **284**(5): R1249-1254.
- Luo, H., Zhang, Y., Zhang, Z. and Jin, Y. (2012). "The protection of MSCs from apoptosis in nerve regeneration by TGFbeta1 through reducing inflammation and promoting VEGF-dependent angiogenesis." Biomaterials **33**(17): 4277-4287.
- Macadam, S. A. and Lennox, P. A. (2012). "Acellular dermal matrices: Use in reconstructive and aesthetic breast surgery." Can J Plast Surg **20**(2): 75-89.
- Mackey, A. L., Donnelly, A. E., Turpeenniemi-Hujanen, T. and Roper, H. P. (2004). "Skeletal muscle collagen content in humans after high-force eccentric contractions." J Appl Physiol (1985) **97**(1): 197-203.
- Mackey, A. L. and Kjaer, M. (2017). "The breaking and making of healthy adult human skeletal muscle in vivo." Skelet Muscle **7**(1): 24.
- Mackey, A. L., Kjaer, M., Charifi, N., Henriksson, J., Bojsen-Moller, J., Holm, L. and Kadi, F. (2009). "Assessment of satellite cell number and activity status in human skeletal muscle biopsies." Muscle Nerve **40**(3): 455-465.

- Mackinnon, S. E. and Dellon, A. L. (1988). Surgery of the peripheral nerve. New York Stuttgart ; New York, Thieme Medical Publishers ; G. Thieme Verlag.
- Magnus, C. R., Arnold, C. M., Johnston, G., Dal-Bello Haas, V., Basran, J., Krentz, J. R. and Farthing, J. P. (2013). "Cross-education for improving strength and mobility after distal radius fractures: a randomized controlled trial." Arch Phys Med Rehabil **94**(7): 1247-1255.
- Mallik, A. and Weir, A. I. (2005). "Nerve conduction studies: essentials and pitfalls in practice." Journal of Neurology, Neurosurgery & Psychiatry **76**(suppl 2): ii23.
- Mantovani, A., Sica, A., Sozzani, S., Allavena, P., Vecchi, A. and Locati, M. (2004). "The chemokine system in diverse forms of macrophage activation and polarization." Trends Immunol **25**(12): 677-686.
- Marconi, S., Castiglione, G., Turano, E., Bissolotti, G., Angiari, S., Farinazzo, A., Constantin, G., Bedogni, G., Bedogni, A. and Bonetti, B. (2012). "Human adipose-derived mesenchymal stem cells systemically injected promote peripheral nerve regeneration in the mouse model of sciatic crush." Tissue Eng Part A **18**(11-12): 1264-1272.
- Margolis, M. (2011). Arduino cookbook: recipes to begin, expand, and enhance your projects, " O'Reilly Media, Inc.".
- Martel, M. L. and Reardon, R. F. (2020). "Aerosol Barrier Hood for Use in the Management of Critically Ill Adults With COVID-19." Ann Emerg Med **76**(3): 370-371.
- Martin, I., Simmons, P. J. and Williams, D. F. (2014). "Manufacturing challenges in regenerative medicine." Sci Transl Med **6**(232): 232fs216.
- Martins, L., Gallo, C. C., Honda, T. S. B., Alves, P. T., Stilhano, R. S., Rosa, D. S., Koh, T. J. and Han, S. W. (2020). "Skeletal muscle healing by M1-like macrophages produced by transient expression of exogenous GM-CSF." Stem Cell Res Ther **11**(1): 473.
- Masgutov, R., Masgutova, G., Mukhametova, L., Garanina, E., Arkhipova, S. S., Zakirova, E., Mukhamedshina, Y. O., Margarita, Z., Gilazieva, Z., Syromiatnikova, V., Mullakhmetova, A., Kadyrova, G., Nigmatzyanova, M., Mikhail, S., Igor, P., Yagudin, R. and Rizvanov, A. (2018). "Allogenic Adipose Derived Stem Cells Transplantation Improved Sciatic Nerve Regeneration in Rats: Autologous Nerve Graft Model." Front Pharmacol **9**: 86.
- Masgutov, R. F., Masgutova, G. A., Zhuravleva, M. N., Salafutdinov, II, Mukhametshina, R. T., Mukhamedshina, Y. O., Lima, L. M., Reis, H. J., Kiyasov, A. P., Palotas, A. and Rizvanov, A. A. (2016). "Human adipose-derived stem cells stimulate neuroregeneration." Clin Exp Med **16**(3): 451-461.
- Matuska, A. M. and McFetridge, P. S. (2015). "The effect of terminal sterilization on structural and biophysical properties of a decellularized collagen-based scaffold; implications for stem cell adhesion." J Biomed Mater Res B Appl Biomater **103**(2): 397-406.

- McIntosh, K., Zvonic, S., Garrett, S., Mitchell, J. B., Floyd, Z. E., Hammill, L., Kloster, A., Di Halvorsen, Y., Ting, J. P., Storms, R. W., Goh, B., Kilroy, G., Wu, X. and Gimble, J. M. (2006). "The immunogenicity of human adipose-derived cells: temporal changes in vitro." Stem Cells **24**(5): 1246-1253.
- McMahon, G., Morse, C. I., Winwood, K., Burden, A. and Onambele, G. L. (2019). "Circulating Tumor Necrosis Factor Alpha May Modulate the Short-Term Detraining Induced Muscle Mass Loss Following Prolonged Resistance Training." Front Physiol **10**: 527.
- Mead, K. and Johnson, D. L. (2004). "An evaluation of portable high-efficiency particulate air filtration for expedient patient isolation in epidemic and emergency response." Ann Emerg Med **44**(6): 635-645.
- Mendez, A., Seikaly, H., Biron, V. L., Zhu, L. F. and Cote, D. W. (2016). "Brief electrical stimulation after facial nerve transection and neurotomy: a randomized prospective animal study." J Otolaryngol Head Neck Surg **45**: 7.
- Mendoza-Novelo, B., Avila, E. E., Cauch-Rodriguez, J. V., Jorge-Herrero, E., Rojo, F. J., Guinea, G. V. and Mata-Mata, J. L. (2011). "Decellularization of pericardial tissue and its impact on tensile viscoelasticity and glycosaminoglycan content." Acta Biomater **7**(3): 1241-1248.
- Menkes, S., Luca, M., Soldati, G. and Polla, L. (2020). "Subcutaneous Injections of Nanofat Adipose-derived Stem Cell Grafting in Facial Rejuvenation." Plast Reconstr Surg Glob Open **8**(1): e2550.
- Menorca, R. M., Fussell, T. S. and Elfar, J. C. (2013). "Nerve physiology: mechanisms of injury and recovery." Hand Clin **29**(3): 317-330.
- Merritt, E. K., Hammers, D. W., Tierney, M., Suggs, L. J., Walters, T. J. and Farrar, R. P. (2010). "Functional assessment of skeletal muscle regeneration utilizing homologous extracellular matrix as scaffolding." Tissue Eng Part A **16**(4): 1395-1405.
- Mohammadi, R., Asadollahi, A. and Amini, K. (2014). "Uncultured undifferentiated adipose-derived nucleated cell fractions combined with inside-out artery graft accelerate sciatic nerve regeneration and functional recovery." Int J Oral Maxillofac Surg **43**(9): 1161-1168.
- Mohammadi, R., Azizi, S. and Amini, K. (2013). "Effects of undifferentiated cultured omental adipose-derived stem cells on peripheral nerve regeneration." J Surg Res **180**(2): e91-97.
- Mohammadi, R., Yadegarazadi, M. J. and Amini, K. (2014). "Peripheral nerve regeneration following transection injury to rat sciatic nerve by local application of adrenocorticotropic hormone." J Craniomaxillofac Surg **42**(6): 784-789.
- Momtahan, N., Poornejad, N., Struk, J. A., Castleton, A. A., Herrod, B. J., Vance, B. R., Eatough, J. P., Roeder, B. L., Reynolds, P. R. and Cook, A. D. (2015). "Automation of Pressure Control Improves Whole Porcine Heart Decellularization." Tissue Eng Part C Methods **21**(11): 1148-1161.

- Monreal, J. (2017). "Functional and Aesthetic Recovery of Congenital Muscular Torticollis with Intramuscular Stromal Vascular Fraction Enriched Fat Grafting." Cureus **9**(1): e975.
- Montarras, D., Morgan, J., Collins, C., Relaix, F., Zaffran, S., Cumano, A., Partridge, T. and Buckingham, M. (2005). "Direct isolation of satellite cells for skeletal muscle regeneration." Science **309**(5743): 2064-2067.
- Moore, B. B., Coffey, M. J., Christensen, P., Sitterding, S., Ngan, R., Wilke, C. A., McDonald, R., Phare, S. M., Peters-Golden, M., Paine, R., 3rd and Toews, G. B. (2000). "GM-CSF regulates bleomycin-induced pulmonary fibrosis via a prostaglandin-dependent mechanism." J Immunol **165**(7): 4032-4039.
- Moratal, C., Raffort, J., Arrighi, N., Rekima, S., Schaub, S., Dechesne, C. A., Chinetti, G. and Dani, C. (2018). "IL-1beta- and IL-4-polarized macrophages have opposite effects on adipogenesis of intramuscular fibro-adipogenic progenitors in humans." Sci Rep **8**(1): 17005.
- Moss, R. L., Lynch, T. L. t. and Fitzsimons, D. P. (2017). "Acting on an impulse (or two): Advantages of high-frequency tetanic onset in skeletal muscle." J Gen Physiol **149**(3): 297-300.
- Mourkioti, F. and Rosenthal, N. (2005). "IGF-1, inflammation and stem cells: interactions during muscle regeneration." Trends Immunol **26**(10): 535-542.
- Nakahara, H., Song, J., Sugimoto, M., Hagihara, K., Kishimoto, T., Yoshizaki, K. and Nishimoto, N. (2003). "Anti-interleukin-6 receptor antibody therapy reduces vascular endothelial growth factor production in rheumatoid arthritis." Arthritis Rheum **48**(6): 1521-1529.
- Novak, C. B., Anastakis, D. J., Beaton, D. E., Mackinnon, S. E. and Katz, J. (2010). "Relationships among pain disability, pain intensity, illness intrusiveness, and upper extremity disability in patients with traumatic peripheral nerve injury." J Hand Surg Am **35**(10): 1633-1639.
- Novak, C. B. and von der Heyde, R. L. (2013). "Evidence and techniques in rehabilitation following nerve injuries." Hand Clin **29**(3): 383-392.
- Novak, M. L. and Koh, T. J. (2013). "Macrophage phenotypes during tissue repair." J Leukoc Biol **93**(6): 875-881.
- Novak, M. L., Weinheimer-Haus, E. M. and Koh, T. J. (2014). "Macrophage activation and skeletal muscle healing following traumatic injury." J Pathol **232**(3): 344-355.
- O'Neill, J. D., Anfang, R., Anandappa, A., Costa, J., Javidfar, J., Wobma, H. M., Singh, G., Freytes, D. O., Bacchetta, M. D., Sonett, J. R. and Vunjak-Novakovic, G. (2013). "Decellularization of human and porcine lung tissues for pulmonary tissue engineering." Ann Thorac Surg **96**(3): 1046-1055; discussion 1055-1046.

- Okazaki, T., Ebihara, S., Takahashi, H., Asada, M., Kanda, A. and Sasaki, H. (2005). "Macrophage colony-stimulating factor induces vascular endothelial growth factor production in skeletal muscle and promotes tumor angiogenesis." J Immunol **174**(12): 7531-7538.
- Orbay, H., Uysal, A. C., Hyakusoku, H. and Mizuno, H. (2012). "Differentiated and undifferentiated adipose-derived stem cells improve function in rats with peripheral nerve gaps." J Plast Reconstr Aesthet Surg **65**(5): 657-664.
- Oud, T., Beelen, A., Eijffinger, E. and Nollet, F. (2007). "Sensory re-education after nerve injury of the upper limb: a systematic review." Clin Rehabil **21**(6): 483-494.
- Oxer, J. and Blemings, H. (2011). Practical Arduino: cool projects for open source hardware, Apress.
- Padovano, W. M., Dengler, J., Patterson, M. M., Yee, A., Snyder-Warwick, A. K., Wood, M. D., Moore, A. M. and Mackinnon, S. E. (2020). "Incidence of Nerve Injury After Extremity Trauma in the United States." Hand (N Y): 1558944720963895.
- Park, J. U. and Kwon, S. T. (2017). "Potential of autologous adipose-derived stem cells to regenerate atrophied muscle in a rat model." Wound Repair Regen **25**(6): 944-955.
- Parmaksiz, M., Dogan, A., Odabas, S., Elcin, A. E. and Elcin, Y. M. (2016). "Clinical applications of decellularized extracellular matrices for tissue engineering and regenerative medicine." Biomed Mater **11**(2): 022003.
- Passipieri, J. A., Dienes, J., Frank, J., Glazier, J., Portell, A., Venkatesh, K. P., Bliley, J. M., Grybowski, D., Schilling, B. K., Marra, K. G. and Christ, G. J. (2019). "Adipose Stem Cells Enhance Nerve Regeneration and Muscle Function in a Peroneal Nerve Ablation Model." Tissue Eng Part A.
- Pearce, J. M. (2012). "Materials science. Building research equipment with free, open-source hardware." Science **337**(6100): 1303-1304.
- Pereira, B. P., Tan, B. L., Han, H. C., Zou, Y., Aung, K. Z. and Leong, D. T. (2012). "Intramuscular nerve damage in lacerated skeletal muscles may direct the inflammatory cytokine response during recovery." J Cell Biochem **113**(7): 2330-2345.
- Pereira, B. P., Tan, J. A., Zheng, L., Tan, B. L., Lahiri, A., Lim, A. Y. and Kumar, V. P. (2006). "The cut intramuscular nerve affects the recovery in the lacerated skeletal muscle." J Orthop Res **24**(1): 102-111.
- Petersen, A. M., Penkowa, M., Iversen, M., Frydelund-Larsen, L., Andersen, J. L., Mortensen, J., Lange, P. and Pedersen, B. K. (2007). "Elevated levels of IL-18 in plasma and skeletal muscle in chronic obstructive pulmonary disease." Lung **185**(3): 161-171.
- Peterson, J. M. and Pizza, F. X. (2009). "Cytokines derived from cultured skeletal muscle cells after mechanical strain promote neutrophil chemotaxis in vitro." J Appl Physiol (1985) **106**(1): 130-137.

- Philippou, A., Maridaki, M., Halapas, A. and Koutsilieris, M. (2007). "The role of the insulin-like growth factor 1 (IGF-1) in skeletal muscle physiology." *In Vivo* **21**(1): 45-54.
- Piccolo, N. S., Piccolo, M. S., de Paula Piccolo, N., de Paula Piccolo, P., de Paula Piccolo, N., Daher, R. P., Lobo, R. P., Daher, S. P. and Piccolo, M. T. S. (2020). "Fat Grafting for Treatment of Facial Burns and Burn Scars." *Clinics in plastic surgery* **47**(1): 119-130.
- Plomgaard, P., Penkowa, M. and Pedersen, B. K. (2005). "Fiber type specific expression of TNF-alpha, IL-6 and IL-18 in human skeletal muscles." *Exerc Immunol Rev* **11**: 53-63.
- Poornejad, N., Buckmiller, E., Schaumann, L., Wang, H., Wisco, J., Roeder, B., Reynolds, P. and Cook, A. (2017). "Re-epithelialization of whole porcine kidneys with renal epithelial cells." *J Tissue Eng* **8**: 2041731417718809.
- Porzionato, A., Stocco, E., Barbon, S., Grandi, F., Macchi, V. and De Caro, R. (2018). "Tissue-Engineered Grafts from Human Decellularized Extracellular Matrices: A Systematic Review and Future Perspectives." *Int J Mol Sci* **19**(12).
- Posterino, G. S., Lamb, G. D. and Stephenson, D. G. (2000). "Twitch and tetanic force responses and longitudinal propagation of action potentials in skinned skeletal muscle fibres of the rat." *J Physiol* **527 Pt 1**: 131-137.
- Pratt, S. J. P., Shah, S. B., Ward, C. W., Kerr, J. P., Stains, J. P. and Lovering, R. M. (2015). "Recovery of altered neuromuscular junction morphology and muscle function in mdx mice after injury." *Cell Mol Life Sci* **72**(1): 153-164.
- Price, A. P., Godin, L. M., Domek, A., Cotter, T., D'Cunha, J., Taylor, D. A. and Panoskaltsis-Mortari, A. (2015). "Automated decellularization of intact, human-sized lungs for tissue engineering." *Tissue Eng Part C Methods* **21**(1): 94-103.
- Primus, F. E. and Harris, H. W. (2013). "A critical review of biologic mesh use in ventral hernia repairs under contaminated conditions." *Hernia* **17**(1): 21-30.
- Qin, H., Holdbrooks, A. T., Liu, Y., Reynolds, S. L., Yanagisawa, L. L. and Benveniste, E. N. (2012). "SOCS3 deficiency promotes M1 macrophage polarization and inflammation." *J Immunol* **189**(7): 3439-3448.
- Qiu, X., Fandel, T. M., Ferretti, L., Albersen, M., Orabi, H., Zhang, H., Lin, G., Lin, C. S., Schroeder, T. and Lue, T. F. (2012). "Both immediate and delayed intracavernous injection of autologous adipose-derived stromal vascular fraction enhances recovery of erectile function in a rat model of cavernous nerve injury." *Eur Urol* **62**(4): 720-727.
- Ranganathan, K., Wong, V. W., Krebsbach, P. H., Wang, S. C., Cederna, P. S. and Levi, B. (2013). "Fat grafting for thermal injury: current state and future directions." *J Burn Care Res* **34**(2): 219-226.
- Rao, N., Agmon, G., Tierney, M. T., Ungerleider, J. L., Braden, R. L., Sacco, A. and Christman, K. L. (2017). "Engineering an Injectable Muscle-Specific Microenvironment for Improved

- Cell Delivery Using a Nanofibrous Extracellular Matrix Hydrogel." *ACS Nano* **11**(4): 3851-3859.
- Reid, M. B. and Li, Y. P. (2001). "Tumor necrosis factor-alpha and muscle wasting: a cellular perspective." *Respir Res* **2**(5): 269-272.
- Riecke, B., Assaf, A. T., Heiland, M., Al-Dam, A., Grobe, A., Blessmann, M. and Wikner, J. (2015). "Local full-thickness skin graft of the donor arm--a novel technique for the reduction of donor site morbidity in radial forearm free flap." *Int J Oral Maxillofac Surg* **44**(8): 937-941.
- Rigamonti, E., Touvier, T., Clementi, E., Manfredi, A. A., Brunelli, S. and Rovere-Querini, P. (2013). "Requirement of inducible nitric oxide synthase for skeletal muscle regeneration after acute damage." *J Immunol* **190**(4): 1767-1777.
- Rigotti, G., Marchi, A., Stringhini, P., Baroni, G., Galie, M., Molino, A. M., Mercanti, A., Micciolo, R. and Sbarbati, A. (2010). "Determining the oncological risk of autologous lipoaspirate grafting for post-mastectomy breast reconstruction." *Aesthetic Plast Surg* **34**(4): 475-480.
- Roberts, S. E., Thibaudeau, S., Burrell, J. C., Zager, E. L., Cullen, D. K. and Levin, L. S. (2017). "To reverse or not to reverse? A systematic review of autograft polarity on functional outcomes following peripheral nerve repair surgery." *Microsurgery* **37**(2): 169-174.
- Roberts, T. L., III, Toledo, L. S. and Badin, A. Z. (2001). "Augmentation of the Buttocks by Micro Fat Grafting." *Aesthetic Surgery Journal* **21**(4): 311-319.
- Robertson, M. J., Dries-Devlin, J. L., Kren, S. M., Burchfield, J. S. and Taylor, D. A. (2014). "Optimizing recellularization of whole decellularized heart extracellular matrix." *PLoS One* **9**(2): e90406.
- Robinson, L. R. (2000). "Traumatic injury to peripheral nerves." *Muscle Nerve* **23**(6): 863-873.
- Roca-Rivada, A., Alonso, J., Al-Massadi, O., Castela, C., Peinado, J. R., Seoane, L. M., Casanueva, F. F. and Pardo, M. (2011). "Secretome analysis of rat adipose tissues shows location-specific roles for each depot type." *J Proteomics* **74**(7): 1068-1079.
- Rodriguez Sanchez, D. N., de Lima Resende, L. A., Boff Araujo Pinto, G., de Carvalho Bovolato, A. L., Possebon, F. S., Deffune, E. and Amorim, R. M. (2019). "Canine Adipose-Derived Mesenchymal Stromal Cells Enhance Neuroregeneration in a Rat Model of Sciatic Nerve Crush Injury." *Cell Transplant* **28**(1): 47-54.
- Ronchi, G., Morano, M., Fregnan, F., Pugliese, P., Crosio, A., Tos, P., Geuna, S., Haastert-Talini, K. and Gambarotta, G. (2019). "The Median Nerve Injury Model in Pre-clinical Research - A Critical Review on Benefits and Limitations." *Front Cell Neurosci* **13**: 288.
- Ronchi, G., Nicolino, S., Raimondo, S., Tos, P., Battiston, B., Papalia, I., Varejao, A. S., Giacobini-Robecchi, M. G., Perroteau, I. and Geuna, S. (2009). "Functional and

- morphological assessment of a standardized crush injury of the rat median nerve." J Neurosci Methods **179**(1): 51-57.
- Ronchi, G., Raimondo, S., Varejao, A. S., Tos, P., Perroteau, I. and Geuna, S. (2010). "Standardized crush injury of the mouse median nerve." J Neurosci Methods **188**(1): 71-75.
- Roth, S. P., Glauche, S. M., Plenge, A., Erbe, I., Heller, S. and Burk, J. (2017). "Automated freeze-thaw cycles for decellularization of tendon tissue - a pilot study." BMC Biotechnol **17**(1): 13.
- Rotshenker, S. (2011). "Wallerian degeneration: the innate-immune response to traumatic nerve injury." J Neuroinflammation **8**: 109.
- Sacco, A., Doyonnas, R., Kraft, P., Vitorovic, S. and Blau, H. M. (2008). "Self-renewal and expansion of single transplanted muscle stem cells." Nature **456**(7221): 502-506.
- Saied, A., Shekaari, M. A., Sadeghifar, A. and Karbalaiekhani, A. (2015). "Introduction of a New Suture Method in Repair of Peripheral Nerves Injured with a Sharp Mechanism." Arch Bone Jt Surg **3**(4): 254-259.
- Saldin, L. T., Cramer, M. C., Velankar, S. S., White, L. J. and Badylak, S. F. (2017). "Extracellular matrix hydrogels from decellularized tissues: Structure and function." Acta Biomater **49**: 1-15.
- Saller, M. M., Huettl, R. E., Mayer, J. M., Feuchtinger, A., Krug, C., Holzbach, T. and Volkmer, E. (2018). "Validation of a novel animal model for sciatic nerve repair with an adipose-derived stem cell loaded fibrin conduit." Neural Regen Res **13**(5): 854-861.
- Santiago, L. Y., Clavijo-Alvarez, J., Brayfield, C., Rubin, J. P. and Marra, K. G. (2009). "Delivery of adipose-derived precursor cells for peripheral nerve repair." Cell Transplant **18**(2): 145-158.
- Sarikcioglu, L., Demirel, B. M. and Utuk, A. (2009). "Walking track analysis: an assessment method for functional recovery after sciatic nerve injury in the rat." Folia Morphol (Warsz) **68**(1): 1-7.
- Sbitany, H. and Serletti, J. M. (2011). "Acellular dermis-assisted prosthetic breast reconstruction: a systematic and critical review of efficacy and associated morbidity." Plast Reconstr Surg **128**(6): 1162-1169.
- Scarritt, M. E., Pashos, N. C. and Bunnell, B. A. (2015). "A review of cellularization strategies for tissue engineering of whole organs." Front Bioeng Biotechnol **3**: 43.
- Schaakxs, D., Kalbermatten, D. F., Raffoul, W., Wiberg, M. and Kingham, P. J. (2013). "Regenerative cell injection in denervated muscle reduces atrophy and enhances recovery following nerve repair." Muscle Nerve **47**(5): 691-701.

- Schilling, B. K., Lamberti, K. K., Snowden, M. J., Baker, J. S., Byrd, K., Komatsu, C., Solari, M. G. and Marra, K. G. (2019). "Design and Fabrication of an Automatable, 3D Printed Perfusion Device for Tissue Infusion and Perfusion Engineering." Tissue Eng Part A.
- Schilling, B. K. and Marra, K. G. (2019). Adipose Tissue-Derived Stem Cells: Sources and Therapeutic Applications. Encyclopedia of Tissue Engineering and Regenerative Medicine. R. L. Reis. Oxford, Academic Press: 45-56.
- Schilling, B. K., Schusterman, M. A., 2nd, Kim, D. Y., Repko, A. J., Klett, K. C., Christ, G. J. and Marra, K. G. (2019). "Adipose-derived stem cells delay muscle atrophy after peripheral nerve injury in the rodent model." Muscle Nerve **59**(5): 603-610.
- Schmidt, C. E. and Leach, J. B. (2003). "Neural tissue engineering: strategies for repair and regeneration." Annu Rev Biomed Eng **5**: 293-347.
- Schwarzer, C., Mucke, T., Wolff, K. D., Loeffelbein, D. J. and Rau, A. (2016). "Donor site morbidity and flap perfusion of subfascial and suprafascial radial forearm flaps: A randomized prospective clinical comparison trial." J Craniomaxillofac Surg **44**(9): 1299-1304.
- Sciorati, C., Rigamonti, E., Manfredi, A. A. and Rovere-Querini, P. (2016). "Cell death, clearance and immunity in the skeletal muscle." Cell Death Differ **23**(6): 927-937.
- Sevivas, N., Teixeira, F. G., Portugal, R., Araujo, L., Carrico, L. F., Ferreira, N., Vieira da Silva, M., Espregueira-Mendes, J., Anjo, S., Manadas, B., Sousa, N. and Salgado, A. J. (2016). "Mesenchymal Stem Cell Secretome: A Potential Tool for the Prevention of Muscle Degenerative Changes Associated With Chronic Rotator Cuff Tears." Am J Sports Med.
- Shankaran, V., Weber, D. J., Reed, R. L., 2nd and Luchette, F. A. (2011). "A review of available prosthetics for ventral hernia repair." Ann Surg **253**(1): 16-26.
- Shehadi, J. A. and Elzein, S. M. (2017). "Review of commercially available demineralized bone matrix products for spinal fusions: A selection paradigm." Surg Neurol Int **8**: 203.
- Sheikh, E. S., Sheikh, E. S. and Fetterolf, D. E. (2014). "Use of dehydrated human amniotic membrane allografts to promote healing in patients with refractory non healing wounds." Int Wound J **11**(6): 711-717.
- Sheikh, Z., Najeeb, S., Khurshid, Z., Verma, V., Rashid, H. and Glogauer, M. (2015). "Biodegradable materials for bone repair and tissue engineering applications." Materials **8**(9): 5744-5794.
- Sicari, B. M., Rubin, J. P., Dearth, C. L., Wolf, M. T., Ambrosio, F., Boninger, M., Turner, N. J., Weber, D. J., Simpson, T. W., Wyse, A., Brown, E. H., Dziki, J. L., Fisher, L. E., Brown, S. and Badylak, S. F. (2014). "An acellular biologic scaffold promotes skeletal muscle formation in mice and humans with volumetric muscle loss." Sci Transl Med **6**(234): 234ra258.

- Sivak, W. N., Bliley, J. M. and Marra, K. G. (2014). "Polymeric biomaterials for nerve regeneration: fabrication and implantation of a biodegradable nerve guide." Methods Mol Biol **1162**: 139-148.
- Smith, C., Kruger, M. J., Smith, R. M. and Myburgh, K. H. (2008). "The inflammatory response to skeletal muscle injury: illuminating complexities." Sports Med **38**(11): 947-969.
- Smith, O. J., Leigh, R., Kanapathy, M., Macneal, P., Jell, G., Hachach-Haram, N., Mann, H. and Mosahebi, A. (2020). "Fat grafting and platelet-rich plasma for the treatment of diabetic foot ulcers: A feasibility-randomised controlled trial." International Wound Journal.
- Snyder, R. J. (2005). "Treatment of nonhealing ulcers with allografts." Clin Dermatol **23**(4): 388-395.
- Sowa, Y., Imura, T., Numajiri, T., Nishino, K. and Fushiki, S. (2012). "Adipose-derived stem cells produce factors enhancing peripheral nerve regeneration: influence of age and anatomic site of origin." Stem Cells Dev **21**(11): 1852-1862.
- Spalding, K. L., Arner, E., Westermarck, P. O., Bernard, S., Buchholz, B. A., Bergmann, O., Blomqvist, L., Hoffstedt, J., Naslund, E., Britton, T., Concha, H., Hassan, M., Ryden, M., Frisen, J. and Arner, P. (2008). "Dynamics of fat cell turnover in humans." Nature **453**(7196): 783-787.
- Stratos, I., Rotter, R., Eipel, C., Mittlmeier, T. and Vollmar, B. (2007). "Granulocyte-colony stimulating factor enhances muscle proliferation and strength following skeletal muscle injury in rats." J Appl Physiol (1985) **103**(5): 1857-1863.
- Stratton, J. A. and Shah, P. T. (2016). "Macrophage polarization in nerve injury: do Schwann cells play a role?" Neural Regen Res **11**(1): 53-57.
- Strong, A. L., Rubin, J. P., Kozlow, J. H. and Cederna, P. S. (2019). "Fat Grafting for the Treatment of Scleroderma." Plastic and reconstructive surgery **144**(6): 1498-1507.
- Su, N., Gao, P. L., Wang, K., Wang, J. Y., Zhong, Y. and Luo, Y. (2017). "Fibrous scaffolds potentiate the paracrine function of mesenchymal stem cells: A new dimension in cell-material interaction." Biomaterials **141**: 74-85.
- Suganuma, S., Tada, K., Hayashi, K., Takeuchi, A., Sugimoto, N., Ikeda, K. and Tsuchiya, H. (2013). "Uncultured adipose-derived regenerative cells promote peripheral nerve regeneration." J Orthop Sci **18**(1): 145-151.
- Sultan, S. M., Barr, J. S., Butala, P., Davidson, E. H., Weinstein, A. L., Knobel, D., Saadeh, P. B., Warren, S. M., Coleman, S. R. and Hazen, A. (2012). "Fat grafting accelerates revascularisation and decreases fibrosis following thermal injury." J Plast Reconstr Aesthet Surg **65**(2): 219-227.

- Sun, F., Zhou, K., Mi, W. J. and Qiu, J. H. (2011). "Repair of facial nerve defects with decellularized artery allografts containing autologous adipose-derived stem cells in a rat model." Neurosci Lett **499**(2): 104-108.
- Sunderland, S. (1951). "A classification of peripheral nerve injuries producing loss of function." Brain **74**(4): 491-516.
- Syed, O., Walters, N. J., Day, R. M., Kim, H. W. and Knowles, J. C. (2014). "Evaluation of decellularization protocols for production of tubular small intestine submucosa scaffolds for use in oesophageal tissue engineering." Acta Biomater **10**(12): 5043-5054.
- Taylor, C. A., Braza, D., Rice, J. B. and Dillingham, T. (2008). "The incidence of peripheral nerve injury in extremity trauma." American journal of physical medicine & rehabilitation **87**(5): 381-385.
- Tedesco, F. S., Dellavalle, A., Diaz-Manera, J., Messina, G. and Cossu, G. (2010). "Repairing skeletal muscle: regenerative potential of skeletal muscle stem cells." J Clin Invest **120**(1): 11-19.
- Terenghi, G. (1999). "Peripheral nerve regeneration and neurotrophic factors." J Anat **194** ( Pt 1): 1-14.
- Tidball, J. G. (2017). "Regulation of muscle growth and regeneration by the immune system." Nat Rev Immunol **17**(3): 165-178.
- Tomita, K., Madura, T., Mantovani, C. and Terenghi, G. (2012). "Differentiated adipose-derived stem cells promote myelination and enhance functional recovery in a rat model of chronic denervation." J Neurosci Res **90**(7): 1392-1402.
- Tonnard, P., Verpaele, A., Peeters, G., Hamdi, M., Cornelissen, M. and Declercq, H. (2013). "Nanofat grafting: basic research and clinical applications." Plast Reconstr Surg **132**(4): 1017-1026.
- Toumi, H., F'Guyer, S. and Best, T. M. (2006). "The role of neutrophils in injury and repair following muscle stretch." J Anat **208**(4): 459-470.
- Tran, K., Cimon, K., Severn, M., Pessoa-Silva, C. L. and Conly, J. (2012). "Aerosol generating procedures and risk of transmission of acute respiratory infections to healthcare workers: a systematic review." PLoS One **7**(4): e35797.
- Tremp, M., Meyer Zu Schwabedissen, M., Kappos, E. A., Engels, P. E., Fischmann, A., Scherberich, A., Schaefer, D. J. and Kalbermatten, D. F. (2015). "The regeneration potential after human and autologous stem cell transplantation in a rat sciatic nerve injury model can be monitored by MRI." Cell Transplant **24**(2): 203-211.
- Tsuchiya, M., Sekiai, S., Hatakeyama, H., Koide, M., Chawewannakorn, C., Yaoita, F., Tan-No, K., Sasaki, K., Watanabe, M., Sugawara, S., Endo, Y., Itoi, E., Hagiwara, Y. and Kanzaki, M. (2018). "Neutrophils Provide a Favorable IL-1-Mediated Immunometabolic Niche that

- Primes GLUT4 Translocation and Performance in Skeletal Muscles." Cell Rep **23**(8): 2354-2364.
- Tucci, M., Quatraro, C., Dammacco, F. and Silvestris, F. (2006). "Interleukin-18 overexpression as a hallmark of the activity of autoimmune inflammatory myopathies." Clin Exp Immunol **146**(1): 21-31.
- Turer, D. M., Good, C. H., Schilling, B. K., Turer, R. W., Karlowsky, N. R., Dvoracek, L. A., Ban, H., Chang, J. S. and Rubin, J. P. (2021). "Improved Testing and Design of Intubation Boxes During the COVID-19 Pandemic." Ann Emerg Med **77**(1): 1-10.
- Turin, S. Y., Fracol, M., Keller, E., Markl, M., Collins, J., Krochmal, D. and Kim, J. Y. S. (2020). "Gluteal Vein Anatomy: Location, Caliber, Impact of Patient Positioning, and Implications for Fat Grafting." Aesthet Surg J **40**(6): 642-649.
- Uezumi, A., Ito, T., Morikawa, D., Shimizu, N., Yoneda, T., Segawa, M., Yamaguchi, M., Ogawa, R., Matev, M. M., Miyagoe-Suzuki, Y., Takeda, S., Tsujikawa, K., Tsuchida, K., Yamamoto, H. and Fukada, S. (2011). "Fibrosis and adipogenesis originate from a common mesenchymal progenitor in skeletal muscle." J Cell Sci **124**(Pt 21): 3654-3664.
- Ungerleider, J. L., Johnson, T. D., Hernandez, M. J., Elhag, D. I., Braden, R. L., Dzieciatkowska, M., Osborn, K. G., Hansen, K. C., Mahmud, E. and Christman, K. L. (2016). "Extracellular Matrix Hydrogel Promotes Tissue Remodeling, Arteriogenesis, and Perfusion in a Rat Hindlimb Ischemia Model." JACC Basic Transl Sci **1**(1-2): 32-44.
- Ungerleider, J. L., Johnson, T. D., Rao, N. and Christman, K. L. (2015). "Fabrication and characterization of injectable hydrogels derived from decellularized skeletal and cardiac muscle." Methods **84**: 53-59.
- Urso, M. L., Szelenyi, E. R., Warren, G. L. and Barnes, B. R. (2010). "Matrix metalloprotease-3 and tissue inhibitor of metalloprotease-1 mRNA and protein levels are altered in response to traumatic skeletal muscle injury." Eur J Appl Physiol **109**(5): 963-972.
- Varejao, A. S., Meek, M. F., Ferreira, A. J., Patricio, J. A. and Cabrita, A. M. (2001). "Functional evaluation of peripheral nerve regeneration in the rat: walking track analysis." J Neurosci Methods **108**(1): 1-9.
- Vela, F. J., Martinez-Chacon, G., Ballestin, A., Campos, J. L., Sanchez-Margallo, F. M. and Abellan, E. (2020). "Animal models used to study direct peripheral nerve repair: a systematic review." Neural Regen Res **15**(3): 491-502.
- Verdu, E., Ceballos, D., Vilches, J. J. and Navarro, X. (2000). "Influence of aging on peripheral nerve function and regeneration." J Peripher Nerv Syst **5**(4): 191-208.
- Villalta, S. A., Deng, B., Rinaldi, C., Wehling-Henricks, M. and Tidball, J. G. (2011). "IFN-gamma promotes muscle damage in the mdx mouse model of Duchenne muscular dystrophy by suppressing M2 macrophage activation and inhibiting muscle cell proliferation." J Immunol **187**(10): 5419-5428.

- Visser, M., Pahor, M., Taaffe, D. R., Goodpaster, B. H., Simonsick, E. M., Newman, A. B., Nevitt, M. and Harris, T. B. (2002). "Relationship of interleukin-6 and tumor necrosis factor- $\alpha$  with muscle mass and muscle strength in elderly men and women: the Health ABC Study." J Gerontol A Biol Sci Med Sci **57**(5): M326-332.
- Vivo, M., Puigdemasa, A., Casals, L., Asensio, E., Udina, E. and Navarro, X. (2008). "Immediate electrical stimulation enhances regeneration and reinnervation and modulates spinal plastic changes after sciatic nerve injury and repair." Exp Neurol **211**(1): 180-193.
- von Moers, A., Zwirner, A., Reinhold, A., Bruckmann, O., van Landeghem, F., Stoltenburg-Didinger, G., Schuppan, D., Herbst, H. and Schuelke, M. (2005). "Increased mRNA expression of tissue inhibitors of metalloproteinase-1 and -2 in Duchenne muscular dystrophy." Acta Neuropathol **109**(3): 285-293.
- Wagner, P. D. (2011). "The critical role of VEGF in skeletal muscle angiogenesis and blood flow." Biochem Soc Trans **39**(6): 1556-1559.
- Walsh, M. E., Sloane, L. B., Fischer, K. E., Austad, S. N., Richardson, A. and Van Remmen, H. (2015). "Use of Nerve Conduction Velocity to Assess Peripheral Nerve Health in Aging Mice." J Gerontol A Biol Sci Med Sci **70**(11): 1312-1319.
- Walsh, S. K., Gordon, T., Addas, B. M., Kemp, S. W. and Midha, R. (2010). "Skin-derived precursor cells enhance peripheral nerve regeneration following chronic denervation." Exp Neurol **223**(1): 221-228.
- Wang, D., Huang, X., Fu, G., Gu, L., Liu, X., Wang, H., Hu, J., Yi, J., Niu, X. and Zhu, Q. (2014). "A simple model of radial nerve injury in the rhesus monkey to evaluate peripheral nerve repair." Neural Regen Res **9**(10): 1041-1046.
- Wang, L., Xue, K., Wang, Y., Niu, L., Li, L., Zhong, T., Guo, J., Feng, J., Song, T. and Zhang, H. (2018). "Molecular and functional characterization of the adiponectin (AdipoQ) gene in goat skeletal muscle satellite cells." Asian-Australas J Anim Sci **31**(8): 1088-1097.
- Wang, S. and Cai, L. (2010). "Polymers for Fabricating Nerve Conduits." International Journal of Polymer Science **2010**: 138686.
- Wang, Y. and Pessin, J. E. (2013). "Mechanisms for fiber-type specificity of skeletal muscle atrophy." Curr Opin Clin Nutr Metab Care **16**(3): 243-250.
- Watanabe, Y., Sasaki, R., Matsumine, H., Yamato, M. and Okano, T. (2017). "Undifferentiated and differentiated adipose-derived stem cells improve nerve regeneration in a rat model of facial nerve defect." J Tissue Eng Regen Med **11**(2): 362-374.
- Watt, M. J. and Hoy, A. J. (2012). "Lipid metabolism in skeletal muscle: generation of adaptive and maladaptive intracellular signals for cellular function." Am J Physiol Endocrinol Metab **302**(11): E1315-1328.

- Wei, Y., Gong, K., Zheng, Z., Wang, A., Ao, Q., Gong, Y. and Zhang, X. (2011). "Chitosan/silk fibroin-based tissue-engineered graft seeded with adipose-derived stem cells enhances nerve regeneration in a rat model." J Mater Sci Mater Med **22**(8): 1947-1964.
- Wright, C. R., Brown, E. L., Della-Gatta, P. A., Ward, A. C., Lynch, G. S. and Russell, A. P. (2014). "G-CSF does not influence C2C12 myogenesis despite receptor expression in healthy and dystrophic skeletal muscle." Front Physiol **5**: 170.
- Wu, R. X., He, X. T., Zhu, J. H., Yin, Y., Li, X., Liu, X. and Chen, F. M. (2019). "Modulating macrophage responses to promote tissue regeneration by changing the formulation of bone extracellular matrix from filler particles to gel bioscaffolds." Mater Sci Eng C Mater Biol Appl **101**: 330-340.
- Wu, S. H., Huang, S. H., Lo, Y. C., Chai, C. Y., Lee, S. S., Chang, K. P., Lin, S. D., Lai, C. S., Yeh, J. L. and Kwan, A. L. (2015). "Autologous adipose-derived stem cells attenuate muscular atrophy and protect spinal cord ventral horn motor neurons in an animal model of burn injury." Cytotherapy **17**(8): 1066-1075.
- Xu, P., Yu, Q., Huang, H., Zhang, W. J. and Li, W. (2018). "Nanofat Increases Dermis Thickness and Neovascularization in Photoaged Nude Mouse Skin." Aesthetic Plast Surg **42**(2): 343-351.
- Xu, Y., Zhang, Z., Chen, X., Li, R., Li, D. and Feng, S. (2016). "A Silk Fibroin/Collagen Nerve Scaffold Seeded with a Co-Culture of Schwann Cells and Adipose-Derived Stem Cells for Sciatic Nerve Regeneration." PLoS One **11**(1): e0147184.
- Yang, R., Fang, F., Wang, J. and Guo, H. (2015). "Adipose-derived stem cells ameliorate erectile dysfunction after cavernous nerve cryoinjury." Andrology **3**(4): 694-701.
- Yang, W. and Hu, P. (2018). "Skeletal muscle regeneration is modulated by inflammation." J Orthop Translat **13**: 25-32.
- Yao, C., Shi, X., Zhang, Z., Zhou, S., Qian, T., Wang, Y., Ding, F., Gu, X. and Yu, B. (2016). "Hypoxia-Induced Upregulation of miR-132 Promotes Schwann Cell Migration After Sciatic Nerve Injury by Targeting PRKAG3." Mol Neurobiol **53**(8): 5129-5139.
- Ying, C., Yang, M., Zheng, X., Hu, W. and Wang, X. (2013). "Effects of intracavernous injection of adipose-derived stem cells on cavernous nerve regeneration in a rat model." Cell Mol Neurobiol **33**(2): 233-240.
- Ying, C. C., Yang, M., Wang, Y., Guo, Y. L., Hu, W. L. and Zheng, X. M. (2019). "Neural-like cells from adipose-derived stem cells for cavernous nerve injury in rats." Neural Regen Res **14**(6): 1085-1090.
- Yoganarasimha, S., Trahan, W. R., Best, A. M., Bowlin, G. L., Kitten, T. O., Moon, P. C. and Madurantakam, P. A. (2014). "Peracetic acid: a practical agent for sterilizing heat-labile polymeric tissue-engineering scaffolds." Tissue Eng Part C Methods **20**(9): 714-723.

- Yong, K. W., Li, Y., Liu, F., Bin, G., Lu, T. J., Wan Abas, W. A., Wan Safwani, W. K., Pingguan-Murphy, B., Ma, Y., Xu, F. and Huang, G. (2016). "Paracrine Effects of Adipose-Derived Stem Cells on Matrix Stiffness-Induced Cardiac Myofibroblast Differentiation via Angiotensin II Type 1 Receptor and Smad7." Sci Rep **6**: 33067.
- You, D., Jang, M. J., Kim, B. H., Song, G., Lee, C., Suh, N., Jeong, I. G., Ahn, T. Y. and Kim, C. S. (2015). "Comparative study of autologous stromal vascular fraction and adipose-derived stem cells for erectile function recovery in a rat model of cavernous nerve injury." Stem Cells Transl Med **4**(4): 351-358.
- You, D., Jang, M. J., Lee, J., Suh, N., Jeong, I. G., Sohn, D. W., Kim, S. W., Ahn, T. Y. and Kim, C. S. (2013). "Comparative analysis of periprostatic implantation and intracavernosal injection of human adipose tissue-derived stem cells for erectile function recovery in a rat model of cavernous nerve injury." Prostate **73**(3): 278-286.
- Young, S., Flynn, L. E. and Amsden, B. G. (2018). "Adipose-derived stem cells in a resilient in situ forming hydrogel modulate macrophage phenotype." Tissue Eng Part A.
- Zammit, P. S. (2017). "Function of the myogenic regulatory factors Myf5, MyoD, Myogenin and MRF4 in skeletal muscle, satellite cells and regenerative myogenesis." Semin Cell Dev Biol **72**: 19-32.
- Zannettino, A. C., Paton, S., Arthur, A., Khor, F., Itescu, S., Gimble, J. M. and Gronthos, S. (2008). "Multipotential human adipose-derived stromal stem cells exhibit a perivascular phenotype in vitro and in vivo." J Cell Physiol **214**(2): 413-421.
- Zhan, W., Marre, D., Mitchell, G. M., Morrison, W. A. and Lim, S. Y. (2016). "Tissue Engineering by Intrinsic Vascularization in an In Vivo Tissue Engineering Chamber." J Vis Exp(111).
- Zhang, D., Zhang, Y., Zhang, Y., Yi, H., Wang, Z., Wu, R., He, D., Wei, G., Wei, S., Hu, Y., Deng, J., Criswell, T., Yoo, J., Zhou, Y. and Atala, A. (2017). "(\*) Tissue-Specific Extracellular Matrix Enhances Skeletal Muscle Precursor Cell Expansion and Differentiation for Potential Application in Cell Therapy." Tissue Eng Part A **23**(15-16): 784-794.
- Zhang, H., Yang, L., Yang, X. G., Wang, F., Feng, J. T., Hua, K. C., Li, Q. and Hu, Y. C. (2019). "Demineralized Bone Matrix Carriers and their Clinical Applications: An Overview." Orthop Surg **11**(5): 725-737.
- Zhang, Q., Hwang, J. W., Oh, J. H., Park, C. H., Chung, S. H., Lee, Y. S., Baek, J. H., Ryoo, H. M. and Woo, K. M. (2017). "Effects of the fibrous topography-mediated macrophage phenotype transition on the recruitment of mesenchymal stem cells: An in vivo study." Biomaterials **149**: 77-87.
- Zhang, Q., Johnson, J. A., Dunne, L. W., Chen, Y., Iyyanki, T., Wu, Y., Chang, E. I., Branch-Brooks, C. D., Robb, G. L. and Butler, C. E. (2016). "Decellularized skin/adipose tissue flap matrix for engineering vascularized composite soft tissue flaps." Acta Biomater **35**: 166-184.

- Zhao, H., Shang, Q., Pan, Z., Bai, Y., Li, Z., Zhang, H., Zhang, Q., Guo, C., Zhang, L. and Wang, Q. (2018). "Exosomes From Adipose-Derived Stem Cells Attenuate Adipose Inflammation and Obesity Through Polarizing M2 Macrophages and Beiging in White Adipose Tissue." Diabetes **67**(2): 235-247.
- Zhou, J., Fritze, O., Schleicher, M., Wendel, H. P., Schenke-Layland, K., Harasztosi, C., Hu, S. and Stock, U. A. (2010). "Impact of heart valve decellularization on 3-D ultrastructure, immunogenicity and thrombogenicity." Biomaterials **31**(9): 2549-2554.
- Zigmond, R. E. and Echevarria, F. D. (2019). "Macrophage biology in the peripheral nervous system after injury." Prog Neurobiol **173**: 102-121.
- Zimmerlin, L., Donnenberg, V. S., Pfeifer, M. E., Meyer, E. M., Peault, B., Rubin, J. P. and Donnenberg, A. D. (2010). "Stromal vascular progenitors in adult human adipose tissue." Cytometry A **77**(1): 22-30.
- Zuo, Q., Wang, S. C., Yu, X. K. and Chao, W. W. (2018). "Response of macrophages in rat skeletal muscle after eccentric exercise." Chin J Traumatol **21**(2): 88-95.